The discrimination between cosmic positrons and protons with the Transition Radiation Detector of the AMS experiment on the International Space Station

Von der Fakultät für Mathematik, Informatik und Naturwissenschaften der RWTH Aachen University zur Erlangung des akademischen Grades eines Doktors der Naturwissenschaften genehmigte Dissertation

vorgelegt von

Diplom-Physiker

Mark Millinger

aus Budapest

Berichter: Univ.-Prof Dr.rer.nat Stefan Schael
em.Univ-Prof Dr.rer.nat Klaus Lübelsmeyer

Tag der mündlichen Prüfung: 08.Oktober 2012

Kurzfassung

Das Ziel dieser Arbeit ist die Entwicklung und Validierung einer Methode zur Teilchenidentifikation mit dem Übergangsstrahlungsdetektor (Transition Radiation Detector, TRD) des Alpha Magnetic Spectrometer AMS-02, um die Bestimmung des Positronanteils im Leptonfluss der kosmischen Strahlung zu ermöglichen.

Unabhängige astrophysikalische und kosmologische Messungen deuten darauf hin, dass ein signifikanter Anteil von etwa 23 % der Energiedichte des Universums aus einer unbekannten Form von Materie besteht, der sogenannten Dunklen Materie. Das Neutralino, als der bekannteste Kandidat für Dunkle Materie, kann ein zusätzliches Signal im Spektrum der kosmischen Strahlung erzeugen.

Der Anteil an Positronen im Leptonfluss kosmischer Strahlung scheint ein solches Signal Dunkler Materie bei hohen Teilchenimpulsen zu enthalten. Die derzeit präzisesten Daten im Bereich des Überschusses wurden dabei von den beiden satellitengestützten Detektoren PAMELA und Fermi geliefert. Impulsabhängige, systematische Unsicherheiten, die insbesondere aus der Fehlrekonstruktion von Protonen als Positronen entstehen, können das erwartete Signal imitieren. Entsteht dieser Überschuss an Positronen jedoch aufgrund von Dunkler Materie, so sollte dieser Anteil ab einer theoretischen Energieschwelle wieder auf den erwarteten Verlauf gemäß der Teilchenpropagation sinken. Der bisher vermessene Energiebereich zeigt diesen Verlauf nicht. Die Signatur soll mit AMS-02, welches einerseits eine wesentlich höhere Statistik erreichen wird und andererseits Teilchen bis zu höheren Energien vermessen kann, überprüft werden.

Die Anzahl an Ereignissen, die mit einem Detektor aufgezeichnet werden kann, wird zum Einen durch die Kombination aus Apertur und beobachtbarem Raumwinkel, quantifiziert durch die geometrische Akzeptanz, und zum Anderen durch die Messdauer limitiert. Da der kosmische Teilchenfluss als Funktion des Teilchenimpulses in etwa einem Potenzgesetz mit Exponent $\gamma \approx -3$ folgt, ist somit der beobachtbare Impulsbereich nach oben hin eingeschränkt. Durch seine große geometrische Akzeptanz von etwa $0.5\,\mathrm{m^2sr}$, seiner langen Messdauer von mindestens 9 Jahren und seines hohen Protonunterdrückungsfaktors von mehr als 10^6 wird AMS-02 umfangreiche und saubere Leptondaten aufzeichnen und damit zur präzisen Vermessung des Positronanteils der kosmischen Strahlung bis zu hohen

Teilchenimpulsen von bis zu 1 TeV beitragen.

Um den hohen Unterdrückungsfaktor von Protonereignissen zu hohen Impulsbereichen hin zu erreichen, wird die Kombination aus elektromagnetischem Kalorimeter (ECAL) und TRD verwendet. Diese Arbeit beschreibt die Teilchenidentifikation mit dem TRD und bestimmt ihre Güte anhand von vorselektierten Ereignissen aus Daten, die bei einem Strahltest vor dem Transport zur Raumstation genommen wurden, und dem auf der Internationalen Raumstation gesammelten Datensatz. Die dafür benötigten Algorithmen zur Ereignisrekonstruktion, Detektorkalibrierung und Teilchenidentifikation werden diskutiert.

Anhand der TRD-unabhängigen Vorselektion von Ereignissen wird der atmosphärische Myonfluss vermessen. Dies erfolgt durch die Kombination von Myonereignisrate, die auf Meereshöhe am Kennedy Space Center aufgezeichnet wurde, und der in Simulationen ermittelten Detektorakzeptanz. Zusätzlich werden die niederenergetischen Daten, die auf der Internationalen Raumstation gemessen wurden, dazu verwendet, das geomagnetische Feld zu untersuchen. Hierbei wird die Impulsschwelle als Funktion von geodätischem Längen- und Breitengrad bestimmt, unter der Teilchen so stark im Erdmagnetfeld abgelenkt werden, dass sie den Detektor nicht mehr erreichen können.

Die Güte der TRD Ereignisrekonstruktion in vorselektierten Datenereignissen wird mit Simulationen verglichen. Die Effizienz von aufeinanderfolgenden Schritten der Ereignisrekonstruktion, die in geometrische Effekte, Spurrekonstruktion, Qualitätsselektion und Abgleich von Spuren unterteilt werden, wird bestimmt. Die auf einer Spur deponierte Energie wird zur Unterscheidung zwischen Proton- und Leptonereignissen verwendet. Um ein invariantes Signal der deponierten Energie zu gewährleisten, werden Kalibrierungsalgorithmen eingeführt, die die Veränderung der Signalhöhe durch die Signalverstärkung, der Weglänge und des Teilchenimpulses korrigieren. Die Güte der Kalibrierungsalgorithmen wird in Studien zur Signalstabilität und deren Einfluss auf die TRD Teilchenidentifikation untersucht.

Die in dieser Arbeit durchgeführten Studien zur Effizienz und Protonunterdrückung des TRD sind entscheidende Schritte für eine präzise Vermessung von kosmischen Leptonflüssen und deren Positronanteils.

Abstract

The aim of this thesis is the development and validation of a particle identification method with the Transition Radiation Detector (TRD) of the Alpha Magnetic Spectrometer AMS-02 to allow for the determination of the positron fraction in the cosmic lepton flux.

Independent measurements indicate that a significant amount of about 23 % of the energy density in the universe consists of an unknown mass contribution, the so-called Dark Matter. The Neutralino, as the most popular Dark Matter particle candidate, may produce an additional signal in the spectrum of cosmic rays.

The fraction of positrons in the cosmic lepton flux possibly contains such a Dark Matter signal at high particle momenta. The currently most precise measurements in the region of this excess are provided by the satellite-borne PAMELA and Fermi detectors. Momentum-dependent systematic uncertainties, especially the mis-identification of protons as positrons, could imitate the signal. However, if this positron excess is produced by Dark Matter the fraction should decrease above a theoretical energy threshold to the expectations, based on particle propagation. The energy region measured up to now does not show such a progress. Due to its significantly increased event statistics and its capability to measure up to higher particle energies, this signature could be observed with AMS-02.

The number of events, which can be recorded by a detector, is limited by the combination of aperture and observable solid angle, quantified by the geometrical acceptance, and the observation time. As the cosmic particle flux follows a power-law in particle momentum with exponent $\gamma \approx -3$, the observable momentum interval is thus constrained by statistics. Due to its large geometrical acceptance of about $0.5\,\mathrm{m^2sr}$, its long observation time of at least 9 years and its high proton suppression factor of $\gtrsim 10^6$ AMS-02 will record large and clean lepton samples and thus provide a precise measurement of the cosmic positron fraction up to particle momenta less or equal to 1 TeV.

The combination of electromagnetic calorimeter (ECAL) and TRD is necessary to provide the high proton suppression factor at high momenta. This work describes the particle identification with the TRD and evaluates its performance on pre-selected events from a dataset taken on the International Space Station and from data, which have been recorded in a beamtest before the transport to the space station. The necessary algorithms, starting from

event reconstruction through detector calibration up to particle identification are discussed.

The TRD independent event pre-selection is used to determine the sea-level muon flux by the combination of muon event rate, as recorded on ground at Kennedy Space Center, and detector acceptance, extracted from simulations. Additionally, low-energy data recorded on the International Space Station is used to investigate the geomagnetic field. Here, the rigidity cutoff, below which particles are deflected by the geomagnetic field too much to reach the detector, is determined as function of geodetic latitude and longitude.

The performance of the TRD event reconstruction on pre-selected data event samples is compared to simulations. The efficiency of consecutive reconstruction steps, assigned to geometric effects, event reconstruction, quality selection and matching of tracks is determined. The energy depositions on a track are used to disentangle lepton and proton events. Calibration algorithms are introduced to provide invariant energy deposition signal by correcting for the signal variation due to gas gain, path length and particle momentum. The performance of the calibration algorithms is evaluated by signal stability studies and their impact on the TRD particle identification performance.

The TRD efficiency and proton suppression studies performed in this work are crucial steps towards the precise measurement of cosmic lepton fluxes and the cosmic positron fraction.

Acknowledgements

'Every new beginning comes from some other beginning's end',

Lucius Annaeus Seneca

Looking back over the last years, I am amazed and impressed by what has happened. Parallel to the assembly of the AMS detector, all the verifications tests on ground and its deployment on the Space Station, my knowledge, skills and personality have developed. Whatever future will bring, this chapter in my life shaped me as a person and has led me to where I am today. I am grateful for all I have experienced during my PhD studies and I am looking forward to what the future brings.

First of all, I would like to thank my PhD supervisor Prof. Dr. Schael for giving me the opportunity to take an active role in the TRD group. I would also like to thank Prof. Dr. Lübelsmeyer and Nobel Laureate Prof. S.C.C. Ting for their enduring curiosity in my work.

I am grateful to all my colleagues in the TRD group. Especially my officemates T. Kirn and S. Siedenburg were an invaluable source of knowledge and inspiration in prosperous periods and of encouragement in hard times. The indestructible cheerfulness and gentleness of my fellow campaigner in TRD software development C. Chung surprised and motivated me over and over again. Although not deeply in touch with each other I highly appreciate the work of A. Sabellek and M. Heil from Karlsruhe and of F. Spada from Rome. I am thankful to I. Gebauer and A. Obermeier for their support and astonishing performance on proofreading. I am also grateful to G. Schwering who is constantly fighting to keep the bureaucratic machinery running but nevertheless always made time for questions, job-related and private matters.

There are countless people in the AMS collaboration I have to thank. The most frequent technical communication I had with leading offline software developer V. Choutko. I am

grateful for everything I learned from him and for his patience regarding the time schedule and rare performance issues of my source code contributions. I also thank A. Eline and P. Goglov for their continuous and fast IT support. In the italian part of the collaboration the outstanding personalities of B. Bertucci, G. Ambrosi and F. Palmonari have left me with everlasting impressions. I feel deeply grateful to J. Berdugo, whom I appreciate as a valuable role model of a physicist, concerning professional and private life. I also thank S. Rosier-Lees, F. Barao and J. Casaus for inspiring and fruitful discussions about various physics topics. The merriest collaborators I ever encountered, J. van Es and A. Pauw, were an inexhaustible source of contagious joy of life.

Over the years, especially in my time abroad, a handful of collaborators and colleagues became friends. I feel very grateful to G. Alberti, M. Duranti, A. Oliva, P. Zuccon, and V. Bindi for the the unforgettable moments we shared.

Last but not least I thank my family and friends. Due to my strong focus on work life they had to suffer a lot for this thesis. I would like to thank my long-lived best friends for their understanding and precious support from afar. I am thankful to my thoughtful grandmother for the inspiration she gives me by her infinite amount of curiosity and fascination. I am also deeply grateful to my parents, my brother and my sister. Whatever I did in my life each single one of them always believed in me and encouraged me in his own peculiar way. And I want to thank my girlfriend for her sustained support over all the years. She definitely had to bear an extraordinarily difficult part in the compilation of this work: me.

And finally I would like to thank you, the reader. As you are reading these lines, I assume you already passed the astract and I'm quite confident that you'll make it at least to the summary and maybe even to some more detailed parts of this thesis.

Thank You!

Contents

Introduction

What is the universe made of? How is its evolution in time in the past and the future? What is the origin of high energy cosmic rays? What is the nature of Dark Matter and Dark Energy? There are many open questions in astroparticle physics. This field of research is the convolution of astronomy, particle physics and cosmology and aims to understand the universe and its evolution by the interpretation of cosmic ray observations. The main difference to classical astronomy is the observation of different messenger particles. The observation of photons in a wide wavelength spectrum from radio- ($\lambda \sim 10^3$ m) up to gamma-ray-astronomy ($\lambda \sim 10^{-12}$ m) is complemented in astroparticle physics by the observation of charged particles and neutrinos. Charged cosmic rays, as the general topic of this work, are discussed in chapter 1. The charged cosmic ray sources and accelerators are commonly considered to be astrophysical objects like e.g. supernovae and their shock-fronts. The most popular production models and acceleration mechanisms for charged cosmic rays are introduced in section 1.1.

Apart from the classical production mechanisms, charged particles may be produced in exotic processes. By the observation of galaxy rotational curves it became evident in the 1940s that more mass is needed to explain the observation by Newtonian gravitation. This mass contribution, called Dark Matter, is discussed in section 1.2. The observational evidences for the existence of Dark Matter are discussed in section 1.2.1. Various candidates for Dark Matter particles exist. One candidate is the Weakly Interacting Massive Particle (WIMP). Like betoken by its name, this hypothetical particle interacts with regular matter only by gravitation and weak interactions. In supersymmetric models the so-called superpartners are introduced as additional particles to each standard model particle. The low cross section of weak interactions implies that superpartners are in general not interacting with regular matter but might rarely annihilate or decay into standard model particles. Hence, if Dark Matter consists of WIMPs, a contribution in the observed particle spectrum is expected. WIMPs and other candidates for Dark Matter particles are reviewed in section 1.2.2.

On their journey from the sources to the terrestrial environment, where they are observed, charged cosmic rays interact with the galactic medium and electromagnetic fields. In these interactions the particle momentum and direction may be modified and secondary parti-

cles could be generated by e.g. spallation. Section 1.3 presents a widely-used model to describe this so-called cosmic propagation. With this model, also called the standard model of cosmic-ray propagation, the general spectrum of observed cosmic rays can be explained. Recent results are presented in section 1.4. Some of the observed features which do not match the expectations, e.g. an excess in the positron fraction, require additional contributions to the particle flux expected from 'standard' astrophysical sources. At this point Dark Matter but also other explanations, like nearby pulsars, could lead to the observed excess of positrons. The uncertainties on the measured positron fraction especially at higher energies ($\gtrsim$ 100 GeV) impede the discrimination of possible models. Reducing the statistical and systematical uncertainties will help to unravel this cosmic mystery.

The aim of this thesis is to elucidate the expected cosmic ray spectrum and to develop an analysis method to reconstruct the cosmic positron fraction observed by the Alpha Magnetic Spectrometer (AMS-02). A special focus is set on the particle identification capabilities of the Transition Radiation Detector (TRD). Proton events, being a factor $\sim 10^4$ more abundant in the cosmic ray spectrum than positrons, represent the main background in the determination of the positron fraction. To suppress the proton contamination of the positron sample to less than $\sim 1\,\%$ a proton discrimination power of $\sim 10^6$ is necessary. This task is distributed between the electromagnetic calorimeter and the TRD. The design specification of the TRD is a proton rejection of at least 100 up to 250 GeV at an electron efficiency of 90 %.

A brief description of the AMS-02 detector and its main detector components is given in chapter 2. In Chapter 3, the two main physics processes contributing to the energy deposited by a particle passing the TRD, namely ionization and transition radiation, and their simulation are discussed. The performance of the TRD is evaluated in chapter 4 on three different datasets: a beamtest performed at CERN, atmospheric muon data taken at Kennedy Space Center and data taken in space. The different datasets and the TRD-independent preselection of events is described in section 4.1 and section 4.2, respectively. The reconstruction algorithms, developed to combine the single channel electronic signals in the TRD to particle tracks, are presented in section 4.3. The TRD particle identification is based on the energy depositions on tracks. Calibration and correction algorithms, presented in section 4.4, are developed to ensure that particles of the same type produce the equivalent energy deposition signatures, independent of space and time. The TRD particle identification method, a likelihood analysis based on probability density functions, is introduced in section 4.5.

The number of electrons in the data sample taken on ground is insufficient to perform a lepton identification study. Instead, the charge ratio and differential rate of cosmic muon events is deduced. Combined with the acceptance extracted from simulations the sea-level muon flux is determined. Contrary to the fixed beam energies and incident angles in beamtests, the natural composition and spectrum of the isotropic cosmic ray flux apply

in space. A preliminary map of the geomagnetic rigidity cutoff is generated from space data. The particle identification algorithm is evaluated in the end, and the performance of the TRD defined in rejection power as function of the efficiency for retaining electrons.

1 Charged Cosmic Rays

Apart from the well-known and for millennia observed photons there are many other particles produced in and propagated through the universe and reaching the terrestrial environment. Among them are the charged cosmic rays, consisting of mainly hydrogen ($\sim 89\,\%$), helium ($\sim 10\,\%$), heavy ions ($\lesssim 1\,\%$) and electrons ($\lesssim 1\,\%$).

In this chapter some of the astrophysical sources and the corresponding production mechanisms are discussed (section 1.1). In section 1.2 the existence of Dark Matter, an assortment of Dark Matter theories and the implications on primary particle spectra are described. Independent of their production method these primary particles are subject to cosmic propagation, which can be subdivided into interactions with traversed matter and electromagnetic fields, decays of unstable particles and production of secondary particles. These processes, occurring in both Interstellar medium and terrestrial environment, are discussed in section 1.3. The observable spectra, composition and flux of charged cosmic rays are summarized in section 1.4.

1.1 Particle Acceleration

The cosmic particle flux observed in the vicinity of the Earth has to be produced somewhere in the universe. The production mechanism of primary particles is known to be nuclear fusion in stars up to helium and to heavier elements in supernovae. But the acceleration of these particles up to the highest energies observed ($\sim 10^{20}\,\mathrm{eV}$) remains not fully understood. The commonly accepted astrophysical acceleration mechanisms for charged particles can be roughly divided into Fermi acceleration (section 1.1.1), an iterative process in which the kinetic energy of the particle changes by small factors, and the acceleration in strong electric fields (section 1.1.2). The former is expected to occur e.g. in Active Galactic Nuclei (AGN) and the latter in Pulsar Wind Nebulae. There are many more exotic models for particle acceleration. Gamma-Ray Bursts (GRBs), as the most representative example, are not treated here but by e.g. Dermer et al. [1] and Barbiellini et al.[2].

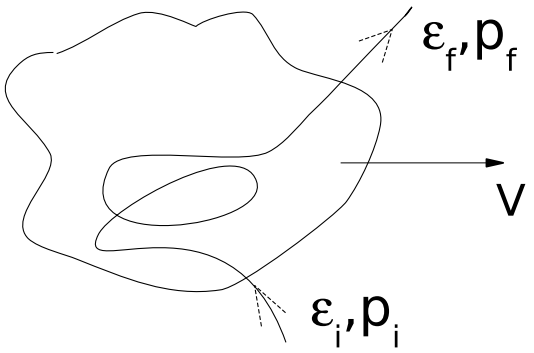

Figure 1.1: Principle of Fermi Acceleration. An electromagnetic particle is scattered off of magnetic irregularities inside a magnetic cloud. The final particle energy is a result of many small energy changes and in general a function of the initial energy, the velocity of the cloud and the incident angle.

1.1.1 Fermi Acceleration

Fermi particle acceleration is based on the fact that particles can gain energy by elastic scattering off magnetic turbulences. Consider a particle of momentum p and energy ϵ that collides with a massive, magnetic cloud moving with a velocity V (figure 1.1). In the center of momentum frame of the cloud, the component of the particles initial relativistic momentum parallel to V is given by

$$p'_{\parallel i} = \gamma(p_{\parallel i} - \frac{\epsilon_i V}{c^2}) \ , \tag{1.1.1}$$

with the Lorentz factor $\gamma = \frac{1}{\sqrt{1-\beta^2}}$ of the cloud. In this frame, the collision is elastic, so the final parallel component of the particle momentum is $p'_{\parallel f} = -p'_{\parallel i}$ and its final energy is equal to its initial one

$$\epsilon'_f = \epsilon'_i = \gamma(\epsilon_i - V p_{\parallel i}) \ . \tag{1.1.2}$$

Transforming to the lab frame the final energy of the particle is

$$\epsilon_f = \gamma(\epsilon'_f + p'_{\parallel f} V) = \gamma(\epsilon'_i - p_{\parallel i} V) \ . \tag{1.1.3}$$

Inserting the expressions for ϵ'_i and $p'_{\parallel i}$ leads to

$$\epsilon_f = \gamma^2[(1 + \frac{V^2}{c^2})\epsilon_i - 2(\mathbf{V} \cdot \mathbf{p_i})] \ . \tag{1.1.4}$$

The observed change in particle energy is thus

$$\Delta\epsilon = \epsilon_f - \epsilon_i = 2\gamma^2(\frac{V^2}{c^2} - \frac{\mathbf{V} \cdot \mathbf{v_i}}{c^2})\epsilon_i \ , \tag{1.1.5}$$

using $p_i = \epsilon_i v_i / c^2$. This means for head-on collision $\mathbf{V} \cdot \mathbf{v_i} < 0$ the particle gains energy and for overtaking collisions $\mathbf{V} \cdot \mathbf{v_i} > 0$ it loses energy.

Second-order Fermi mechanism Considering N scattering centers per unit volume with collisional cross-section σ the rate

$$R \sim N\sigma|\mathbf{v} - \mathbf{V}| \sim N\sigma v(1 - \frac{\mathbf{v}\cdot\mathbf{V}}{v^2}) \tag{1.1.6}$$

for a direction $\mathbf{V}$ (with $\gamma \approx 1$) shows that head-on collisions are more probable than overtaking encounters. The average energy gain per time can be extracted by averaging $\Delta\epsilon$ over all possible directions of $\mathbf{V}$

$$\langle\frac{d\epsilon}{dt}\rangle \sim N\sigma v\langle(1 - \frac{\mathbf{v}\cdot\mathbf{V}}{v^2})\Delta\epsilon\rangle \ , \tag{1.1.7}$$

where $\Delta\epsilon$ is given by Eq. 1.1.5. Using $\mathbf{v}\cdot\mathbf{V} = vV\cos\Theta$, $\langle cos^2\Theta\rangle = \frac{1}{3}$ and $\langle\cos\Theta\rangle = 0$ for an isotropic velocity distribution the mean energy gain (Eq. 1.1.5) per unit time can be written as

$$\langle\frac{d\epsilon}{dt}\rangle \sim \frac{8}{3}N\sigma v\frac{V^2}{c^2}\epsilon \tag{1.1.8}$$

and the mean energy gain per collision is

$$\frac{\langle\Delta\epsilon\rangle}{\epsilon} \sim \frac{\langle d\epsilon/dt\rangle}{\langle R\rangle} \sim \frac{8}{3}\frac{V^2}{c^2} \ . \tag{1.1.9}$$

This famous initial result of Fermi, the so-called Second-Order Fermi Acceleration, is demonstrating that by collisions of particles with scattering centers one can expect an average energy gain that is second order in $\beta = \frac{V}{c}$. This is a stochastic acceleration process which leads to an average systematic energy gain from many small, non-systematic energy changes.

This result rearranged to $\langle d\epsilon/dt\rangle = \alpha\epsilon$, where $\alpha = \frac{8}{3}N\sigma\frac{V^2}{c^2}$, implies that $\epsilon(t) = \epsilon_0 e^{\alpha t}$ and the characteristic timescale of the acceleration process is $t_{acc} \sim \frac{1}{\alpha}$. Assuming the particle can also escape from the acceleration region on the timescale t_{esc} the flow of particle energy under the influence of stochastic Fermi acceleration can be described by a diffusion equation. The evolution of the particle population can be described by

$$\frac{dn(\epsilon,t)}{dt} + \frac{\delta}{\delta\epsilon}[\langle\frac{d\epsilon}{dt}\rangle n(\epsilon,t) - \frac{\delta}{d\epsilon}(Dn(\epsilon,t))] \approx -\frac{n}{t_{esc}} + Q(\epsilon,t) \ , \tag{1.1.10}$$

where $dn = n(\epsilon,t)d\epsilon$ is the number density of particles with energy in the range $(\epsilon, \epsilon + d\epsilon)$. The term in the square brackets is the mean particle energy flux which is the difference between the rates of mean energy gain and energy diffusion described by the energy diffusion coefficient D. The last term on the right side is source term describing the injection of particles.

Neglecting energy diffusion and the source term Q and considering a steady-state solution $dn/dt = 0$ it simplifies to

$$\frac{d}{d\epsilon}(\alpha\epsilon n) + \frac{n}{t_{esc}} \approx 0 \ . \tag{1.1.11}$$

Differentiating and rearranging gives

$$\frac{dn(\epsilon)}{d\epsilon} \approx -(1 + \frac{1}{\alpha t_{esc}})\frac{n}{\epsilon} \tag{1.1.12}$$

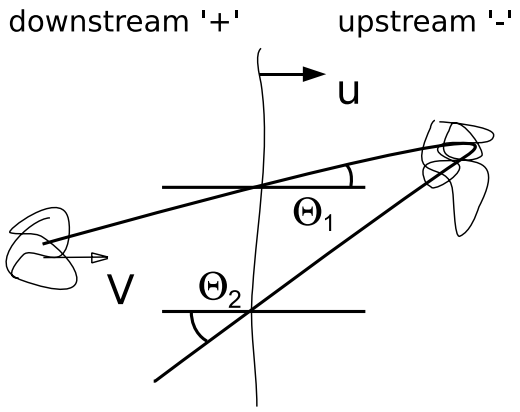

Figure 1.2: Schematic view of diffusive shock acceleration also called First-Order Fermi Acceleration. An electromagnetic particle gains energy by successive reflections between the relativistic shock front and the stationary plasma.

and thus a power law particle distribution $n(\epsilon) \propto \epsilon^{-\gamma}$ with spectral index $\gamma = 1 + (\alpha t_{esc})^{-1}$. Second-order Fermi acceleration is usually expected to lead to particle spectra that are typically flat ($\gamma < 2$). On the other hand observations indicate that $\gamma \approx 2.7$ over a wide range of different sources (see figure 1.12). This mismatch between expected and observed particle spectra over a variety of different sources summoned Fermi to revise his theoretical model of particle acceleration (see below). Taking into account the particle propagation (see section 1.3) the spectrum emitted from the source will most probably not match the observed spectrum. For example an acceleration mechanism similar to the one presented here can occur during the propagation of particles through magnetized clouds and lead to hardening of the spectrum. This process is called diffusive reacceleration.

First-order Fermi mechanism In the previous paragraph equation 1.1.5 indicated that the scattering process underlying Fermi acceleration predicts a small particle energy gain per scattering event. In case of randomly moving scattering centers the energy gain averaged over all directions is proportional to β^2. A special geometry which favors head-on collisions results in a systematic energy increase $\mathcal{O}(\beta)$. Consider for example a stream of scattering centers moving towards an elastically reflecting wall. An incoming particle gains energy every time it completes a cycle of reflecting off the wall into the stream and scattering back towards the wall. This principle, which has it's mechanical analogon in a ping-pong ball between two approaching paddles, forms the basic principle of particle acceleration near an astrophysical shock-front. A simple but instructive model is the propagation of a planar shock-front with velocity U through a stationary plasma (see figure 1.2). In the undisturbed region ahead of the shock (i.e. 'upstream'), the plasma is at rest. The 'downstream' region swept up by the shock is moving in the same direction as the shock-front but not as fast as U. In the rest frame of the shock, the upstream fluid moves towards the shock with velocity

$v_1 = |U|$, pressure p_1, temperature T_1 and mass density ρ_1. The downstream fluid moves away from the shock with velocity v_2 and its pressure p_2, temperature T_2 and density ρ_2.

The physical properties of the upstream and downstream fluid are related by the equations for conservation of mass (I), momentum(II) and energy(III) across the shock. For fluxes across a stationary boundary, these conservation relations are

$$(I) \qquad \nabla \cdot (\rho \mathbf{v}) = 0 \Rightarrow \rho_1 v_1 = \rho_2 v_2 \tag{1.1.13}$$

$$(II) \qquad \nabla \cdot (\rho \mathbf{v})\mathbf{v} = -\nabla p \Rightarrow p_1 + \rho_1 v_1^2 = p_2 + \rho_2 v_2^2 \tag{1.1.14}$$

$$(III) \qquad \nabla \cdot [(\frac{1}{2}v^2 + w)\rho \mathbf{v}] = 0 \Rightarrow (\frac{1}{2}v_1^2 + w_1)\rho_1 v_1 = (\frac{1}{2}v_2^2 + w_2)\rho_2 v_2 \ . \tag{1.1.15}$$

Here, $w = \epsilon_{int} + p/\rho$ is the specific enthalpy and ϵ_{int} is the internal energy. For an ideal gas, the internal energy and pressure are related via the adiabatic index γ, with $p/\rho = (\gamma - 1)\epsilon_{int}$. For example for a mono atomic ideal gas: $\gamma = 5/3$ and $p/\rho = \frac{2}{3}\epsilon_{int} = kT/\mu m_p$. To describe the downstream quantities in terms of the upstream quantities one can introduce the following definitions for the upstream fluid:

$$\text{compression ratio } \ r = \frac{\rho_2}{\rho_1} \tag{1.1.16}$$

$$\text{speed of sound } \ c_1 = (\frac{\gamma p_1}{\rho_1})^{1/2} \tag{1.1.17}$$

$$\text{Mach number } \ M_1 = \frac{v_1}{c_1} \ . \tag{1.1.18}$$

Solving the conservation equations leads to the shock jump conditions

$$r = \frac{\rho_2}{\rho_1} = \frac{v_1}{v_2} = \frac{(\gamma+1)}{(\gamma-1) + 2/M_1^2}, \ \ \frac{p_2}{p_1} = \frac{2\gamma M_1^2 - (\gamma - 1)}{(\gamma + 1)} \ . \tag{1.1.19}$$

Note that in the limit of very strong shocks $M_1 \gg 1$, $r \to \frac{(\gamma+1)}{(\gamma-1)}$ the compression converges to a finite value but the pressure is proportional to M_1^2. Hence shocks can heat gas to high temperatures. For a strong shock in a fully ionized gas $v_2 \approx \frac{1}{4}v_1$ and $v_1 = |U|$ in the rest frame of the shock.

Now consider a fast particle in the upstream region. In the rest frame of the upstream fluid, the shock is advancing at speed U and the downstream fluid is advancing at speed $\frac{3}{4}U$. When the particle crosses the shock-front it undergoes head-on collisions with the scattering centers in the advancing downstream flow. Now in the rest frame of the downstream flow, the upstream flow is advancing at a speed $\frac{3}{4}U$. Hence, when the particle crosses the shock again, it undergoes a further energy gain process. If the shock is subrelativistic ($U \ll c$) and the particle is relativistic the fractional energy gain is $\frac{\Delta\epsilon}{\epsilon} \sim (\frac{U}{c})\cos\Theta$. The energy gain per complete cycle of shock crossings depends on the angle Θ between a particles momentum and the shock front normal. Consider a relativistic particle moving across a subrelativistic shock-front from downstream to upstream (see figure 1.2). The notation is chosen to be '+'

and '-' for rest frames of the downstream and upstream flows respectively. In the rest frame of the upstream flow the particles initial energy upon entering is

$$\epsilon_i^- = \epsilon_i^+(1 + \frac{V}{c}\cos\,\Theta_1) \ , \tag{1.1.20}$$

where Θ_1 is the angle between the particles initial momentum and the shock normal. The particle then collides with a scattering center in the upstream flow and recrosses the shock front at an angle Θ_2. Its final energy in the rest frame of the upstream flow is

$$\epsilon_f^- = \epsilon_f^+(1 + \frac{V}{c}\cos\,\Theta_2) \ . \tag{1.1.21}$$

Since the scattering is elastic in this reference frame $\epsilon_f^- = \epsilon_i^-$ and so

$$\frac{\epsilon_f^+}{\epsilon_i^+} = \frac{1 + \frac{V}{c}\cos\,\Theta_1}{1 + \frac{V}{c}\cos\,\Theta_2} \ . \tag{1.1.22}$$

Rearranging gives

$$\xi = \frac{\Delta\epsilon^+}{\epsilon^+} = \frac{V}{c}(\cos\,\Theta_1 - \cos\,\Theta_2) \ . \tag{1.1.23}$$

To calculate the average energy gain per cycle one needs to know that the probability of a particle crossing the shock-front at an angle between Θ and $\Theta + d\Theta$ is $P(\Theta) \propto \cos\,\Theta\,\sin\,\Theta\,d\Theta$. This is because the number of particles arriving with Θ in this range is proportional to $\sin\,\Theta\,d\Theta$, while the rate at which they arrive per unit time is proportional to $\cos\,\Theta$. Using $\mu = \cos\,\Theta$ and integrating over $0 \leq \Theta \leq \pi/2$ for head-on collisions over a complete cycle gives

$$\frac{\langle\Delta\epsilon\rangle}{\epsilon} = \frac{V}{c}\int_0^1 d\mu_1 \int_0^1 d\mu_2 \mu_1\mu_2(\mu_1 - \mu_2) \Longrightarrow \frac{4}{3}\frac{V}{c} \ . \tag{1.1.24}$$

Thus, the average energy gain is first order in β. This so-called ' First-Order Fermi Acceleration Mechanism ' is also referred to as diffusive shock acceleration because it relies on the diffusion of the particles towards the shock front. Contrary to the diffusive reacceleration, which is expected to occur mainly during propagation, this process only occurs in regions of strong directed shock fronts, e.g. supernova remnants.

The energy spectrum for First-Order Fermi Acceleration can be calculated using the average energy $\epsilon = \frac{4}{3}\frac{V}{c}\epsilon_0$ of a particle after one cycle and the probability $(1 - P_{esc})$ that the particle remains in the accelerating region after that cycle, with escape probability P_{esc}. In this case after k collisions there are $n = n_0(1 - P_{esc})^k$ particles with energies $\epsilon_n = \epsilon_0(1 + \xi)^k$. Eliminating k gives

$$\frac{n}{n_0} = (\frac{\epsilon}{\epsilon_0})^\Gamma \ , \tag{1.1.25}$$

where $\Gamma = ln(1 - P_{esc})/ln(1 + \xi)$ can be approximated for $\xi \ll 1$ and $P_{esc} \ll 1$ to $\Gamma \approx -\frac{P_{esc}}{\xi}$. To calculate the expected spectral index the escape probability can be deduced by setting the particle rates from upstream to downstream in relation to the rates crossing an imaginary border far downstream. The former is the projection of the isotropic particle flux of density

ρ onto the shock front plane: $c\rho/4$. The escape rate due to downstream convection is the same density times the convection velocity v_2. The escape probability P_{esc}, as ratio of escape to encounter rate is given by

$$P_{esc} = \frac{\rho v_2}{c\rho/4} = 4\frac{v_2}{c} \ . \tag{1.1.26}$$

Now Γ can be expressed in terms of the compression ratio r as $\Gamma \approx -\frac{P_{esc}}{\xi} = \frac{3v_2}{v_2 - v_1} = \frac{3}{1-r}$. By inserting and differentiating equation 1.1.25 the differential spectrum is obtained: $\frac{dn}{d\epsilon} \propto (\frac{\epsilon}{\epsilon_0})^\gamma$, with $\gamma = \frac{2+r}{1-r}$. The well-known example of mono-atomic gas with $\gamma_{gas} = 5/3$ and in the limit of strong shocks $r \to \frac{\gamma_{gas}+1}{\gamma_{gas}-1} = 4$ yields a spectral index of $\gamma = -2$. Weaker shocks lead to a softening of the spectral index, e.g. $\gamma = -3$ for $r = 2.5$.

1.1.2 Electric Fields

Complementary to magnetic fields the dynamics of charged particles are also governed by the electromagnetic fields, which pervade the entire Universe. The equation of motion of a particle of charge q, momentum $\mathbf{p} = \gamma m \mathbf{v}$ and Lorentz factor γ in a magnetic field $\mathbf{B}$ and electric field $\mathbf{E}$ is

$$\frac{d\mathbf{p}}{dt} = q(\mathbf{E} + \mathbf{v} \times \mathbf{B}) \ . \tag{1.1.27}$$

In many astrophysical situations, static electric fields cannot be sustained because ionized plasmas are electrically conducting and the charged particles move freely to short out any component of $\mathbf{E}$ parallel to $\mathbf{B}$. Perpendicular to $\mathbf{B}$ particle motion is restricted by a magnetic field to a circular motion with gyro frequency

$$\Omega = \frac{|q|B}{\gamma m} \ . \tag{1.1.28}$$

Here the sense of gyration is right-handed for negative charges. The gyro radius is $R = \frac{v_\perp}{\Omega} = \frac{p_\perp}{|q|B}$ where $v_\perp = v \sin \alpha$ is the velocity component perpendicular to $\mathbf{B}$ and α is called the pitch angle. Combined with the parallel velocity component $v_\parallel = v \cos \alpha$ the resulting motion of a charged particle in a magnetic field is a spiraling motion.

From equation 1.1.27 the work done on a charged particle is $W = \mathbf{v} \cdot d\mathbf{p}/dt = q\mathbf{v} \cdot \mathbf{E}$. Thus, since magnetic fields do no work and static electric fields cannot be sustained acceleration of charged particles to high energies can only be attributed to the time-varying electric field induced by a time-varying magnetic field according to Faraday's law $\nabla \times \mathbf{E} = -\partial \mathbf{B}/\partial t$.

Although this acceleration mechanism appears to be an efficient and natural particle acceleration mechanism, whether it can account for the highest energy cosmic rays is an open question. To see what the requirements are for electric field acceleration one can do the following order-of-magnitude calculation: $\frac{E}{L} \sim \frac{B}{L/c} \Rightarrow E \sim Bc$ where L is a characteristic length scale over which the field varies. The total energy that can be transferred to a particle is given by

$$\epsilon = \gamma m c^2 \sim \int qEdl \sim qBcL \ . \tag{1.1.29}$$

The corresponding expected physical parameters of some extreme astrophysical objects like neutron stars $B \sim 10^6\,\mathrm{T}$ and $L \sim 100\,\mathrm{km}$ lead to $\epsilon \sim 5\,\mathrm{J} \sim 10^{19}\,\mathrm{eV}$ which is close to the highest cosmic ray events $E \gtrsim 10^{20}\,\mathrm{eV}$observed by Fly's Eye / AGASA [3] and the Auger collaboration [4].

1.2 Dark Matter

From different observational techniques it becomes evident that our comprehension of the mass composition of the universe is incomplete. Additional contributions from a yet unknown source need to be added to the cosmological model to explain the observed phenomena described in this section. This missing mass contribution was postulated by Fritz Zwicky in 1934 as 'Dark Matter'. Following an overview of Dark Matter evidences (section 1.2.1) the most common theoretical candidates are briefly depicted (section 1.2.2).

1.2.1 Observation

There is a variety of indications for the presence of Dark Matter in the universe coming from astronomical and cosmological observations. In the following paragraphs some of them, namely the Galaxy Rotational Curves, the Cosmic Microwave Background and the Bullet Cluster, are listed.

Rotational Curves A hint to the existence of Dark Matter arises from the rotational curves of galaxies. For the simplest case of a static and spherical symmetric space-time in General Relativity one can describe a line element as [5]:

$$ds^2 = -e^{2\Phi/c^2}c^2dr^2 + \frac{dr^2}{1-\frac{2Gm}{c^2r}} + r^2d\Omega^2 \ , \tag{1.2.1}$$

where $d\Omega = d\Theta + sin^2\Theta\, d\phi^2$. The gravitational potential $\Phi(r)$ and the mass function $m(r)$ are functions of the radial coordinate only. The Einstein's equations are

$$m' = -\frac{4\pi r^2}{c^2}T^t{}_t \ , \tag{1.2.2}$$

$$(1-2\frac{mG}{c^2r})\frac{\Phi'}{c^2} - \frac{mG}{c^2r^2} = \frac{4\pi Gr}{c^4}T^t{}_t \ , \tag{1.2.3}$$

where prime denotes $' \equiv \partial/\partial r$. These equations are completed by the conservation equation of the matter-energy generating the curvature of the spacetime. In the case of a perfect fluid the stress-energy tensor is given by $T_{\mu\nu} = (\rho + p/c^2)u_\mu u_\nu + pg_{\mu\nu}$ [6], where the density is $\rho = (1+\epsilon)\rho_0$ and ρ_0 is the rest mass energy density and ϵ is the internal energy per unit mass, u^μ is the co-moving four velocity, normalized as $u_\mu u^\nu = -c^2$ and p is the pressure. The conservation equation $T^\mu_{\nu\mu} = 0$ implies the field equation

$$(\rho c^2 + p)\frac{\Phi'}{c^2} + p' = 0 \ . \tag{1.2.4}$$

The motion of test particles in such spacetime is determined by the geodesic equations and, for test particles in circular motion, there is a relationship between the gravitational potential Φ and the rotation velocity of the particle v_t

$$\frac{\Phi'}{c^2} = \frac{\beta_t^2}{r} \ , \tag{1.2.5}$$

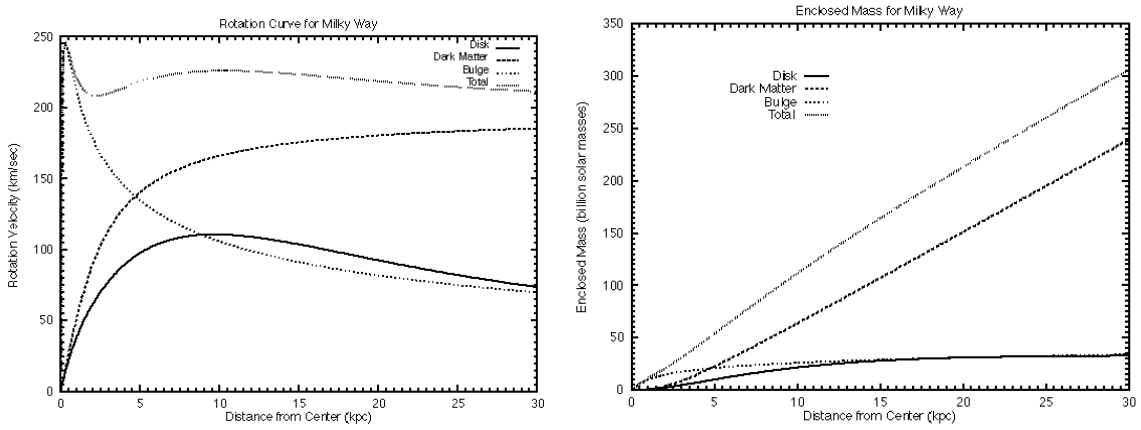

Figure 1.3: Rotation of the Milky Way [7]. *Left*: above some kpc the rotational speed of visible mass can not be explained by visible matter in form of the 'Bulge' (dotted line) and 'Disk' (solid line) region. In this model only an additional mass contribution of Dark Matter allows to explain the observed curve (dashed line). *Right*: the amount of enclosed mass reveals that after about 10 kpc the total amount of visible matter is enclosed but the boundary of the Dark Matter halo is still not reached.

where $\beta_t^2 = \frac{v_t^2}{c^2}$. This velocity is the one measured directly by observations of rotational curves in galaxies. Thus v_t is an observable function and the gravitational potential can directly be determined.

In general the observed rotation curves differ from what one would expect by just taking the luminous visible matter into account (see figure 1.3). Instead of the expected $\frac{1}{\sqrt{R}}$ an almost flat dependency can be observed.

Cosmology Cosmology studies the evolution of galaxies on the largest scales. The only effective force at this scale is gravity. A distant galaxy with mass m has the potential

$$V = -G\frac{mM}{R} \ , \tag{1.2.6}$$

in the gravitational field of a galaxy cluster of total mass M with G being the gravitational constant and R the distance in between. Assuming a spherical shape for the galaxy cluster the potential energy can be rewritten as a function of its mean density

$$V = -\frac{4\pi}{3}GmR^2\rho \ . \tag{1.2.7}$$

The total energy of the distant galaxy is the sum of it's potential and kinetic energy

$$\begin{aligned} E &= \frac{1}{2}m\dot{R}^2 - \frac{4\pi}{3}GmR^2\rho \\ &= \frac{1}{2}mR^2(\frac{\dot{R}^2}{R^2} - \frac{8\pi}{3}G\rho) \\ &= \frac{1}{2}mR^2(H^2 - \frac{8\pi}{3}G\rho) \ , \end{aligned} \tag{1.2.8}$$

where the definition of the Hubble constant $H \equiv \frac{\dot{R}}{R}$ was inserted. The density for which the terms in the bracket cancel is called the critical density

$$\rho_c = \frac{3H^2}{8\pi G} \ . \tag{1.2.9}$$

From equations 1.2.8 and 1.2.9 it becomes evident that for densities lower than the critical one the total energy becomes positive. Hence, like in the case of a rocket launch where the body escapes the gravitational potential, the galaxy cluster expands. This situation can be conveyed to the cosmos. In case the density is lower than the critical density, the universe will expand forever. For a supercritical density the expansion will stop and the universe will be contracted to a so-called 'Big Crunch'. The former case is also referred to as an 'open universe' and the latter as 'closed universe'. If $\rho = \rho_c$ the expansion rate will asymptotically drop to zero, this case is called 'flat universe'. Hence the material density of the universe is linked to the evolution of the universe.

Usually equation 1.2.8 is rewritten by introducing a parameter k

$$k = -\frac{2E}{mc^2} = \frac{R^2}{c^2}(\frac{8\pi}{3}G\rho - H^2) \ . \tag{1.2.10}$$

Then one can rearrange this to the famous Friedmann equation

$$(\frac{\dot{R}}{R})^2 + \frac{kc^2}{R^2} = \frac{8\pi}{3}G\rho \ . \tag{1.2.11}$$

By introducing the Ω parameter

$$\Omega = \frac{\rho(t)}{\rho_c} \tag{1.2.12}$$

equation 1.2.11 can be written as

$$H^2 = \frac{8\pi}{3}G\Omega\frac{3H^2}{8\pi G} - \frac{kc^2}{R^2} = \Omega H^2 - \frac{kc^2}{R^2} \tag{1.2.13}$$

or

$$H^2(\Omega - 1) = \frac{kc^2}{R^2} \ . \tag{1.2.14}$$

The Ω parameter now determines if the expansion of the universe is asymptotically decelerated ($\Omega = 1$), forever ongoing ($\Omega < 1$) or changed into a contraction ($\Omega > 1$). According to the ΛCDM model (see section 1.2.2), the main constituents of Ω are baryons (Ω_b), Cold Dark Matter (Ω_c) and Dark Energy (Ω_Λ)

$$\Omega = \Omega_b + \Omega_c + \Omega_\Lambda \ . \tag{1.2.15}$$

The currently most constraining measurement of the mass density of the universe is performed by observations of the cosmic microwave background (CMB) and its anisotropies by the Wilkinson Microwave Anisotropy Probe (WMAP). In the Hot Big Bang Model the universe was much hotter and denser in the past than now. During expansion it cooled

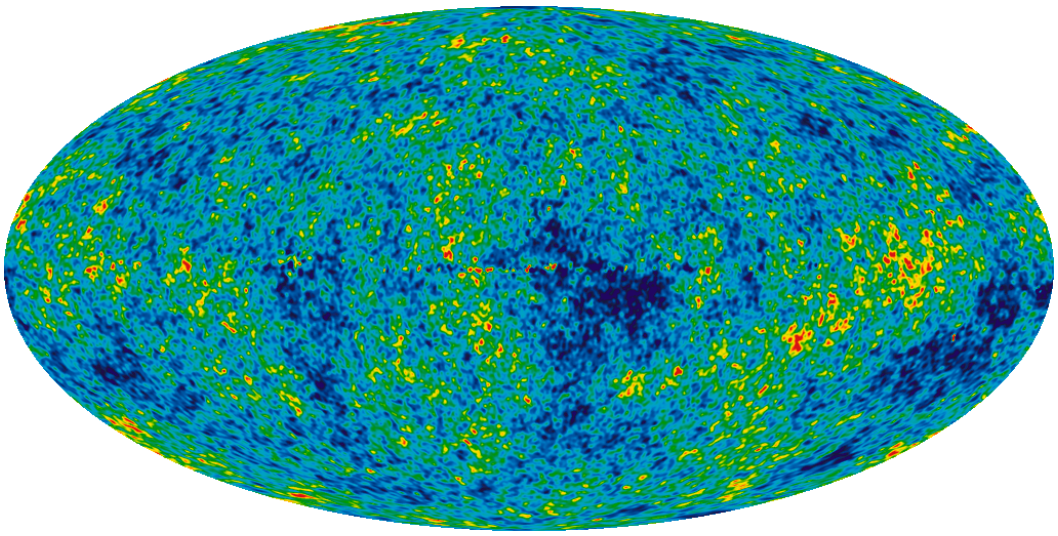

Figure 1.4: The all-sky picture of the Cosmic Microwave Background (CMB) created from seven years WMAP data. The image reveals 12.7 billion year old temperature fluctuations. The signal of our galaxy was subtracted using multi-frequency data. The color scale corresponds a temperature range of $\pm 200\,\mu$K [8].

down adiabatically. At early times the universe was almost entirely ionized. Photons and baryons were tightly coupled by Compton scattering and electromagnetic interactions. At a redshift of about 1000 [1] the universe cooled enough to form Hydrogen. With the rapid drop in the free electron density the photon-matter interactions effectively ceased. What can be observed today in the Cosmic Microwave Background is a snapshot of the universe at that redshift. Among other things WMAP measures this so-called 'surface of last scattering' , which corresponds to the decoupling of matter and radiation and is leading to the first observable photons. The fluctuations across the sky are the precursors of the large scale structure around us today. Recently the WMAP collaboration published the results of their 7 year measurement of the cosmic microwave background (see figure 1.4). From the measured fluctuations one can deduce the fluctuations at recombination and the relative density of baryonic and non-baryonic matter. Additionally some of the properties of the non-baryonic matter can be determined: its self-interactions, mass and interactions with ordinary matter [9]. By measuring the total mass of the universe to be compatible with $\Omega = 1$, WMAP determined that the universe is flat. This is equivalent to a mass density of $\rho = 9.9 \times 10^{-20}\,\mathrm{g/cm^3}$, which is equivalent to about 5.9 protons per cubic meter. This total density can be broken down into:

[1] Redshift is correlated to the distance of objects and due to the finite speed of light to the age of the observed objects by $t_{\Delta z} = \frac{1}{H_0}\int_z^{z+\Delta z} \frac{dz'}{(1+z')\frac{H(z')}{H_0}}$, where $z \equiv \frac{\lambda_{obs}-\lambda_{emit}}{\lambda_{emit}}$ is the redshift value and H_0 is the Hubble constant today

Figure 1.5: A composite observation of two colliding galaxies known as the Bullet Cluster '1E 0657-56'. Regular matter, identified by the synchrotron light of colliding gas clouds (shown in red), is slowed down by interactions and producing a bow-shock. In contrast Dark Matter, revealed by its mass observed by Gravitational Lensing (shown in blue) is leaving the collision center without being affected by interactions [11].

- $73.4 \pm 2.9\,\%$ Dark Energy (Ω_Λ)
- $22.2 \pm 2.6\,\%$ Dark Matter (Ω_{DM})
- $4.5 \pm 2.8\,\%$ Ordinary Matter (Ω_m) .

Here, Dark Energy is a hypothetical form of energy. The two most familiar theoretical models to describe Dark Energy are the cosmological constant and the quintessence [10]. The former being equivalent to the vacuum energy and homogeneously distributed and the latter being a dynamic field variable in space and time. For a more detailed discussion of the WMAP analyses please refer to [9].

Bullet Cluster An impressive evidence on the existence of Dark Matter is the collision of two galaxies known as the 'Bullet Cluster' (figure 1.5). This structure was examined using different observational methods. Visible light verifies that the stars contained in each galaxy are slowed down by gravitational forces but still leaving the collision center. Observations in the X-ray range reveal the synchrotron emission produced in the interaction of the galactic gas clouds. These clouds represent the largest constituent to the mass of visible baryonic matter. Due to their interactions they slow down and separate from the stars. The third observational method, the Gravitational Lensing, is directly detecting the mass distribution in the cluster. According to theories without Dark Matter the dominant contribution to the galaxy mass is baryonic matter. But the strongest lensing effect appears in two

regions separated from the gas clouds. The fact that these regions are spherical and hence leave the collision region apparently unaffected corroborates the idea of weakly interacting Dark Matter in galactic halos.

1.2.2 Candidates

Although cosmological observations are providing convincing evidence that Dark Matter is the main mass constituent of the Universe (see section 1.2.1), the exact nature of Dark Matter remains a mystery. There are countless models trying to integrate Dark Matter into the Standard Model of particle physics. One usually distinguishes between baryonic and non-baryonic Dark Matter: faint stars, black holes, and inter-galactic gas are examples of the former, while weakly-interacting massive particles (WIMPs) and topological defects of gauge fields arising from quantum symmetries are examples of the latter. Non-baryonic matter can broadly be grouped into two kinds: 'hot' and 'cold'. These adjectives indicate how fast a Dark Matter particle was moving when it decoupled from the baryonic matter. Massive neutrinos are an example of Hot Dark Matter (HDM) particles, and axions and primordial black holes are examples of Cold Dark Matter (CDM). However, the various WIMP candidates show some common properties: the Dark Matter particle is stable or at least very long-lived and neutral under electric charge and color charge.

Brown Dwarfs Brown Dwarfs are objects with a low mass in the sense of sustaining hydrogen fusion, which separates them from stars. They are also commonly referred to as missing links between gas giants, e.g. Jupiter, and red dwarfs, which are the smallest, lowest mass true stars.

As Brown Dwarfs are not able to illuminate, the most important observational signature is the intensity fluctuations on stars or quasars induced by their microlensing effects due to their mass. This effect would be observable for objects over the entire brown dwarf mass range of $\sim 10 - 90\, m_{Jupiter} \approx 3200 - 26000\, m_{Earth}$. In fact some theories [12] state that the galactic Dark Matter is only of baryonic origin and already observed. They favor a bottom-up scenario of galactic structure building from clumps over planets to galactic scales. Micro brown dwarfs (μBDs) grouped in Jeans clusters are predicted by the theory of gravitational hydrodynamics and are supported by an impressive sum of observations: quasar microlensing, planetary nebulae, 15 K cold dust temperatures, 'cirrus clouds', scattering events, parabolic events, direct observations and long duration radio events. This model provides answers to many paradoxes like e.g. the Lyman-alpha forest, iron planet cores, and young stars near the black hole in the Galaxy center.

Neutrinos Neutrinos, as weakly interacting particles, could be expected as the ideal hot Dark Matter (HDM) candidate. The question is if neutrinos carry mass or not. Due to their abundance, even very light neutrinos would contribute significantly to the mass of Dark Matter. Up to now direct observations were not able to determine neutrino masses, only upper limits are available (e.g. $m_{\nu_e} < 2\,\text{eV}$ at $90\,\%$ CL [13]).

From the expected density of primordial neutrinos one can derive an upper limit to the total mass contained in the three neutrino flavors. One can expect about the same amount of black body neutrinos as black body photons. Assuming a number density of $N \approx 300\,\text{cm}^{-3}$ and $\Omega = 1$ (corresponding to the critical density $\rho_c \approx 2 \times 10^{-29}\,\text{g/cm}^3$ at an age of $\sim 10^{10}$ years) the limit on the total mass is given by

$$N \times \sum m_\nu \leq \rho_c \tag{1.2.16}$$

$$\sum m_\nu \leq 40\,\text{eV} \ . \tag{1.2.17}$$

Here, the sum is taken over all sequential neutrinos including the antineutrinos. Assuming that neutrinos and antineutrinos have the same masses the total mass of the three known neutrino flavors is $\sum m_\nu = 2(m_{\nu_e} + m_{\nu_\mu} + m_{\nu_\tau})$. Hence, for each single neutrino flavor the upper limit on the mass is given by $2m_\nu \leq 40\,\text{eV} \Leftrightarrow m_\nu \leq 20\,\text{eV}$. Surprisingly, by applying simple cosmological assumptions one can improve the upper limits on the neutrino masses given by particle physics (e.g. $m_{\nu_\tau} < 15\,\text{MeV/c}$ [14]) by many orders of magnitude.

If the contribution of neutrino masses to Dark Matter is estimated as large ($\Omega_\nu h^2 = \frac{\sum m_\nu}{93\,\text{eV}} > 0.1$) one can derive with the same argument as above a lower limit on the sum of the neutrino masses $\sum m_\nu > 4\,\text{eV}$. Assuming a mass hierarchy similar to the charged leptons ($m_e < m_\mu < m_\tau \rightarrow m_{\nu_e} < m_{\nu_\mu} < m_{\nu_\tau}$) the mass of the τ-neutrino can be limited to $2\,\text{eV} \leq m_{\nu_\tau} \leq 20\,\text{eV}$. Neutrinos are relativistic and hence represent a typical Hot Dark Matter (HDM) candidate. With HDM it is difficult to explain small structures (on the order of galaxies) in the universe. Neutrinos, as mentioned earlier, would have emerged from the Big Bang with such highly relativistic velocities that they would tend to smooth out any fluctuations in matter density. In the early Universe, the neutrino density was enormous, and so most of the matter density could be accounted for by neutrinos. Given their high velocity, neutrinos would tend to freely stream out of any overdense regions [2]. This process implies that density fluctuations could appear only after the neutrinos slowed down considerably. Note that most of todays remaining HDM theories are therefore mixed models in which Dark Matter consists of HDM and CDM.

It is possible to further constrain the allowed neutrino mass range. To contribute to the Dark Matter Halo of a galaxy, Neutrinos have to be bound to it by Gravitation. Or in other words, their velocity has to be lower than the escape velocity v_{esc}. Treating the neutrinos as

[2] regions with densities greater than the average density in the Universe

a relativistic Fermi gas in the ground state ($T = 0$) with Fermi Energy

$$E_F = \hbar c (3\pi 2 n_{max})^{1/3} = p_{max} c \ , \tag{1.2.18}$$

where n_{max} is the number density, one can derive an estimate of the neutrino mass density

$$n_{max} \times m_\nu = \frac{m_\nu^4 v_{esc}^3}{3\pi^2 \hbar^3} \ . \tag{1.2.19}$$

To describe galactic Dark Matter only by neutrino masses, $n_{max} \times m_\nu$ has to be in the same order as the Dark Matter density. From $v_{esc} = \sqrt{2GM/r}$ with the mass of the galaxy M and its radius r one can derive a lower limit on the neutrino mass density $m_\nu > 10\,\mathrm{eV}$.

The cosmological reasoning strongly constrains the range for the neutrino masses to $10 - 20\,\mathrm{eV}$. This is not necessarily contradictory to the observations of neutrino oscillations. Such experiments measure the difference between squared masses of neutrinos. From the deficit of atmospheric muon neutrinos follows

$$\Delta m_{12}^2 = 8 \times 10^{-5}\,\mathrm{eV} \ . \tag{1.2.20}$$

If $(\nu_\mu - \nu_\tau)$-oscillations are leading to this effect, the masses of the muon- and tau-neutrino could still be close to each other without violating the cosmological mass limits. In case one applies the known mass hierarchy of the charged lepton sector to the neutrino sector $m_{\nu_\mu} \ll m_{\nu_\tau}$ the result m_{ν_τ} is in contradiction to the cosmological limits.

If light neutrinos would be the main constituents of the galactic halo one would expect a distinct absorption line in the spectrum of high energy neutrinos. The observation of such a absorption line would be a direct evidence for a neutrino halo. Furthermore, one could extract the neutrino mass from the position of the absorption line. For a neutrino mass of 10 eV the position of the absorption line can be determined ($\nu + \bar{\nu} \to Z^0 \to$ hadrons / leptons) to

$$E_\nu = \frac{M_Z^2}{2 m_\nu} = 4.2 \times 10^{20}\,\mathrm{eV} \ . \tag{1.2.21}$$

The verification of such an absorption line is experimentally challenging.

Recently new cosmological limits on the neutrino mass were published [15]. By combining data from WMAP 5-year CMB, baryon acoustic oscillations, supernovae and Hubble Space Telescope prior on h the upper limit is $\sum m_\nu \leq 0.28\,\mathrm{eV}$ $(95\%\,\mathrm{CL})$ on the sum of neutrino masses assuming a flat ΛCDM cosmology.

Weakly Interacting Massive Particles The so-called Weakly Interacting Massive Particles (WIMPs) are the most studied Dark Matter candidates as they are found in many theories, intrinsically have the correct relic density, a mass in the range $m_{wimp} \sim 10\mathrm{GeV} - \mathrm{TeV}$ and may be detected in multiple ways. As an introduction to WIMP theories a brief description

of one of the Standard Model (SM) problems, namely gauge hierarchy problem, shall be given.

The gauge hierarchy problem is the question of why the physical Higgs boson mass m_h is so small. There are three fundamental constants: the speed of light c, Planck's constant h and Newton's gravitational constant G_N. One combination of these is the Planck mass $M_{Pl} \equiv \sqrt{hc/G_N} \simeq 1.2 \times 10^{19}\,\text{GeV}$. It is therefore natural to expect dimensionful parameters to be either 0 if enforced by a symmetry or of the order of M_{Pl}. In the Standard Model (SM) electroweak symmetry is broken and the Higgs boson mass is non-zero. The gauge hierarchy problem is the question of why $m_h \sim 100\,\text{GeV} \ll M_{Pl}$. This problem is enhanced in the SM by quantum corrections. The physical mass of the SM Higgs boson is $m_h^2 = m_{h0}^2 + \Delta m_h^2$, where m_{h0}^2 is the tree-level mass and

$$\Delta m_h^2 \sim \frac{\lambda^2}{16\pi^2} \int^{\Lambda} \frac{d^4p}{p^2} \sim \frac{\lambda^2}{16\pi^2}\Lambda^2 \tag{1.2.22}$$

is the quantum correction resulting from loop-level diagrams, where the integral is over the momenta of particles in the loops. The parameter λ is a dimensionless coupling and Λ is the energy scale at which the SM is no longer valid. Because Δm_h^2 is proportional to Λ^2 it is natural to expect the Higgs mass to be pulled up to within an order of magnitude of Λ by quantum corrections. In the SM with $\Lambda \sim M_{Pl}$ this implies that m_{h0}^2 and Δm_h^2 must cancel to 1 part in 10^{36} to yield the correct physical Higgs mass, which is difficult to motivate.

The gauge hierarchy problem may be eliminated if $\Lambda \lesssim 1\,\text{TeV}$ leading to new physics at the weak scale $m_{weak} \sim 10\,\text{GeV} - 1\,\text{TeV}$. The gauge hierarchy problem is the leading motivation for WIMPs. If a WIMP exists and is stable, it is naturally produced with a relic density consistent with that required of Dark Matter. Dark Matter may be produced in a simple and predictive manner as a thermal relic of the Big Bang. Initially the early Universe is dense and hot, and all particles are in thermal equilibrium. The Universe then cools to temperatures T below the Dark Matter particle pass m_χ, and the number of Dark Matter particles becomes Boltzmann suppressed, dropping exponentially as $e^{-m_\chi/T}$. The number of Dark Matter particles would drop to zero if the Universe would not be expanding. After some time the Universe becomes so large and the Dark Matter particles gas becomes so dilute that they cannot find each other to annihilate. The Dark Matter particles then "freeze-out", with their number asymptotically approaching a constant, namely their thermal relic density. Note that the freeze-out, also known as chemical decoupling, is distinct from kinetic decoupling because after thermal freeze-out interactions that change the number of Dark Matter particles become negligible but their interactions that mediate energy transfers between Dark Matter and other particles may remain efficient.

The freeze-out is described quantitatively by the Boltzmann equation

$$\frac{dn}{dt} = -3Hn - \langle \sigma_A v \rangle (n^2 - n_{eq}^2) \ , \tag{1.2.23}$$

where n is the number density of Dark Matter particle χ, H is the Hubble parameter, $\langle \sigma_A v \rangle$ is the thermally average annihilation cross section, and n_{eq} is the Dark Matter number density in thermal equilibrium. On the right hand side the first term accounts for dilution from expansion. The n^2 term arises from processes $\chi\,\chi \to SM\,SM$ that destroy χ particles, where SM denotes Standard Model particles and the n_{eq}^2 arises from the reverse process creating χ particles.

The thermal relic density is determined by solving the Boltzmann equation numerically. However, a simple solution is highly instructive and can be achieved by defining the freeze-out to occur when $n\langle \sigma_A v \rangle = H$

$$n_f \sim (m_\chi T_f)^{3/2} e^{-m_\chi / T_f} \sim \frac{T_f^2}{M_{Pl} \langle \sigma_A v \rangle} \ , \tag{1.2.24}$$

where the subscripts f denote freeze-out quantities. The ratio $x_f \equiv m_\chi / T_f$ appears in the exponential and is therefore highly insensitive to Dark Matter properties and may be considered as constant of typically $x_f \sim 20$. The thermal relic density is then

$$\Omega_\chi = \frac{m_\chi n_0}{\rho_c} = \frac{m_\chi T_0^3}{\rho_c} \frac{n_0}{T_0^3} \sim \frac{m_\chi T_0^3}{\rho_c} \frac{n_f}{T_f^3} \sim \frac{x_f T_0^3}{\rho_c M_{Pl}} \langle \sigma_A v \rangle^{-1} \ , \tag{1.2.25}$$

where ρ_c s the critical density and the subscripts 0 denote todays quantities. Obviously the thermal relic density is insensitive to the Dark Matter mass m_χ and inversely proportional to the annihilation cross section $\langle \sigma_A v \rangle$.

Although m_χ does not contribute explicitly to Ω_χ, in many theories it is the mass scale that determines the annihilation cross section

$$\sigma_A v = k \frac{g_{weak}^4}{10 \pi^2 m_\chi^2} [v^2] \ , \tag{1.2.26}$$

where the factor v^2 is absent/present for S/P-wave annihilation and higher-order terms in v are neglected. The constant $g_{weak} \simeq 0.65$ is the weak interaction gauge coupling and k parametrizes deviations from this estimate.

With this parametrization, given a choice of k, the relic density is a function of m_χ (see figure 1.6). The width of the band comes from considering both S- and P-wave annihilation and letting k vary between 0.5 and 2. It can be seen that a particle that makes up all of Dark Matter is predicted to have mass $m_\chi \sim 100\,\text{GeV} - 1\,\text{TeV}$ and a particles that makes up 10 % of Dark Matter mass has mass $m_\chi \sim 30 - 300\,\text{GeV}$. Hence, the weak-scale particles make excellent Dark Matter candidates. This is referred to as the WIMP miracle. As a remark many details were neglected here and there are more exotic models for which k lies outside the illustrated range. Nevertheless the WIMP miracle implies that many models of particle physics naturally provide Dark Matter candidates and this is the strongest reason to expect that central problems in particle physics and astrophysics are related.

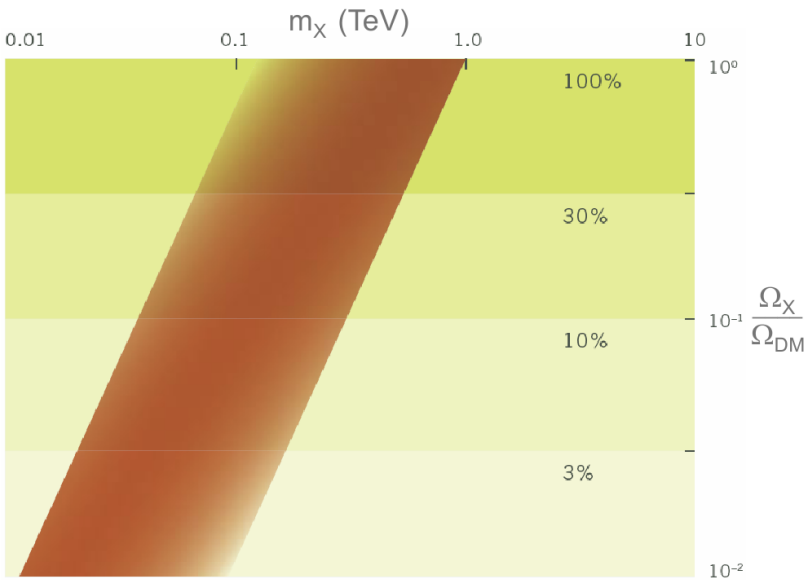

Figure 1.6: The band of natural values of m_χ and Ω_χ/Ω_{DM} for the thermal relic χ with $\Omega_{DM} \approx 0.23$ being the required total dark matter density [16].

The gauge hierarchy problem is elegantly solved by Supersymmetry (SUSY). In the SUSY extension of the SM, every SM particle has a new, yet undiscovered partner particle, which has the same quantum number and gauge interactions, but differs in spin by 1/2. The introductions of new particles with opposite spin statistics supplements the SM quantum corrections to the Higgs boson mass with opposite sign contributors, modifying equation 1.2.22 to

$$\Delta m_h^2 \sim \frac{\lambda^2}{16\pi^2}\int^\Lambda \frac{d^4p}{p}|_{SM} - \frac{\lambda^2}{16\pi^2}\int^\Lambda \frac{d^4p}{p}|_{SUSY} \sim \frac{\lambda^2}{16\pi^2}(m_{SUSY}^2 - m_{SM}^2) ln\frac{\Lambda}{m_{SUSY}} \quad , \quad (1.2.27)$$

where m_{SM} and m_{SUSY} are the masses of the SM particles and their SUSY partners, also called superpartners. For $m_{SUSY} \sim m_{weak}$ this is at most a correction of order one even for $\Lambda \sim M_{Pl}$. This does not solve but stabilizes the gauge hierarchy problem and still leaves the open question why $m_{SUSY} \sim m_{weak} \ll M_{Pl}$. However, there are some ways to generate such a hierarchy [17]. Given such a mechanism, the above relation implies that quantum effects will not destroy the hierarchy and the gauge hierarchy problem may be considered solved.

The doubling of the SM particle spectrum has many implications for cosmology. For Dark Matter it is natural to begin listing the neutral supersymmetric particles

$$\begin{aligned} \text{Spin } 3/2 \text{ Fermion:} &\quad \text{Gravitino } \tilde{G} \\ \text{Spin } 1/2 \text{ Fermions:} &\quad \tilde{B}, \tilde{W}, \tilde{H}_u, \tilde{H}_d \rightarrow \text{Neutralinos } \chi_1, \chi_2, \chi_3, \chi_4 \\ \text{Spin 0 Scalar:} &\quad \text{Sneutrinos } \tilde{\nu}_e, \tilde{\nu}_\mu, \tilde{\nu}_\tau \ . \end{aligned} \quad (1.2.28)$$

The neutral spin 1/2 Sfermions mix to form four mass eigenstates called Neutralinos. The lightest of these $\chi = \chi_1$ can not decay further into SUSY particles and is hence an ideal

WIMP Dark Matter candidate[3]. The Sneutrinos are not good Dark Matter candidates, as both their annihilation and scattering cross sections are too large, so they are on the one hand not abundant enough and on the other hand excluded by null results from direct detection experiments for all masses near m_{weak} [18]. The Gravitino is not a WIMP but nevertheless a viable Dark Matter candidate.

A general SUSY extension contains many unknown parameters. To be able to handle it is typical to consider specific models in which simplifying assumptions unify many parameters. The canonical model for SUSY studies is minimal Supergravity, which is minimal in the sense that it includes the minimum number of particles and drastically reduces the number of independent model parameters to five

$$m_0, m_{1/2}, A_0, \tan\beta, sign(\mu) \ , \tag{1.2.29}$$

where m_0 is the universal scalar mass and $M_{1/2}$ is the universal gaugino mass, both defined at the scale of grand unified theories $m_{GUT} \simeq 2 \times 10^{16}\,\text{GeV}$.

The assumption of a universal gaugino mass and the choice of m_{GUT} are supported by the fact that the three SM gauge couplings unify at m_{GUT} in SUSY theories [19]. The parameter A_0 governs the strength of cubic scalar particle interactions and $\tan\beta$ and $sign(\mu)$ are parameters that enter the Higgs boson potential. Contrary to the first two, the last three parameters have only for extreme values a significant impact on collider and Dark Matter phenomenology.

Modified Theory of Gravity Observations of the rotational speed of galaxies (see figure 1.3) show that the orbital velocity in such systems is not proportional to $\frac{1}{\sqrt{R}}$, where R is the distance from the center of mass, like one would expect by extrapolating from the Solar System to larger structures. If the orbits of stars in the galaxy are only governed by the central gravitational force and there is no additional contribution from Dark Matter, one would expect that the stars at the outer edge of the galaxy would have lower orbital velocity than those near the galaxy center. Contradictory, observations show that stars near the outer edge are orbiting about the same speed as the inner stars. To explain this flattening of the rotational curve without the necessity of additional mass Modified Newtonian Dynamics (MOND) was propounded in the early 1980s.

The fundamental idea of this theory is to disentangle between kinematics and kinetics in the description of motion. The kinematics is the part of the dynamics wherein the mass is irrelevant (e.g. displacement, velocity) and kinetics does depend on mass like force and inertial moment. Each of them has its own type of acceleration, namely the 'kinematic' and the 'kinetic' acceleration. If a particle is moving on a circular path then it would experience

[3] valid in case of R-parity conservation. R-parity is defined as $p_R = (-1)^{3(B-L)+2s}$ with baryon number B, lepton number L and spin s and typically separates standard-model from supersymmetric particles

a centripetal acceleration $\frac{v^2}{r}$ also referred as pseudo centrifugal acceleration. On the other hand the gravitational acceleration, e.g. a star in the arm of a spiral galaxy, can be derived from Newton laws as $a_N = \frac{GM}{r^2}$ corresponding a kinetic acceleration. In general, both accelerations are considered equal and there has been no need for differentiation. Exactly this is the assumption which MOND does not rely on. Here, the kinematic acceleration is converted into an effective kinematic acceleration $a_{eff} = a(\mu)$. The μ parameter is usually 1 but less than 1 if the acceleration is extremely small. In all circumstances the kinetic equals the effective kinematic acceleration $a_N = a_{eff}$. The right hand side will be equal to kinematic acceleration or less depending whether the value of usual kinematic acceleration is greater than critical value ($a_0 \approx 10^{10} m/s^2$) or less than that. Hence, the effective kinematic acceleration is given as

$$a_{eff} = a\mu(\frac{a}{a_0}) \ , \tag{1.2.30}$$

where $\mu(\frac{a}{a_0})$ is termed as μ-function. The function is defined as follows

$$\mu(\frac{a}{a_0}) = \begin{cases} = 1 & \text{for } a \ll a_0, \\ = \frac{a}{a_0} & \text{for } a \gg a_0 \ . \end{cases} \tag{1.2.31}$$

Applying this to the gravitational attraction force between an object to the central galaxy core of mass M,

$$a_N = a_{eff} \Leftrightarrow \frac{GM}{r^2} = a\mu(\frac{a}{a_0}) \ . \tag{1.2.32}$$

At large distances the kinematical acceleration a is smaller than a_0 hence the function $\mu(\frac{a}{a_0}) = \frac{a}{a_0}$. Inserting this into the equation above

$$\frac{GM}{r^2} = a\frac{a}{a_0} \Leftrightarrow a = (\frac{GMa_0}{r^2})^{\frac{1}{2}} \ . \tag{1.2.33}$$

On the other hand, the equation that relates the centripetal acceleration of an object orbiting in a circular orbit of radius r with a velocity v in the galaxy is

$$a = \frac{v^2}{r} \ . \tag{1.2.34}$$

Combining both equations leads to

$$v = (GMa_0)^{\frac{1}{4}} \ . \tag{1.2.35}$$

This states that the velocity of a star on circular orbit from the center is constant and does not depend on the distance r, in other words the rotational velocity profile is flat. The above relationship between the flat rotational velocity v to the observed mass M of the galaxy matches with observed flat velocity to luminosity L known as Tully-Fisher relation [20].

Due to the negligibly small value of the critical acceleration a_0 the effect of MOND could not be observed on small scales, where $\mu(\frac{a}{a_0}) = 1$ thus $a_{eff} = a$, and it just becomes visible

on large scale structures like galaxies. MOND is able to describe the galaxy cluster rotation [21], especially the flat rotational velocity profile of galaxy arms (see figure 1.3), without the need of Dark Matter. However, this theory is not able to explain some of the observed phenomena related to Dark Matter, like e.g. the Bullet Cluster (see figure 1.5).

1.3 Propagation

Independent of their origin all cosmic ray particles we can observe are subject to propagation. For energies lower than $10^{15} - 10^{17}$ eV cosmic rays are confined in our Galaxy and their propagation is dominated by the interaction with the interstellar medium (ISM) and the interstellar radiation field (ISRF). At higher energies cosmic rays cannot be bound by galactic magnetic fields and are therefore mainly of extragalactic origin. During their propagation through our Galaxy, cosmic rays are affected by many processes. In the low-energy range, one of the most important processes is magnetic diffusion, which is produced by random magnetic turbulences that fill all the ISM. The interaction of charged particles with these turbulences leads to a random walk: if the gyro-radius of the particle is equal to the scale of the turbulence resonant scattering can occur. Cosmic rays are scattered isotropically off the magnetic turbulences of matching scale. Therefore, contrary to uncharged particles which travel along straight lines, charged cosmic rays cannot be traced back to their origin. In addition, cosmic rays interact with the gas present in the interstellar medium. In case the cosmic ray particles are instable they could also decay during their propagation and produce other types of cosmic rays. These effects are discussed in section 1.3.1.

Apart from the effects on the galactic scale, which dominate the propagation, influence associated to Solar Activity may not be neglected. The Sun has 11-year cycles during which its activity increases and decreases periodically. One of its manifestation is the increment of the Solar Wind Flux, which acts as a potential on cosmic rays by pushing them away from the Solar System and reducing their energy. The influence of the Solar Activity on the cosmic ray fluxes is described in section 1.3.2.

Finally, cosmic ray particles approaching the terrestrial environment are subject to the Earth's magnetic field and its atmosphere. The Earth's magnetic field is strongly depending on the spherical position (longitude, latitude) and acts as a potential on the cosmic ray fluxes by suppressing low energetic particles. Compared to the low densities in the interstellar medium the atmosphere is a dense region in which the primary cosmic particles interact and produce extensive showers of secondary particle. These phenomena are described in section 1.3.3.

1.3.1 Interstellar Medium

A suitable equation to describe the propagation of cosmic rays that includes all the known physics processes can be written as

$$\begin{aligned}\frac{\partial\psi(\mathbf{r},p,t)}{\partial t} =& q(\mathbf{r},p,t) + \nabla\cdot(D_{xx}\nabla\psi - \mathbf{V}_c\psi) + \frac{d}{dp}p^2 D_{pp}\frac{d}{dp}\frac{1}{p^2}\psi \\ &- \frac{\partial}{\partial p}[\dot{p}\psi - \frac{p}{3}(\nabla\cdot\mathbf{V}_c\psi)] - \frac{1}{\tau_f}\psi - \frac{1}{\tau_r}\psi \ ,\end{aligned} \tag{1.3.1}$$

with $\psi(\mathbf{r},p,t)$ as Cosmic Ray density per unit of momentum p at position $\mathbf{r}$. Below the single terms and hence all the quantities will be reviewed one by one.

The first term $q(\mathbf{r},p,t)$ is the source function that describes the injection spectrum, composition and space-time distribution of point-like sources producing primary particles. The distribution of Cosmic Ray sources is chosen to reproduce the observed Cosmic Ray fluxes. The spectrum of injected primary nuclei is modeled as a power law in momentum $\frac{dq}{dp} \propto p^{-\gamma}$, where γ can vary with particle species. These assumptions as well as a small break in γ is allowed in the framework of diffusive shock acceleration models [22].

The second term represents the isotropic diffusion, defined by the rigidity dependent coefficient

$$D_{xx} = \beta D_0(\rho/\rho_0)^\delta \tag{1.3.2}$$

which is in general a function of $\mathbf{r}, \beta, p/Z$, where $\beta = \frac{v}{c}$ is the particle velocity and Z is the charge and p/Z is the rigidity which also determines the gyro-radius in a given magnetic field. For a Kolmogorov spectrum of magnetohydrodynamic (MHD) turbulences the parameter $\delta = 1/3$. In some models there is an optional break in the sense of two different $\delta_\pm$ below and above the break rigidity ρ_0. The convection velocity $\mathbf{V}_c$ is assumed to be a linear function of the distance z from the Galactic plane leading to a constant adiabatic energy loss.

Stochastic re-acceleration [23], which is basically the Second Order Fermi Acceleration discussed in section 1.1.1, can be described as diffusion in momentum space and is determined by the diffusion coefficient D_{pp} which is related to the space diffusion coefficient D_{xx} by the Alfven velocity V_A

$$D_{pp}(D_{xx}, V_A) = \frac{4p^2V_A^2}{3\partial(3-\partial^2)(4-\partial)wD_{xx}} \ , \tag{1.3.3}$$

where w is a parameter describing the level of turbulence and equal to the ratio of wave energy density to magnetic field energy density. In general $w = 1$ is assumed but the relevant quantity is rather V_A/w.

The first part of the fourth term describes continuous energy losses, e.g. by synchrotron radiation or bremsstrahlung with $\dot{p}$ being the loss rate. The second part of the fourth term containing $\nabla\cdot\mathbf{V_c}$ describes the influence of the Galactic wind. It represents the adiabatic

momentum gain or loss in the flow of gas by scattering of cosmic rays on magnetic field inhomogeneities. This is also called adiabatic cooling.

The last two terms specify the influence of fragmentation and radioactive decays with the characteristic time scales τ_f and τ_r respectively. Here, τ_f is a function of the total spallation cross-section and the amount of matter traversed by cosmic rays, which can be estimated based on surveys of gas clouds.

In the description of propagation, interstellar helium with a relative abundance of about 10% compared to hydrogen must be taken into account but heavier components of the ISM are contributing negligibly to the production of secondary cosmic rays. The spectrum of secondary particles is related to the energy dependence of the primary fluxes. There is an intrinsic secondary energy distribution related to the production cross-sections, known from acceleration experiments on Earth [24].

The number of particles produced in hadronic collision, like in the proton-proton case, grows faster than in leptonic collisions. In general, lighter mesons are produced in big quantities, especially pions and kaons. Those have decay modes containing many other types of particles like neutral pions, which are well known as an efficient source of gamma-rays, as well as charged pions, which are efficient in the production of positrons and electrons. Positive and negative mesons are produced in equal number due to conservation laws. However, the average particle energy is higher for electrons than for positrons. This difference is related to polarization effects in the muon production caused by the left-right asymmetry in weak interactions [25].

The amount of traversed matter and the propagation time of particles can be extracted from observations. However, to be able to retrieve the local interstellar spectrum (LIS) of cosmic rays from the spectrum observed in the vicinity of the Earth, the solar (see section 1.3.2) and the terrestrial modulation (see section 1.3.3) have to be taken into account.

1.3.2 Solar System

When cosmic rays are approaching the Solar System, the influence of the Solar Wind increases and the particles are pushed away from the solar neighborhood. The intensity in the cosmic ray repulsion depends directly on the Solar Activity. The repulsion inflicts an energy loss and hinders the cosmic ray particles in reaching the Earth.

A simple approach to describe this phenomenon is the Force-Field Modulation ([26], [27]), which models this effect as an electrical potential, which reduces the cosmic ray energy and redistributes them. The cosmic ray intensity $J_\odot$ observed inside the Solar System is related

to the interstellar intensity J_∞ as follows

$$J_\odot(\epsilon) = \frac{\epsilon^2 - m^2}{\epsilon_\infty^2 - m^2} J_\infty(\epsilon_\infty), \tag{1.3.4}$$

where ϵ_∞ is the cosmic ray energy at the boundary of the heliosphere. Depending on their energy, cosmic ray particles are affected differently

$$\epsilon_\infty = \begin{cases} \epsilon + \Phi + p \log(\frac{p_c - \epsilon_c}{p + \epsilon}) & \epsilon < \epsilon_c \\ \epsilon + \Phi & \epsilon_c \leq \epsilon \end{cases} \tag{1.3.5}$$

where ϵ_c represents the limit where those are affected by two different modulation regimes [28]. This is an approximative description of the heliospheric transport equation (see e.g. [29]). The low-energy regime is rarely used, however it is consistent with Solar Flare studies. At a Solar Minimum, a typical value for p_c is $\sim 0.1 - 1\,\mathrm{GeV}$ [30].

The commonly used higher energy regime depends on an energy shift which is related to the modulation potential ϕ,

$$\Phi = |Z|e\phi, \tag{1.3.6}$$

where $|Z|e$ is the absolute value of cosmic ray electric charge. The modulation potential should vary in time and can be estimated from diffusion coefficient and Solar Wind velocity. In practice it is typically considered as a free parameter that should be determined for each observation period separately. Temporal correlations between Neutron Monitor measurements, the Solar Activity and intensity of cosmic rays have been found [31]. The information obtained by such analyses improves the accuracy in the determination of ϕ.

1.3.3 Terrestrial Environment

The interaction of cosmic rays in the terrestrial environment can be subdivided into interaction with the geomagnetic field and with matter in the Earth's atmosphere.

Magnetic Field The International Association of Geomagnetism and Aeronomy (IAGA) provides a standard mathematical description of the Earth's main magnetic field that is used in studies of the Earth's deep interior, its crust and its Ionosphere and Magnetosphere. The International Geomagnetic Reference Field (IGRF) considers the geomagnetic field as current free outside the Earth and describes the field itself and its secular variation by the gradient of a scalar potential Φ which can be represented by following expansion:

$$\Phi(r, \Theta, \varphi, t) = \sum_{n=1}^{n_{max}} (\frac{R_E}{r})^{n+1} \sum_{m=0}^{n} (g_n^m(t) \cos\, m\varphi + h_n^m \sin\, m\varphi) P_n^m(\Theta) \tag{1.3.7}$$

where R_E is the Earth's radius, r, φ and Θ are the spherical geographic coordinates, P_n^m is the Schmidt normalized Legendre polynomial of degree n and order m and g_n^m and h_n^m are the

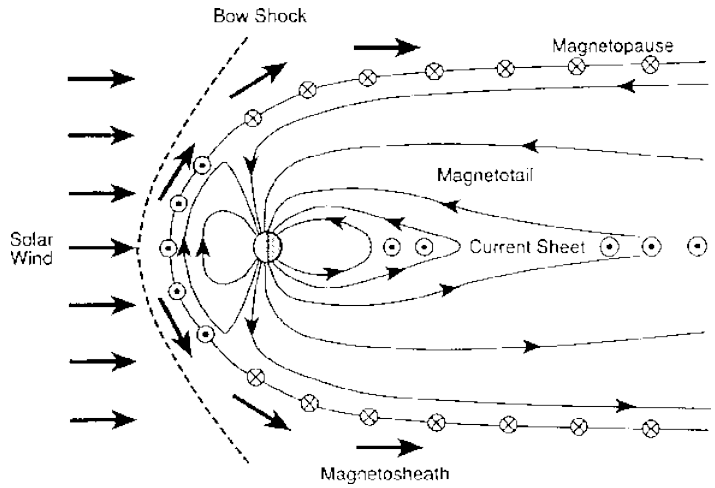

Figure 1.7: The magnetopause generated by the solar wind pressure on the Earth's magnetic field [34].

Gauss spherical harmonic coefficients. The latter are derived from magnetic field measurements of geomagnetic stations around the world, shipborne magnetometers and satellites. Recently the IAGA issued a new set of Gauss coefficients defining the 11th generation of the IGRF model [32].

For many applications a satisfactory approximation of the geomagnetic field is obtained by limiting the development of the equation above to terms of order 1 what leads to the so-called Earth's centered geomagnetic dipole field with an axis tilted with respect to the Earth's rotation axis. The momentum M_0 of the geomagnetic dipole is given by

$$M_0 = \sqrt{(g_1^0)^2 + (g_1^1)^2 + (h_1^1)^2}. \tag{1.3.8}$$

The geocentric spherical coordinates Θ_{dip} and φ_{dip} of the geomagnetic dipole axis are defined by

$$\cos\,\Theta_{dip} = g_1^0/M_0, \tan\,\varphi_{dip} = h_1^1/g_1^1. \tag{1.3.9}$$

Additionally to the geomagnetic field induced by sources inside the Earth there is a contribution from currents outside the Earth in the magnetosphere and on its external boundary the magnetopause. This so-called external magnetosphere magnetic field is described by the Tsyganenko models [33], which consider the external magnetic field as correlated to the geomagnetic field in the geomagnetic dipole approximation. The external magnetic field is produced by different systems of modular currents with shape and strength depending on the dipole tilt axis on the solar wind dynamic pressure and the interplanetary magnetic field (IMF). The contributions from the ring current, the field aligned currents and the magnetosheath currents are confined into a specific model of the magnetopause (see figure 1.7). The magnetopause is represented by a semi-ellipsoid in the front, continued by a cylindrical surface in the far tail ($\approx 60R_E$). The axis of the magnetopause is parallel to the geocentric

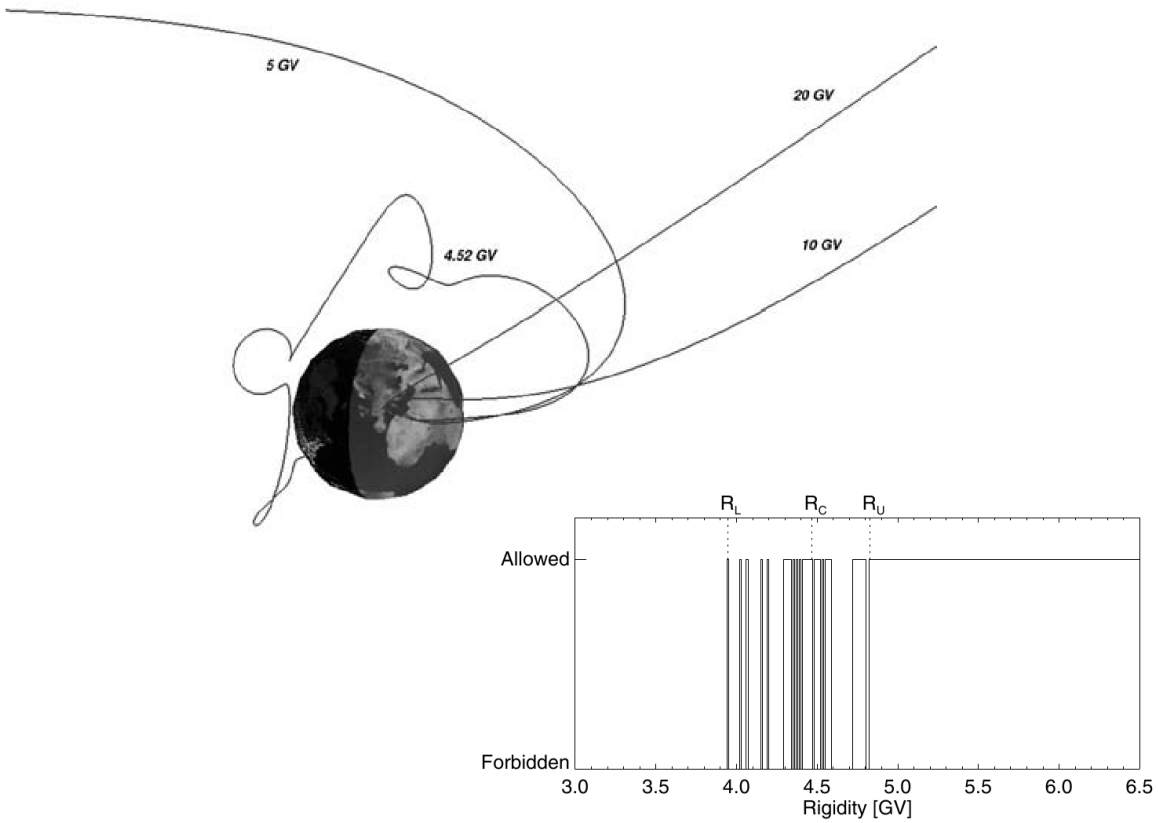

Figure 1.8: Trajectories of 20, 10, 5, 4.52 GV positively charged particles in the geomagnetic field in vertical direction at 20 km above Jungfraujoch (Switzerland). With decreasing rigidity particles get more and more deflected. For all rigidities $R > R_U$ particles are observable. For rigidities $R < R_L$ no particles are reaching the observer. In the region between these two values ('Penumbra') some rigidity bands are allowed and some are forbidden [35].

solar magnetoshperic (GSM) equatorial plane. The size of the magnetopause is inverse proportional to the solar dynamic pressure P_{dyn} which can be described by $P_{dyn} = \rho v$ where ρ and v represent the solar wind density and velocity respectively.

For Cosmic Ray measurements it is crucial to quantify the lower rigidity limit called geomagnetic cutoff above which cosmic rays can cross the Earth's magnetosphere and reach a specific position from a specific observational direction. It is important to mention that this cutoff does not have a distinct rigidity limit. By simulating the propagation of particles through the magnetosphere one can see that there are three distinct regions in rigidity spectrum of allowed trajectories (see figure 1.8). A high rigidity region where all trajectories are allowed, a low rigidity region where all trajectories are forbidden and an intermediate region called 'Penumbra' where several bands of allowed and forbidden trajectories exist. The rigidity of the last allowed trajectory before the first forbidden one is called the upper cutoff rigidity R_U. The rigidity of the last allowed trajectory below which all trajectories are forbidden is called the lower cut-off rigidity R_L. Some trajectories, not shown in the figure, which can neither reach the surface nor leave magnetic field are trapped in the mag-

netosphere. The effective cutoff rigidity is given by $R_C = R_U - n\partial R$, where n represents the number of allowed trajectories in the penumbral region. Maps of the values obtained with the simulation package 'Planetocosmics' [36] for R_U and $R_U - R_L$ as a function of geomagnetic longitude and latitude are shown in figure 1.9. In general the rigidity cutoff is a function of latitude with the highest values $R_U \approx 12 - 15\,\mathrm{GeV}$ in the equatorial region and decreasing to $R_U \lesssim 1\,\mathrm{GeV}$ at latitudes greater $40\,^\circ$. In the southern hemisphere at about $-50 - 0\,^\circ$ geographic latitude and $-90 - 40\,^\circ$ geographic longitude there is a special region called the 'South Atlantic Anomaly' (SAA) [37]. It corresponds to an area where the Earth's inner Van Allen radiation belt comes close to the Earth's surface. This is caused by the non-concentricity of the Earth and its magnetic dipole. The result is that here the Earth's magnetic field is extraordinary weak and more low energetic particles penetrate deep into the Earth's vicinity.

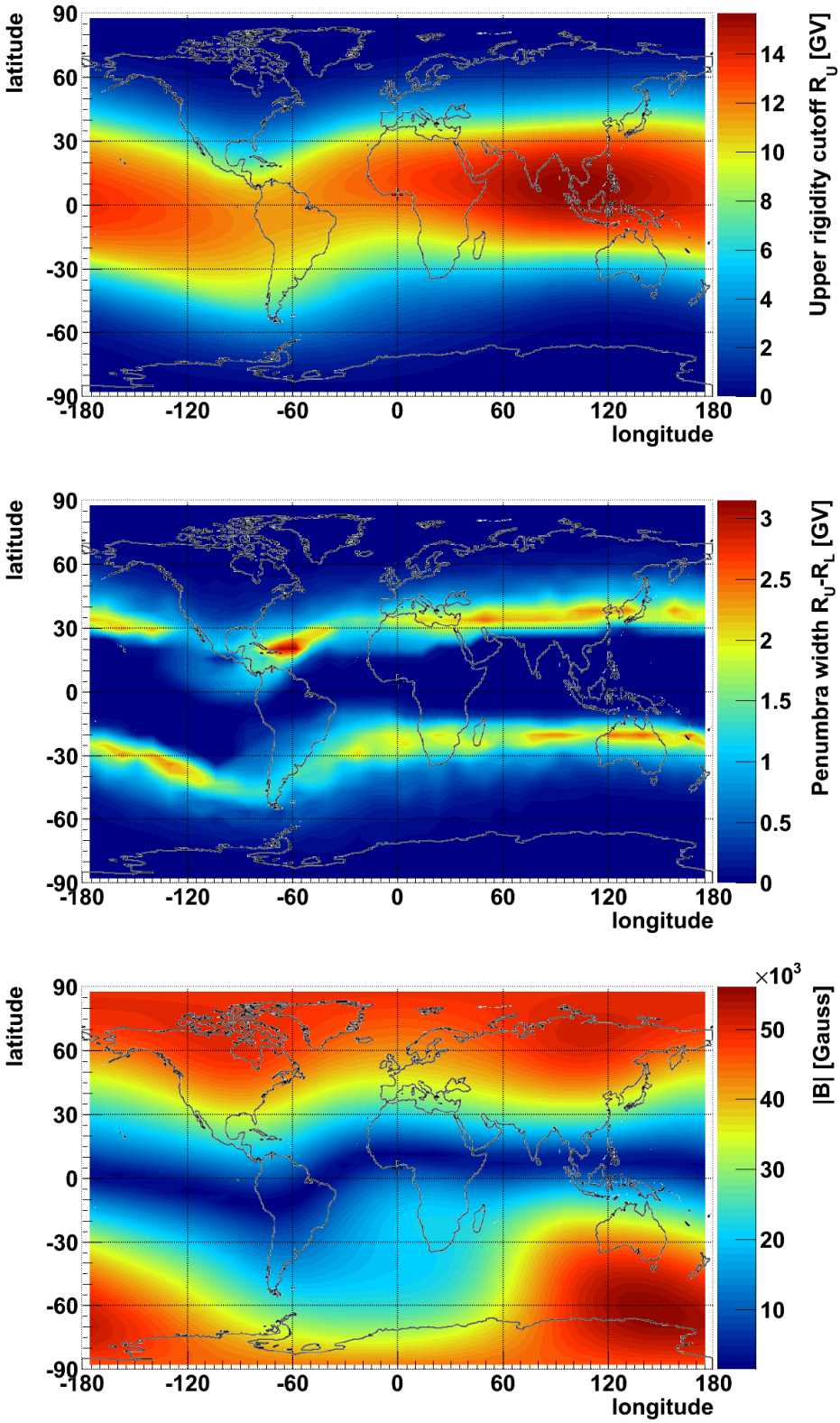

Figure 1.9: Vertical rigidity cutoff parameters R_U (*upper*), $R_U - R_L$ (*center*) and total magnetic field intensity (*lower*) at 350 km altitude as a function of longitude and latitude.

Atmosphere The production of secondary particles does also occur when cosmic particles enter the Earth's atmosphere. The amount of matter traversed in the atmosphere is typically many times larger than the matter traversed by the primary particle on its way from its source to the top of the atmosphere. Hence, the probability and frequency of interactions is enhanced and a so-called extensive air shower is generated in the atmosphere (see figure 1.10). The number of particles is increasing rapidly as function of the shower depth. In the numerous interactions the mean particle energy is decreasing and at a certain point it is limiting the production of new particles. After this shower maximum more particles are stopped than created and the number of particles declines. The shower can be divided into three components: the muonic, electromagnetic and hadronic component.

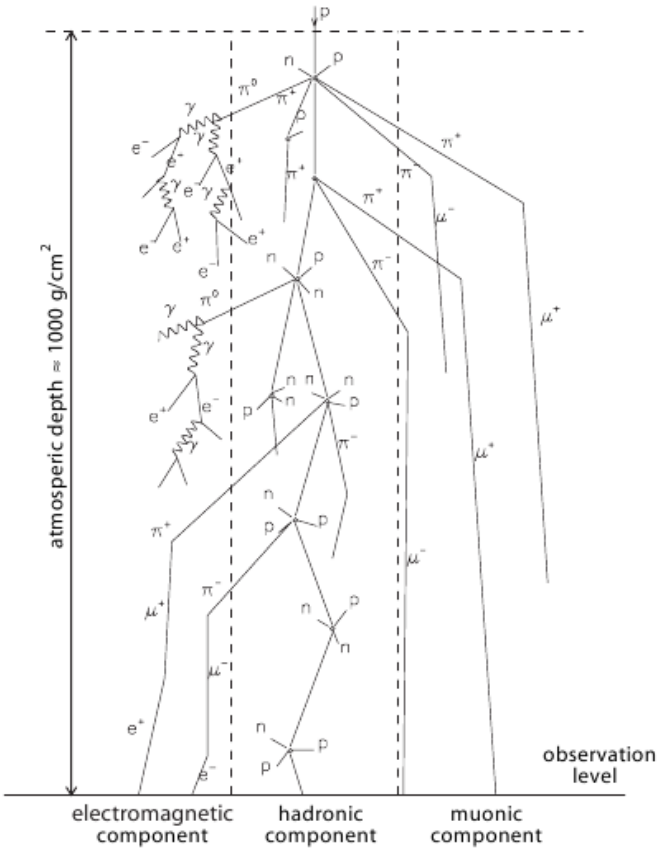

Figure 1.10: Schematic view of an extensive air shower generated by the interaction of a high energy cosmic particle in the atmosphere [38].

Muons, as the most abundant charged particles at sea level, will briefly be depicted in the following. In general they are produced near the top of the atmosphere and lose about 2 GeV to ionization before reaching the ground. Their sea level flux is a result of the production spectrum, the energy loss in the atmosphere and the decay. The energy spectrum of sea level muons is shown in figure 1.11. With increasing zenith angle the average muon energy increases as the amount of traversed matter is increased and hence the probability to absorb low energy muons is higher. The muon charge ratio reflects the charge asymmetry in the cosmic ray spectrum and the fact that positive mesons are favored in the forward fragmentation region of proton interactions. These interactions with the atmosphere conceal the primary particle and its properties. This is the reason for direct observations being performed at high altitudes by balloon or satellite experiments.

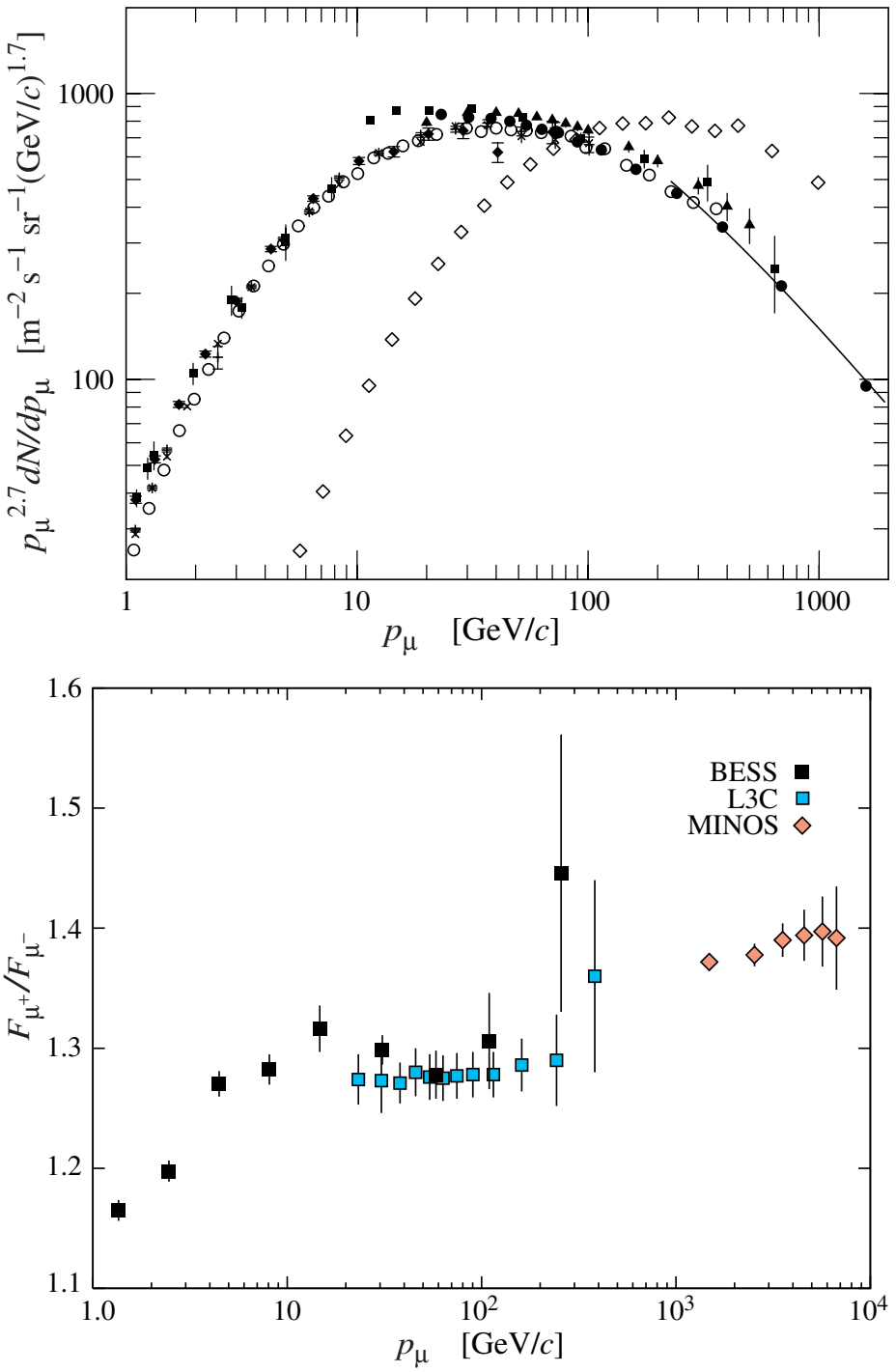

Figure 1.11: Sea level muon spectrum (*top*) observed by different experiments at $\Theta = 75°$ (open diamonds) and $\Theta = 0°$ (all other markers). The solid line reflects the respective parametrization. Muon charge ratio (*bottom*) as function of momentum. Both taken from [39].

1.4 Recent Data

As described in the preceding sections cosmic ray particles are generated in astrophysical sources and propagate through the Galaxy. Some of them are entering the Solar System and the terrestrial environment and become locally observable.

1.4.1 Primary Spectra

The cosmic particle flux incident at the top of the atmosphere basically includes all stable charged particles and nuclei with reasonably long lifetime. The composition is $\sim$ 89 % hydrogen, $\sim$ 10 % helium, $\lesssim$ 1 % heavier elements and $\lesssim$ 1 % electrons. Figure 1.12 shows the differential flux of the most abundant cosmic rays measured by various, direct and indirect, particle detectors.

The energy spectrum of observed cosmic rays is spread over many orders of magnitude and follows in general a power law dependency $A \times E^{-\gamma}$ with the spectral index $\gamma \approx 2.7$. Hence with rising particle energy direct measurement becomes more and more difficult and larger instrumented volumes are necessary to detect the same number of events. At energies above about 10^{15} eV the direct detection is not feasible anymore and indirect observations techniques like air shower experiments are necessary. At higher energies, in the regime of indirect measurements, the differential energy spectrum has been multiplied by $E^{2.7}$ to resolve the structure in the steep spectrum. The change in the spectral index at $10^{15} - 10^{16}$ eV is known as the 'knee' and the one at $\sim 10^{19}$ eV is called the 'ankle' of the spectrum. Under the assumption that the cosmic ray spectrum below 10^{18} eV is of galactic origin the knee could reflect the maximum particle energy most cosmic accelerators in the Galaxy can provide. The ankle can be construed as the result of an extragalactic, higher-energetic population of particles overtaking a galactic one. Another possible interpretation of this feature is the 'GZK-Cutoff', which is the energy loss of primary protons due to photo-meson production $\gamma_{CMB} p \rightarrow p + \pi$ with the 2.7 K photons of the cosmic microwave background radiation. As the primary does not get absorbed but subsequently looses energy until it falls below the pion production threshold, high-energy primaries are 'shifted' to lower energies. Hence this process is rather a suppression or 'pile-up' than a cut-off. Since CMB photons are everywhere, above the threshold of about 6×10^{19} eV, the universe will become partially opaque for the primaries, limiting them to a mean free path of about 50 Mpc [4] above the threshold.

[4] 50 Mpc $\approx$ 160 Mly $\approx 1.5 \times 10^{24}$ m corresponds to about the scale of the local supercluster, containing inter alia the Local Group and the Virgo Cluster

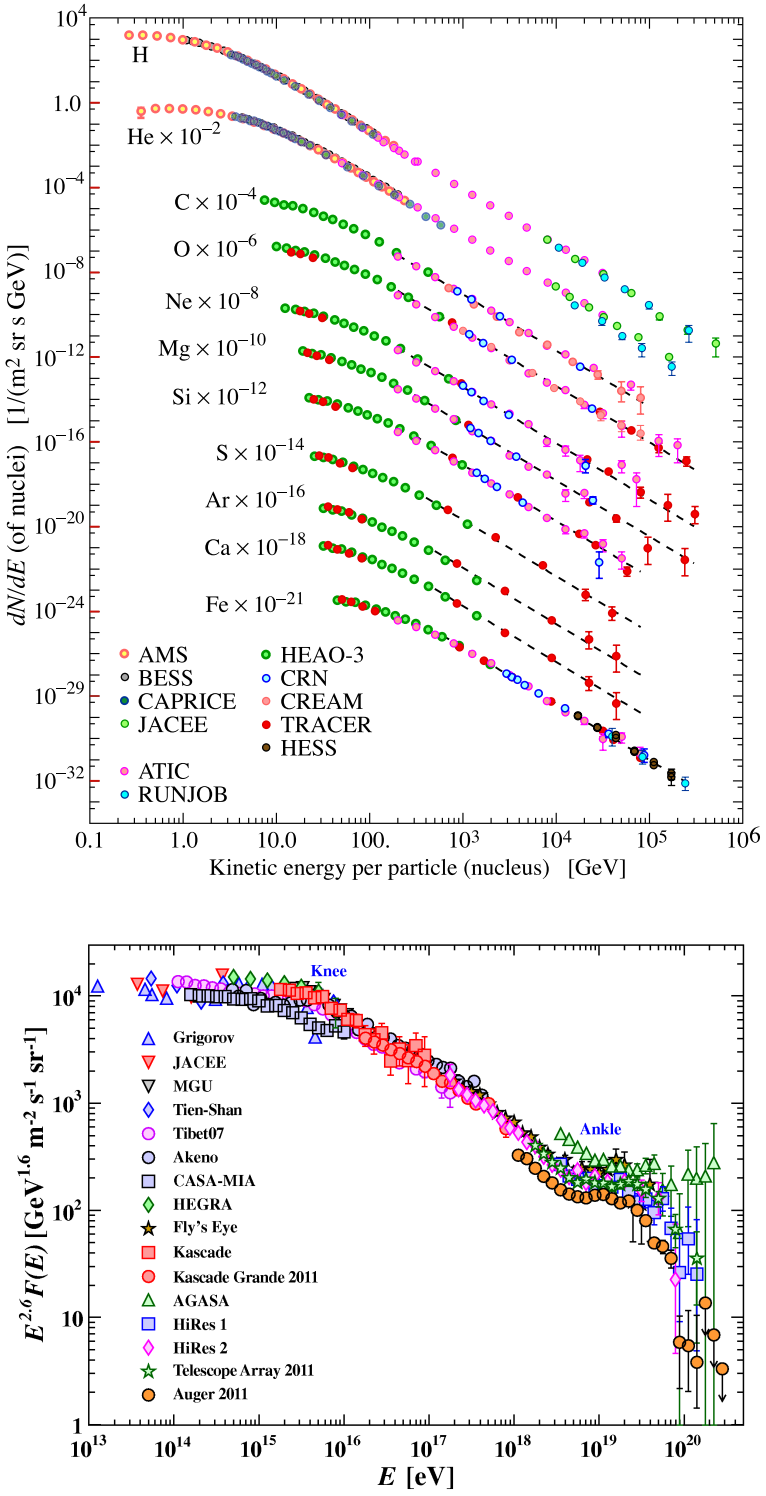

Figure 1.12: Cosmic ray fluxes observed by mainly balloon- and satellite-borne direct measurements (top) and ground-based indirect detection techniques (bottom) [39]. The former is resolving the composition and the latter is showing the all particle spectrum.

1.4.2 Secondary Ratios

The cosmic ray spectrum consists of 'primary' cosmic rays, which are the particles produced and accelerated in the sources, and 'secondaries', which are produced mainly in interactions of the primaries with the ISM. Protons and helium are more likely to be primary particles as they are essentially emitted in supernovae. Less-abundant end-products of stellar nucleosynthesis, like lithium, beryllium and boron, are typically generated in interactions and therefore rather secondary cosmic rays. The ratios of primary to secondary particles provide valuable information on cosmic propagation. In fact, the Boron-to-Carbon (B/C) ratio is used to constrain the average amount of matter traversed by cosmic rays during their propagation from their source to the observer. More energetic particles tend to escape faster from the galaxy and, on the other hand, low energy particles tend to be scattered by magnetic field more often and thus would spend more time to reach the observer. The combination of these two mechanisms lead to the shape of the B/C spectrum, which first rises with energy to a peak value at about 1 GeV/n and then decreases at higher energies. Diffusion and re-acceleration are two main components of the transport equation describing cosmic propagation (see section 1.3). Diffusion and convection are related to the escape time of the primaries from the galaxy and hence to the total number secondaries produced in interactions. Therefore these processes determine the overall height of the spectrum . Re-acceleration, induced by moving magnetic turbulences, hardens the spectrum and therefore influences the peak position [40].

Another primary-to secondary ratio of large impact is the Be^{10}/Be^{9} ratio (see figure 1.14). This corresponds to a radioactive 'clock' which measures the mean age and hence the propagation time of cosmic rays. Among other products two beryllium isotopes are produced by spallation of mainly heavy ion cosmic rays on hydrogen and helium of the ISM: the stable Be^{9} and the decaying Be^{10} with a half-life of ~ 1.6 Myr. Together with the known production cross sections the Beryllium-10 fraction is used to determine the propagation time. A high observed ratio would mean that the cosmic rays are relatively young. A low ratio would implicate that most of the Beryllium-10 had time to decay because the primaries have been traveling the galaxy for much longer than their half-life. Recent analyses (e.g. [42]) point to a propagation time scale of ~ 100 Myr.

1.4.3 Dark Matter Signal

Apart from the expected dependencies, which can be explained by common production and propagation models, the observed cosmic ray spectra also contain unexpected features, which may be introduced by 'exotic' particle sources like Dark Matter (see section 1.2). The cosmic leptons spectrum shown in figure 1.15 observed by various direct and indirect mea-

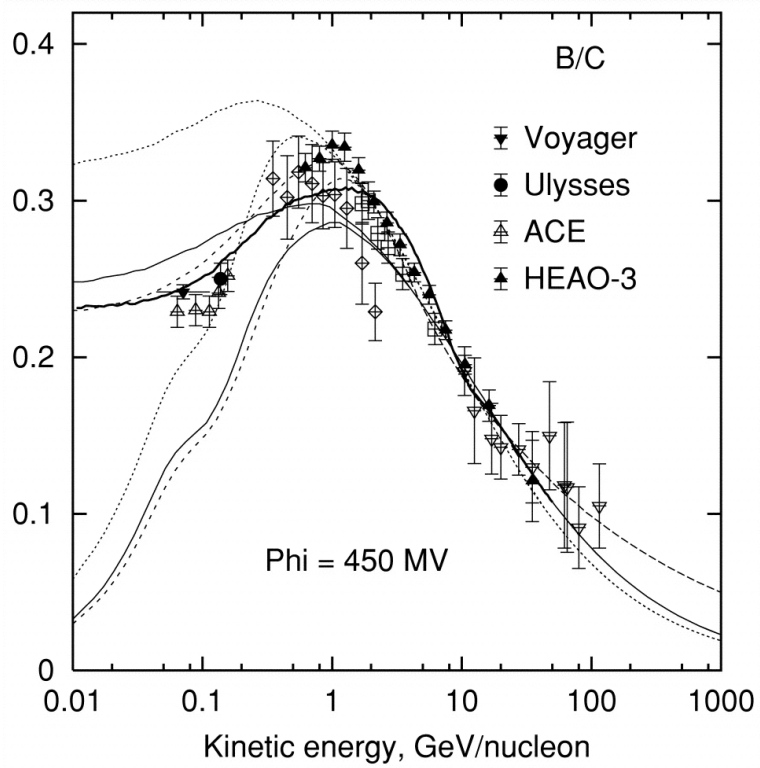

Figure 1.13: The cosmic Boron-to-Carbon ratio as observed by different experiments compared to expectations based on propagation models 'Diffusion and Convection' (solid line), 'Diffusive Reacceleration' (dashed line) and 'Plain Diffusion' (dotted line). The lower curves correspond interstellar and the upper ones to the solar modulated ($\Phi = 450\,\mathrm{MV}$) spectra [41].

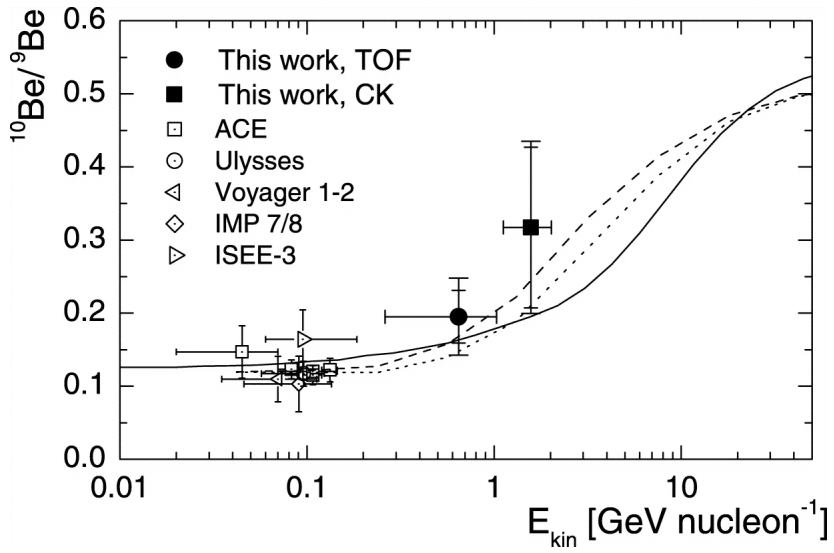

Figure 1.14: The cosmic Beryllium-10 to Beryllium-9 ratio as observed by different experiments compared to expectations from propagation models 'Diffusion and Reacceleration' (solid line), 'Leaky Box' with hydrogen density $n_H = 0.2\,\mathrm{cm}^{-3}$ (dotted line) and 'Leaky Box' in which the solar system is part of a low-density Local Bubble and the rest of the Galaxy has a hydrogen density $n_H = 0.5\,\mathrm{cm}^{-3}$ [43].

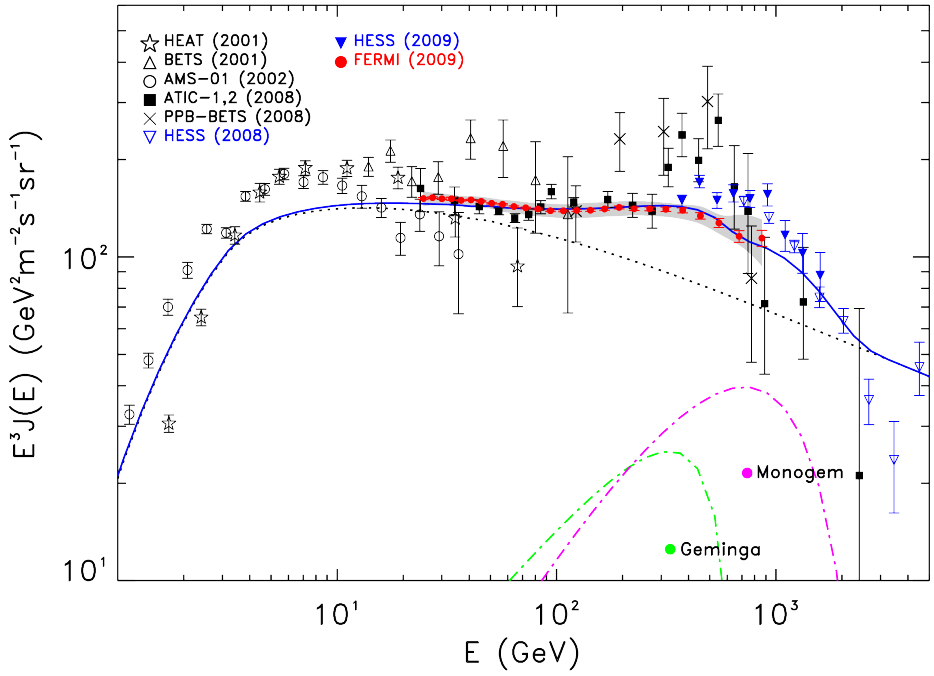

Figure 1.15: The absolute cosmic lepton spectrum as observed by different experiments in comparison to computations (blue line) based on observed pulsars with distance $d < 1\,\mathrm{kpc}$ and expected secondary contribution during cosmic ray propagation (dashed black like). The dominant contributors Monogem and Geminga are indicated by colored dot-dashed lines. The gray band represents systematic errors on Fermi-LAT data [44].

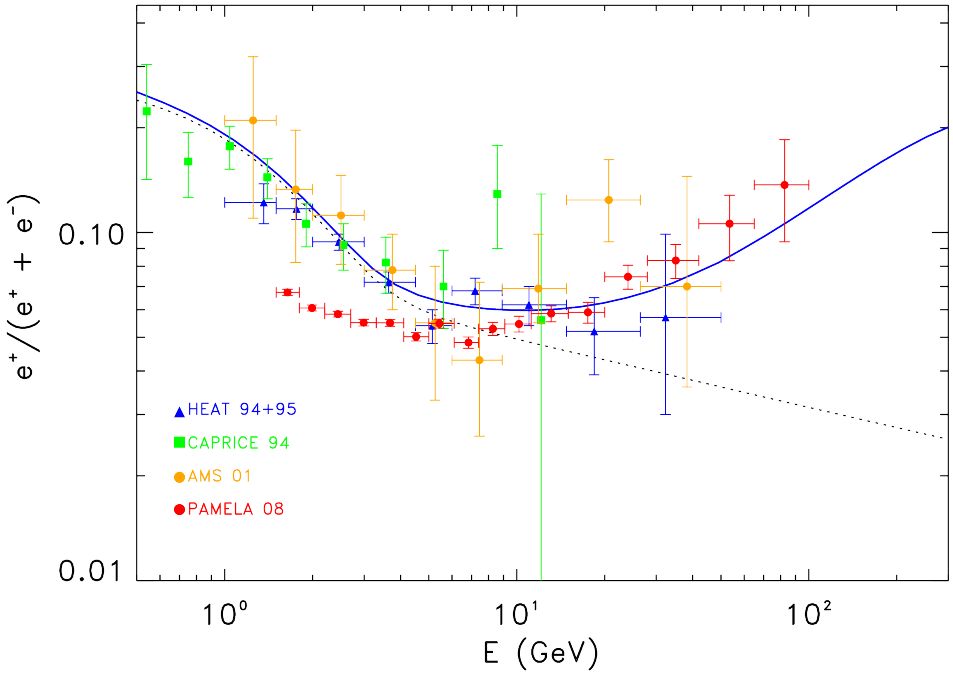

Figure 1.16: The cosmic positron fraction $e^+/(e^- + e^+)$ as observed by different experiments (data points) compared to the expected secondary contribution during cosmic ray propagation (black dotted line). The additional contribution of nearby pulsars coherent to figure 1.15 is indicated (blue line) [44].

surements consists of three main regimes. The lower energy regime $E \lesssim 20\,\text{GeV}$ is dominated by the geomagnetic field, which is deflecting low energy particles proportional to the geomagnetic field intensity. In the central regime $20\,\text{GeV} \lesssim E \lesssim 1\,\text{TeV}$ the spectrum follows a power-law dependency with spectral index $\gamma \approx -3$. At higher energies observations denote a break in the spectrum leading to a steepening with spectral index $\gamma \approx -4$. A widely discussed feature of this spectrum, namely the excess in the region $0.4 - 1\,\text{TeV}$ above the expected standard propagation model expectation, could arise from an additional contribution from nearby pulsars or Dark Matter. However, recent measurements of the position and the shape of this excess are contradictory. This is mainly due to statistical and systematical uncertainties in the flux measurement. Another approach to the same issue is to investigate the ratio of positrons in the total lepton flux (see figure 1.16). This partially cancels out uncertainties like detector acceptance and observation time. The general trend of the ratio spectrum is a decrease with rising particle energy. This is consistent with solutions to Eq. 1.3.1 as implemented in the Galprop code including only supernova remnants as sources [49]. At energies above about 30 GeV the observed positron fraction becomes significantly higher than the expected one. In general the decay or annihilation of Dark Matter particles is expected to be symmetric so nearly the same amount of positrons and electrons should be produced. If Dark Matter would be the dominant source, the positron

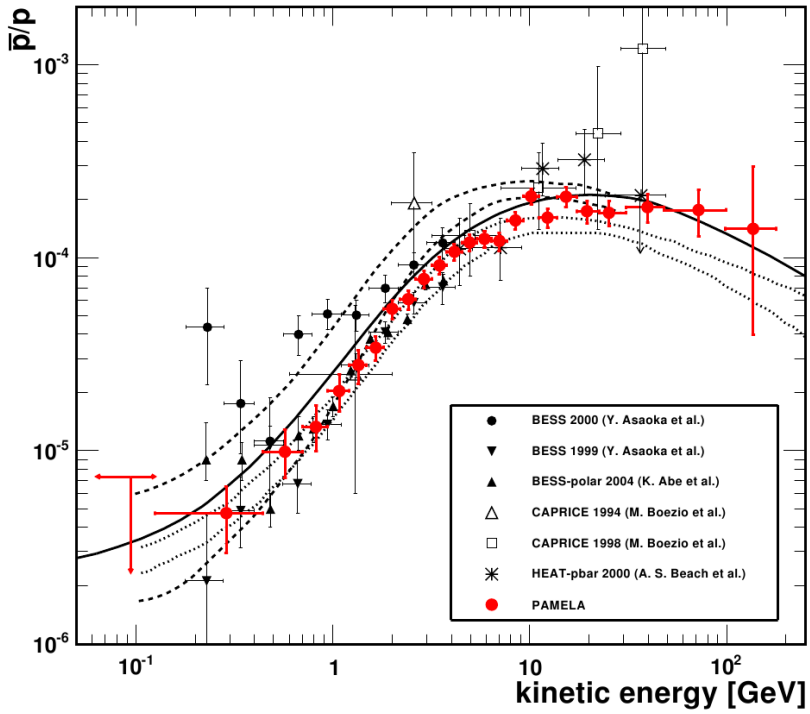

Figure 1.17: The cosmic antiproton to proton ratio as observed by different experiments (data points) compared to the expected secondary contribution during cosmic ray propagation based on different models ('Leaky Box' limits - dashed line; 'Diffusion Reacceleration with Convection' limits - dotted line; 'Plain Diffusion' calculation - solid line) [48].

ratio should approach towards 0.5 up to the Dark Matter particle mass and then drop back to the 'background' ratio, which means the expected ratio of secondary positrons. From this mass edge one could deduce the Dark Matter particle mass. However, currently there is no indication for such a decrease. Remarkably, the very same signature can be explained by Pulsars. Also for them the expectation is that electrons and positrons are produced in an approximately same amount. In fact, these astrophysical objects are the main contestants to Dark Matter in the explanation of the excess. Various recent analyses (e.g. [45]) show that the observed feature in the electron and positron spectra can be generated by including nearby pulsars. A special feature of this model is the fact that it motivates at the same time the observed antiproton-to-proton ratio (see figure 1.17). Recent measurements show no evidence for an excess from conventional astrophysical production. In WIMP dark matter antiprotons are produced in hadronic decays of W bosons [46] and should therefore lead to an observable excess. To explain this absence of additional antiprotons in Dark Matter theories 'leptophilic' models (like [47]) needed to be developed. The pulsar explanation does not need to make these efforts as it 'naturally' results in a large positron fraction together with a 'standard' antiproton ratio.

However, one should also keep in mind the presence of the uncertainties related to cosmic propagation which could explain or at least relativize the excess seen in the positron fraction

[49]. The necessary step to resolve the cosmic positron excess riddle could be the measurement of the total shape of the excess, which reveals the Dark Matter particle mass for Dark Matter theories and the upper limit pulsar acceleration models. However, the absence of a drop at higher energies could also hint to uncertainties or new effects in cosmic propagation. To unravel this mystery the cosmic propagation parameters have to be constrained and the cosmic electron and positron spectra have to be measured precisely to energies as high as possible.

2 The AMS-02 Detector

The Alpha Magnetic Spectrometer AMS-02 [50] is a particle physics detector designed for operation on the International Space Station (ISS). Using this unique environment it measures the flux and composition of cosmic rays and therefore contributes inter alia to the search for Antimatter and Dark Matter. Space Shuttle Endeavour, with the AMS-02 detector inside its cargo bay, was launched on May 16th 2011 to the ISS in the scope of Space Shuttle mission STS-134 [51]. Since May 19th 2011 the detector is installed on the ISS Payload Attach Point S3 on the main truss. Orbiting the Earth at an altitude of $300 - 400\,\mathrm{km}$ AMS-02 will measure cosmic rays for the lifetime of the ISS which is expected to last at least until 2020 and might be extended to 2028. Due to the high statistics and the state-of-the-art detector components AMS-02 will perform unprecedented high-precision measurements.

A schematic view of the AMS-02 instrument is shown in figure 2.1. The core piece of the instrument is the spectrometer, which consists of the silicon-strip Tracker (TRK) and the permanent magnet. The magnetic field is bending charged particles with momentum P and electromagnetic charge c dependent on their electromagnetic rigidity $R = P/c$. The particle trajectory, similar to a hyperbola[1], is reconstructed by a 3D track finding algorithm based on the intersections with the Tracker layers.

From the reconstructed curvature the electromagnetic rigidity $R = Br$ is calculated, where B is the magnetic field and r is the curvature. By determining the bending direction and hence the charge sign of the particle it is possible to distinguish between matter and antimatter. Additionally the absolute charge of the particle can be reconstructed by the energy deposited in the silicon Tracker. In total the Tracker measures the rigidity, charge sign and absolute charge of a particle and is able to deduce its momentum.

The Time-Of-Flight (TOF) system is needed to trigger the passage of a particle through the detector. It consists of four layers of staggered scintillator panels from which two are installed above (upper TOF or UTOF) and two below the Tracker (lower TOF or LTOF). The TOF is additionally used to measure the particle velocity and the absolute charge by the energy deposited in the scintillator panels.

The Anti-Coincidence Counter (ACC) is necessary to ensure that only clean event topolo-

[1] In the idealized case the trajectory is straight outside the magnetic field ($B = 0$) and circular inside ($B = const$)

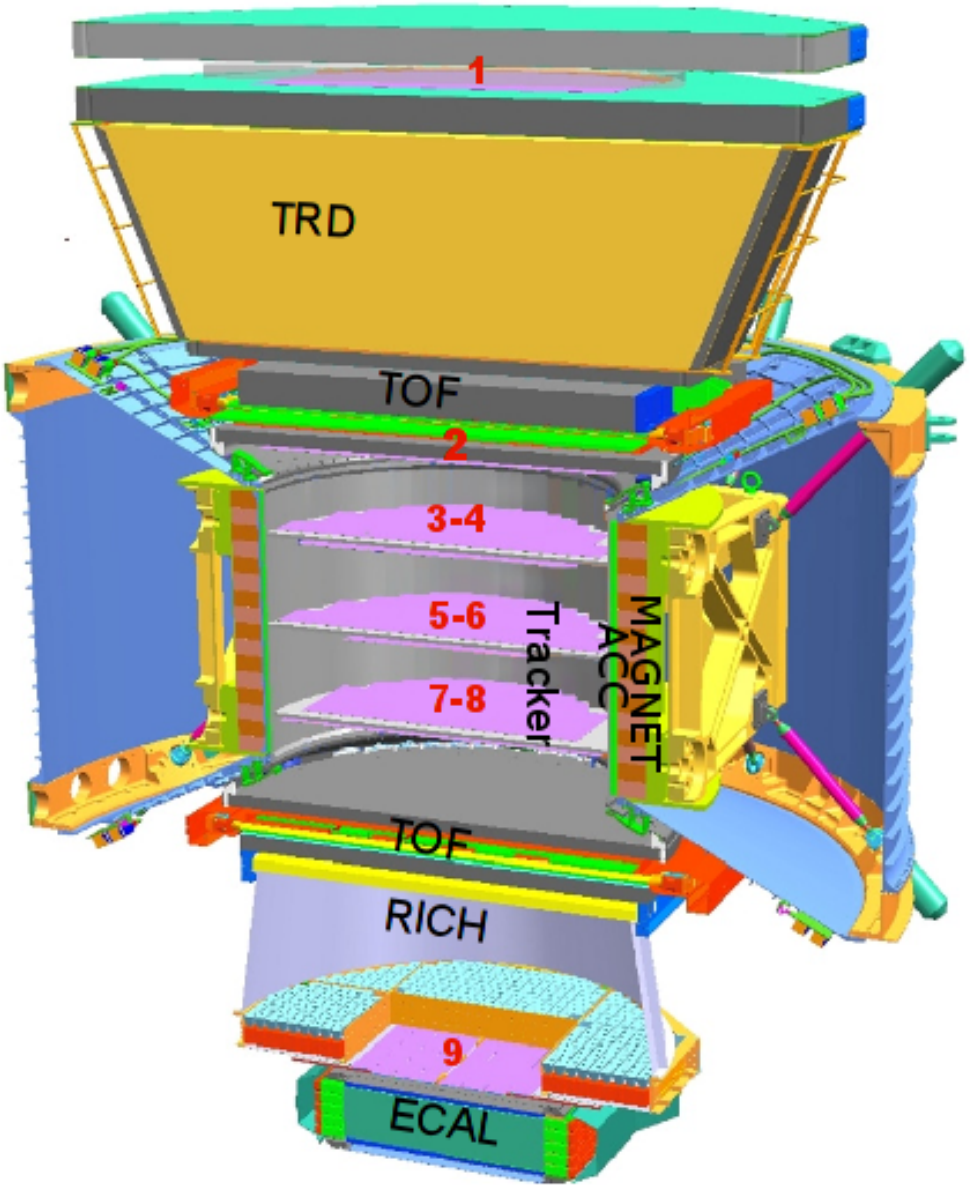

Weight	$\sim 7\,\mathrm{t}$
Dimensions	$5\,\mathrm{m} \times 4\,\mathrm{m} \times 3\,\mathrm{m}$
Magnetic field Intensity	1250 Gauss
Power consumption	$\sim 2.5\,\mathrm{kW}$

Figure 2.1: Schematic view of the AMS-02 Detector with following main components from top to bottom: Transition Radiation Detector (TRD), Time-Of-Flight (TOF), permanent magnet (MAGNET), Anti-Coincidence Counter (ACC), Tracker (TRACKER), Ring-Imaging-Čerenkov-Counter (RICH) and Electromagnetic Calorimeter (ECAL). The position of the Tracker layers is illustrated by red numbers.

gies are recorded. As the ISS is orbiting the Earth at an altitude of about 350 km, its atmospheric and geomagnetic shielding against the high flux of low-energetic cosmic rays is reduced. Therefore it may happen that multiple particles cross the detector volume at the same time. If particles enter the detector from the side, they can not be reconstructed correctly but may impede the reconstruction of coincident particles from top. Complex event topologies are also generated in interactions of the primary particles with high density materials like the magnet or mechanical structures of AMS-02 or ISS components. Especially in hadronic interactions many secondary particles are produced which inhibit the reconstruction of the primary particle and could lead to misreconstruction of particle properties. The ACC is surrounding the inner Tracker to suppress such events by giving a veto signal to corresponding trigger candidates. It consists of slotted scintillator panels to minimize inefficiency against charged particles in the junction between two panels.

The Ring-Imaging-Čerenkov-Counter (RICH) is located below the lower TOF and is detecting the Čerenkov light emitted by a charged particle in the radiator material on its top. The emitted light cone leads to an elliptic structure on the detection layer at the bottom. A pattern recognition algorithm is used to reconstruct the particle direction and velocity β from the detected structure and its charge c by the amount of collected photons on the ring.

The TRD, located above the upper TOF, consists of 20 layers of radiator fleece material in combination with gas-filled proportional chambers in which the energy deposited by the passage of particles is collected. In the radiator material charged particles generate transition radiation photons depending on their Lorentz gamma factor $\gamma = \sqrt{\frac{1}{1-\beta^2}}$ with velocity $\beta = \frac{v}{c}$. The signal generated by the absorption of transition radiation photons in the TRD gas is used to distinguish particles with high γ (typically leptons) from slower ones (typically protons).

The electromagnetic calorimeter (ECAL) is located at the bottom of AMS-02. In the high density materials of the ECAL the probability for charged particles to produce electromagnetic showers is highly increased. Typically hadrons deposit a fraction of their energy in a broad shower while leptons deposit all of its energy in a collimated shower. The total energy deposit and the shower shape are used to identify lepton events. Due to its high density and its ability to identify leptons the ECAL is able to detect photon events. Hereby, the electron-positron pairs generated in photon conversions are identified and used to reconstruct the photon energy and direction. A specific trigger channel to detect photon events is implemented independent of the TOF trigger in the trigger logic.

In the following sections the main AMS-02 detector components will be reviewed briefly going from top to bottom. In section 2.7 the data acquisition system is described.

2.1 Transition Radiation Detector (TRD)

Transition radiation (TR) is the emission of photons by charged particles crossing a boundary between two media with different dielectric constants. The probability to emit such a x-ray photon depends on the Lorentz gamma factor of the charged particle. To increase the probability of TR emission from about 1% per single boundary to a significant amount multiple boundaries in form of fleece radiator material are used. The photons generated in the radiator are detected by an absorber material located below. As the absorption is based on the photo-effect, the electron density of the absorber material has to be high. Contrary, to ensure that the energy deposition of fast particles is significantly higher than for slow particles, one has to maximize the difference between ionization and transition radiation energy depositions by reducing the material density. A common trade-off solution is the usage of Xenon gas as absorber material. A volume fraction of about 20% of CO_2 is used as quenching gas to sustain the high voltage applied to the tubes and to damp signal strokes. To allow for tracking of charged particles through the TRD the absorber gas Xe/CO_2 is filled into 'straw tube' proportional chambers. The transition radiation energy deposition, in addition to the expected ionization energy deposition, is used to disentangle leptons from the cosmic particle background, mainly consisting of proton and helium. The design value for the inverse proton efficiency is $10^2 - 10^3$ at 90 % electron efficiency. Contrary to the ECAL measurement, with radiation length $\sim 17\, X_0$, the particle detection in the TRD is non-destructive. The integrated TRD radiation length is $\sim 0.1\, X_0$ which corresponds to about 10 % energy loss for high energy electrons.

Detector layout The sensitive volume of the TRD consists of 5248 tubes, each with a diameter of 6 mm. The tube walls are made of two overlapping multilayer foils, which mainly consist of 25 μm Kapton material (see figure 2.2). A thin aluminum film on both sides leads to electrically conducting walls. The total wall thickness is 72 μm. A sense wire made of 30 μm gold plated Tungsten is located in the center of each tube. Each module consists of 16 tubes and has a length between 0.8 and 2 m, depending on its position in the detector. To improve mechanical stability six carbon fiber stiffeners run along each module. Both ends of a module are closed by polyurethane end pieces which provide the gas supply and center the wires which are tensioned to 1 N. The gas supply and Front-End-Electronics, which supplies the high voltage and decouples the anode wire signal, are connected to opposite end pieces. In total there are 328 straw tube modules assembled in a mechanical support structure of conical shape reducing from a width of 2.2 m at the top to 1.5 m at the bottom (see figure 2.3). The mechanical structure is fabricated of aluminum-honeycomb material with carbon fiber skins. The sidewalls and the bulkheads contain slots to house the straw tube modules in 20 layers. To allow for 3D tracking (see section 4.3.2) the top and bottom 4

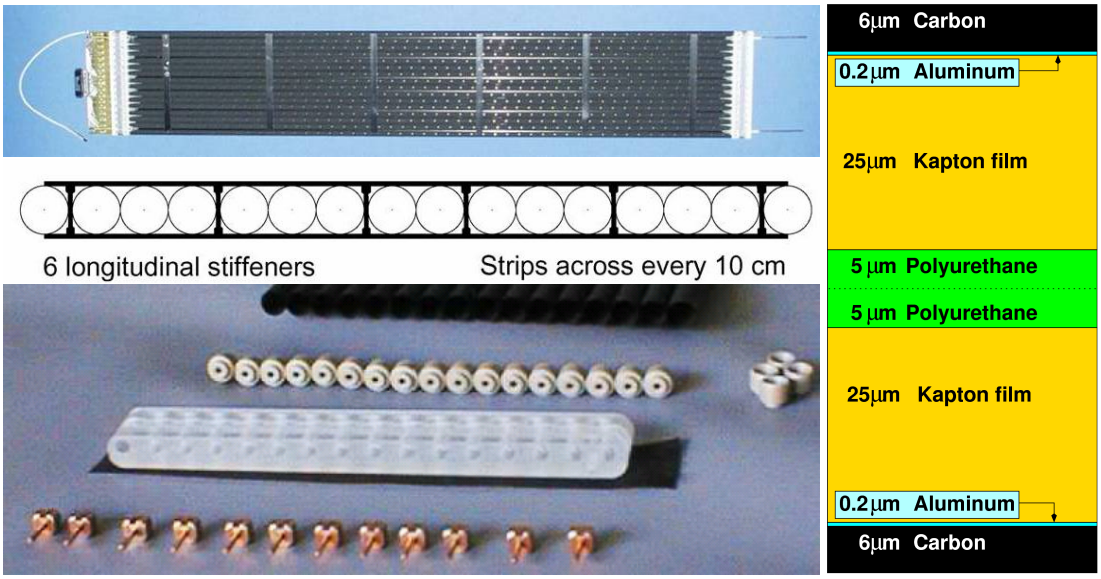

Figure 2.2: Construction principle of a TRD straw module [52]. Modules, consisting of 16 gas tubes (left top), are mechanically supported by longitudinal stiffeners (left center). Sense wires in the center of the tubes are connected to the gas supply, high voltage and readout electronics in the tube end pieces (left bottom). The tube walls are made of multilayer aluminized capton foil (right).

layers are rotated by 90° with respect to the center 12 layers.

Gas System The TRD is operated with a Xe/CO_2 (80/20) gas mixture at about $1.0 - 1.5$ bar on ground and at about $0.8 - 1.0$ bar in space. Gas losses, by e.g. diffusion through the tube walls, are compensated by periodic refills via the TRD Gas System. It consists of two main components (see figure 2.4), one to store and mix gas (Box-S) and one to inject and homogenize the gas by circulation pumps (Box-C). Box-S stores Xe and CO_2 in separate vessels containing ~ 48 kg in 27 l storage volume and ~ 5 kg in 11.4 l of storage volume, respectively. The 328 straw tube modules are grouped to 41 independent gas circuits supplied by ten gas manifold channels (see figure 2.5). One gas circuit consists of eight modules in series, arranged in two adjacent columns of four modules. While pumping, gas is pushed from the manifold into the inlet of the first module through eight of its tubes to its other end where it gets redirected to flow back through the other eight tubes of the same module. The outlet of each module is connected to the inlet of the following one until the manifold is reached again and hence a reference gas volume has passed a gas circuit. After refills the detector gas has to be homogenized by multiple circulations.

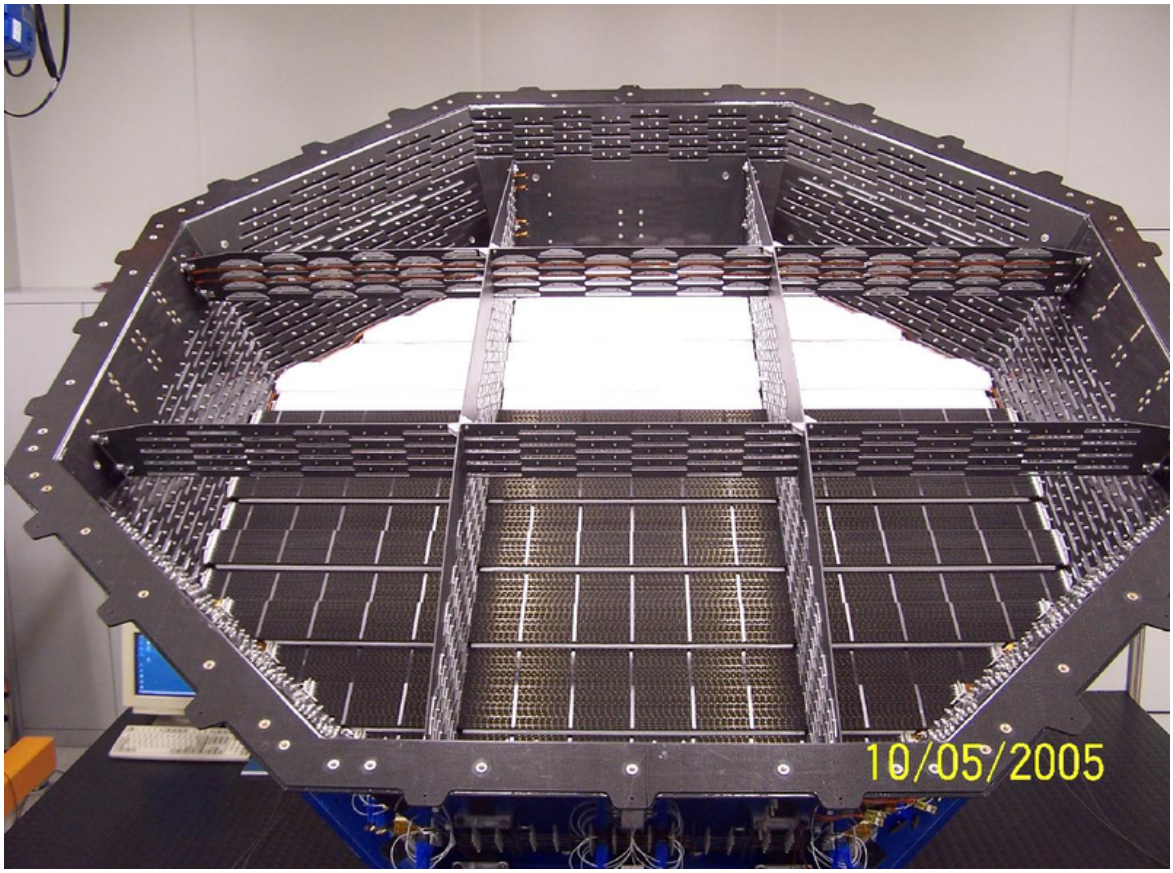

Figure 2.3: The TRD mechanical structure. Picture taken at TRD assembly [53].

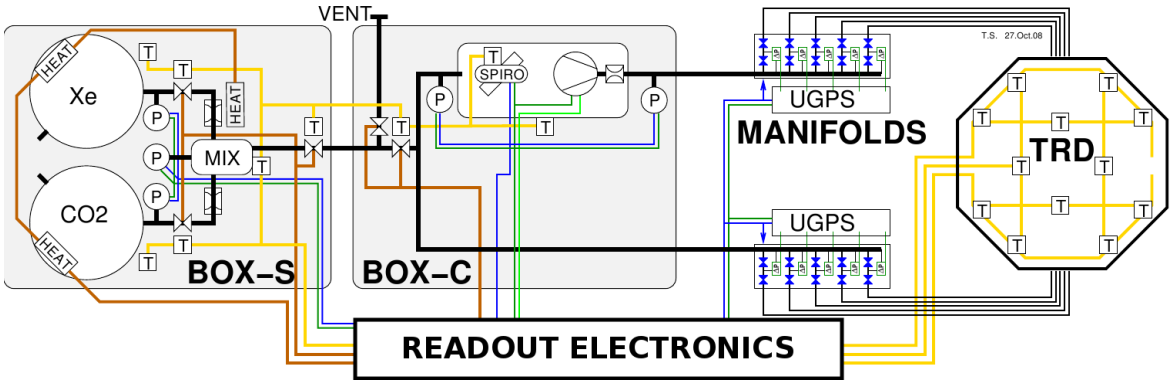

Figure 2.4: A schematic view of the TRD Gas System. The TRD is connected to the Gas System via flow restrictors in two manifold pairs (five channels each), leading to ten gas groups that can be isolated individually. BOX-C is used to monitor gas status by absolute pressure sensors and a spirometer and to homogenize the detector gas by pumping. BOX-S stores the Xe and CO_2 gas and is used for mixing gas compositions and injecting them to BOX-C. Pressure/temperature sensor locations are marked with 'P'/'T' respectively [54].

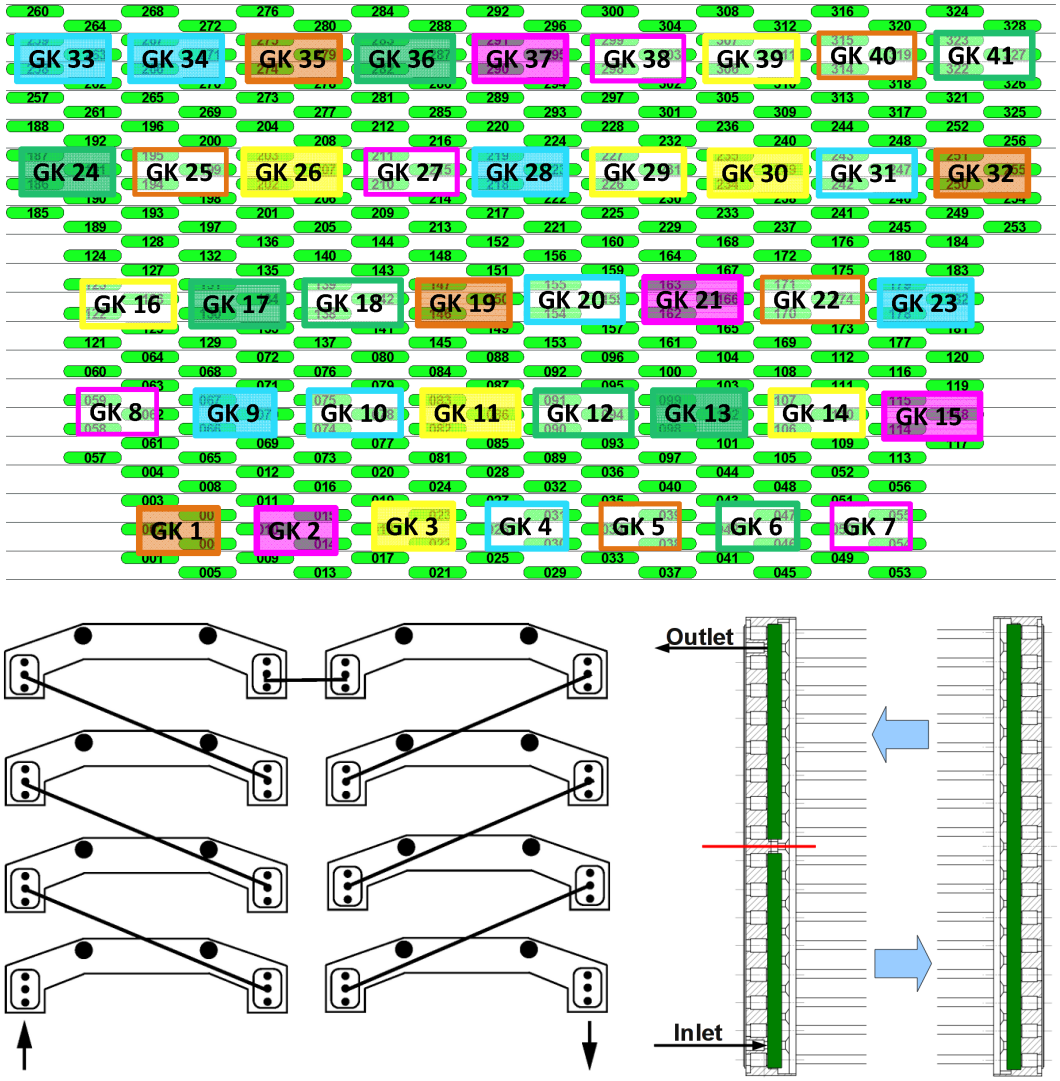

Figure 2.5: TRD gas flow [55]. The TRD is subdivided into 41 gas circuits (GK) supported by ten manifold channels, where associated GK are color coded. Each GK is subdivided into two adjacent columns of four modules above each other, where the outlet of each module is connected to the inlet of the following module. In one module the gas flows through half of its 16 tubes towards the opposite tube end piece where it gets redirected to flow back through the other eight tubes.

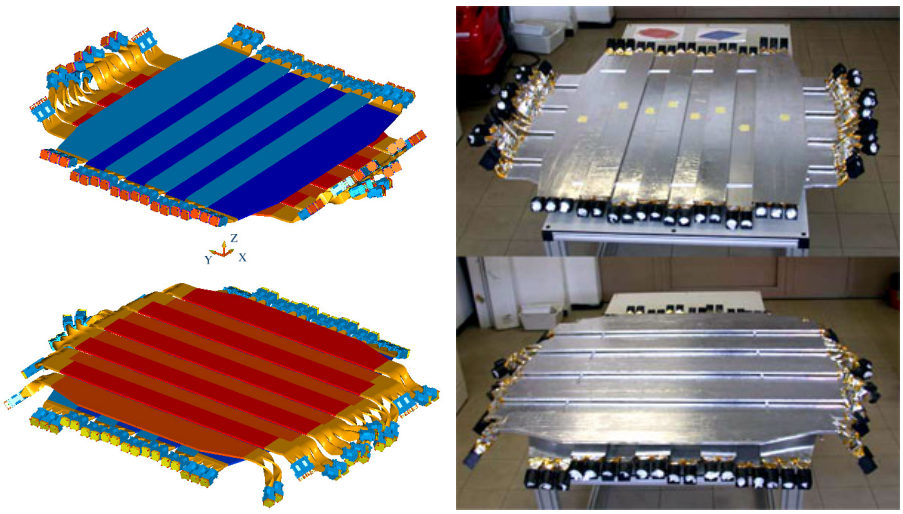

Figure 2.6: The Time-Of-Flight (TOF) layers in a schematic view (left) and corresponding picture taken at integration (right). The two layers in the upper and lower part of the TOF are perpendicular to allow 3D reconstruction [50].

2.2 Time-Of-Flight (TOF)

The TOF system is composed of four planes of plastic organic scintillator paddles (see figure 2.6), two above and two below the Tracker. The respective layer pairs are mounted cross-wise to enhance the 3D resolution of particle intersections. There are eight staggered paddles with 0.5 cm overlap in each layer apart the third layer from top which has ten. Each couple of adjacent panels is covered in a light-tight carbon fiber envelope and read out by two photomultipliers per side. The scintillation light is internally reflected until it reaches the ends, where plexiglas light guides route it to the photomultipliers. The scintillator and light guides are enclosed in Mylar foil to improve reflectivity, shield against external light and protect surfaces from dust. Light tightness is ensured by a 0.7 mm thick carbon fiber enclosure which is wrapped around the structure of two adjacent panels and their photomultipliers.

The main function of the TOF is to trigger particles crossing the detector. The corresponding geometrical acceptance is $\sim 0.5\,\mathrm{m^2sr}$. The TOF panels are read out from both sides to allow for the reconstruction of particle intersections along the panel with an accuracy of $\sim 10\,\mathrm{cm}$. The duration to pass from the upper to the lower TOF is measured and with the track length ($dz \approx 1.2\,\mathrm{m}$) the velocity $\beta = \frac{v}{c}$ can be determined. In particular the TOF system can distinguish between upward and downward going particles with a rejection power of 10^{-9}. This is necessary to suppress the identification of upward going particles as antiparticles due to misreconstructed charge signs. The TOF velocity resolution was determined by beamtest data to $\frac{\sigma_\beta}{\beta} \approx 4/2\%$ for protons / ions respectively with an approximate timing resolution of the order of 160 ps [56].

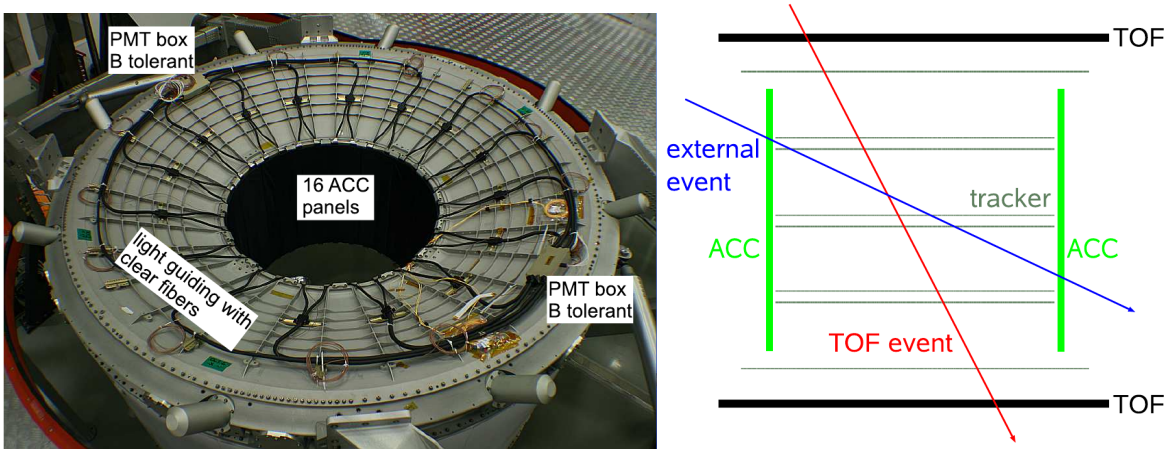

Figure 2.7: The Anti-Coincidence-Counter is surrounding the inner Tracker (left) and prevents the misreconstruction of particle events due to particles entering the detector from the side (right) [57].

2.3 Anti-Coincidence-Counter (ACC)

The functionality of the ACC is similar to the TOF but it is used to produce veto signals for complex event topologies. It consists of 16 scintillator panels arranged in a cylindrical structure of 1.1 m diameter and 8 mm thickness around the inner Tracker. The scintillation light produced by the passage of charged particles is absorbed by wavelength shifting fibers, re-emitted to a longer wavelength and propagated to the clear fiber light guides at the panel ends, which route them to the photomultiplier tubes. Two adjacent panels share the same readout photomultiplier on top and bottom. In total there are four PMT boxes containing four PMT tubes each to read out the 16 panels. The ACC system surrounds the Tracker to assure a clean event topology by giving veto signals to the trigger system. Additional particles entering from the side or particle interactions could lead to mis-reconstructed trajectory and hence to wrong particle rigidities. This becomes especially important in regions of high particle rates, e.g. in the South Atlantic Anomaly (see section 1.3.3) or close to the polar regions, where the trigger rate is limited by the electronics dead time of the data acquisition system. The ACC was designed to have an inefficiency for the detection of particle passage of $I < 1 \times 10^{-4}$. The inefficiency has been determined by cosmic muon data to $I = \frac{N_{missed}}{N_{all}} < 7.2 \times 10^{-5} (95\% CL)$ [57] and beamtest data to 1.9×10^{-5} [58].

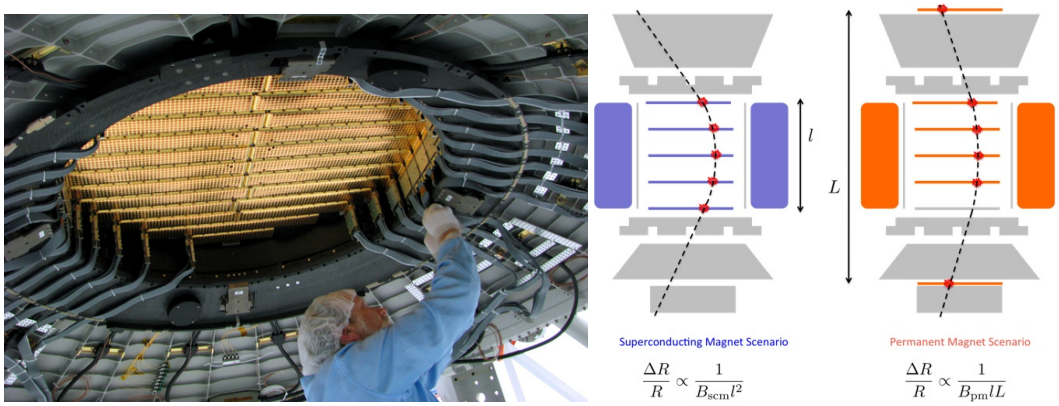

Figure 2.8: The Silicon Tracker. *Left:* an integrated Tracker layer containing silicon sensors grouped to rectangular 'ladders'. *Right:* Tracker layout re-design from superconducting magnet (blue) to permanent magnet (orange) with corresponding rigidity resolutions $\frac{\Delta R}{R}$ [50].

2.4 Magnet and Silicon Strip Tracker (TRK)

Originally the AMS-02 detector was designed for three years of operation on the International Space Station. For this layout a superconducting magnet was built with a maximum magnetic field of $B = 0.8\,\mathrm{T}$, cooled by liquid helium. It was operated during cosmics data taking, the first beamtest in February 2010 and in the Large Space Simulator at the European Space Research and Technology Centre (ESTEC). The limitation of detector life time by the amount of liquid helium was estimated by its operation at ESTEC to 28 ± 6 months. In spring 2010 NASA announced that the ISS lifetime will be extended to at least 2020. To benefit from this, the superconducting magnet has been replaced by a permanent magnet with a magnetic field of $B = 0.14\,\mathrm{T}$. To preserve the same spectrometer performance, to be more precise maximum detectable rigidity $MDR \approx 2.3\,\mathrm{GV}$, the lower magnetic field was compensated by the reconfiguration of the Tracker layers. This upgrade from superconducting to permanent magnet is described in detail in [59].

The silicon Tracker in its final layout consists of nine layers of silicon sensors disposed on six planes (see figure 2.8). There are three double-sided planes in the inner Tracker surrounded by the magnet and in total three single-sided planes located on top of the TRD, below the upper TOF and above the ECAL. Each of the nine layers contains approximately 24 ladders on a circular support structure of $sim1$ m diameter. Each ladder consists of 7-15 of double-sided silicon sensors grouped along the x direction. The double-sided silicon sensor with dimensions $\sim 72.045 \times 41.360 \times 0.300\,\mathrm{mm}^3$ is the basic element of the Tracker. On one of the two surfaces p^+ strips with a pitch of 27.5 μm are implanted and read out with 110 μm pitch. On the other side n^+ strips are mounted orthogonally with an implantation pitch of 104 μm and a readout pitch of 208 μm. The higher granularity p-side strips are used to measure in the bending plane of the magnet (yz in AMS coordinate system). The total sensitive area

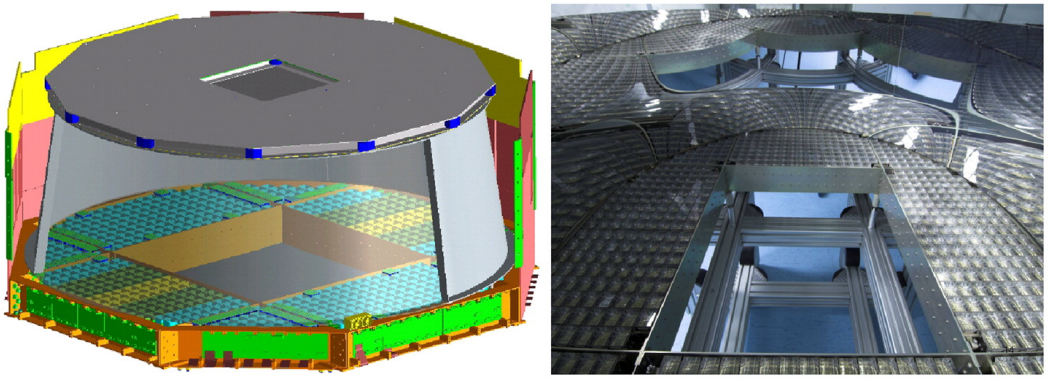

Figure 2.9: The schematic layout of the RICH detector (left) and a picture of its inner volume taken at detector integration (right) [61].

of 6.75 m^2 is distributed on 2264 silicon sensors mounted on 192 ladders. For the stable performance of the Tracker two additional subsystems are installed: the Tracker thermal control system (TTCS) and the laser alignment system (TAS). The TTCS is a two-phase CO_2 heat exchanging system that controls the temperature of the Tracker components. The TAS is used to monitor the relative alignment of the inner Tracker planes. The final alignment of all layers is done based on reconstructed particle tracks on the level of $\lesssim 10\,\mu$m. A detailed discussion of the alignment performed on ground with atmospheric muon data is provided in [60].

2.5 Ring Imaging Čerenkov Counter (RICH)

The proximity focusing Ring Imaging Čerenkov Counter (see figure 2.9) is located in the lower part of AMS-02 between the lower TOF and the ECAL. It has a conical shape of 60 /67 cm radius at top / bottom and 47 cm in height. It covers $\sim$ 80 % of the magnet acceptance and mainly consists of two radiator materials, namely silica aerogel ($n = 1.050$) and sodium fluoride ($n = 1.334$), a high reflectivity conical mirror and a detection layer of 680 photomultiplier tubes coupled to light guides. The mirror made of aluminum-nickel-coated silica is used to increase the number of collected photons. When a charged particle is crossing one of the radiator materials with velocity $v > \frac{c}{n}$ (speed of light in the medium) it will emit Čerenkov radiation with a characteristic aperture of $\cos\Theta_c = \frac{1}{\beta n}$. In combination with the particle trajectory, the Čerenkov angle Θ_c and therefore the particle velocity β can be determined. The intensity detected by the PMTs on the ring structure is proportional to the square of the absolute particle charge. The RICH provides a high accuracy velocity measurement of $\frac{\Delta\beta}{\beta} \sim 10^{-3} - 10^{-4}$ and allows for charge identification of nuclei up to iron [50]. The RICH is also used to suppress upward going particles, which could be misreconstructed as antiparticles due to the change in bending direction.

Each layer is rotated by 90 ° with respect to the previous one such that the fibers are either along the x- or the y-axis of the AMS coordinate system.

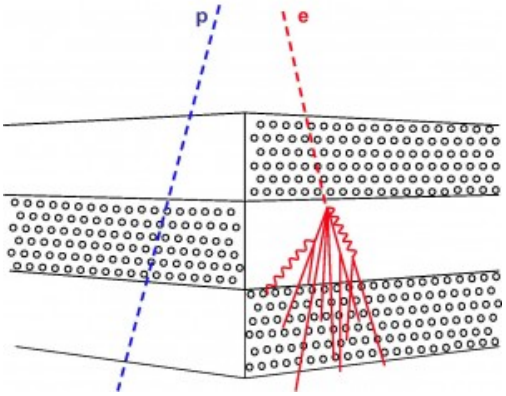

Figure 2.10: Picture of the ECAL mechanical structure (left) schematic view of particles passing a superlayer (right) [50].

2.6 Electromagnetic Calorimeter (ECAL)

The 3D sampling electromagnetic calorimeter (ECAL) is located at the bottom of AMS below the lower external Tracker plane. Its major function is the identification of electrons, positrons and photons and the measurement of their energies. It consists of nine modules, so-called superlayers, of lead and scintillating fibers with area $648 \times 648\,\mathrm{mm}^2$ and depth 18 mm ($\sim 1.8\,X_0$) each (see figure 2.10) . Each fiber is read out on one end by photomultipliers. As one photomultiplier has four independent pixels each layers can be subdivided into elementary cells of area $9 \times 9\,\mathrm{mm}^2$ corresponding to 35 fibers and about 0.5 Moliere radii in transverse and 0.9 radiation lengths in longitudinal dimension of an electromagnetic shower. In total there are 1296 cells read out by 324 photomultipliers. A particle crossing the ECAL vertically passes $\sim$ 16.5 radiation lengths sampled by 18 independent measurements. The energy resolution measured in beamtest is 2.5 to 3 % [62]. In combination with the particle momentum measured by Tracker the efficiency for proton events being mis-identified as positrons is designed to be $\lesssim 10^{-4}$.

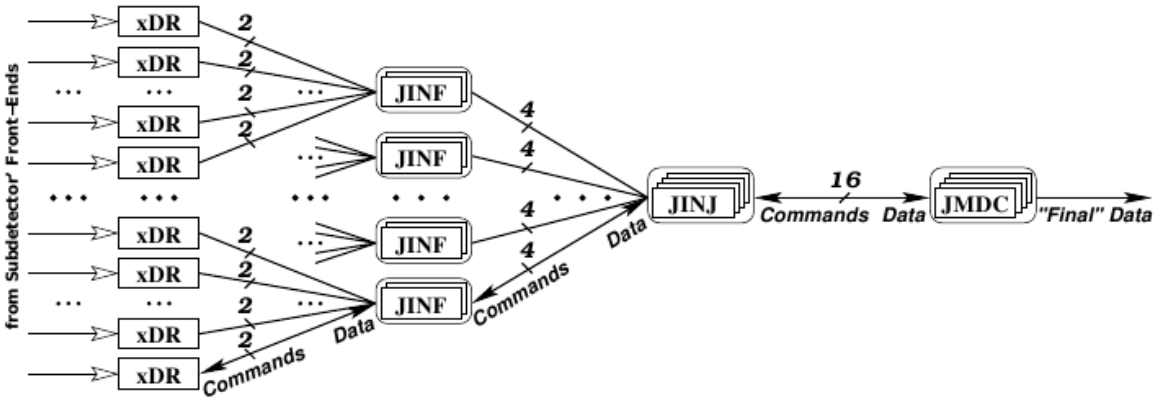

Figure 2.11: General data acquisition and commanding scheme [50]. Data is collected from Front-End-Electronics via different redundant collection levels to the four-fold redundant main DAQ computer JMDC where the collected data of an event is quality selected and buffered for transfer to ground stations. Commands sent from ground are distributed the other way round via JMDC to subdetector specific components.

2.7 Data Acquisition

The AMS-02 data acquisition collects the isochronous signal of the $\sim 2.3 \times 10^5$ detector channels. In general the detector-specific electronic components are similar and tagged by a specific letter: 'U' for TRD, 'S' for TOF/ACC, 'T' for Tracker, 'R' for RICH and 'E' for ECAL. In the following 'x' denotes any of the former options. The lowest level general electronics component in the hierarchy (see figure 2.11) is a data reduction board (xDR), which is gathering data directly from the detector front end electronics. Each xDR is connected to two redundant JINF boards which can control up to 24 xDR slaves. Each JINF has two redundant JINJ boards connected, which can control up to 24 JINFs. Each of the JINJs is connected to all four main DAQ computers (JMDC). In general the xDRs read and buffer the data from the front end boards continuously. When a particle is crossing the detector a trigger signal is generated based on the data of TOF, ACC and ECAL readout. The trigger signal is distributed to the JINFs and then propagated down to the connected xDR nodes with a detector specific controllable delay. When a xDR receives a trigger signal the digitization of the analog front end signals is performed by Analog-to-Digital Converters (ADCs). The subdetector specific digital signal processor (DSP) processes the incoming data and stores the signal above noise in the event output buffer. The JINFs collect and buffer the event fragments of the xDR nodes. The JINJs combine the subdetector fragments of all JINFs and provides it to JMDC, where the event fragments are combined to the AMS-02 event data block format. To suppress noisy events and to provide at the same time a high efficiency for all desired physics channels the AMS-02 trigger logic, an 'OR' of 6 independent physics triggers (see Tab. 2.1), is applied here on each event. The 'unbiased charged' trigger requires that at least 3 out of 4 TOF planes have a hit. This trigger branch is mainly

Trigger	TOF	Charge	Comment
Unbiased charged	3/4	>=1	scaled $\sim$ 100
Single charged nonEM	4/4	>=1	Nacc=0
Normal Ions	3/4	>=2	-
Strange Ions	3/4	>=2	slow
Electrons	3/4	>=1	ECAL shower
Photons	-	-	ECAL shower & angle
Unbiased EM	-	-	ECAL shower, scaled $\sim$ 1000

Table 2.1: The individual physics trigger channels of AMS-02 [63].

needed to check for biases by demanding more complex trigger restrictions. It is scaled by a factor of 100. The unbiased 'electromagnetic trigger' is a trigger signal generated only by the ECAL selecting electromagnetic events. It is scaled by a factor of 1000. One of the more important and hence not scaled physics triggers is the 'Z=1' trigger which requires that 4 of 4 TOF planes have a hit and that there is no veto given by the ACC. Additionally there are the 'BZ'- and 'Slow ion'-trigger signals which are sensitive to high energy depositions by charged particles in the 4 TOF layers. The 'electron trigger' requires that at least 3 of 4 TOF layers having a hit and that there is a significant energy deposition in the ECAL. The 'photon trigger' requires an ECAL energy deposition along with an angular cut on the shower axis to ensure that the photon passed the detector but did not produce energy depositions along its track, like charged particles would. If at least one of these trigger channels applies, the corresponding event is buffered for transmission to ground.

The AMS-02 detector has two communication interfaces to the International Space Station (ISS): the Low Rate Data Link (LRDL) and the High Rate Data Link (HRDL). The LRDL is used to transmit housekeeping information from the detector on the Ku-band via TDRS satellites through NASA centers to the AMS-02 Payload Operations and Control Center (POCC) in near real-time. This information is important to ensure safe operation of the detector. The available rate is $\sim$ 10 kBit/s. The LRDL is also preferably used for sending commands from the POCC to AMS. The HRDL is used to transfer the physics event data and a copy of the monitoring data. It is connected to the high rate down link of the ISS by fiber optics and runs at 125 MBaud. The connection between POCC and AMS is limited by periods of no connectivity (Loss-Of-Signal / LOS) between periods of connectivity (Acquisition-Of-Signal / AOS). This is caused by the limited amount of communication satellites and the corresponding area of coverage. To be able to continue the data taking during LOS periods the HRDL data is buffered, sent to ground during AOS and merged chronologically on ground. From NASA ground stations the data is transmitted via Internet to AMS data storage at CERN, where it is available for analysis.

3 TRD Physics

In this chapter the models for TRD signals and corresponding simulation algorithms are presented. The passage of particles through matter implies in general atomic interactions. The emission of transition radiation photons in the radiator material and their absorption in various materials is discussed in section 3.1. Photon absorption leads to energy depositions in the sensitive volume of the TRD, the gas-filled tubes. Additional energy depositions arise from the collision of the charged particles with electrons bound in the tube gas. The corresponding ionization process is reviewed in section 3.2. In general energy depositions in the TRD tube gas lead to free electrons. They are collected in the tube anode wire by an applied high voltage. The conversion of the anode wire signal to a hit is reviewed in section 3.3.

3.1 Transition Radiation

Generation When a charged particle is crossing the boundary between two media of different dielectric properties the Coulomb field of the particle has to readjust itself. This happens in the form of the emission of so-called Transition Radiation (TR) photons. The material medium can be considered as an electron gas with dielectric constant

$$\epsilon(\omega) = 1 - \frac{\omega_P^2}{\omega^2} = 1 - \xi^2 \ , \tag{3.1.1}$$

where ω_P is the plasma frequency of the medium given by:

$$\omega_P^2 = 4\pi\alpha\frac{n_e}{m_e} \ , \tag{3.1.2}$$

with fine-structure constant $\alpha \approx \frac{1}{137}$, electron density n_e and mass m_e. A partial density ρ of a component leads to the contribution:

$$\omega_P^2 = 4\pi\alpha\frac{Z}{A}N_A\frac{\rho}{m_e} \simeq 2\frac{Z}{A}\frac{\rho}{\mathrm{g/cm^3}}(21\mathrm{eV})^2 \ , \tag{3.1.3}$$

where N_A is the Avogadro constant. For two media and $\gamma \gg 1$, $\xi_1^2, \xi_2^2 \ll 1$ and $\Omega \ll 1$ (forward direction) the radiation intensity can be approximated by [64]:

$$\frac{d^2W}{d\omega d\Omega} = \frac{\alpha}{\pi^2}\left(\frac{\Theta}{\gamma^{-2} + \Theta^2 + \xi_1^2} - \frac{\Theta}{\gamma^{-2} + \Theta^2 + \xi_2^2}\right)^2 \ . \tag{3.1.4}$$

A time or length of formation can be introduced as 'formation zones'

$$Z_{(1,2)} = \frac{4\pi c}{\omega}(\gamma^{-2} + \omega^2 + \frac{\omega_{P,(1,2)}}{\omega^2})^{-1} \quad . \tag{3.1.5}$$

This zone represents the distance along the particle trajectory after which the separation between the particle and the photon is about one photon wavelength. This corresponds to the length needed for the electromagnetic field to reach its new state of equilibrium and results in the separation of photon and primary particle. Hence the given intensity is reached only when the charged particle is able to traverse a distance on the order of the formation zone in the medium. This becomes important as soon as considering thin slabs of finite thickness, where higher energies of the emission spectrum are suppressed for $Z_{1,2} > l_{1,2}$, with $l_{1,2}$ being the thickness of the two media. For $\Theta \sim \gamma^{-1}$ and $\omega \ll \omega_{P,(1,2)}\gamma$ the formation zone is increasing with frequency as $Z_{1,2} = 4\pi c\frac{\omega}{\omega_{P,(1,2)}}$ and reaches its maximum $Z_{1,2}^{max} = \frac{2\pi c}{\omega_{P,(1,2)}}\gamma$ at a frequency of about $\omega_{P,(1,2)}\gamma$. For practical application equation 3.1.4 can be rewritten using $d\Omega = \sin\Theta\, d\Theta\, d\phi$ to

$$\frac{d^2W}{d\omega d\Theta} = \frac{2\alpha\hbar}{\pi}\Theta^3(\frac{1}{\gamma^{-2} + \Theta^2 + \xi_1^2} - \frac{1}{\gamma^{-2} + \Theta^2 + \xi_2^2})^2 \quad . \tag{3.1.6}$$

Integration gives the total intensity emitted at a single boundary:

$$W = \int\int \frac{d^2W}{d\omega d\Omega} d\omega d\Omega = \frac{\alpha\hbar}{\pi}\frac{(\omega_{P,1} - \omega_{P,2})^2}{\omega_{P,1} + \omega_{P,2}}\gamma \quad , \tag{3.1.7}$$

with Lorentz gamma γ, fine structure constant α and Planck constant $\hbar = \frac{h}{2\pi}$.

In a realistic case the incident particle has to traverse at least two interfaces like a single slab. To enhance the low transition radiation yield on the order of α per interface to a significant effect multiple interfaces have to be used. The simplest solution are equally spaced thin slabs, known as periodic radiator (discussed in [65]).

A more realistic model, the XTR radiator [66], is incorporated in the simulation of transition radiation. In this model the radiator is not considered exactly periodic but with fluctuating thicknesses around the mean values $l_{1,2}$. The fluctuation is given by

$$p(l_i) = (\frac{\nu_i}{\bar{l}_i})^{\nu_i}\frac{l_i^{\nu_i - 1}}{\Gamma(\nu_i)}e^{(-\frac{\nu_i l_i}{\bar{l}_i})} \qquad i = 1,2 \qquad , \tag{3.1.8}$$

with Euler gamma function Γ, mean thickness $\bar{l}_i$ of the i-th medium and parameter ν_i describing the relative fluctuation δ_i of l_i given by

$$\delta_i^2 = \frac{< (l_i - \bar{l}_i)^2 >}{\bar{l}_i^2} = \nu_i^{-1} \quad . \tag{3.1.9}$$

As for this case the analytical expressions become more complicated and their exact solution exceeds the scope of this thesis the numerical results gained by Monte-Carlo simulations will be presented in the following. A detailed theoretical discussion is given in [66].

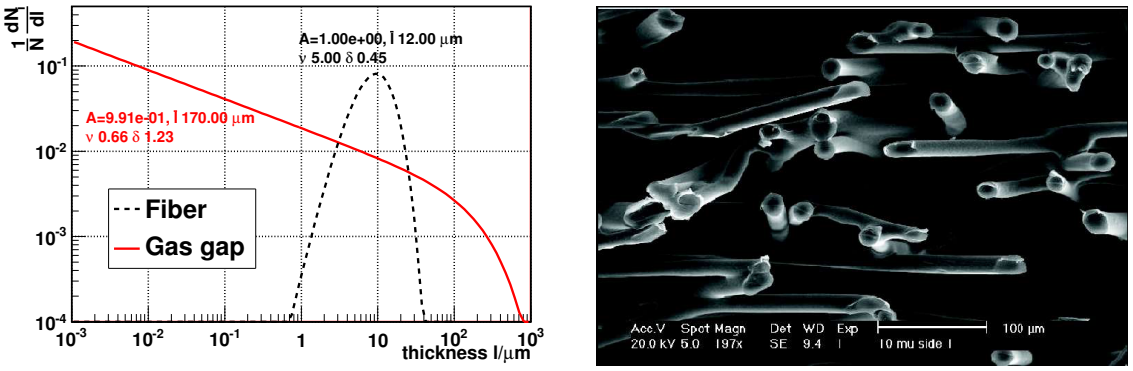

Figure 3.1: Thickness and fluctuation parameters of TRD radiator material LRP375BK components. *Left:* mean thickness $\bar{l}$, fluctuation parameter ν and relative fluctuation δ are given for fiber (dashed black line) and gas material (solid red line). *Right:* electron microscope image of a LRP375BK radiator mat [68].

The AMS-02 TRD radiator consists of 2 cm thick LRP375BK radiator material with mean density 60 mg/cm^3 located above straw tube modules, which are used to detect the emitted x-ray photons (see below). To simulate the emission of transition radiation following parameters need to be defined:

$\omega_{P,i}$	Plasma frequencies
$\bar{l}_i$	Mean thicknesses
ν_i	Thickness fluctuation parameters
n	Mean number of interfaces .

As the total thickness and density of the radiator are known, two parameters can be eliminated, typically $\bar{l}_{gas}$ and n. The plasma frequencies $\omega_{P,i} \propto \rho_{e,i}$ can be calculated for nominal material properties to $\omega_{P,fiber} = 20.75\,\text{eV}$ and $\omega_{P,gas} = 0.73\,\text{eV}$ (Air). Thus three parameters remain as free parameters: the mean fiber thickness and the fluctuation parameters. The currently implemented values are determined by an optimization to describe the beamtest data of a TRD prototype containing the identical radiator material [67]. The mean thickness of the AMS-02 TRD radiator material components, namely gas and fiber, and their determined fluctuation parameters are shown in figure 3.1. The determined mean fiber thickness is 12 μm with low relative fluctuation $\delta \approx 0.45$. The gas gaps are determined to be 170 μm in average with comparatively large fluctuation $\delta \approx 1.23$. A comparison to the electron microscope image of a radiator mat shows that the determined parameters seem realistic. The corresponding spectrum of transition radiation photons is shown in figure 3.2. It can be seen that the mean number and the mean energy of emitted TR photons is rising with Lorentz gamma γ. At low gamma factors $\gamma \lesssim 100$ the emission of transition radiation is negligible. The mean number and mean energy of generated TR photons is increasing up to $\gamma \approx 10000$ where it saturates to about 4 photons and 6 keV per photon on average in 2 cm of radiator material.

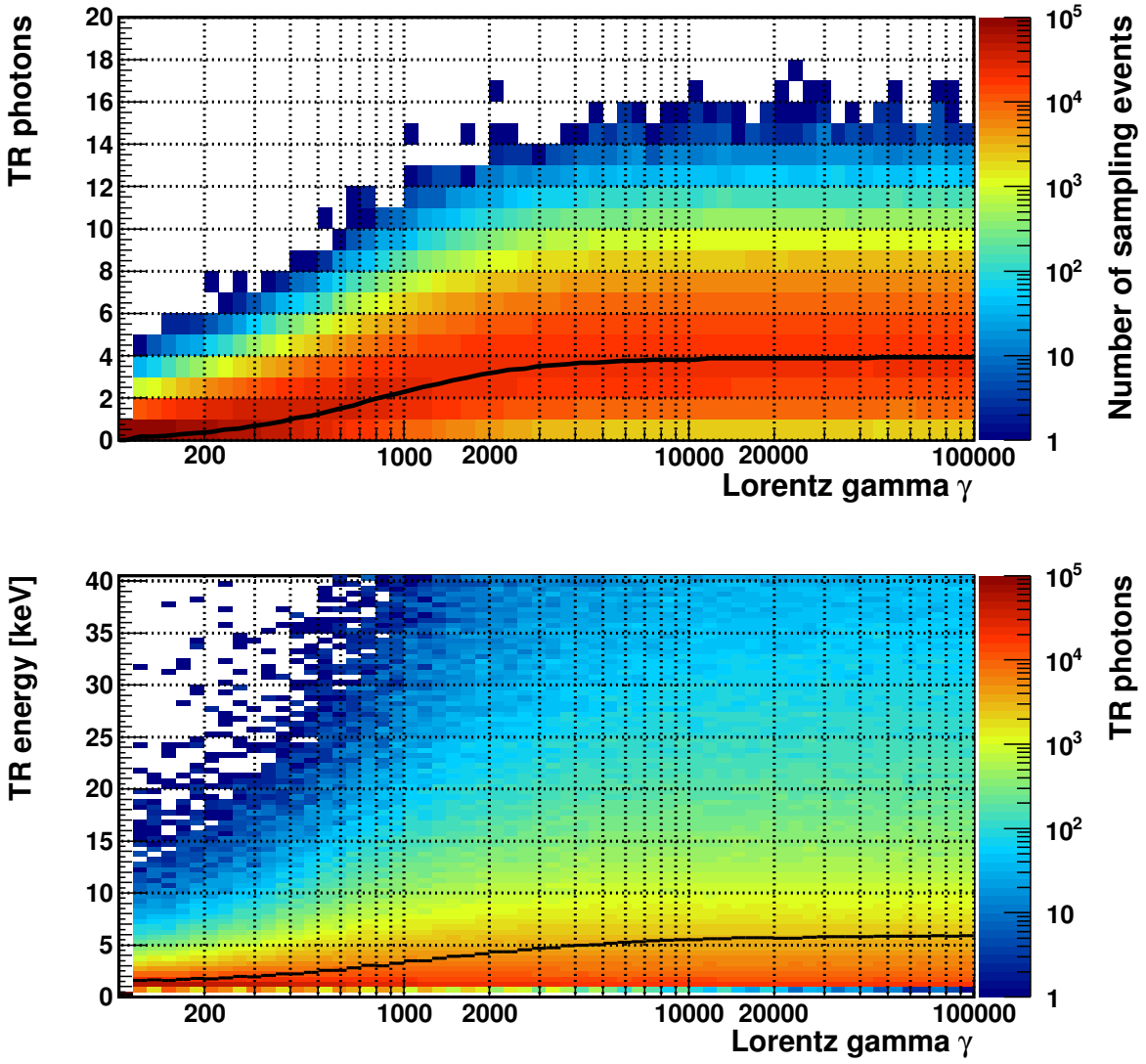

Figure 3.2: Simulated transition radiation photon spectrum for 2 cm of AMS-02 radiator material. *Top:* the mean number (black line) of generated photons and its sampling by a Poisson distribution (histogram) is shown as a function of Lorentz gamma γ. *Bottom:* energy spectrum (histogram) of generated TR photons and its mean value (black line) as a function of γ.

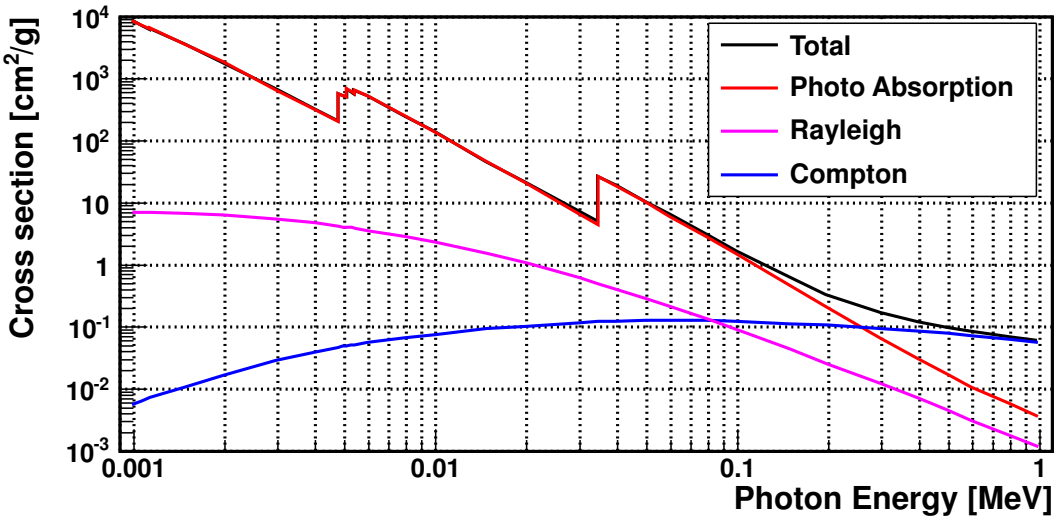

Figure 3.3: Photon cross section in Xe/CO_2 (generated using NIST XCOM [69]). At photon energies below 100 kev the dominant process is photo-electric absorption. The attenuation coefficient μ can be converted to a cross section σ for given atomic density N by $\sigma = \frac{\mu}{N}$.

Absorption The transition radiation photons generated in the radiator mainly interact with electrons bound in the atoms of traversed materials. In such collisions the photon energy is either totally (photo-electric absorption) or partially (Compton scattering) transferred to an electron or the photon is scattered elastically (Rayleigh scattering). In figure 3.3 the cross section of nominal TRD gas for photons is shown. The cross section is characterized by discontinuities, called absorption edges, corresponding ionization thresholds for different atomic shells. The dominant process for typical TR photons of $E \lesssim 10\,\text{keV}$ is photo-electric absorption. For density $\rho = 5\,\text{mg/cm}^3$ and attenuation coefficient $\mu = 200\,\text{cm}^2/\text{g}$ (corresponds to approximately $4 - 10\,\text{keV}$ in the picture) the mean free path of a photon is $l = (\mu * \rho)^{-1} = 1\,\text{cm}$. Absorption may not only occur inside the tube gas but in all materials passed by the photon. In figure 3.4 the spectra of absorbed photons in some selected TRD materials is shown. Of all generated transition radiation photons a large fraction ($\sim 95\,\%$) gets re-absorbed in the radiator material, about 2 % are absorbed in the mechanical structure, mainly in the tube walls, and about 2% are absorbed in the tube gas. The energy shown here is the energy deposited in the material in the simulation of the photo-absorption process. Therein, a part of the photon energy may be transferred to the emitted electron and hence not deposited in this process. Therefore one can see peaks at distinct energies, corresponding to the absorption edges, which exceed the initial number of emitted photons at the given energy. Transition radiation typically contributes to the total energy deposition spectrum in form of a shift of a fraction of the ionization peak by $\sim 6\,\text{keV}$.

Obviously, photons absorbed in the tube gas are not necessarily produced in the radiator material of the same layer. The simulated photons emitted in the topmost layer 20 have

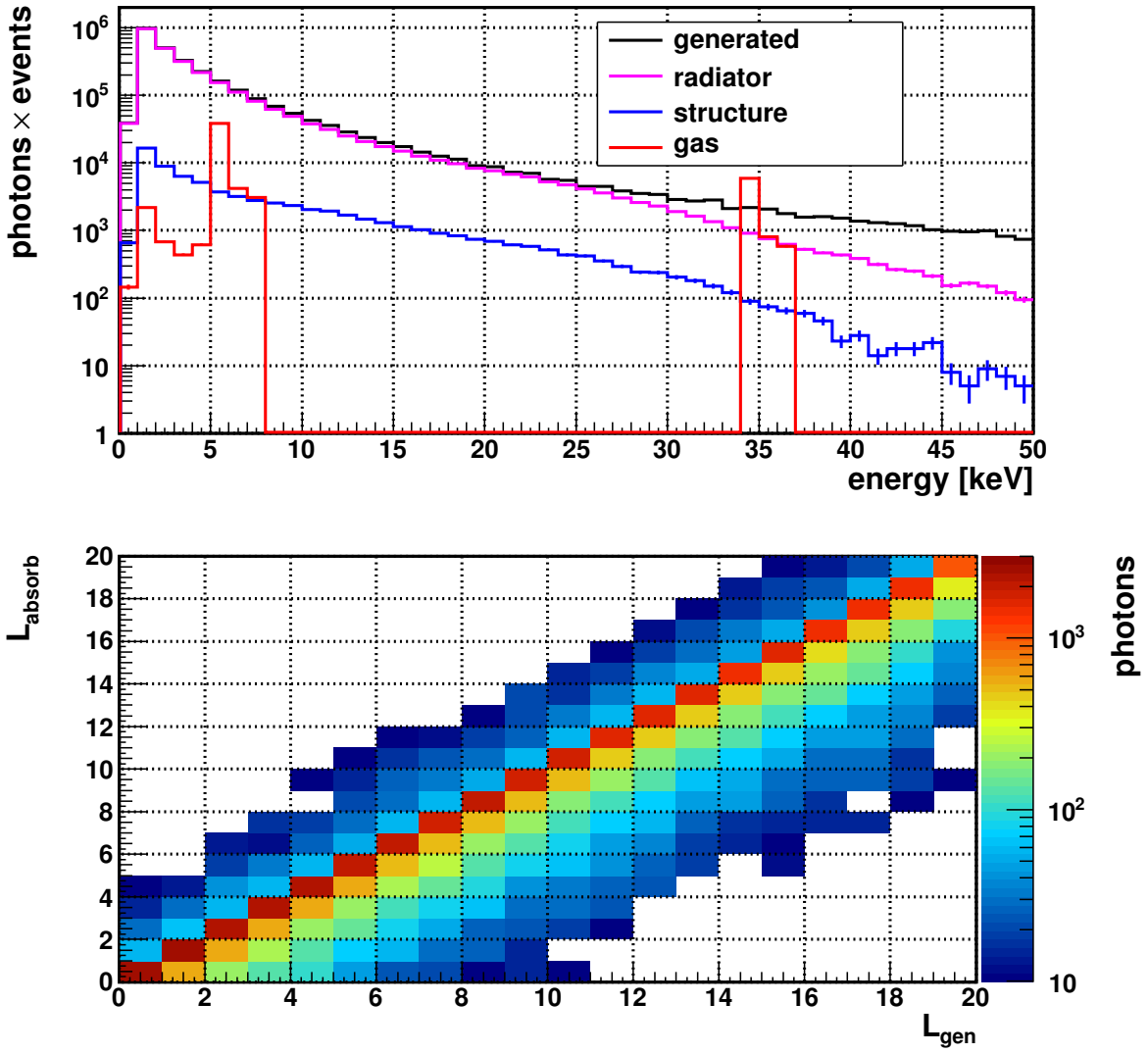

Figure 3.4: Absorption of transition radiation photons. *Top:* spectrum of photons generated in the radiator material and absorbed in different components of the TRD. *Bottom:* The correlation of absorption layer L_{absorb} and generation layer L_{gen} for photons absorbed in the TRD gas.

$\sim 55/20/10\,\%$ probability to be absorbed in layer 20/19/18 respectively. This leads to an increase of transition radiation contribution to the tube energy depositions with detector depth. To take this into account, the probability density functions used for the likelihood analysis (see section 4.5) are defined layer-wise for electrons.

3.2 Ionization

All particles propagating through a medium may collide with electrons, which are in general bound in atoms. The energy loss of charged particles in a medium can be described by the Bethe-Bloch formula [70] [71]:

$$-\frac{dE}{dx} = 4\pi n Z \frac{(z\alpha\hbar c)^2}{m_e v^2}\left[\ln\frac{2\gamma^2 m_e v^2}{I} - \beta^2 - \frac{\delta}{2}\right] , \tag{3.2.1}$$

with

α	Fine structure constant
$\hbar$	Dirac constant
c	Speed of light
m_e	Electron mass
n	Atomic density
Z	Atomic number
I	Ionization potential
z	Particle charge
v	Particle velocity
γ	Lorentz factor
δ	Density effect correction .

Usually, the stopping power is expressed in units of $\frac{\mathrm{MeV}}{(\mathrm{g/cm^2})}$ so the distance x has to be replaced by the area mass density ρx in $\frac{\mathrm{g}}{\mathrm{cm^2}}$:

$$-\frac{dE}{d(\rho x)} = -\frac{dE}{\rho dx} = 4\pi\frac{NZ}{A}\frac{(z\alpha\hbar)^2}{m_e\beta^2}\left[\ln\frac{2\gamma^2 m_e v^2}{I} - \beta^2 - \frac{\delta}{2}\right] . \tag{3.2.2}$$

In figure 3.5 the stopping power for particles with charge one in different materials is shown. The stopping power is a function of the particle velocity $\beta\gamma = \frac{p}{mc}$. The minimum, corresponding minimum ionizing particles, is located at $(\beta\gamma)_{MIP} \approx 3-4$ depending on material density. The stopping power is decreasing approximately as $(\beta\gamma)^{-2}$ up to the minimum and increasing above due of the γ^2 term inside the logarithm. At very high γ values this so called relativistic rise is reduced by density effects reaching an almost constant region called the Fermi-plateau. The stopping power is approximately independent of the material as the only material-dependent terms are $\frac{Z}{A}$ and the ionization potential I. Since I is suppressed inside the logarithm and $\frac{Z}{A} \approx \frac{1}{2}$ for all elements except hydrogen the

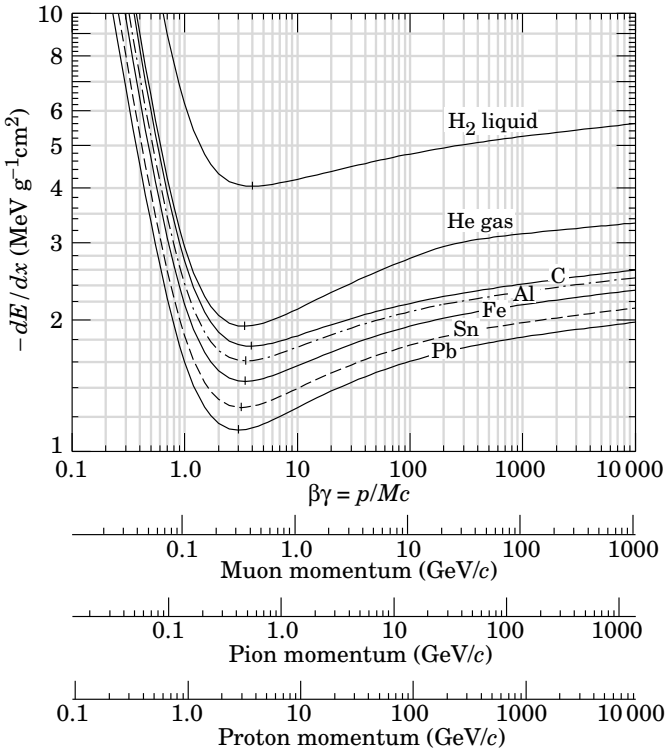

Figure 3.5: Mean energy loss rate in various materials as function of $\beta\gamma$ and different particle momenta [39].

stopping power for a minimum ionizing particle (MIP) is about

$$|\frac{dE}{dx}|_{MIP} \approx 1.5\,\mathrm{MeV}/(\mathrm{g/cm^2}) \tag{3.2.3}$$

and about twice as large for hydrogen. Up to now the mean energy deposited by a charged particle in a medium was considered. The underlying process, the collision with atomic electrons, is of stochastic nature. Hence, the energy deposited by particles is fluctuating around the mean value following a distribution or straggling function. There are two main factors influencing the total energy deposit on a particle trajectory of length x: the number of collisions and the energy loss per collision. For thin absorbers the first contribution dominates the shape of the distribution. The most popular straggling function, called 'Landau function' is derived directly from the Rutherford cross section (see [72]). The Landau function and more sophisticated straggling functions, developed by e.g. Vavilov and Urban, are discussed in detail in [73].

An approximate way to describe ionization is to consider the emission of virtual photons which are absorbed by the material. This is called the Fermi-Virtual-Photon method (FVP) or Photo-Absorption-Ionization-Model (PAI). The differential cross section of a relativistic charged particle is treated proportional to the photo absorption cross section of the material

given by [74] :

$$\frac{d\sigma_i}{d\omega} = \frac{\alpha}{\pi\beta^2|\epsilon(\omega)|^2}\left\{\frac{\tilde{\sigma}_\gamma(\omega)}{\omega}\left[\ln\frac{2mv^2}{\omega|1-\beta^2\epsilon|} - \frac{\epsilon_1-\beta^2|\epsilon|^2}{\epsilon_2}\arg(1-\beta^2\epsilon^*)\right] + \frac{1}{\omega^2}\int_{I_1}^{\omega}\tilde{\sigma}_\gamma(\omega')d\omega'\right\} , \tag{3.2.4}$$

where $\epsilon_2(\omega)$ and $\epsilon_1(\omega)$ are the components of the complex dielectric constant $\epsilon = \epsilon_1 + i\epsilon_2$, $\beta = v/c$ is the particle velocity, Z the effective atomic number, N the number of atoms per unit volume, $\hbar$ the Planck constant and m and e the electron mass and charge. The material specific constant I_1 is its first ionization potential and $\omega_{max} \sim 100\,\text{keV}$ is the maximum allowed energy transfer. In practice the photo-absorption cross section is parametrized by:

$$\sigma_\gamma(\omega) = \sum_{k=1}^{4} a_k^{(i)}\omega^{-k}, \tag{3.2.5}$$

with material specific coefficients $a_k^{(i)}$ in each energy interval i. The number of ionizing collisions for a given step length is simulated by a Poisson distribution with a mean value proportional to the total cross section:

$$\sigma_i = \int_{I_1}^{\omega_{max}} \frac{d\sigma(\omega')}{d\omega'} \ . \tag{3.2.6}$$

The energy transfer of each collision is simulated proportional to

$$\sigma_i(>\omega) = \int_{\omega}^{\omega_{max}} \frac{d\sigma(\omega')}{d\omega'}d\omega' \ . \tag{3.2.7}$$

This method is implemented in the G4PAIModel of the Geant4 simulation package [75] and is used to simulate the energy depositions inside the AMS-02 TRD gas. The nominal tube gas is a mixture of Xe and CO_2 in volume fraction 80 to 20 respectively with a density of $\rho = 0.6\frac{\text{mg}}{\text{cm}^3}$. The spectra of simulated energy depositions in dependence of $\beta\gamma$ for an isotropic flux on a single tube is shown in figure 3.6. The mean path length inside the tube is about its diameter of 6 mm but varies between 0 and 8 mm, depending on radial distance to tube center and particle incident angle. The number of interactions is following the expected Bethe-Bloch shape with about 25 collisions in average for MIPs ($\log_{10}(\beta\gamma) \approx 0.5$). The deposited energy is correlated to the number of collisions and at $\sim 1\,\text{keV}$ for MIP and $\sim 2\,\text{keV}$ for relativistic particles. The energy deposition spectrum for the generated particle spectrum (flat in $\log_{10}(\beta\gamma)$) is peaked at $\sim 2\,\text{keV}$ and reaches up to $\lesssim 15\,\text{keV}$. Only ionization energy depositions generated by the primary particle are treated here. Additional contributions, by e.g. secondaries or δ-rays, are not explicitly discussed but contribute to the total energy deposition in data and simulation. Tube energy deposition spectra are shown in the data analysis section (see e.g. figures 4.68).

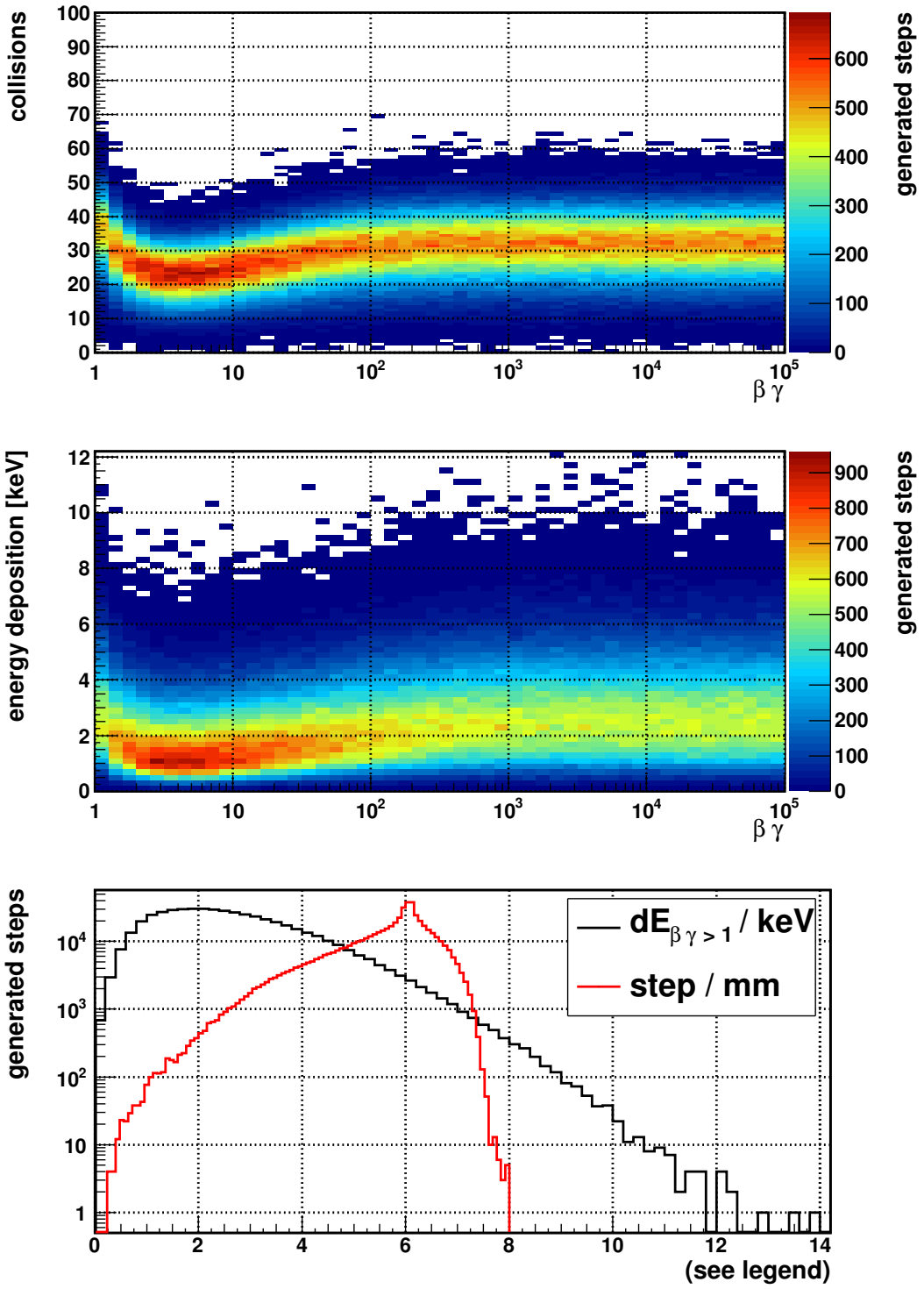

Figure 3.6: Simulated ionization spectra dN/dx (top) and dE/dx (center) for realistic path length distribution and nominal TRD gas as function of $\beta\gamma$. The path length distribution taken from space data (red) and the total deposited energy (black) are shown on the bottom.

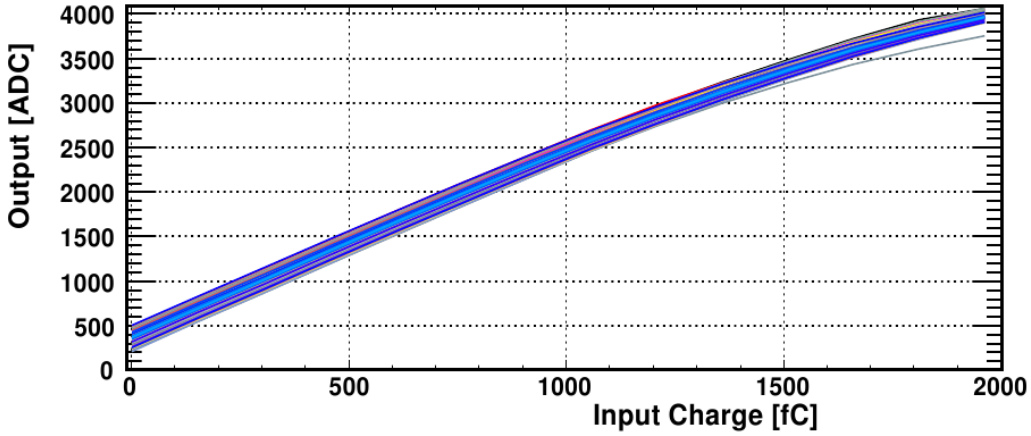

Figure 3.7: Linearity of signal digitization for 64 electronics channels. The correlation between digital signal amplitude denoted by 'Output' and the input charge is linear up to $\sim$ 1300 fC $\Leftrightarrow$ 3000 ADC units [76].

3.3 Hit Digitization

The electronic signal on each straw tube anode wire needs to be converted into a hit amplitude. In the Front-End-Electronics custom hybrid VA chips are used to amplify and shape the analog signal and 12-bit Analog-to-Digital Converters (ADC) of the type AD7476 are used to digitize the signal. A linear conversion of the collected charge up to $\sim$ 3000 ADC units has been verified (see figure 3.7), where $\sim$ 50 ADC units correspond to the most probable energy deposition of a MIP. Each channel has an individual pedestal value of about 400 ADC units constant in time on the $\sim$ 2 ADC level. This corresponds to the signal without any particle passage and thus to the zero point of energy deposition. The pedestal position A_{ped} and width $\sigma_{ped} \approx 9 - 15$ ADC is determined for each channel in a calibration procedure at the beginning of each data taking run. In the current data taking operations this is equivalent to about every 23 minutes. In regular data taking mode the digital signal processor (DSP) calculates the hit amplitude A_{hit} by the subtraction of the pedestal amplitude A_{ped} from the raw hit amplitude A_{raw}. A common mode (CM) correction is applied to correct for electronics fluctuations . Here, the mean amplitude $A_{CM} = \langle A_{hit} \rangle$ of all channels of each HV supply channel [1] is calculated and subtracted from each single channel amplitude $A_{corr} = A_{hit} - A_{CM}$. To prevent distortions by erroneous channels different prevention algorithms are implemented in the DSP. One of them is the suppression of noisy channels by requiring $A_{hit} < 10\,\sigma_{raw}$ to include a channel into calculation of A_{CM}. A detailed discussion on the DSP and TRD electronics can be found in [77].

[1] More precisely one mean is calculated per VA chip. One HV channel consists of two VA chips, supporting four modules upon each other (two per VA chip) and 64 tubes in total

4 Data Analysis

In this chapter the performance of the TRD is evaluated with the AMS offline software framework [78] for data from beamtest, atmospheric muons and space. The event samples and the TRD independent event preselection are described in section 4.1 and section 4.2 respectively. The TRD related algorithms are subdivided into event reconstruction, calibration and particle identification and discussed in sections 4.3, 4.4 and 4.5, respectively. The presented algorithms have been developed, implemented into the AMS offline software framework, and evaluated in the scope of this thesis.

4.1 Event Samples

An overview on the detector setup and the environmental parameters is given in section 4.1.1 for beamtest data, in section 4.1.2 for atmospheric muon data and in section 4.1.3 for space data.

4.1.1 Beamtest

In 2010 two AMS-02 beamtest campaigns were performed at CERN, the first one in February with the outdated design layout containing the superconducting magnet (see section 2.4). In Spring 2010 NASA announced the extension of the ISS lifetime to at least 2020. To profit from the lifetime extension it was decided to reconfigure AMS-02 to a permanent magnet and rearrange the Tracker layout (see section 2.4). After completion in July 2010 the second beam test was conducted in the period of 8th to 20th August 2010. In addition to the main goal of evaluating the Tracker momentum resolution also the particle identification performance of the detector system was investigated. In this work the performance of the TRD in the second beam test, with final AMS-02 setup, is discussed.

The beamtest was performed in the experimental area PPE 168 of the H8 beamline at CERN. The AMS-02 beamtest setup is illustrated in figure 4.1. In the beamtest the detector was targeted by different beam settings, leading to a set of beam energies, compositions and focusing. The various beam settings are summarized in table 4.1. The first one corresponds

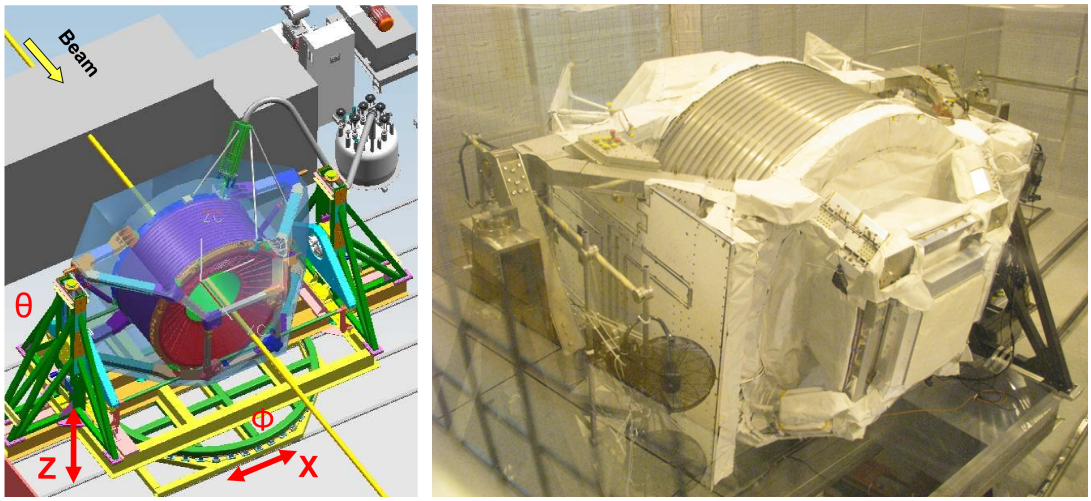

Figure 4.1: The AMS-02 detector in the rotational stand at beamtest [79].

Type	Particle	Energies [GeV/c]	Rate [kHz]	Spot [cm]	Composition
Primary	p^+	400	2.5	0.2-0.3	$\gtrsim 0.99$
Secondary	p^+	120, 180	0.5	4	0.5-0.8 p^+, π^+, K^+
Secondary	$e^\pm$	100, 120, 180	0.5	4	$\sim 0.7 e^\pm$, $\pi^\pm$, $K^\pm$
Tertiary	π^+	20, 60, 80	0.2	10	0.7-0.8 π^+,K^+,e^+
Tertiary	e^+	20, 80	0.1-0.2	10	0.1-0.2 e^+, π^+, K^+

Table 4.1: Estimated parameters of AMS-02 test beams [80].

AMS Setting	X [cm]	Y [cm]	Z [cm]	Θ [°]	ϕ [°]
101	-2	-2	195	0	0
104	-43.44	36.85	195	10	134.7
105	-76.44	78.25	195	18.3	134.3
110	-22.6	17.67	195	5	135
111	-59.28	60.34	195	15	134.5
112	37.74	15.09	195	3.3	10.84
113	-35.32	-23.56	195	3.5	-143.5

Table 4.2: Angular settings at beamtest

to the so-called 'microbeam' setting which is extracted directly from the SPS and is characterized by high proton purity and a small beam spot. The other settings correspond to secondary and tertiary beams with different target and magnet configurations with typically high pion contamination and larger beam spots. The focused and high-intensity illumination of the TRD straw tubes by the microbeam setting is known to cause artifacts by so-called ghost hits. These hits are remainders of previous energy depositions which are generated by electronics undershoots (indicated in figure 4.2) and hence systematically reduce measurement of energy depositions. After the passage of a particle the trigger signal has to be processed and the shaping of the electronics is performed. The maximum signal is reached after $\sim 2.4\mu s$ [77] depending on operating conditions and an undershoot up to $\sim 500\,\mu s$ and maximum at $\sim 140\,\mu s$ is observed. Due to this systematic uncertainty the microbeam data is excluded from analysis performed in this work.

The rotational stand shown in figure 4.1 is used to control the incident angle of the beam in the AMS-02 reference frame. The selected angular settings are listed in table 4.2. These settings are all focused on the ECAL volume and passing the TRD volume to allow for lepton/hadron differentiation studies. Excluding the microbeam setting, the total number of triggered events for negative and positive beam settings is 22,721,973 and 47,429,736 respectively.

4.1.2 Cosmics

After the last beamtest at CERN the AMS-02 detector was shipped on 26. August 2010 by U.S. Air Force to Kennedy Space Center (KSC) in Cape Canaveral (FL/USA). During its stay at KSC the AMS-02 detector was located at the Space Shuttle Processing Facility and was taking data up to April 2011, when it had to leave the SSPF for launch preparations. In the considered period 11-17 Nov 2010 the AMS-02 detector was operated in a class 100000 clean room, the so-called 'High Bay', of the Space Shuttle Processing Facility (see figure 4.3).

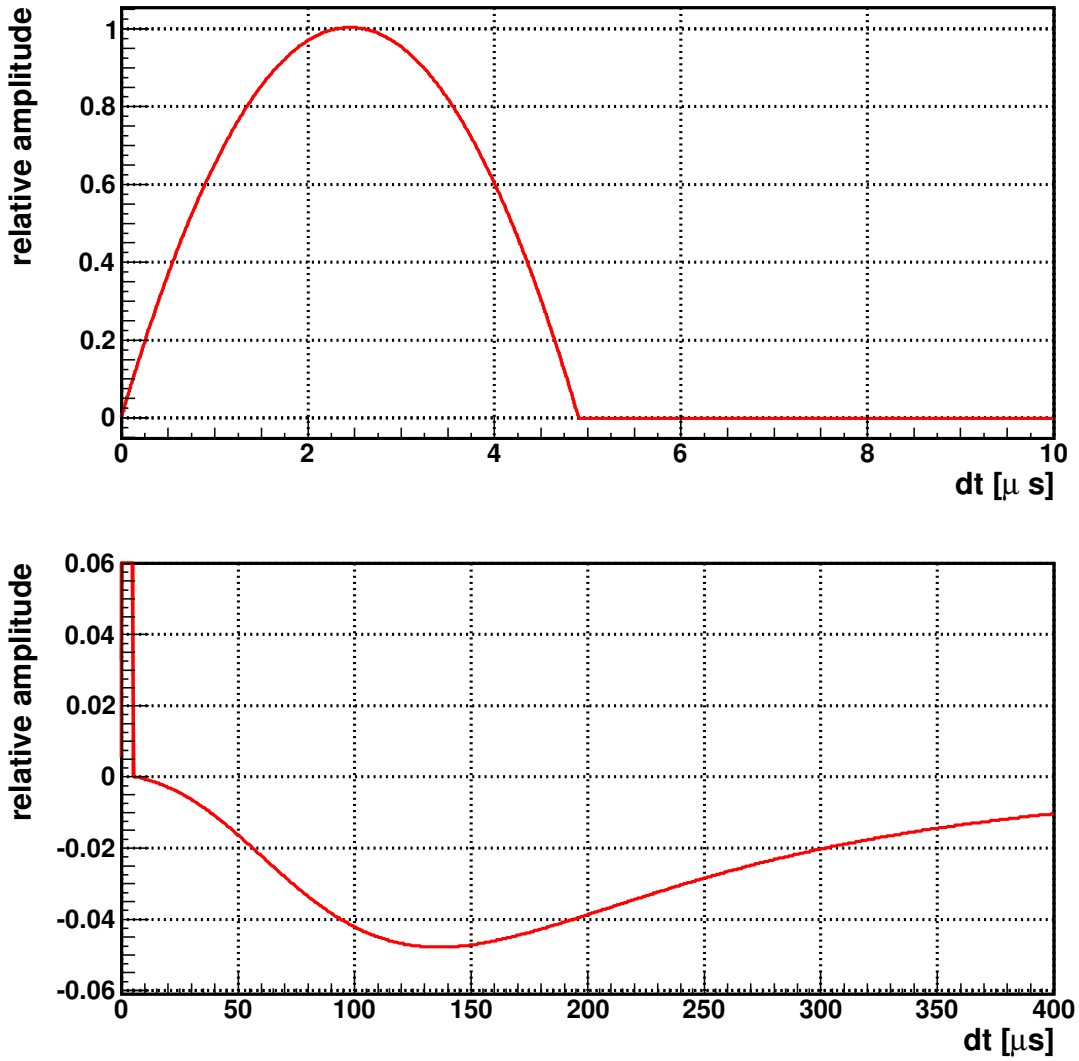

Figure 4.2: Analytical description (sum of a 2nd order polynomial and a landau distribution) of the relative amplitude of TRD hits extracted from data including ghost hits generated by TRD electronics undershoot.

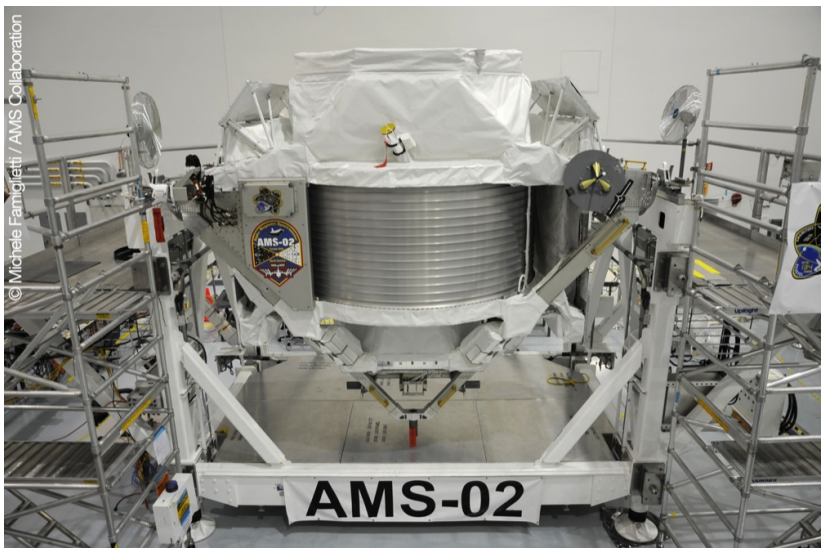

Figure 4.3: The AMS-02 detector in the Space Shuttle Processing Facility at Kennedy Space Center [50].

This period is characterized by continuously stable data taking and detector operation conditions and focused subdetector calibrations. The total number of triggered muon events is 39,209,746.

4.1.3 Space

Space Shuttle Endeavour was launched on 16 May 2011 (see figure 4.4) to bring the AMS-02 detector to the International Space Station (ISS). On 19 May 2011 AMS-02 was installed on the main truss of the ISS and commissioned. Since then it is continuously taking data. The AMS-02 detector is orbiting the Earth at an altitude of about 350 km. At this height it is not shielded by the atmosphere and it is subject to the quasi-isotropic cosmic particle flux following a power-law energy spectrum (see figure 1.12). In figure 4.5 the time difference δt between subsequent events is shown. One can see different slopes in the distribution of δt, corresponding to different particle flux contributions. The average δt of 1800 μs is equivalent to an average trigger rate of $\sim$ 556 Hz. At low values of δt events are not recorded due to electronics deadtime. The data acquisition livetime, defined as fraction of time the detector is ready to record data, is shown in figure 4.6 as function of orbital position, given in geodetic longitude and latitude. The power-law spectrum of cosmic particle leads to high particle fluxes at regions of low geomagnetic field (see section 1.3.3). Due to the decrease in δt an increased fraction of time is spent on processing incoming data (deadtime) and more events passing the detector are not triggered and therefore missed.

The time period analyzed in this work is 19 May 2011 to 27 July 2011 corresponding about 6×10^6 seconds. In figure 4.7 the number of triggered events is shown as function of time. The observed periodicity of trigger rate on the daily scale reflects the passage of the ISS

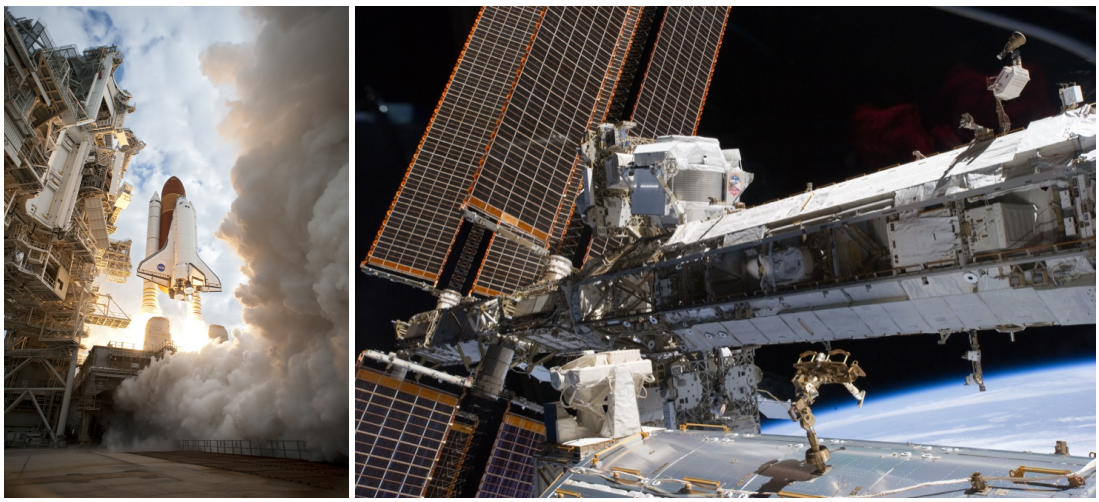

Figure 4.4: Launch of Space Shuttle Endeavour (left) and view on the installed AMS-02 detector (right) at its final position on the main truss of the International Space Station (pictures provided by NASA).

orbit through the polar region. In the beginning of the data taking period up to the end of May the optimization of data taking and detector operation parameters lead to lower event rates than afterwards. In total about 2.8 billion triggered events are analyzed in this work.

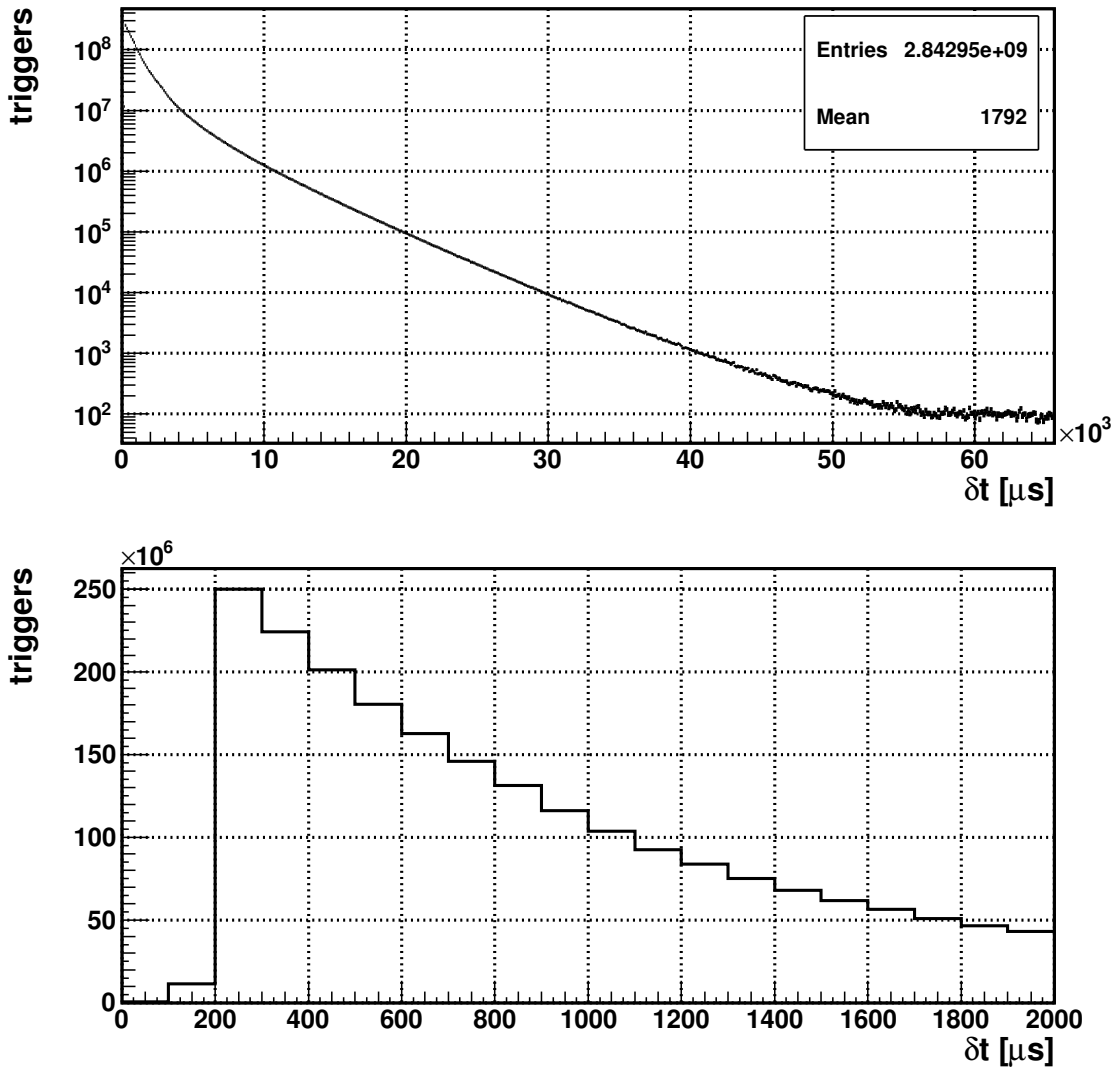

Figure 4.5: Time difference δt between subsequent triggers (top). The zoomed view on δt (bottom) reveals the suppression at $\lesssim 200\,\mu$s due to trigger dead time.

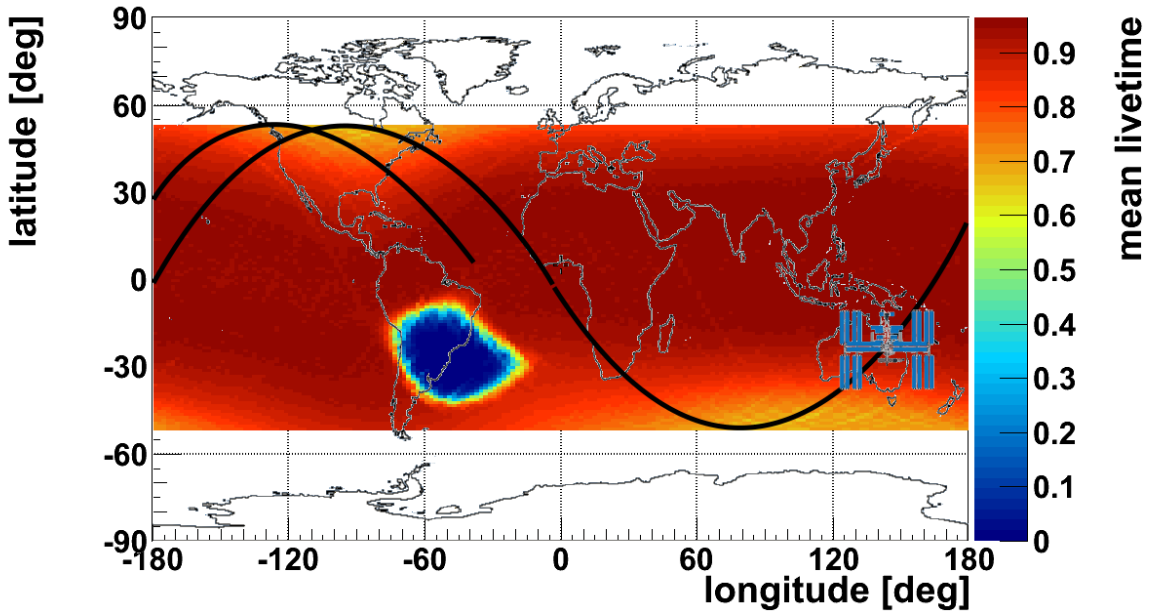

Figure 4.6: Mean livetime as function of orbit parameters. Regions of low geomagnetic field intensity (South Atlantic Anomaly / polar regions) show lower livetime values due to higher particle flux.

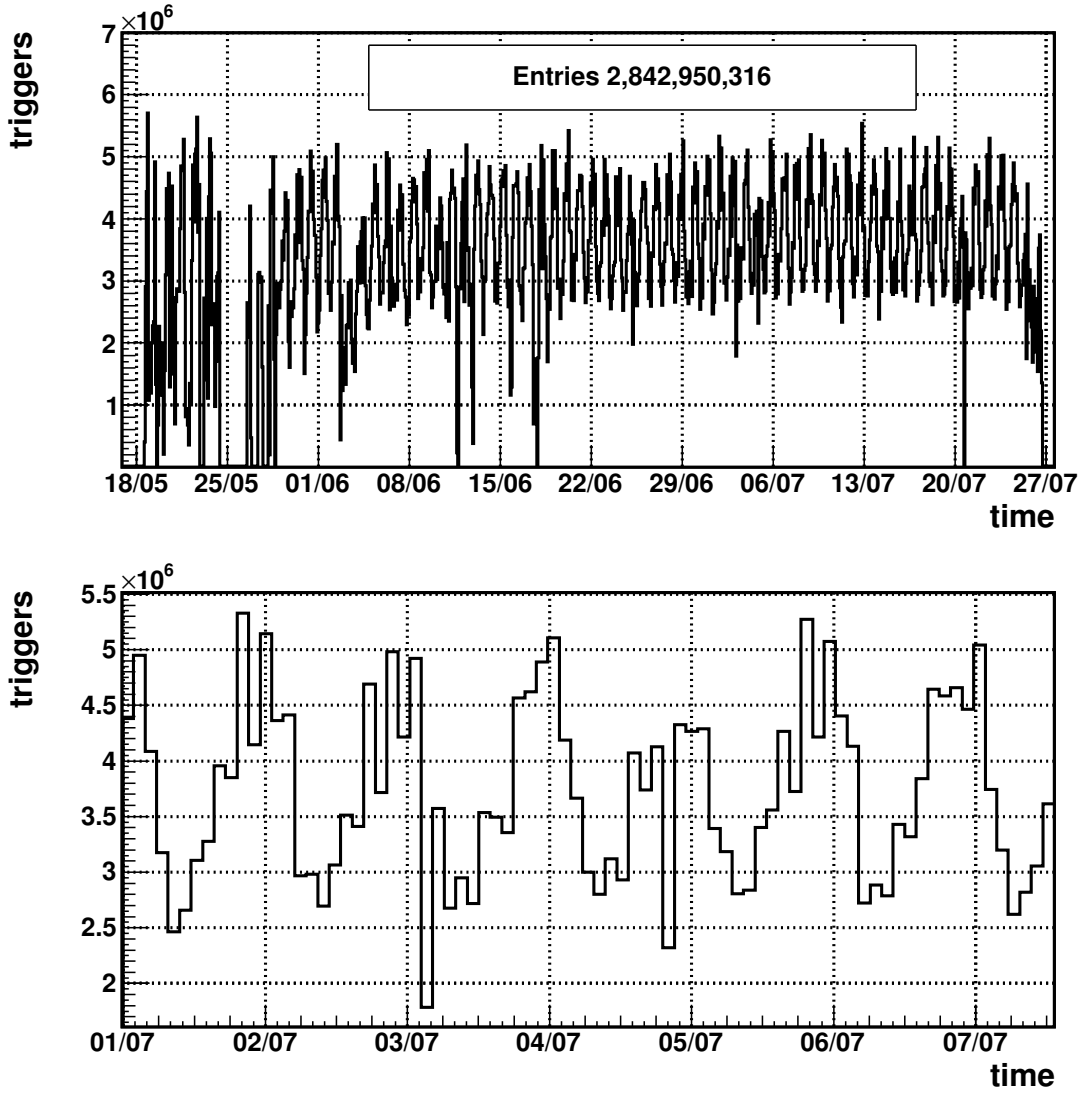

Figure 4.7: Number of triggered events as function of time for the whole period considered in this analysis (top) and for a week (bottom).

Detector	Selection
TOF	4/4 layers, $\beta > 0.5$, Rate $< 3\,\text{kHz}$, Livetime > 0.5
ACC	no hits
Tracker	1 track, 4+/7 inner layers, $\frac{\chi^2}{NDF}\vert_{X,Y} < 5$, $\sigma_{1/R} R < 0.5$
ECAL	1 track, associated to Tracker track

Table 4.3: Subdetector event selection

4.2 TRD-independent Event Selection

The description of the event selection in section 4.2.1 is followed by the determination of the sea-level muon flux and charge ratio in section 4.2.2 and the geomagnetic cutoff in section 4.2.3.

4.2.1 Selection Criteria

Events reconstructed in the different AMS-02 subdetectors have to be quality selected for analysis. In general a clean event topology and well reconstructed subdetector events are required. The quality selection of subdetector events is summarized in table 4.3. A clean event has to be reconstructed in all 4 TOF layers and the ACC is required to have no hits. The reconstructed particle velocity has to be $\beta > 0.5$ to suppress events passing the detector upwards. Regions of high particle flux are suppressed by Rate $< 3\,\text{kHz}$ and Livetime > 0.5 to decrease complex TRD event topologies like multi-track events. Four of the seven inner Tracker layers have to contain a hit on a reconstructed track: the top inner layer and at least one side of the remaining 3 double-sided layers. The track fit has to fulfill moderate fit quality selections on $\frac{\chi^2}{NDF}$ and $\sigma_{1/R} R$. The latter cut is performed on the inverse of the reconstructed rigidity R because this corresponds to the curvature of the bended track which has a gaussian uncertainty, while the uncertainty on rigidity is non-gaussian. An ECAL shower has to be associated to the track extrapolation. Additionally, exactly one track in the Tracker and one shower in the ECAL is allowed for cleanly reconstructed single-track events.

To analyze the TRD particle signature and identification performance a classification of the events into different particle types is performed independent of the TRD. The reconstructed absolute charge, determined in TOF, Tracker and RICH, has to be consistent and equal to one. Electrons are identified by ECAL based on the total deposited energy E and the longitudinal and lateral shower evolution. In contrast to hadrons, which are considered here as ideal minimum ionizing particles of $E < 1\,\text{GeV}$, leptons emit high-energy photons by bremsstrahlung in the dense material of the ECAL which can produce electron-positron pairs and form an electromagnetic shower. This multiplication of secondary particles is

done until the threshold for pair production is reached. Hence the energy deposition along the shower and its maximum is a function of lepton energy. The ECAL electron identification consists of a cut on the 'Boosted Decision Tree (BDT)'-classifier $C_{BDT} > 0$ and a selection on the reconstructed energy to momentum ratio $E/P < -0.6$. A restriction on positive rigidities for protons and negative ones for electrons is applied additionally to increase the sample purities. The performance of the event classification is visualized in figure 4.8 For space data the number of classified proton and electron events is 3,860,946 and 20,883 respectively. In total there are 13,459,246 muon and 173 electron events identified for KSC atmospheric muon data. As just a handful of sea-level events can be classified as electrons the statistics is too low to include this dataset in the discussion of TRD particle identification in section 4.5.

Inner Tracker Rigidity Resolution With the presented selection the rigidity resolution of the inner Tracker can be determined from space data. In figure 4.9 the E/P ratio is shown as function of reconstructed ECAL energy. The ECAL energy resolution is given by $\frac{\sigma_E}{E} = \frac{0.099}{\sqrt{E/\mathrm{GeV}}} \oplus 0.015$ [81]. The uncertainty of the ECAL energy reconstruction is decreasing for absorbed showers with particle energy and the uncertainty of the Tracker rigidity reconstruction is increasing with particle momentum. Hence at high electron energies the width of the E/P distribution is dominated by the Tracker resolution. The relative width of the distribution in each energy interval is approximated by $(\frac{\sigma_{E/P}}{E/P})^2 = (\frac{\sigma_E}{E})^2 + (\frac{\sigma_{1/P}}{1/P})^2$, where σ_E is calculated from energy resolution formula at given energy. The maximum detectable rigidity $MDR \approx 227.8^{+18.9}_{-16.2}\,\mathrm{GeV}$ is determined by the extrapolation to relative width 1. The rigidity resolution of the inner Tracker has also been determined independently in beamtest data to $MDR_{BT} \approx 220\,\mathrm{GeV}$ [82].

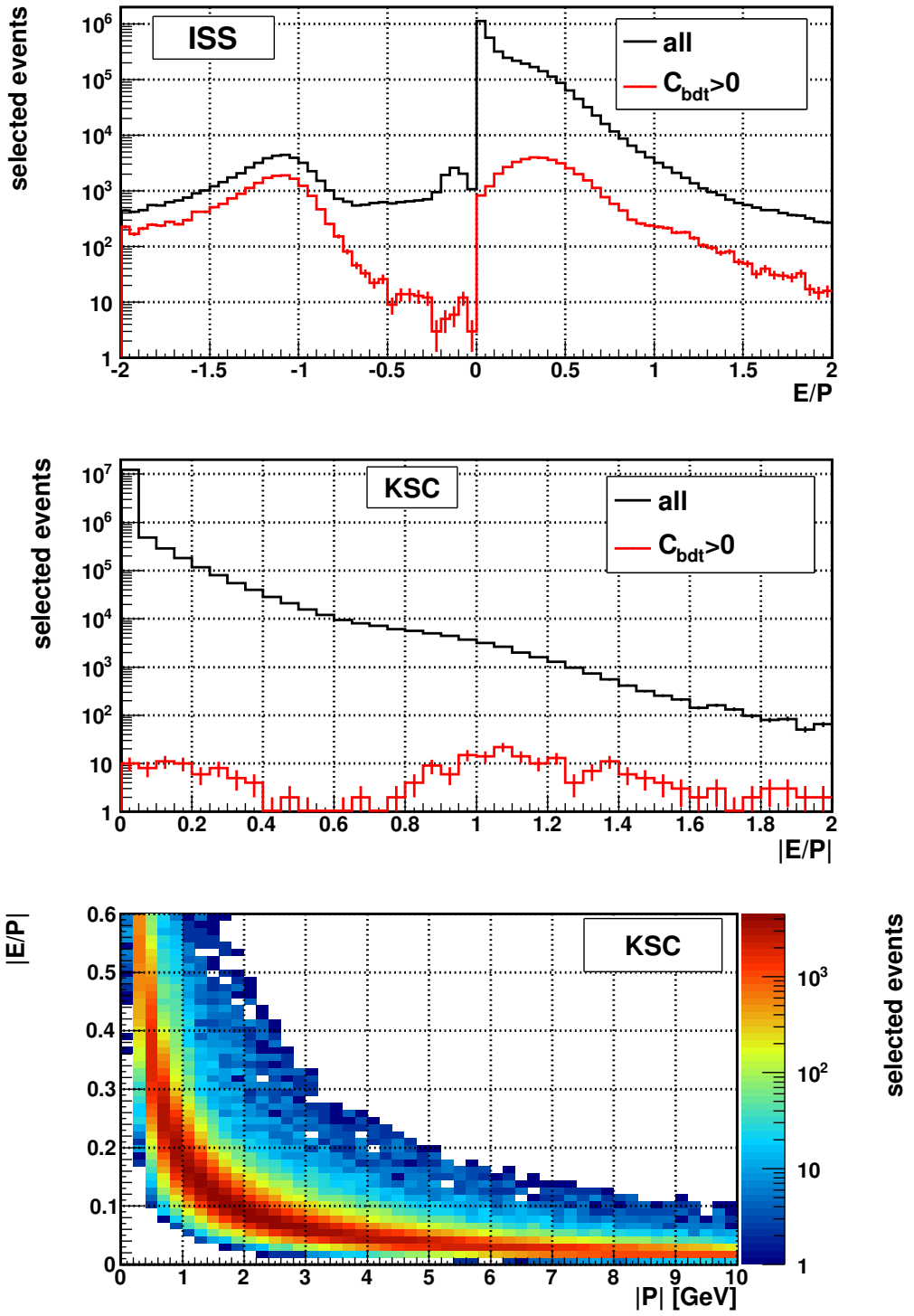

Figure 4.8: The influence of the ECAL electron selection $C_{bdt} > 0$ on the distribution of reconstructed E/P values, with energy E deposited in the ECAL and momentum P reconstructed in the inner Tracker, for space (top) and atmospheric muon data (center). Electrons are absorbed in the ECAL and therefore group in general at $|E/P| \approx 1$. In atmospheric muon data large $|E/P|$ values are mainly generated by low momentum MIPs (bottom).

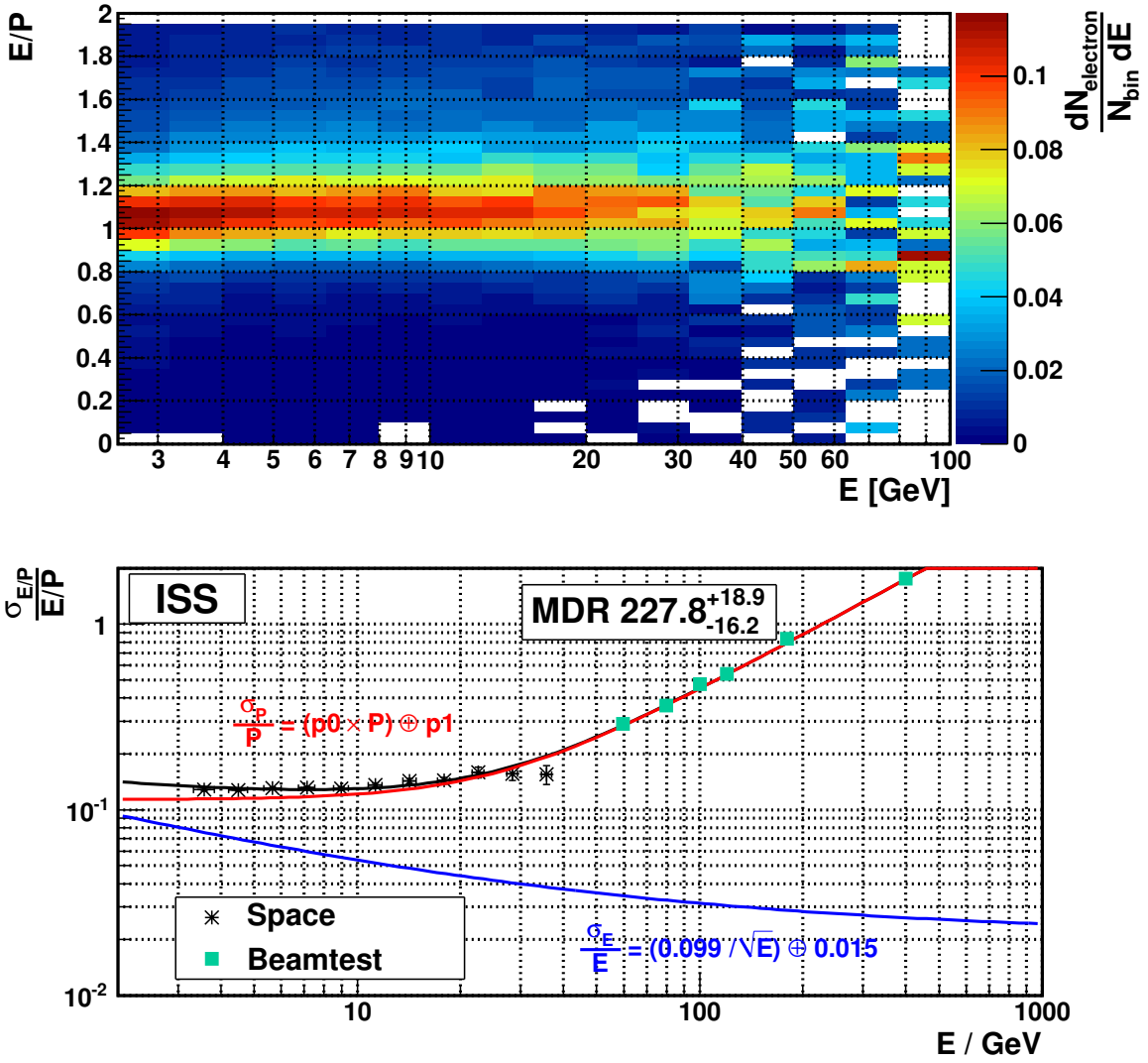

Figure 4.9: The rigidity resolution of the inner Tracker. *Top:* the energy-momentum ratio $|E/P|$ as function of deposited energy E. Bottom: The width of the $|E/P|$ distribution can be approximated analytically (black line) by the quadratic sum of ECAL energy resolution and Tracker momentum resolution.

Additional selection for beamtest data The event classification of beamtest data by the reconstructed subdetector tracks is supported by external trigger signals. The external trigger system (see figure 4.10) consists of two scintillator panels (S0, S2) and two threshold Čerenkov counters (CHRV1, CHRV2). In Čerenkov counters the particle velocity is determined by the emission of Čerenov light, above a threshold energy. For a given beam energy the particle velocity is used to disentangle different particles by their mass. The density of the gas in the Čerenkov counters is therefore adjusted for each beam setting to suppress corresponding background events. Scintillator panels are used to ensure that particles are passing the Čerenkov counters. Only in this case, one can deduce from the absence of a Čerenkov signal that the particle velocity is below the threshold. Protons are selected by the absence of Čerenkov signal while the particle is passing the scintillators. The presence of both Čerenkov signals is required for pions and leptons. In general the trigger bits and Čerenkov thresholds were optimized to select a pion sample, contaminated by electrons, and to suppress slower particle events. Leptons can be identified and separated from pions by TRD and ECAL. The beam contamination by muons and kaons is expected to be low [84] and thus neglected in this work. The electron/pion separation power of the TRD is investigated on pre-selected beam test event samples. The size of particle samples depends on the time spent in the given beam setting, the beam composition and the efficiencies of reconstruction, selection and identification. In the total beamtest data sample 584,930 pion and 20914 electron events are classified. The number of pions is $\sim 10^5$ at each beam energy. The number of electrons is decreasing with rising beam energy due to beam contamination by pions from $\sim 10^4$ at 20 GeV to $\lesssim 10^3$ at 120 GeV.

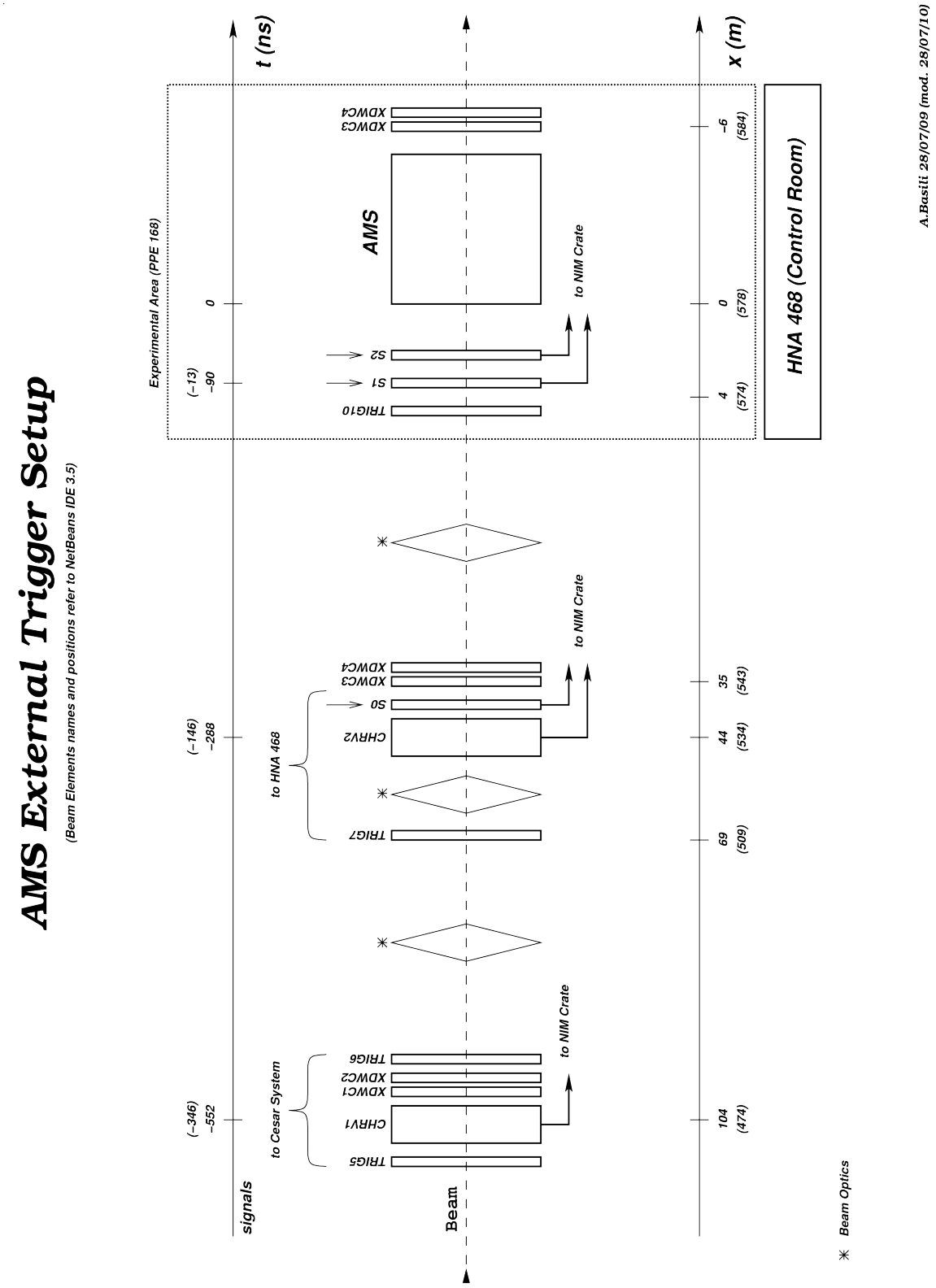

Figure 4.10: Schematic view of the beamtest external trigger system. Its main components are the two Čerenkov counters CHRV1/CHRV2 (left / center part) and the scintillator panels S0/S2 (center/ right part) [83].

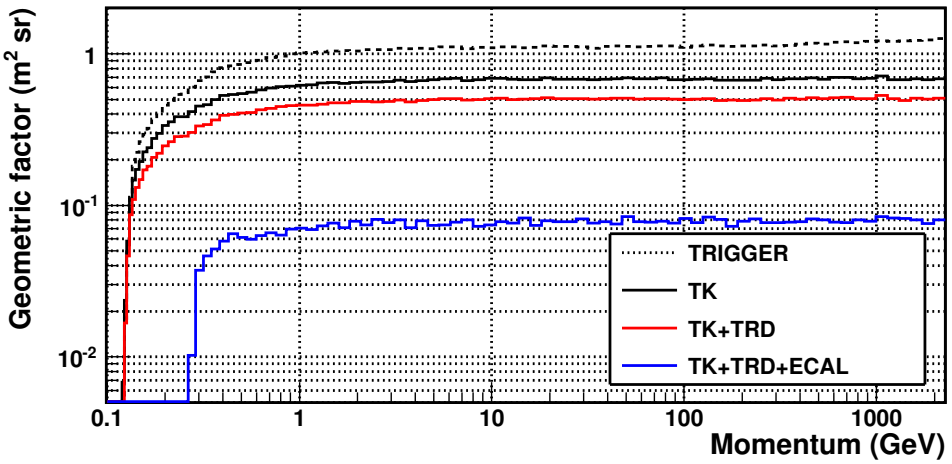

Figure 4.11: The geometric factor of relevant Tracker (TK), TRD and ECAL combinations determined by independent analysis of MC simulation data.

4.2.2 Sea-level Muon Flux

The determination of particle fluxes is based on the event rate and detection acceptance. The acceptance can be interpreted as an effective area of an instrument towards a specific kind of event. In general the acceptance can be divided into single components: geometric factor, reconstruction and selection efficiency. All of them depend on the definition of the desired event class. For example protons may be reconstructed by the combination of Tracker and TOF with high purity but positrons have a high background of protons, which needs to be suppressed by the identification of a lepton signature in TRD and ECAL. This lowers the solid angle of allowed particle trajectories and hence the geometric factor. For space data analysis of particle identification in section 4.5 the combination of TRD, inner Tracker and ECAL is necessary to classify electron and proton events.

The acceptance can be determined from MC simulations by generating a sample of events N_{gen} with known geometric factor A_{gen} and counting the number of selected events N_{sel}. Then the generated geometric factor is simply scaled by the efficiency to get the selection acceptance: $A_{sel} = A_{gen}\frac{N_{sel}}{N_{gen}}$. Crucial for this calculation is that the generated geometric factor fully covers the desired acceptance. The generated geometric factor is determined in each angular interval by $A_{bin} = F \times \frac{\Omega_{bin}}{\Omega_{gen}}$, with generated aperture F, generated solid angle Ω_{gen} and solid angle $\Omega_{bin} = 2\pi \int_{\Theta_{bin,min}}^{\Theta_{bin,max}} \sin\Theta \, d\Theta$. The simulations used here were generated flat in $\cos^2\Theta$ with $F = 3 \times 3\,\mathrm{m}$ and $\cos\Theta_{gen,min} = 0.7$, leading to $\Omega_{gen} = 2\pi(1 - \cos\Theta_{gen,min})\big|_{(\Theta_{gen,min}=0.7)} \approx 1.5\,\mathrm{sr}$.

The geometric factor of relevant combinations of inner Tracker, TRD and ECAL is shown in figure 4.11. The geometric factor of the inner Tracker is $\sim 0.65\,\mathrm{m^2sr}$, for the combination of Tracker and TRD it is $\sim 0.47\,\mathrm{m^2sr}$ and for the combination of all three detectors it is

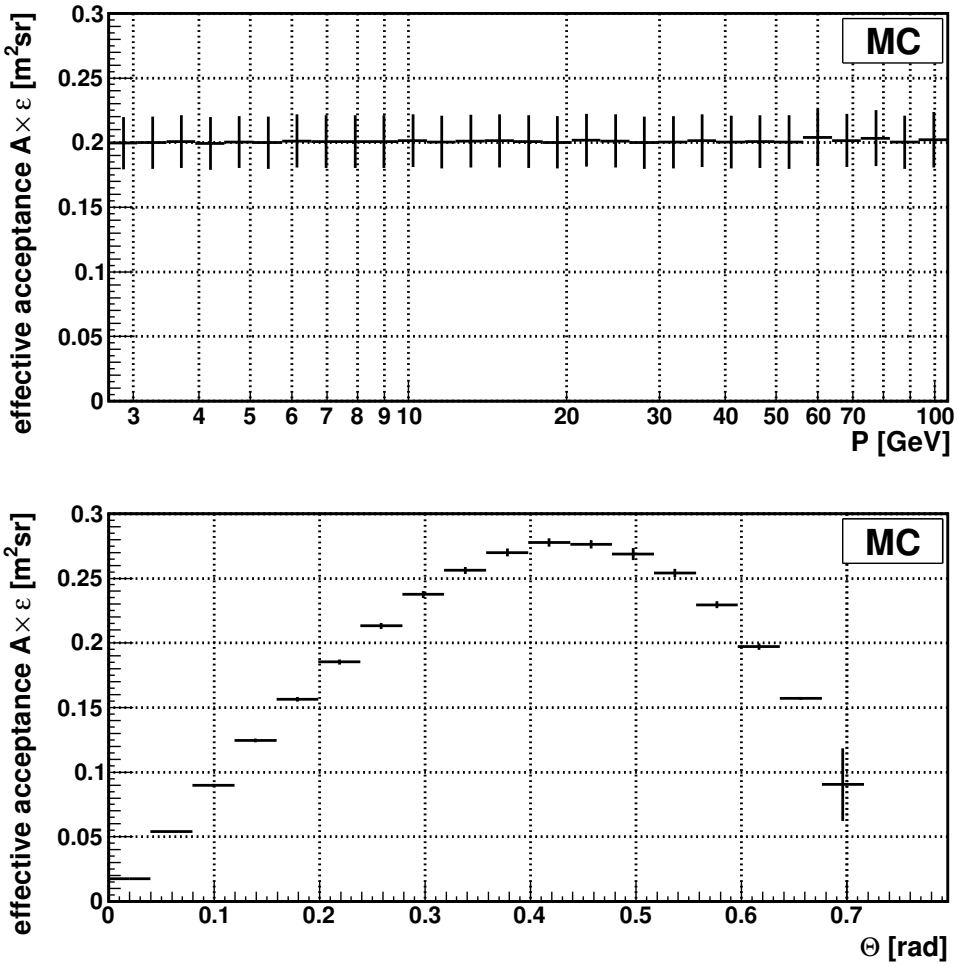

Figure 4.12: The effective acceptance for atmospheric muon events as function of momentum P (top) and zenith angle Θ (bottom).

$\sim 0.08\,\mathrm{m^2sr}$. At low rigidities the magnetic deflection of particles limits the geometric factor.

In general the detector-specific reconstruction and selection efficiencies depend on the particle type. In figure 4.12 the effective acceptance $G = A \times \varepsilon$, with geometric factor A and selection efficiency ε, is shown for the muon event selection described in section 4.2.1. The effective acceptance is $\sim 0.22\,\mathrm{m^2sr}$ above a few GeV and reduced by the geometric factor at lower energies. Its angular dependency peaks at $\Theta \approx 0.4\,\mathrm{rad}$ with a maximum value of $\sim 0.28\,\mathrm{m^2sr}$.

The event rate is a simple counting of events for a given selection normalized to the effective data taking time: $R = \frac{N}{t\tau}$, with event rate R, number of events N, time t and livetime τ. The rate of selected muon events as function of momentum and zenith angle is shown in figure 4.13. The distribution is decreasing from about 1 to $8 \times 10^{-4}\,(\mathrm{s\,GeV})^{-1}$ from 4 to 100 GeV and is peaked at $\Theta \approx 0.3\,\mathrm{rad}$. While the momentum dependence is mainly introduced by the primary particle flux and interactions the angular dependency is affected by the solid angle and the limited angular detector acceptance.

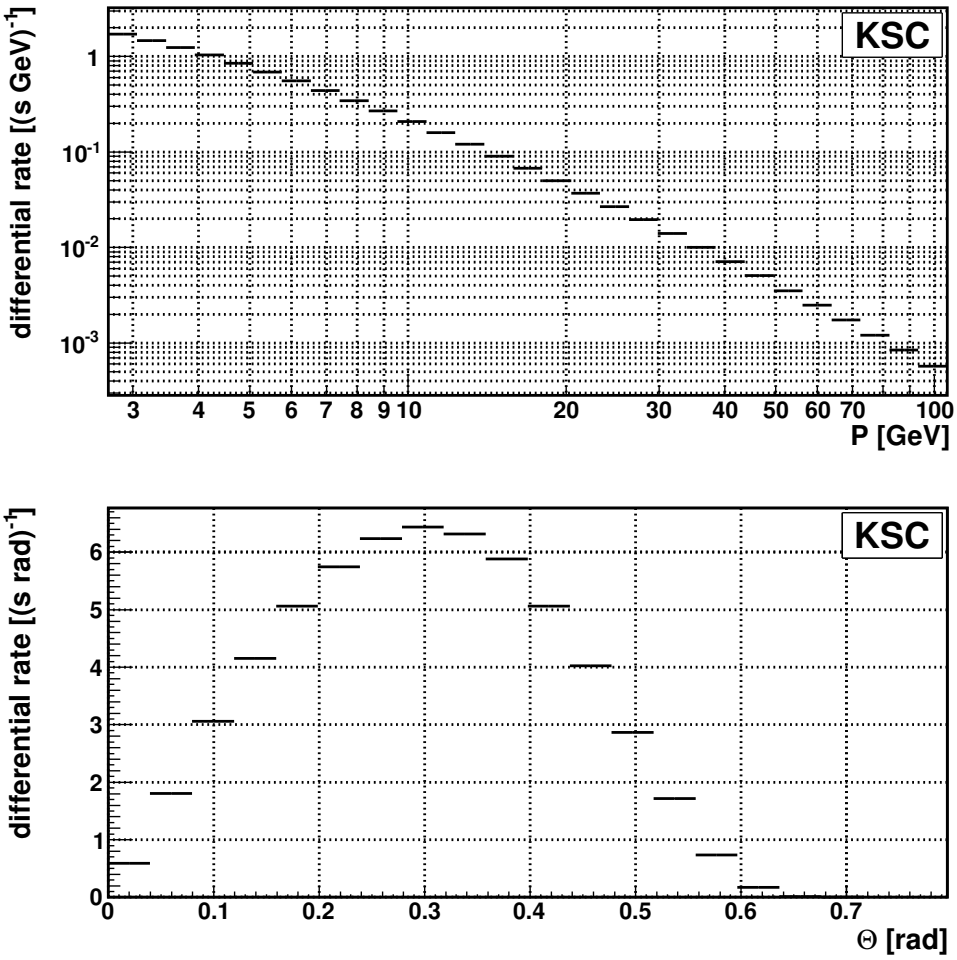

Figure 4.13: The reconstructed differential muon event rate as function of momentum P (top) and zenith angle Θ (bottom).

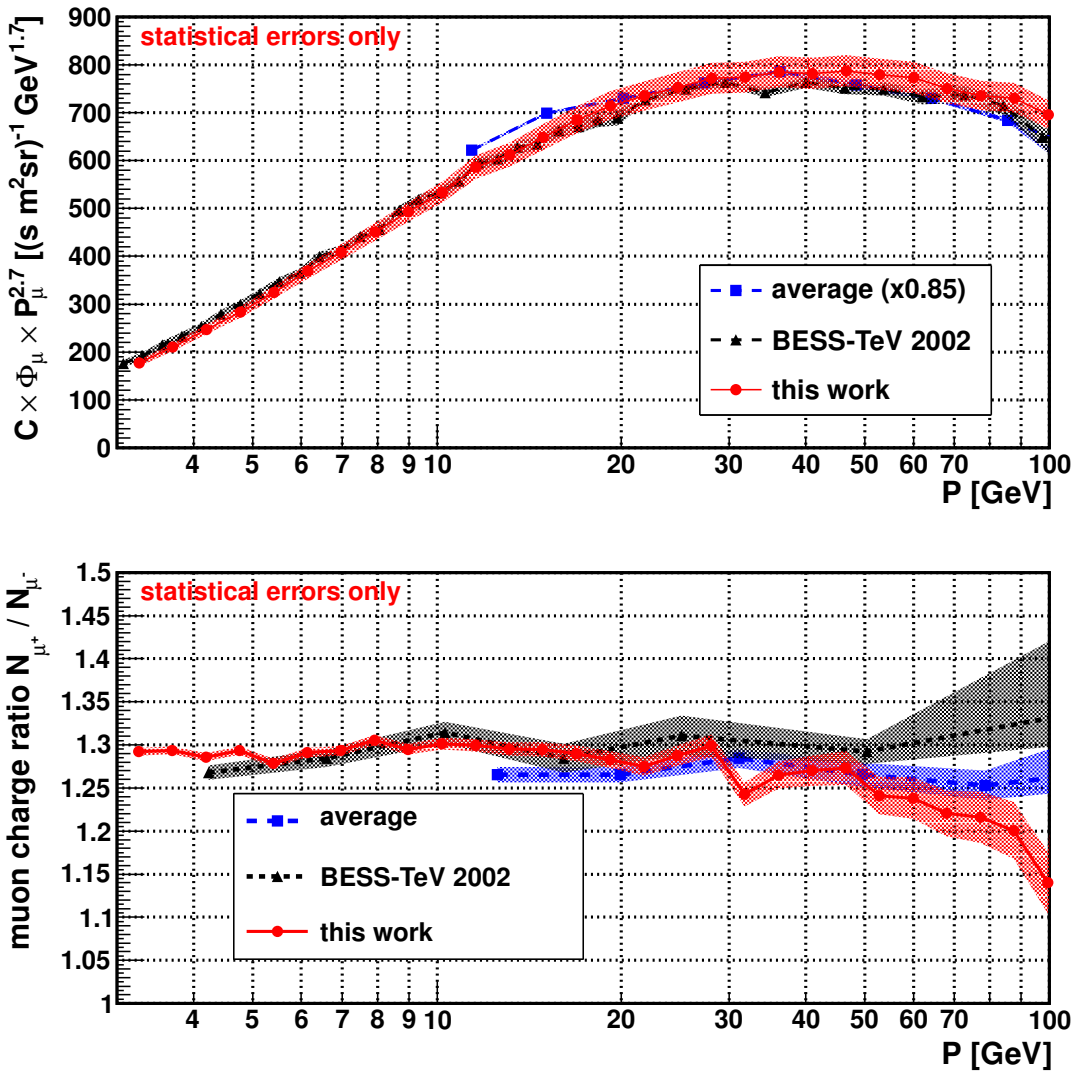

Figure 4.14: The atmospheric muon flux determined in this analysis (red markers) compared to BESS data [85] (black dotted) and world average [86] (blue dashed).

Dividing the event rate in each momentum and Θ interval by the corresponding effective acceptance gives the flux of atmospheric muons shown in figure 4.14. The obtained data points are listed in table 4.4. In this analysis just the inner Tracker with a maximum detectable rigidity of $\sim 200\,\text{GeV}$ is used to determine the particle rigidity. Reconstructed particle rigidities above 100 GeV have an expected uncertainty of at least 50 % and are therefore not considered in this analysis. The reconstructed muon flux is lower than BESS measurements [85] below $\sim 10\,\text{GeV}$ and higher above $\sim 80\,\text{GeV}$, where the limited inner Tracker resolution leads to a systematic overestimation of the particle flux. The results are in good agreement based on the statistical uncertainties. The reconstructed muon charge ratio provides values of $R = N_{\mu_+}/N_{\mu_-} \approx 1.28$ compatible with BESS results and the world average [86]. The comparison between the datasets is generally influenced by many detector-independent systematic effects like e.g. solar variation, amount of material in front of the

p [GeV]	$\Phi \times p^{2.7}$ $[\mathrm{GeV}^{1.7}(\mathrm{sm}^2\mathrm{sr})^{-1}]$	$\sigma^{-}_{\Phi,stat}$	$\sigma^{+}_{\Phi,stat}$	N_{μ^+}	N_{μ^-}	$R = \frac{N_{\mu^+}}{N_{\mu^-}}$	σ_R
3.06 - 3.47	176.69	7.17	7.33	192220	148755	1.292	0.004
3.47 - 3.94	210.26	8.62	8.81	184250	142426	1.294	0.005
3.94 - 4.48	247.34	10.11	10.33	174325	135590	1.286	0.005
4.48 - 5.08	283.69	11.62	11.87	163243	126204	1.293	0.005
5.08 - 5.77	324.62	13.35	13.65	148994	116505	1.279	0.005
5.77 - 6.54	369.14	15.38	15.73	136839	105972	1.291	0.005
6.54 - 7.43	408.52	16.79	17.16	123574	95554	1.293	0.006
7.43 - 8.43	450.92	18.47	18.87	110497	84647	1.305	0.006
8.43 - 9.57	492.87	20.36	20.81	96904	74835	1.295	0.006
9.57 - 10.86	533.76	21.98	22.46	85467	65673	1.301	0.007
10.86 - 12.33	586.46	24.34	24.88	74371	57226	1.300	0.007
12.33 - 13.99	612.09	25.09	25.63	63672	49165	1.295	0.008
13.99 - 15.88	648.81	26.77	27.35	54117	41806	1.294	0.008
15.88 - 18.02	685.35	28.23	28.84	46134	35758	1.290	0.009
18.02 - 20.46	714.57	29.74	30.40	38603	30092	1.283	0.010
20.46 - 23.22	735.00	30.40	31.06	32257	25299	1.275	0.011
23.22 - 26.36	752.86	31.04	31.72	26673	20720	1.287	0.012
26.36 - 29.91	771.96	31.97	32.66	22231	17114	1.299	0.013
29.91 - 33.95	773.76	32.19	32.90	17647	14201	1.243	0.014
33.95 - 38.54	785.33	32.24	32.94	14569	11516	1.265	0.016
38.54 - 43.74	782.03	32.46	33.17	11633	9160	1.270	0.018
43.74 - 49.64	787.14	32.52	33.22	9486	7452	1.273	0.020
49.64 - 56.35	779.91	32.56	33.29	7355	5926	1.241	0.022
56.35 - 63.95	773.05	32.21	32.93	5957	4811	1.238	0.024
63.95 - 72.59	750.43	31.30	31.99	4643	3804	1.221	0.027
72.59 - 82.39	735.94	30.57	31.23	3669	3017	1.216	0.030
82.39 - 93.51	730.43	30.81	31.49	2903	2418	1.201	0.033
93.51 - 106.14	696.02	29.26	29.91	2171	1904	1.140	0.036

Table 4.4: The flux and charge ratio of atmospheric muons at sea level as obtained in this work

Observation	Location	Coordinates	Date	Rigidity Cutoff	ϕ_0
BESS TeV-2002	Lake Tsukuba	36.2 N, 140.1 W	Oct 2002	11.4 GV	800 MV
this work	KSC SSPF	28.5 N, 80.6 W	Nov 2010	2.2 GV	400 MV

Table 4.5: Observational parameters of BESS-TeV 2002 [85] and this work. Solar modulation parameters ϕ_0 taken from [87].

experiment (ceiling, atmospheric depth) and geomagnetic rigidity cutoff. The relevant differences in observational parameters are listed in table 4.5. The increased charge ratio at low rigidities is known to arise due to different geomagnetic rigidity cutoff values [88]. With rising particle momentum the observed shape reveals a slight decrease. This decrease might be generated by the momentum resolution which leads to an uncertainty in the reconstructed muon momentum of about 50 % at 100 GV and a corresponding charge sign confusion probability of about 2 %.

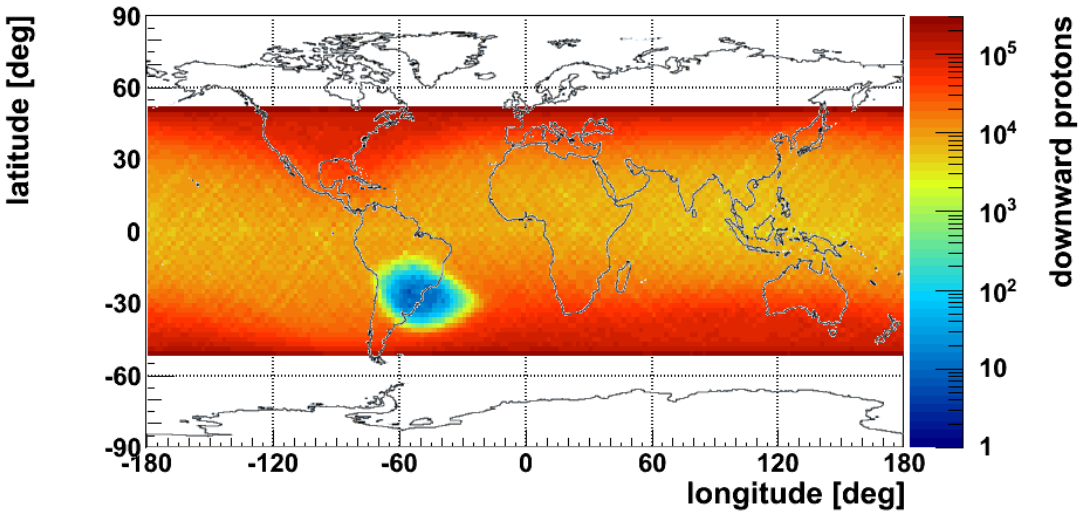

Figure 4.15: Number of identified proton events passing the detector volume downwards.

4.2.3 Geomagnetic Cutoff

To reconstruct the geomagnetic cutoff rigidity (see section 1.3.3) the number of particle events as function of geomagnetic position and reconstructed rigidity is determined. In figure 4.15 the number of proton events passing the detector from top to bottom is shown as function of orbital position, given in geodetic latitude and longitude. One can clearly see different regions of proton rates. The observed proton rate depends on the rigidity cutoff and the power-law spectral index. At the South Atlantic Anomaly the trigger and reconstruction efficiency for protons is reduced due to electronics deadtime and multi-particle events. The number of downward going protons as function of latitude and reconstructed rigidity is shown in figure 4.16. In the polar regions at latitude $\gtrsim 50^\circ$ the most frequently reconstructed rigidity is $\sim 2\,\mathrm{GeV}$. By approaching the equatorial region this maximum in the rigidity distribution is shifted to higher values up to $\sim 18\,\mathrm{GeV}$ at the equator. A second distribution of low-energetic particles becomes observable. These low-energetic particles, below the geomagnetic cutoff rigidity, are understood as particles trapped in the geomagnetic field.

The suppression of low-rigidity particles by the geomagnetic cutoff is modeled here by

$$f(R) = AR^{-\gamma}\frac{1}{1+(R/R_{reco})^{-\alpha}} \ , \tag{4.2.1}$$

with particle rigidity R, normalization factor A, spectral index γ, rigidity cutoff R_{reco} and parameter α describing the steepness of the transition similar to Fermi functions. This approximation is applied to the observed rigidity spectrum in each observed interval of latitude and longitude. In figure 4.17 the reconstructed geomagnetic cutoff map is shown and compared to expected values R_U obtained from simulations (see section 1.3.3). The reconstructed cutoff map matches the expected shape with an uncertainty of $\lesssim 10\,\%$. Fig-

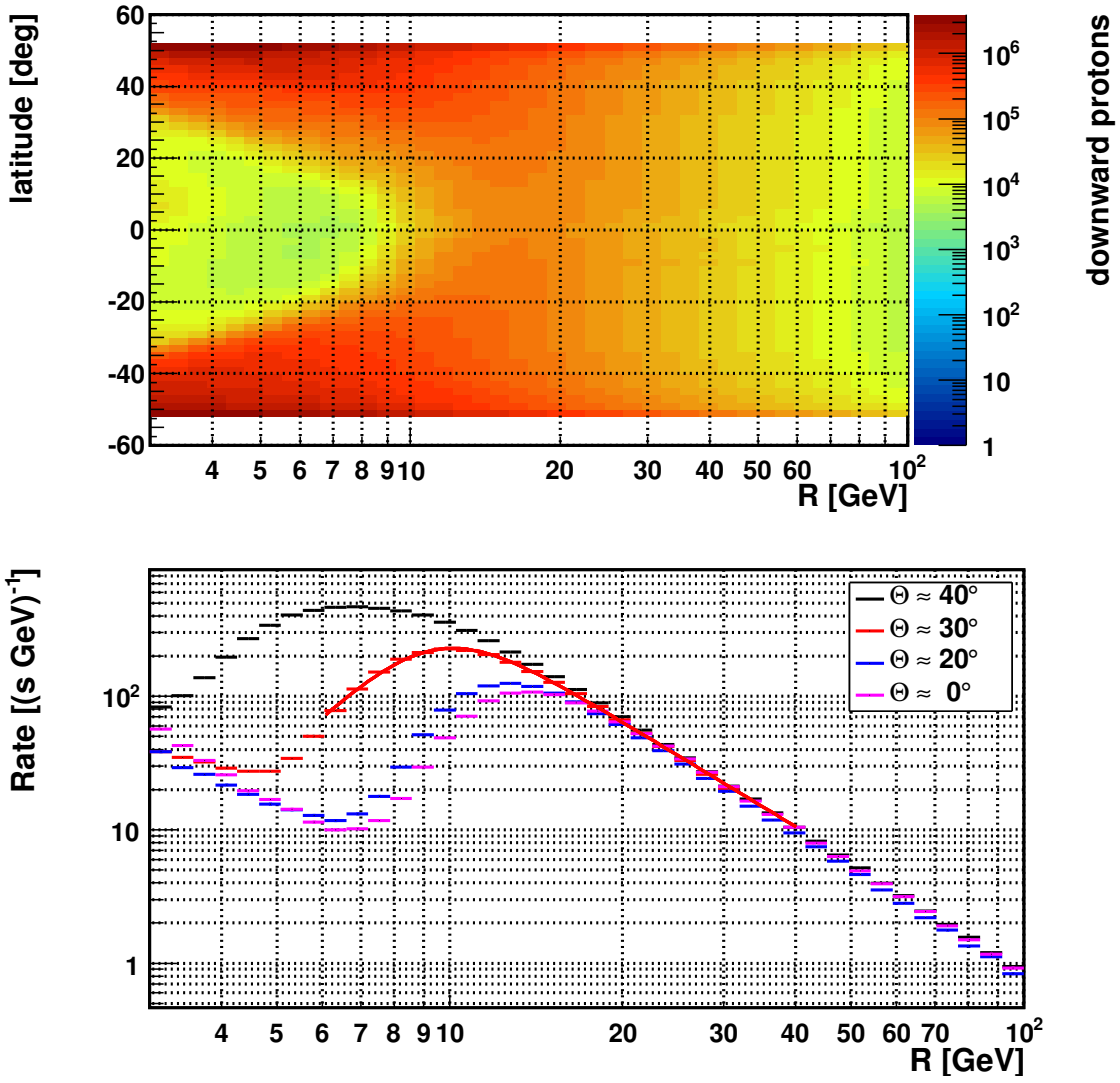

Figure 4.16: The number downward going proton events as function reconstructed rigidity (top). The reconstructed rigidity distribution in different latitude intervals is approximated by an analytical function to determine the position geomagnetic cutoff rigidity (bottom).

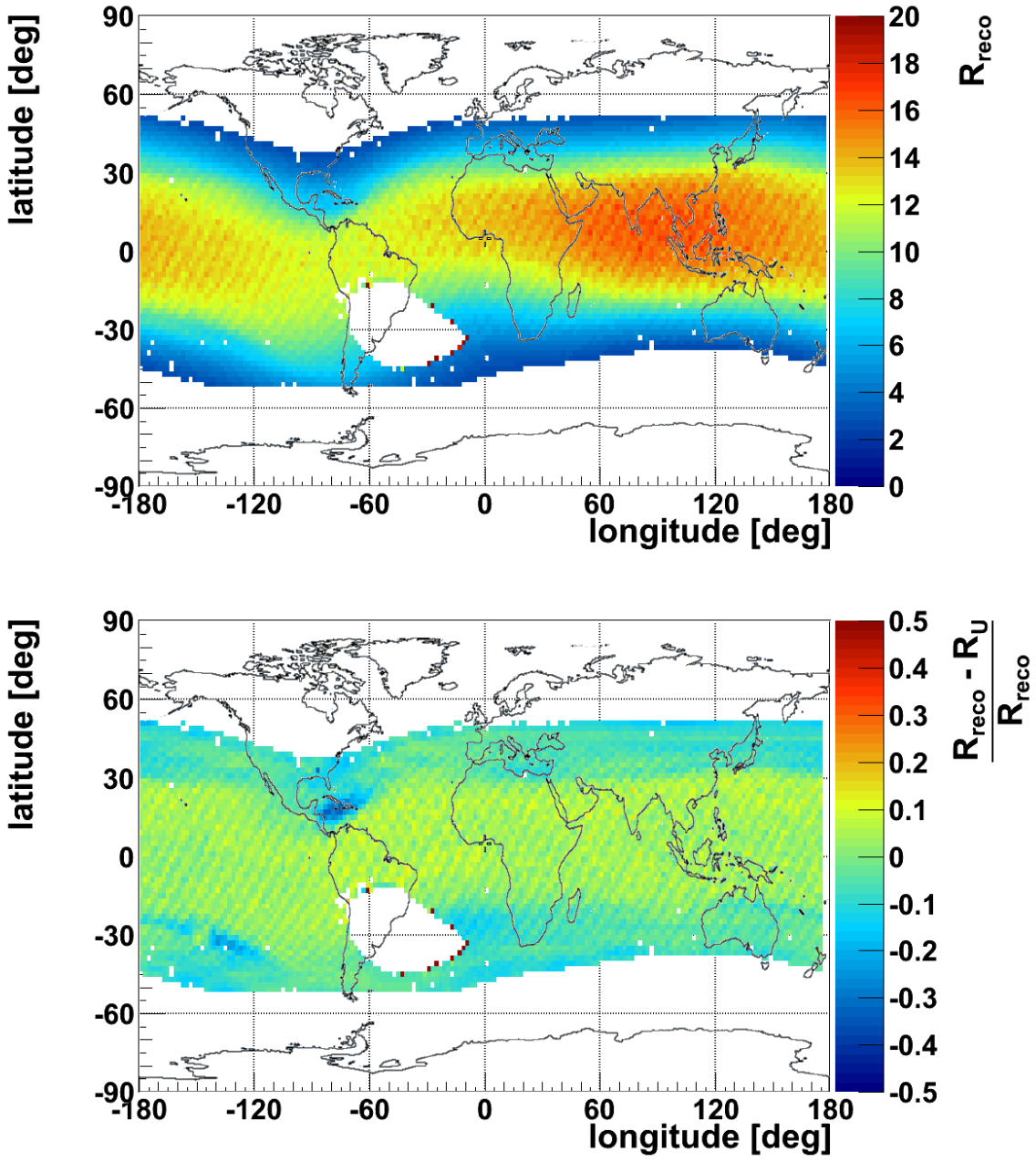

Figure 4.17: The reconstructed rigidity cutoff R_{reco} (top) and its comparison $(R_{reco} - R_U)/R_U$ to expectation R_U generated by simulations based on IGRF as function of orbit (bottom).

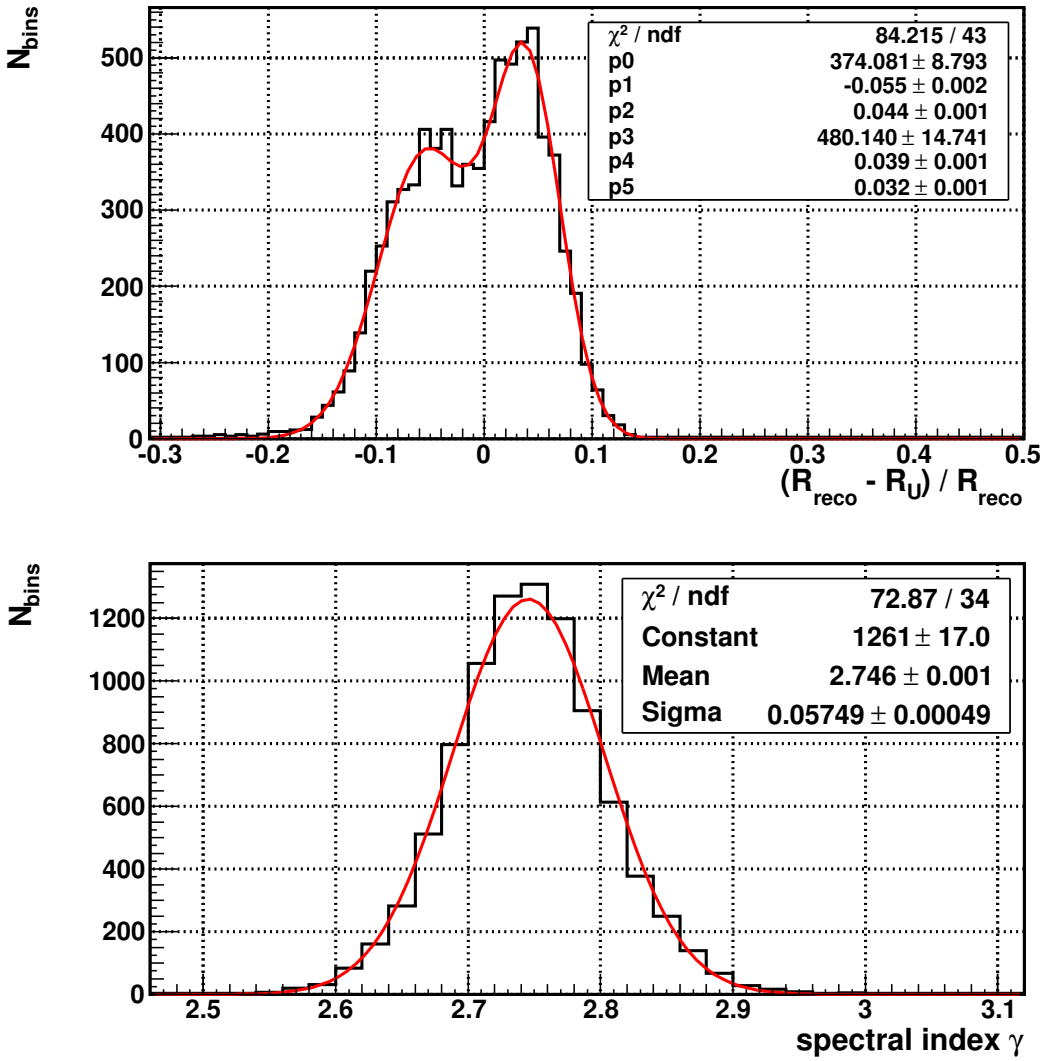

Figure 4.18: The distribution of relative deviations $(R_{reco} - R_U)/R_U$ between fitted R_{reco} and expected R_U cutoff rigidities(top) and the distribution of determined spectral indices γ determined in each longitude and latitude interval (bottom).

ure 4.18 shows the distributions of relative deviations $(R_{reco} - R_U)/R_U$ and spectral indices determined in each longitude and latitude interval. It becomes evident that there are two populations in the distribution of relative deviations: one population with positive deviation peaked at $\sim$ 3.9 % and second one with lower negative deviation $\sim$ 5.5 %. The first can be associated to the equatorial region and the latter is rather located in the polar region. The differences between measured and expected rigidity cutoff are expected to be generated by the event selection. While simulations were performed for vertical incidence the data analysis was performed on the quasi-isotropic cosmic data. As higher inclined particles are in average deflected stronger in the geomagnetic field, isotropic data is expected to return higher cutoff values. Particles detected in the equatorial region have to pass a higher magnet field intensity and therefore inclined tracks show a larger deflection. Regions of low

R_{reco}, especially above the Caribbean, are related to large penumbra widths (see figures 1.8 and 1.9), where the comparison to R_U leads to systematically underestimated cutoff values.

The obtained spectral index of $2.746 \pm 0.001(fit)$ barely matches the results obtained by AMS01 $\gamma = 2.79 \pm 0.012(\text{fit}) \pm 0.019(\text{sys})$ [89] and PAMELA $\gamma = 2.801 \pm 0.007 \pm 0.002$ $(20 - 80\,\text{GV})$ [90]. As the spectral index of cosmic rays should not depend on the orbital position it is assumed that the fit function introduces correlations between its parameters. Therefore the width of the distribution of spectral indices $\sigma = 0.057$ might reflect the systematic uncertainty introduced by the approximation. Including this basic estimation of systematic uncertainty the results become compatible.

4.3 TRD Event Reconstruction

For the event reconstruction a track finding algorithm is needed to assign the recorded TRD hits (see chapter 3) to individual particles passing the detector and to separate hits generated by particles from noise. Such an algorithm, constructed from conceptual ideas of Dr. Siedenburg and implemented into the AMS software framework, is presented in the following and evaluated on simulated and measured events.

Four data samples with corresponding software versions are selected for comparison: muon data (B512), muon simulation (B524), proton data (B550) and proton simulation (B550). For the evaluation of TRD efficiencies the inner tracker and the ECAL are used to preselect events (see section 4.2.1). Systematic effects on the preselection efficiency and purity which might be introduced by the different software versions are not investigated here. All distributions and efficiencies shown in this section as function of momentum P or incident angle Θ contain an additional selection $\Theta < 20^\circ$ or $P > 10\,\mathrm{GeV}$ respectively.

The geometric efficiency of the TRD for tracks extrapolated from the inner tracker to the TRD volume is investigated in section 4.3.1. The track reconstruction algorithm is presented and evaluated in section 4.3.2. The quality selection of reconstructed TRD tracks, discussed in section 4.3.3, is followed by the efficiency of the matching of selected TRD tracks to tracker extrapolations 4.3.4.

4.3.1 Geometric efficiency

The TRD event reconstruction is based on recorded hits in the TRD. The maximum number of reconstructed hits generated by a particle depends on the number of tubes its trajectory crosses. If a particle is not fully passing the detector volume from top to bottom the number of TRD layers containing hits is reduced. To evaluate the geometric efficiency preselected tracks from the inner Tracker tracks passing the ECAL volume are extrapolated from the inner Tracker to the TRD. The fraction of tracks passing the TRD volume as function of incident angle is shown in figure 4.19. For nearly-vertical tracks all particle trajectories allowed by the selection on inner Tracker and ECAL pass the ECAL volume. At an incident angle of $22 - 28^\circ$ the fraction of extrapolated tracks passing the TRD is decreasing due to the limited coverage of solid angle. This effect depends on the particle rigidity and is shown here for particle rigidities $R \gtrsim 10\,\mathrm{GV}$. For lower values the efficiency is decreased due to the magnetic bending.

Even if a particle is passing the detector volume it might pass in between the straw tubes and therefore not produce a hit. The geometric efficiency of a TRD module can be estimated as shown in figure 4.20. By the subtraction of the given inner tube diameter from the effective area for incident angle Θ the geometric efficiency of the inter-tube gap can be

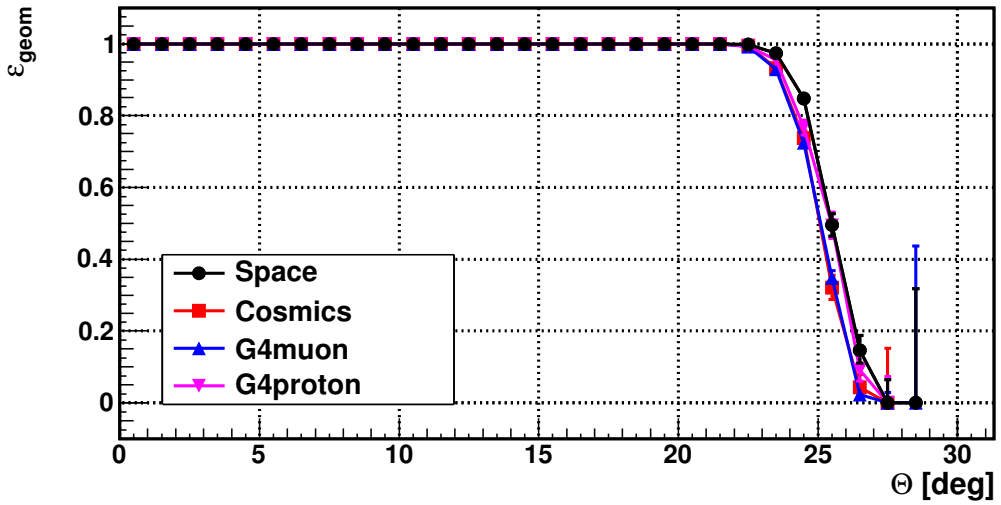

Figure 4.19: TRD geometric efficiency determined by fraction of extrapolated tracks from the Tracker which pass the TRD volume as function of reconstructed incident angle Θ.

estimated. For the 16 tubes of a module there are 9 gaps between two adjacent tubes and 6 gaps where additional stringers support the module (see section 2.1). The total efficiency of a module for 1 mm path length inside the tube is $\sim 94\,\%$ at $\Theta = 0$. Here, the path length is given in the plane of the module cross section. Three-dimensional path lengths increase the maximum allowed radial distance and therefore the efficiency is increased towards the 0 mm limit. The efficiency of a TRD layer is given by the geometric efficiency of the modules and the inefficiency introduced by the bulkheads in the yz projection.

The total number of hits in the TRD for different data samples is shown in figure 4.21. For space data the number of hits as function of momentum is decreasing with increasing particle momentum. Events in the low momentum region are recorded in regions of low geomagnetic rigidity cutoff, where the number of multi-particle events is increased and therefore the total number of hits is increased. For atmospheric muon data the number of hits is increasing with the particle momentum. This is expected to occur due to the angular distribution of particle momenta. With rising inclination the fraction of low momentum muons is decreased as they are absorbed in the atmosphere. The number of TRD raw hits is lower in simulation because just single particle events are simulated and no noise is generated.

The noise rate is investigated by isolated hits in the TRD. Here, isolated hits are characterized by the absence of hits within $dz < 4\,\text{cm}$ and $dr < 2\,\text{cm}$. This corresponds to no hits within the adjacent three tubes and one layer above and below. The distribution of isolated hits is shown in figure 4.22. The probability to have an isolated hit in a TRD channel is in average 8×10^{-4} per triggered event. However, a clear structure of tubes with up to factor ten higher rates is observable. These additional noise hits are assumed to be generated by

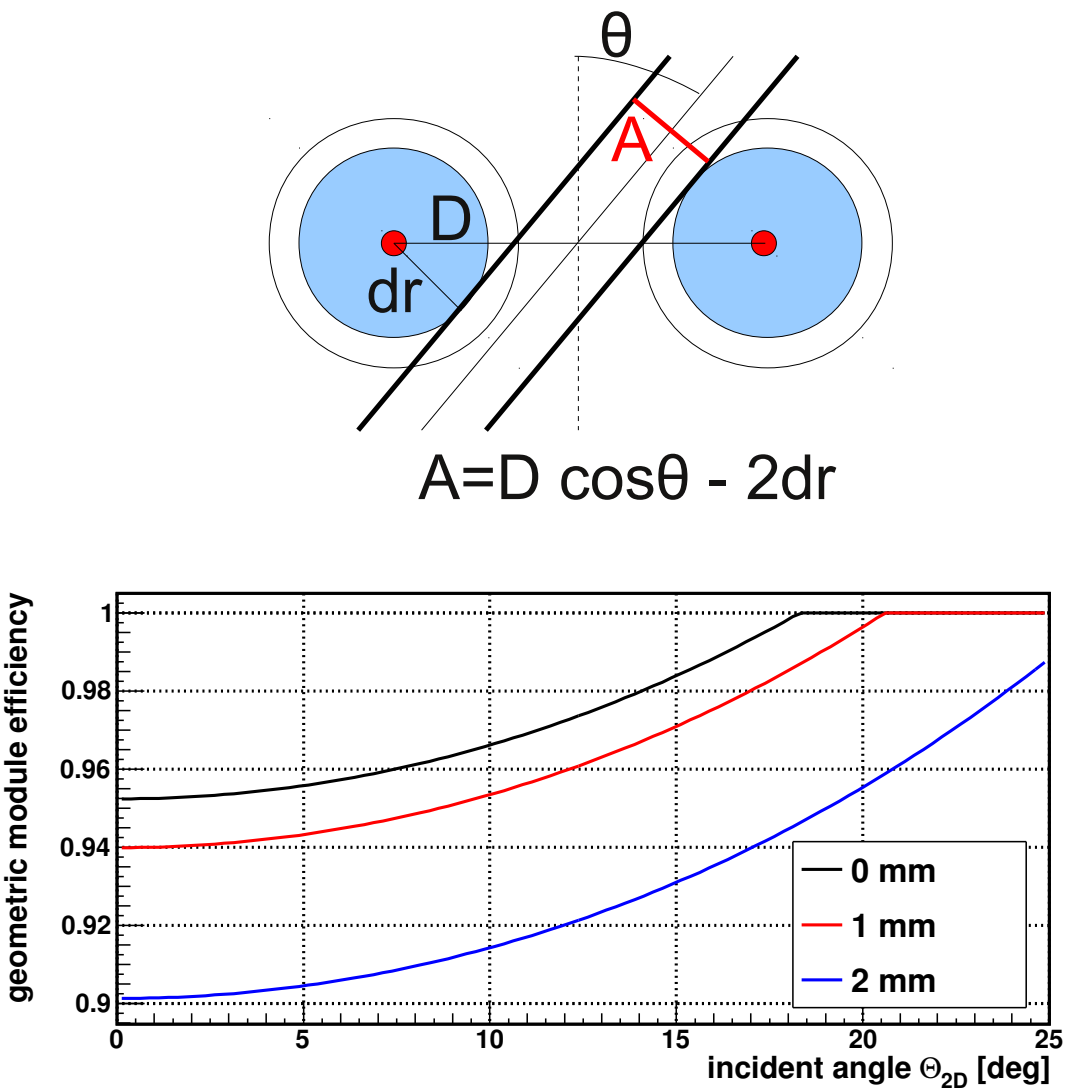

Figure 4.20: Calculated geometric efficiency of a TRD module. *Top:* effective gap A between two tubes as function of Θ and maximum allowed radial distance dr. Bottom: geometric efficiency of a module of 16 tubes given as function of Θ for three different minimum path lengths.

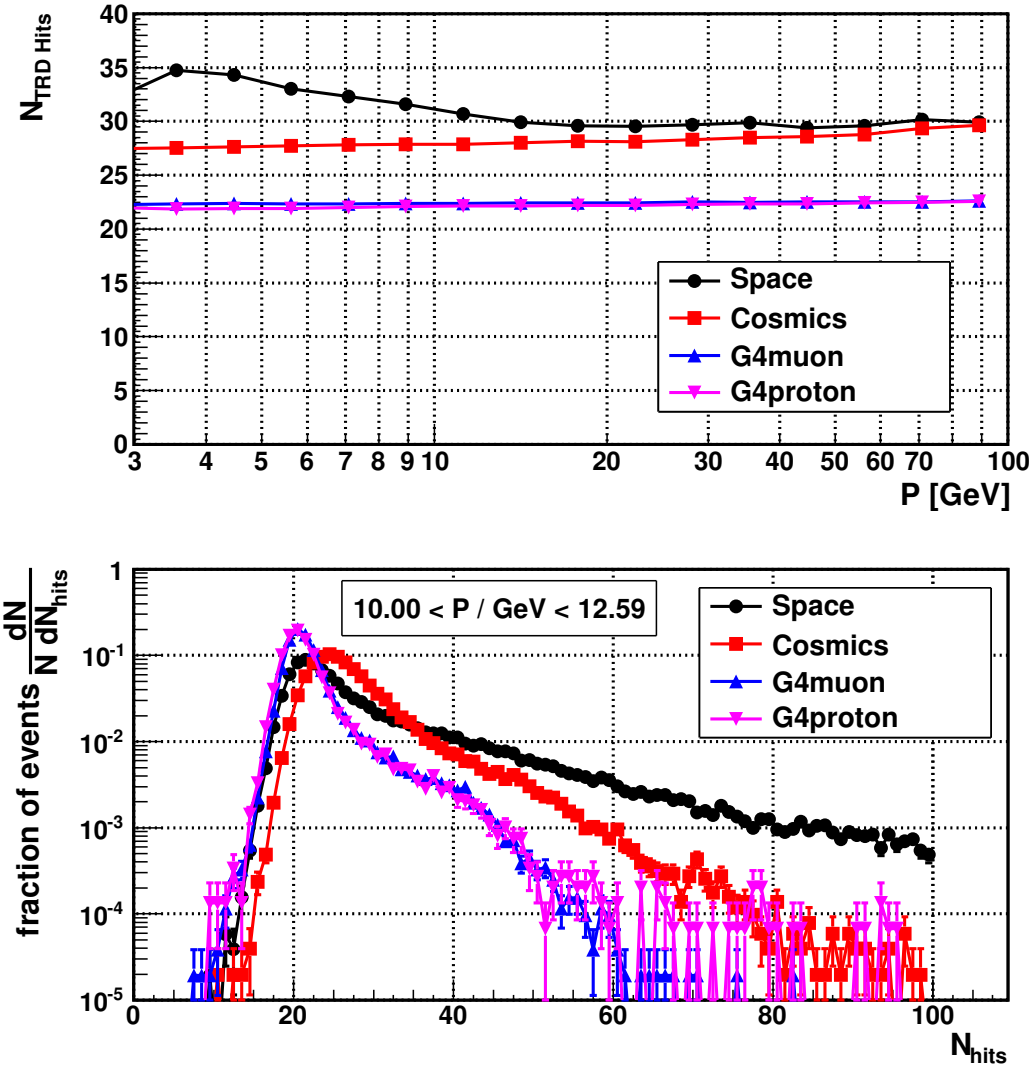

Figure 4.21: Number of hits in the TRD for preselected events passing the TRD volume as function of particle momentum (top) and the corresponding distribution in the momentum interval $10.00 < P/\text{GeV} < 12.59$ (bottom).

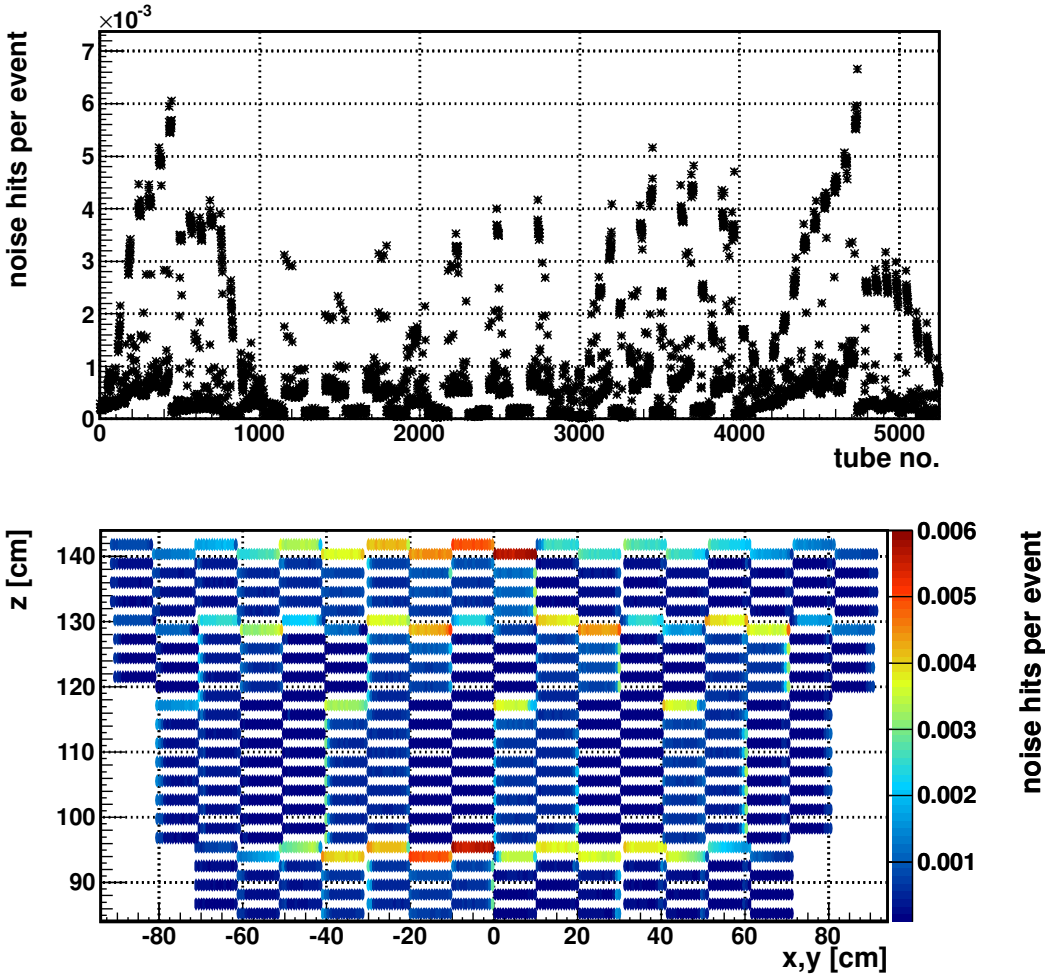

Figure 4.22: TRD noise rate in space expressed in terms of probability for each tube to have an isolated noise hit per triggered event (top). The geometric position of the tubes with higher noise level (bottom).

electronics cross-talk at the readout of TRD dallas sensor strips (see section 4.4.4). This interpretation is supported by the localization of the high rate tubes in specific TRD layers, where dallas sensor strips are located.

The pulse height spectra of isolated hits is shown in figure 4.23. The spectrum of high rate hits, defined by rate $r > 3\langle r \rangle$, is peaked at $\sim 100\,\mathrm{GeV}$, while the remaining distribution matches the expected decrease of pedestals tails. The cut on pedestal width has been modified in space to suppress noise hits (see section 3.3). Noise hits in general distort the reconstruction of particle tracks and in particular high signal noise hits hinder the TRD particle identification performed in section (4.5).

The number of TRD layers N_{layer} containing a hit on the track extrapolated from the inner Tracker is shown in figure 4.24. There is a significant difference observed of about one hit less in data than in simulations. Two effects are identified as possible reasons. On the one hand the relative alignment of the TRD with respect to the inner tracker is not considered in this analysis but is known to differ from the nominal alignment used in simulations. On the other hand the reconstruction of tracks in the inner tracker has a systematic uncertainty introduced by the multiplicity of tracker hits in the topmost inner layer. This leads to an absolute offset between the extrapolated track and the hits in the TRD.

The single layer efficiency to find a TRD hit on the track extrapolation from inner Tracker into the TRD as function of momentum is shown in figure 4.25 for space data and in figure 4.26 for atmospheric muon data. With decreasing particle momentum the impact of multiple scattering is increased and hence less TRD layers with hits are found on the extrapolation. This effect, depending on particle β at given momentum, is different for protons and muons and reproduced well by simulations. The additional effect introduced by the tracker hit multiplicity or a misalignment in x is observable here as a significantly lower efficiency in the central 12 TRD layers in comparison to simulated proton events.

Digitization, which is basically a cut depending on pedestal position and width, also has an impact on $\langle N_{layer} \rangle$. The dependency of $\langle N_{layer}^{3\,\mathrm{cm}} \rangle$ on detector parameters is shown in figure 4.27. Here, the systematic effects discussed above are suppressed by loosening the definition of hits on track from $dr < 3\,\mathrm{mm}$ to $dr < 3\,\mathrm{cm}$. In general, a higher gas gain leads to a higher digitization efficiency. Hence, $\langle N_{layer}^{3\,\mathrm{cm}} \rangle$ is proportional to the applied high voltage and inverse proportional to the partial CO_2 pressure. The optimal set of detector parameters to operate the TRD has not been determined yet. Higher gas gains reduce the loss of hits due to digitization but lowers the maximum detectable pulse height due to the limited effective ADC range of 3600 ADC. The z^2 dependency of the ionization energy deposition leads to an upper limit on the highest identifiable ion to approximately carbon, dependent on the pulse height $dE_{MIP} \approx 60$ ADC of minimum ionizing charge one particles. The separation of protons and electrons depends on the distinction of ionization and transition energy con-

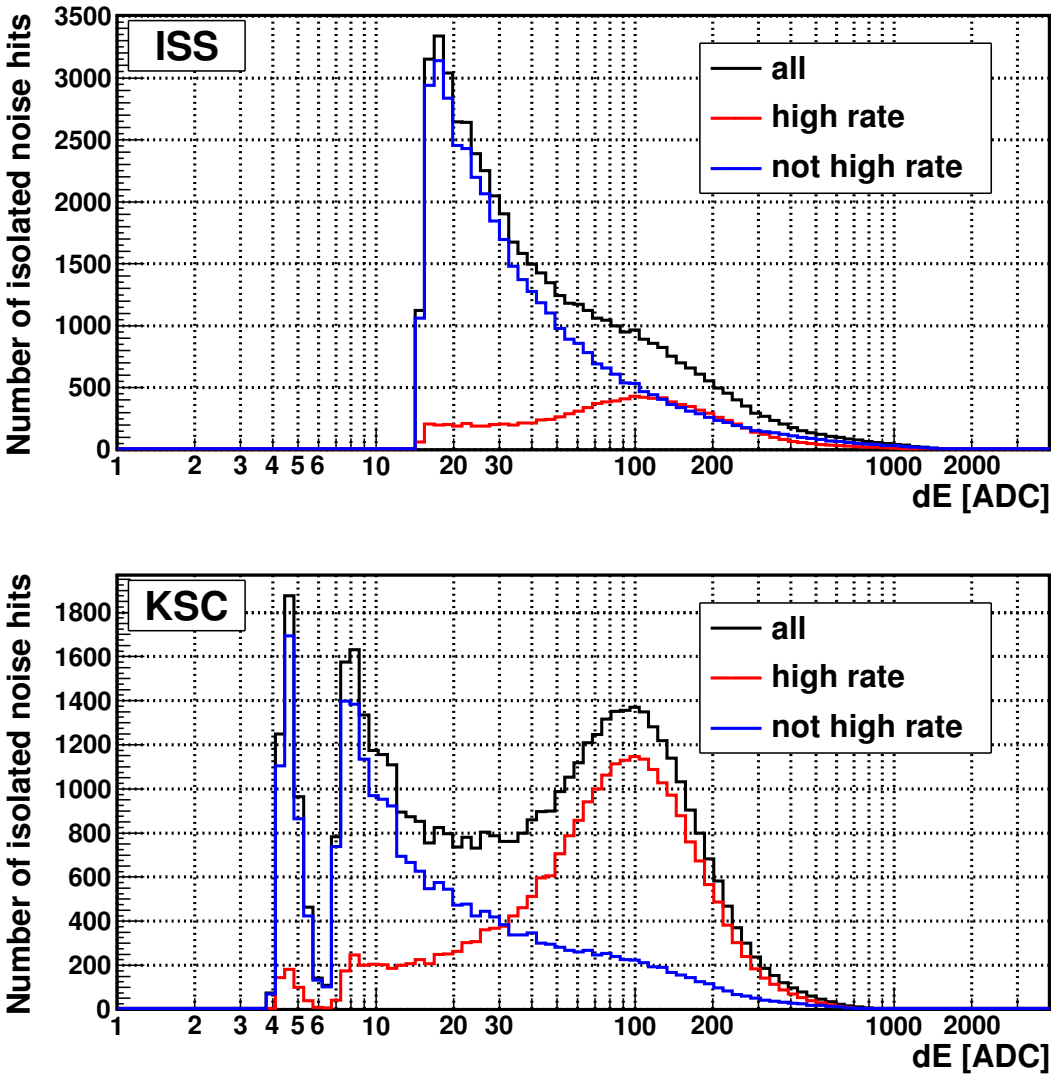

Figure 4.23: Pulse height spectra of noise hits. The spectra of high rate noise hits (red) is characterized by high pulse heights of about 100 ADC. The spectrum of remaining noise hits (blue) matches the expectation of gaussian pedestal tails. Different digitization algorithms are implemented for ISS (top) and KSC (bottom) sample, leading to different lower limits of the spectra.

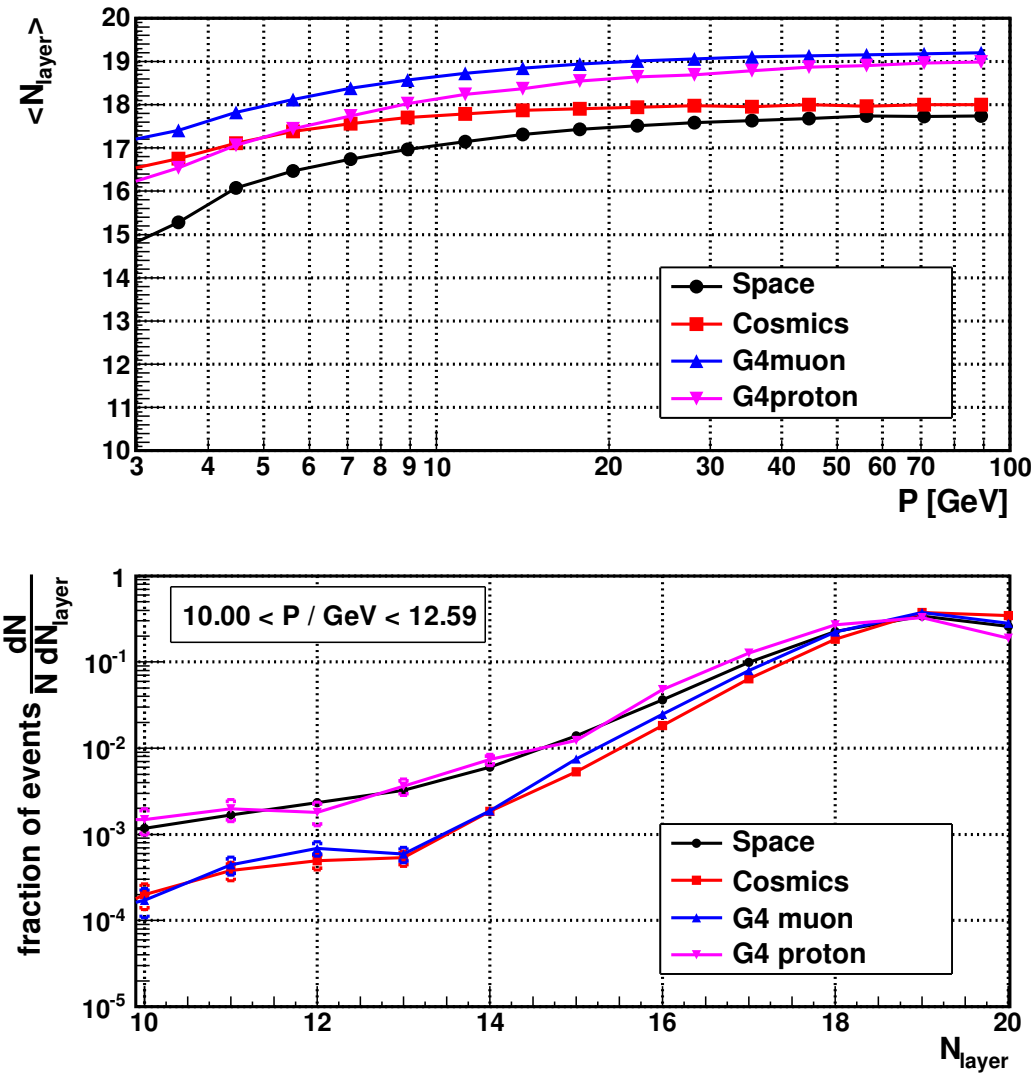

Figure 4.24: Number of TRD layers containing a hit on the track extrapolated from the inner Tracker. *Top:* the mean number of TRD layers containing at least one hit on a preselected track from the Tracker extrapolated into the TRD volume as function of particle momentum. *Bottom:* the distribution of corresponding number of layers in the momentum interval $10 < \mathrm{P} / \mathrm{GeV} \lesssim 12.59$.

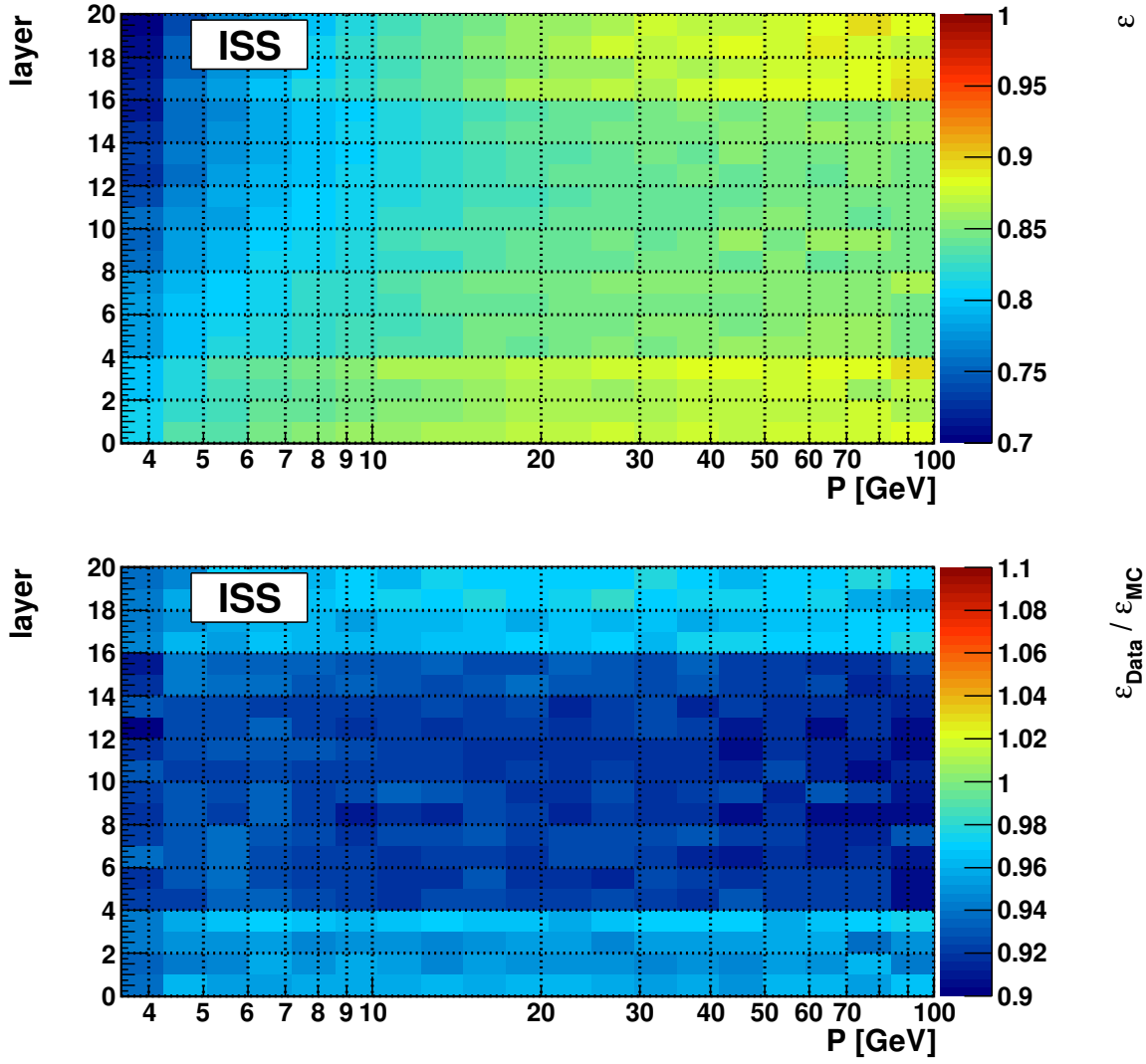

Figure 4.25: Efficiency ε to find a hit in a TRD layer on a track extrapolated from inner Tracker as function of momentum for space data (top) and in comparison $\frac{\varepsilon_{Data}}{\varepsilon_{MC}}$ to simulations (bottom).

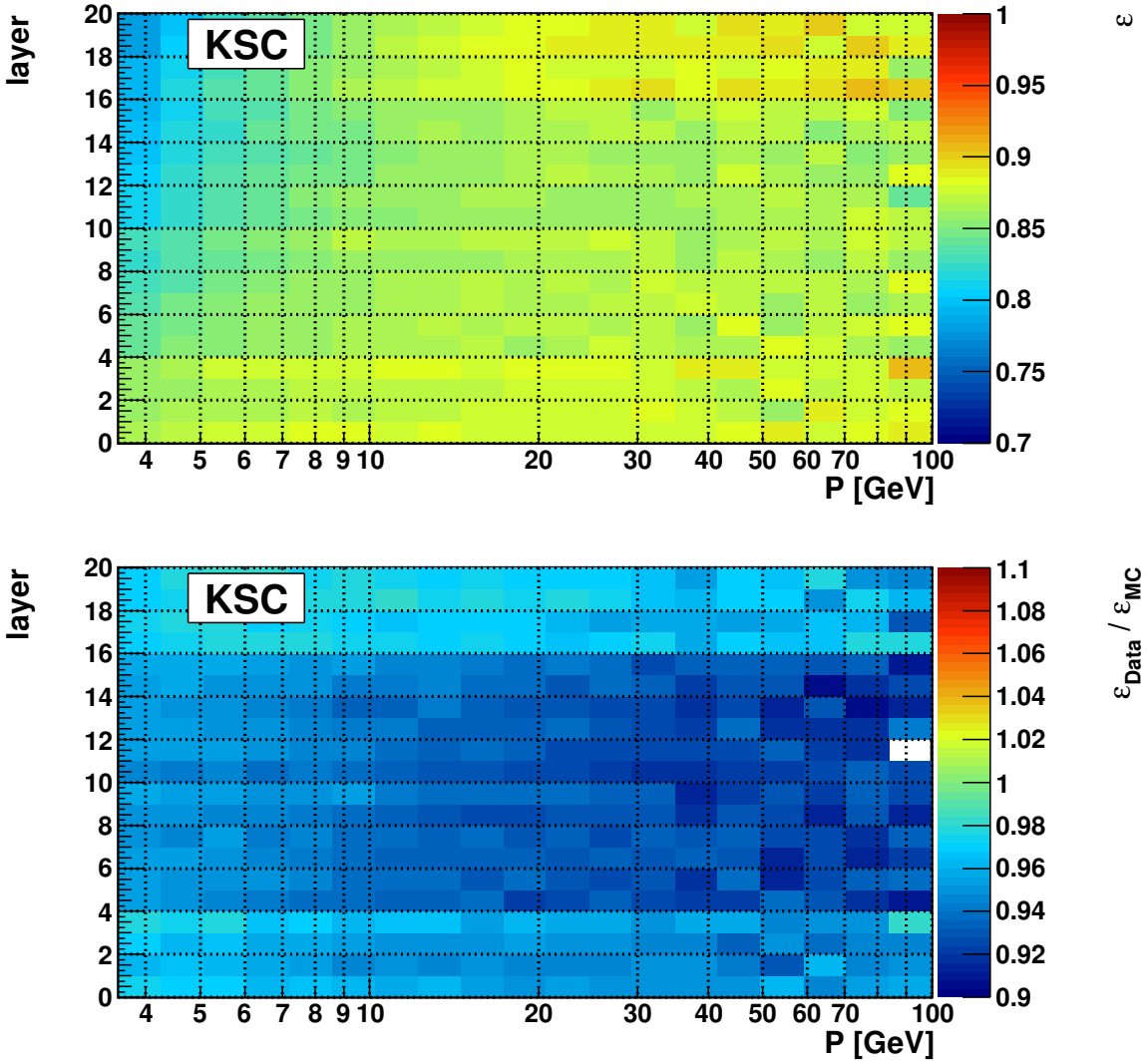

Figure 4.26: Efficiency ε to find a hit in a TRD layer on a track extrapolated from inner Tracker as function of momentum for atmospheric muon data (top) and in comparison $\frac{\varepsilon_{Data}}{\varepsilon_{MC}}$ to simulations (bottom).

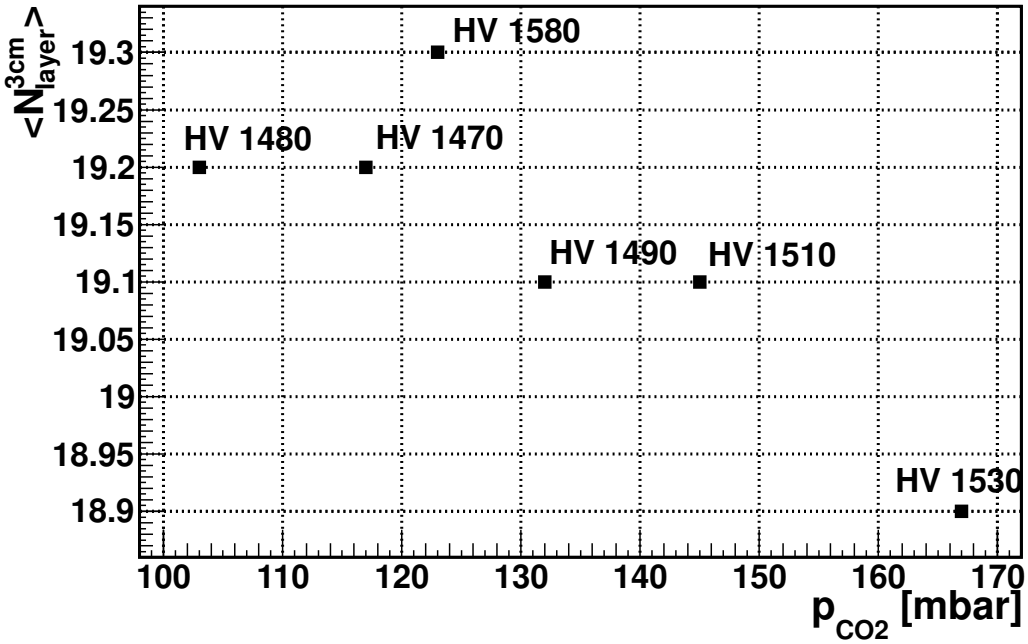

Figure 4.27: Number of TRD layers containing hits with residuals $dr < 3\,\text{cm}$ towards the extrapolated track from inner Tracker as function of detector parameters. An increased gas gain, proportional to the applied high voltage and inverse proportional to the partial density of CO_2, leads to an increased digitization efficiency and therefore to more layers with hits in the TRD.

tributions to the pulse height spectrum. Ionization mainly depends on the total density and transition radiation on the partial density of Xe (see section 3). This leads to another trade-off between the partial densities of Xe and CO_2 and the total density. The evaluation of this multi-dimensional parameter space is not performed in the scope of this thesis. The parameter space is currently scanned carefully in regular detector operations.

4.3.2 Track Reconstruction

The TRD track finding algorithm is based on hits in electronics channels, which are related to corresponding straw tubes at given geometrical coordinates. As the tubes can be considered one-dimensional in this context just two of the spatial coordinates can be determined. The reconstruction is performed first in the two independent projections xz and yz of the AMS coordinate system, leading to two-dimensional tracks called segments, and are combined afterwards to three dimensional tracks.

Segments Each hit in one projection (xz or yz) of the TRD is characterized by coordinates (r, z) with $r = x, y$. In the pre-fit algorithm each pair of hits is considered a line. The slope $s = \frac{dr}{dz}$ and offset r in the center plane of the TRD ($z = 113.5\,\text{cm}$) is determined for each line and filled into a two dimensional histogram (see figure 4.28). As the magnetic field in the TRD is treated as negligible the trajectories are expected to be straight and hence all hits on a track should be on a straight line. Consequently such a trajectory is represented in the histogram as an accumulation of hit pairs with identical slope and offsets in a maximum. An algorithm has been developed to browse the histogram bins and localize maxima boxes of 3×3 bins. To get the parameters (s, o) of such a segment candidate the weighted mean of the 3×3 box is calculated, based on the number of bin entries n times the maximum span $dz = z_{max} - z_{min}$ of hit pairs in the bin: $w = n \times dz$. If the total weight inside the box is large enough $\sum_{i=1}^{9} w_i > 15$ and $dz > 8\,\text{cm}$ the segment candidate passed the pre-fit algorithm and is further processed. The minimum requirement to fulfill this criterion is given by three hits within three consecutive layers, leading to $w = \frac{n\times(n-1)}{2} dz \approx 3 \times 9\,\text{cm} = 27\,\text{cm}$.

Hits are associated to the segments according to an extrapolation into the hit plane and a residual cut:

$$r_{exp} = r_s + m_s \times (z_h - z_s) = r_s + m_s \times |dz| \tag{4.3.1}$$

$$|dr| = |r_h - r_{exp}| < d_{tube} + |dz| \times e_s \ , \tag{4.3.2}$$

with hit coordinates r_h, z_h, segment parameters r_s, m_s, z_s, tube diameter $d_{tube} = 6\,\text{mm}$ and an uncertainty on the segment extrapolation based on the span of the segment $e_s = d_{tube}/dz_s$. The corresponding hits are collected for each candidate and an iterative linear regression process is started. In each step the segment parameters and their uncertainties are determined by linear regression and the hit selection above is repeated. After the first iteration e_s is defined by the linear regression uncertainties. If there is no change in the number of associated hits or a maximum number of allowed iterations is reached the iterative process is stopped and the segment is stored for the three-dimensional tracking algorithm.

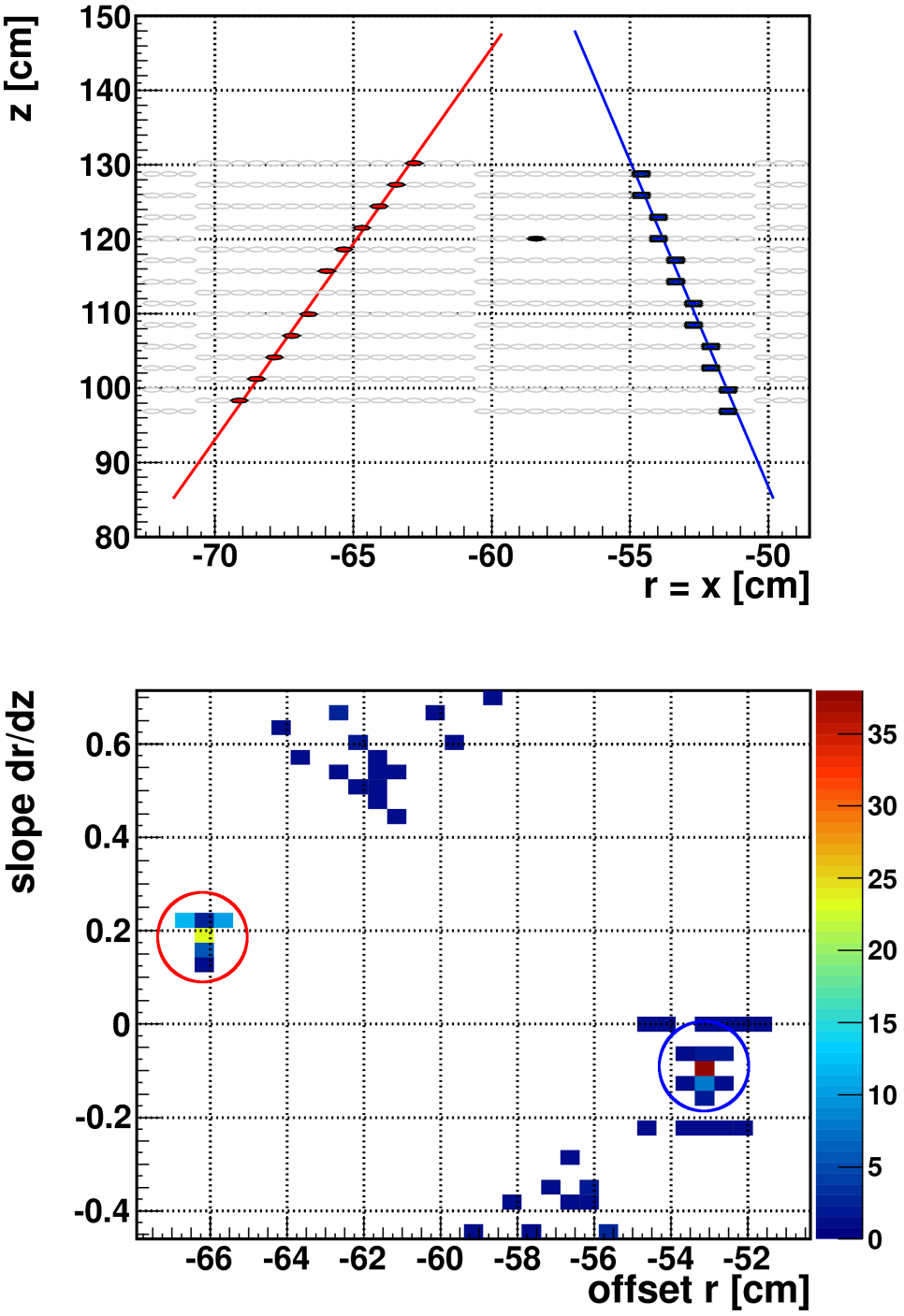

Figure 4.28: The pre-fit algorithm illustrated on an example double-track event. Hits in the xz projection of the TRD are located on straight tracks (top). Hits matching a segment are assigned graphically by colors (red/blue). Unassociated hits, in general isolated noise hits, remain black in this illustration. A histogram filled with the slope and offset of lines defined by each hit pair (bottom) provides two distinct peaks which define a segment (2D track) candidate.

Tracks The combination of the two-dimensional segments to tracks is a non-trivial process. Although in case of one segment in each projection the combination is bijective, in case of more segments the topology gets complicated. The basic idea of the association of segments is to allow all possible combinations of segments, to rule out as many combinations as possible and if just one combination of segments remains to store the corresponding tracks. This way the efficiency of tracks may be lower than for segments but the association of uncorrelated segments is suppressed.

There are two methods implemented to exclude segment combinations. The first approach, based on the TRD geometry, is to consider the combination of two segments as a track and extrapolate it to the z coordinate of each of its hits. By doing so the hit can now be allocated in three dimensions. If the additional hit coordinate along the corresponding straw tube would be located outside the TRD volume the combination of segments is ruled out. The second method relies on hits in the two upper TOF layers. As the scintillator panels are highly efficient, a track candidate passing them has to have a corresponding hit. The combination of two segments is ruled out if no matching hit is found in its extrapolation to the upper TOF layers.

In case just one combination of segments remains, the corresponding tracks are stored. Here, multi-track events might be contained if the association of the segments is bijective. Otherwise no tracks are generated. At a higher level of reconstruction subdetector tracks are matched to each other to identify particles passing all detectors. Ambiguous events, which could not be resolved by the methods above, may be recovered here. If an extrapolated Tracker track has no matching TRD track but two matching TRD segments, one per projection, they are combined to a track.

4.3.3 Quality Selection

The quality selection of TRD events, is depicted step-by-step in the following. Unless mentioned explicitly the efficiency in each consecutive step is given relative to the sample defined by the preceding selections, i.e. the efficiencies factorize.

A selection based on the sum of pulse heights on track per layer E_l is performed for each track. The TRD is divided into three sections according to the tube orientation in the AMS coordinate system along x/y/x in layers 1-4/5-16/17-20. In each of the four layers on top and on bottom at least 2 out of 4 and in the center layers at least 8 out of 12 layers with $E_l > 10$ ADC are required for quality selected tracks.

The fraction of preselected events passing the TRD geometry with at least one selected TRD track is shown in figure 4.29 For muon data and simulation the efficiency of this selection is $\sim 96\,\%$ independent of particle momentum. For simulated proton events the efficiency is

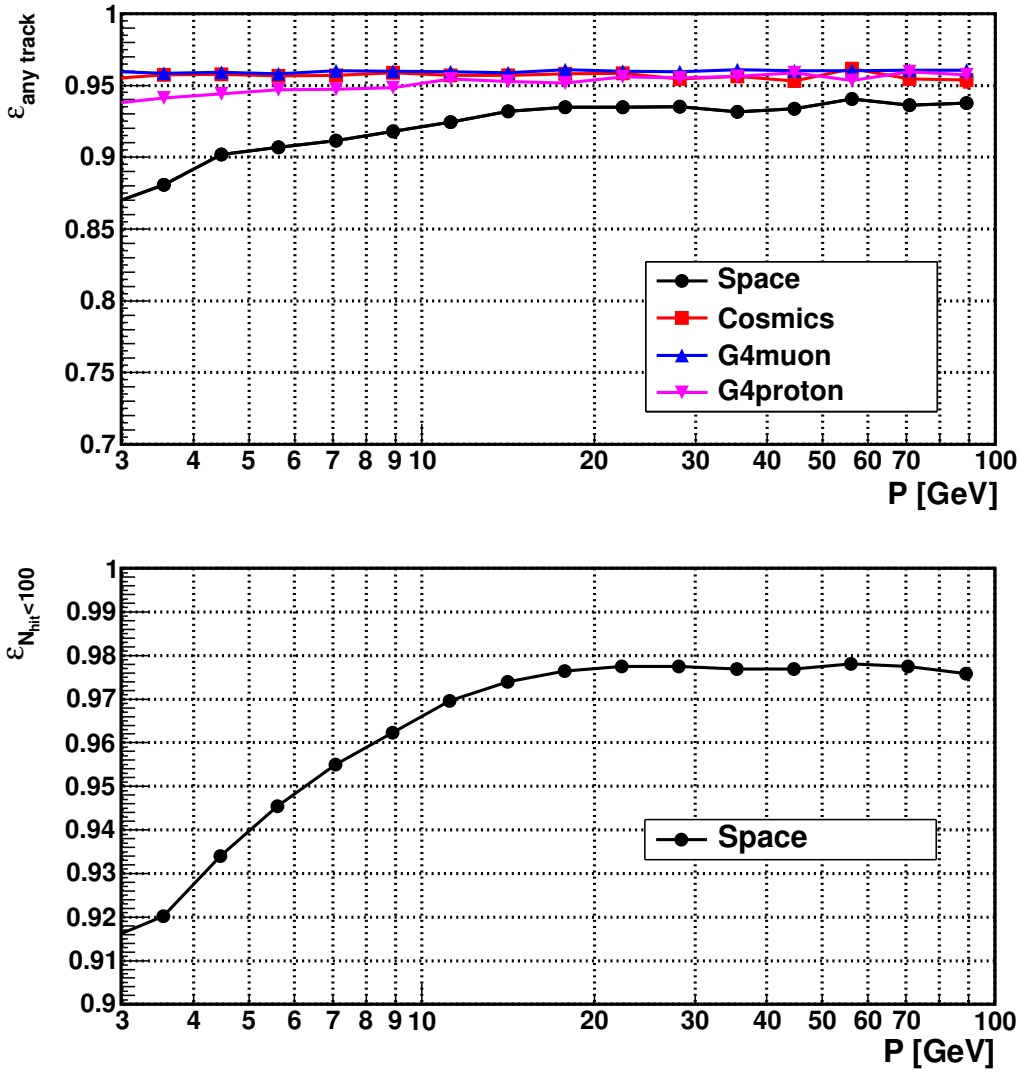

Figure 4.29: Fraction of events with a preselected track from the inner Tracker passing the TRD geometry which contain at least one selected TRD track (top) and the efficiency of the selection $N_{hit} < 100$ for space data (bottom).

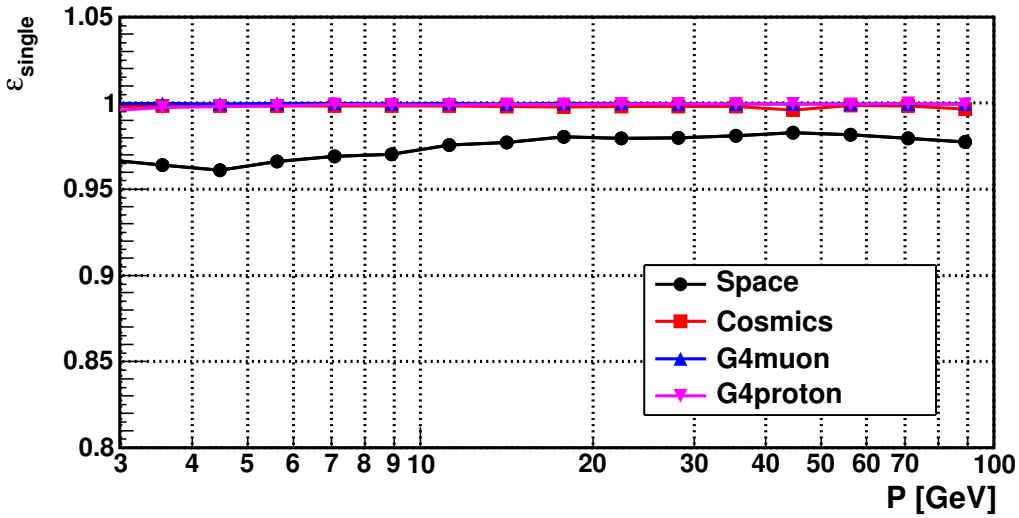

Figure 4.30: Fraction of events with exactly one reconstructed track which fulfills the selection criteria.

decreasing at lower rigidities. This is understood as the impact of multiple scattering leading to a kink in the particle trajectory inside TRD for a fraction of simulated trajectories. Such tracks can not be described well by the straight line approximation. The difference between proton simulations and space data is introduced by the limit on the maximum allowed number of TRD hits of 100. Events containing more hits are expected to be multi-particle or noisy events and are not reconstructed. The momentum dependence of the efficiency is introduced by the correlation of the trigger rate to the geomagnetic rigidity cutoff. Low momentum particles are recorded mainly in regions of low geomagnetic cutoff and therefore high trigger rate. Due to the much lower trigger rate this effect is not observable in atmospheric muon data. In the simulated datasets always single particles are propagated through the detector and thus this effect is not treated. Increasing the efficiency by an increased cut value here would be compensated by a lower efficiency in the following selection of single-particle events.

To select single-particle events just exactly one track and up to three segments in the TRD are allowed. The fraction of single track events is shown in figure 4.30 Almost all events reconstructed in simulated and muon data are single particle events. For space data $2-4\,\%$ of the selected TRD events contain more than one reconstructed track. As the efficiency for both, event selection and reconstruction, is lower for multi-particle than for single particle events this can be treated as a lower limit for the total fraction events with multiple particles in the TRD.

The number of layers containing hits on the inner Tracker extrapolation of at least 1 mm path length is shown in figure 4.31 for simulated proton and in figure 4.32 for simulated muon events. The number of TRD layers containing energy depositions of the primary

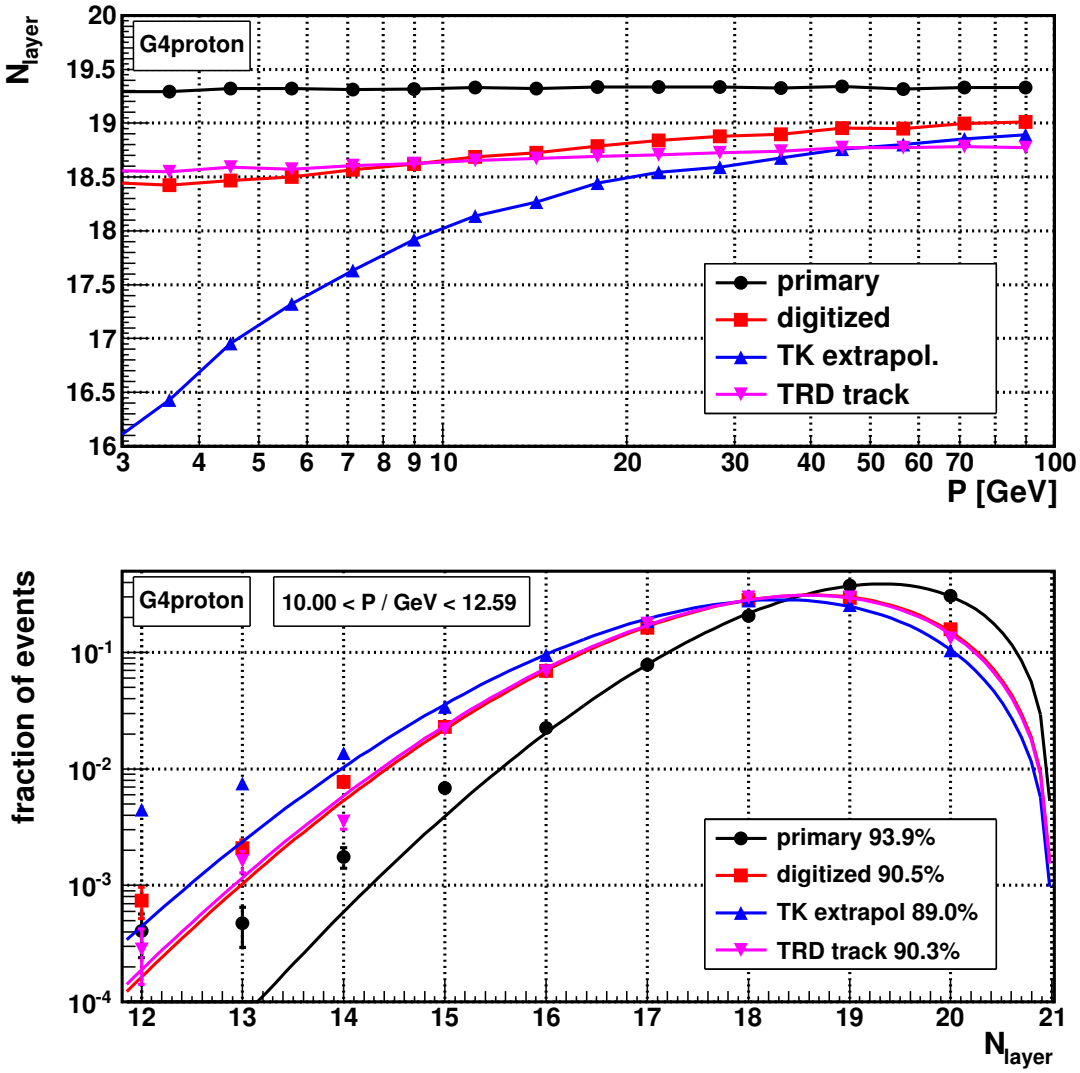

Figure 4.31: Number of TRD layers containing hits of at least 1 mm path length as function of momentum (top) and the corresponding distribution in momentum interval $10.00 < P/\text{GeV} < 12.59$ (bottom) for the simulated primary protons (black), after digitization (red), on the extrapolated track from inner Tracker (blue) and on the reconstructed TRD track (magenta).

particle reflects the geometric efficiency of the TRD. For muon and protons simulation this number is 19.3 which corresponds to an efficiency of $\sim$ 94 %. The number of layers containing a reconstructed hits in tubes passed by the primary particle is lower for proton than for muon data. This can be explained by the different simulation of digitization processes in the two software versions used for simulations. The older muon version underestimated the pedestals widths and shows a higher efficiency of $\sim$ 92 %. The software version used for protons contains the most recent simulation of digitization, containing a realistic set of pedestals taken from data. The extracted single layer efficiency is $\sim$ 90.5 %. This introduces a difference in the number of layers with hits on reconstructed tracks for simulated proton and muon events. The corresponding efficiency for extrapolated tracks from the inner Tracker is 89.0 % for protons and 90.2 % for muons. This efficiency can be increased by implementing a relative alignment of TRD to inner Tracker and by a correction of the track extrapolation for multiple scattering. The single-layer efficiency to find a hit on the reconstructed TRD track is 90.3 % and 91.5 % for simulated proton and muon events respectively. In figure 4.33 the number of TRD layers $N_{layer}^{TRDtrack}$ containing hits on the TRD track with at least 1 mm path length is shown for simulated and data events. Notably, the path lengths are determined here by the reconstructed TRD track. For protons the decrease of $\langle N_{layer}^{TRDtrack} \rangle$ with decreasing particle momentum, introduced by digitization and multiple scattering, is described well in simulations. The number of layers is $\sim$ 0.3 hits lower for data events. This is understood as the impact of different digitization efficiencies introduced by the time-dependent gas parameters, which was found to be on the same scale in figure 4.27. The higher values of $\langle N_{layer}^{TRDtrack} \rangle$ for simulated muon events are generated by the overestimated digitization efficiency as discussed above. The decrease with rising particle momentum observed in muon data has not been fully understood yet. Presumably it is related to muon showers, which might be generated in interactions with the ceiling of the experimental area. These collimated showers might lead to an increase in the total number of hits on a reconstructed track and the total energy deposition towards low momenta.

The single layer efficiency to find a TRD hit on the reconstructed TRD track as function of momentum is shown in figure 4.34 for space data and in figure 4.35 for atmospheric muon data. The individual layer efficiencies are about 90 % and quasi-independent of particle momentum. The efficiency is about 2 % lower for top and bottom layers in the yz projection, to be specific in the layers 1,4, 16 and 20. This indicates that the assumption of a straight line is not fully adequate in this projection. Apparently, the track segments in the top and bottom four layers have on average a different inclination. The track fit leads to a straight line through the two centers of gravity. The probability for the 'outer' layers is therefore reduced. The efficiency obtained in simulations matches the data results on the percent level. The average ratio of space data to proton simulation efficiencies is 98.6 ± 0.1 % with a standard deviation 0.5 ± 0.1 %. For muons the corresponding distribution width is identical

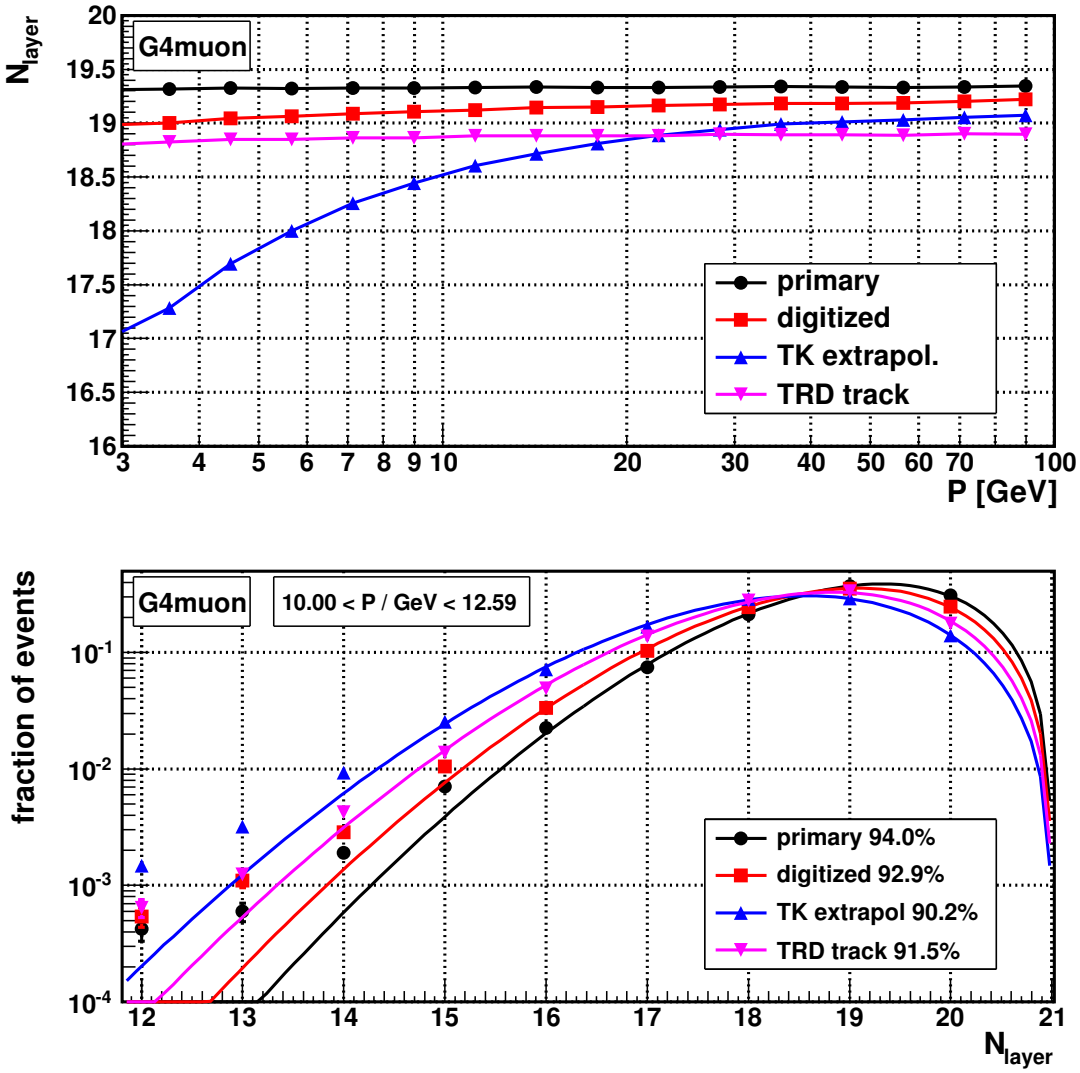

Figure 4.32: Number of TRD layers containing hits of at least 1 mm path length as function of momentum (top) and the corresponding distribution in momentum interval $10.00 < P/\text{GeV} < 12.59$ (bottom) for the simulated primary muons (black), after digitization (red), on the extrapolated track from inner Tracker (blue) and on the reconstructed TRD track (magenta).

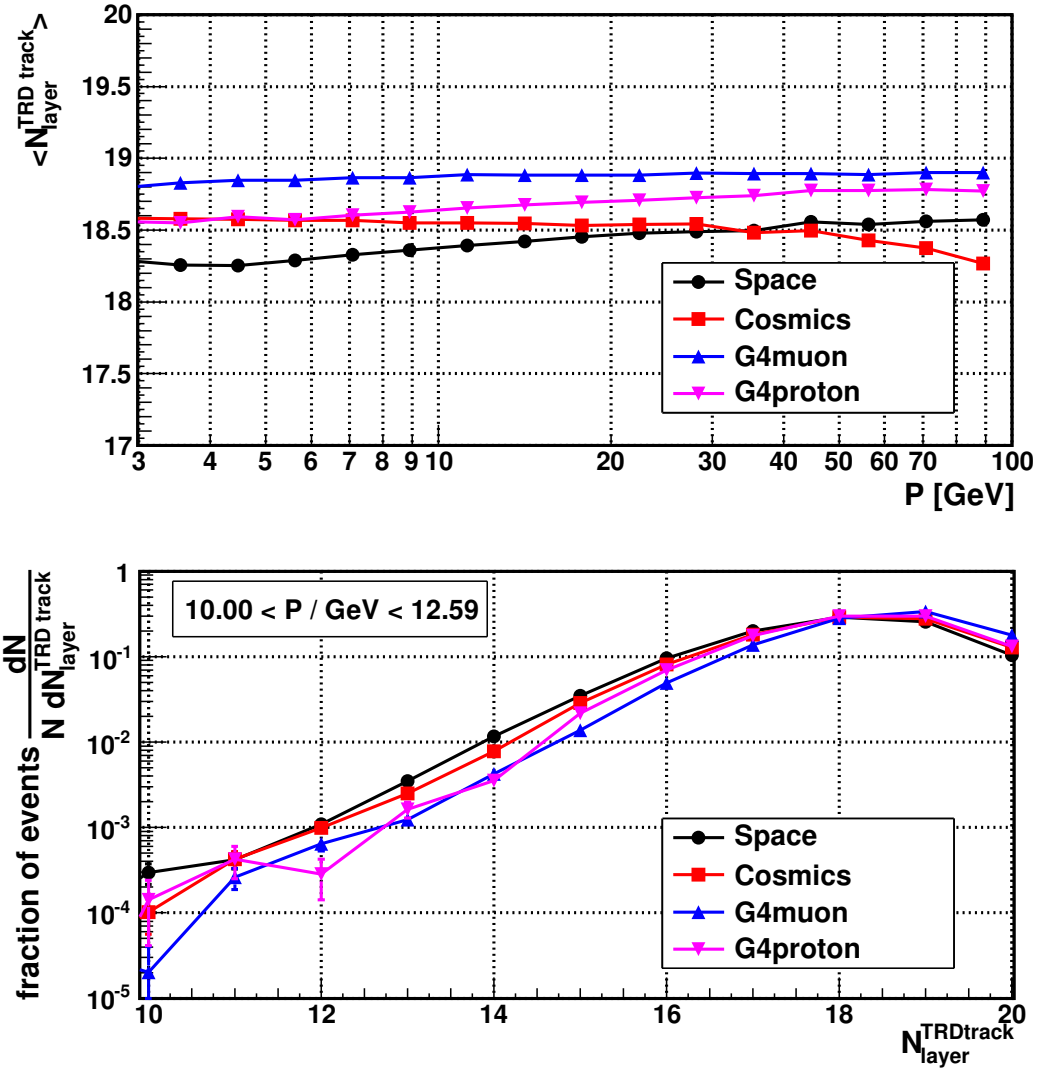

Figure 4.33: Number of TRD layers with hits on the reconstructed TRD track for different datasets as function of particle momentum (top) and the corresponding distribution in momentum interval $10.00 < P/\text{GeV} < 12.59$ (bottom).

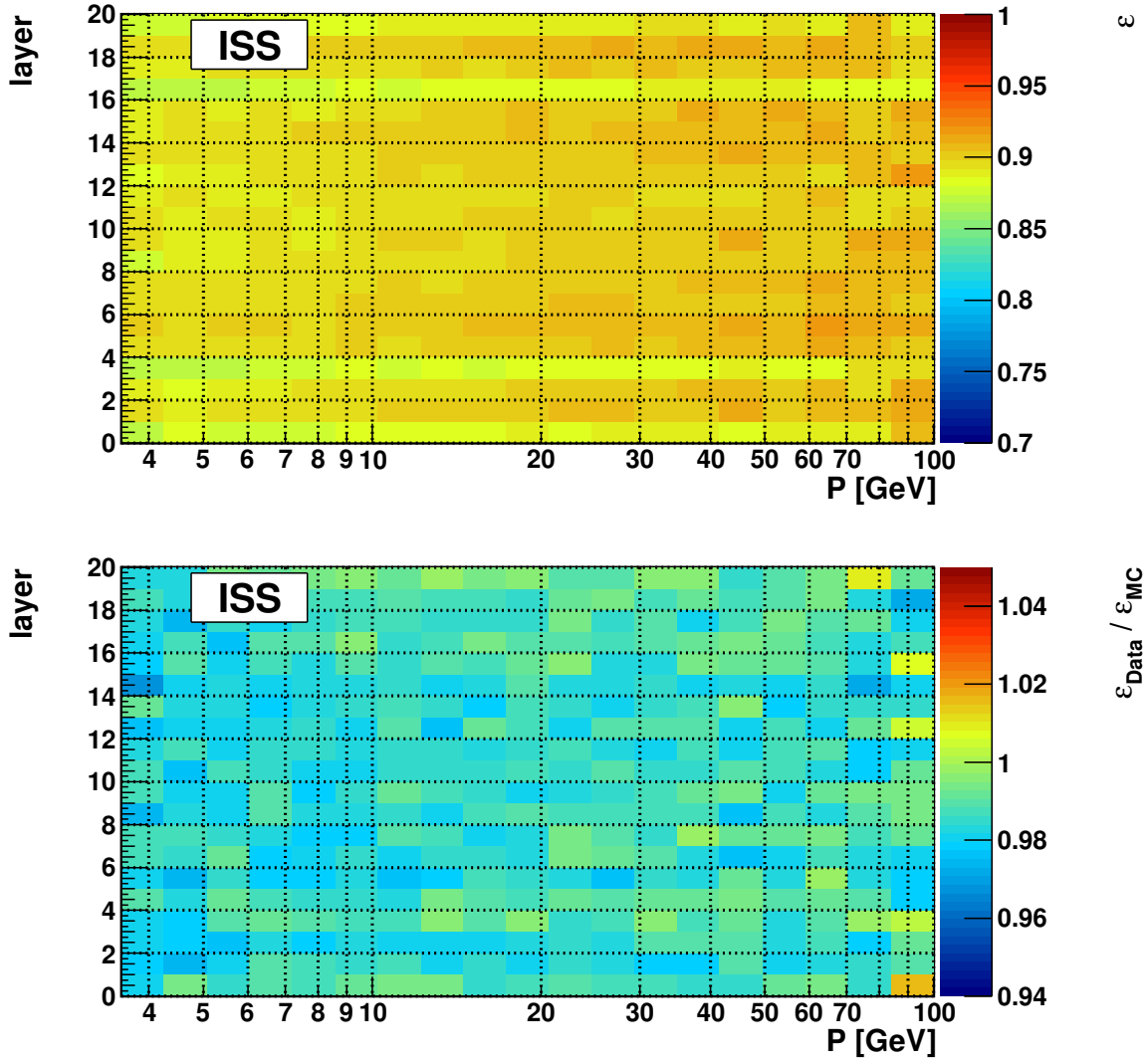

Figure 4.34: Efficiency ε to find a hit in a TRD layer on a reconstructed TRD track as function of momentum for space data (top) and in comparison $\frac{\varepsilon_{Data}}{\varepsilon_{MC}}$ to simulations (bottom).

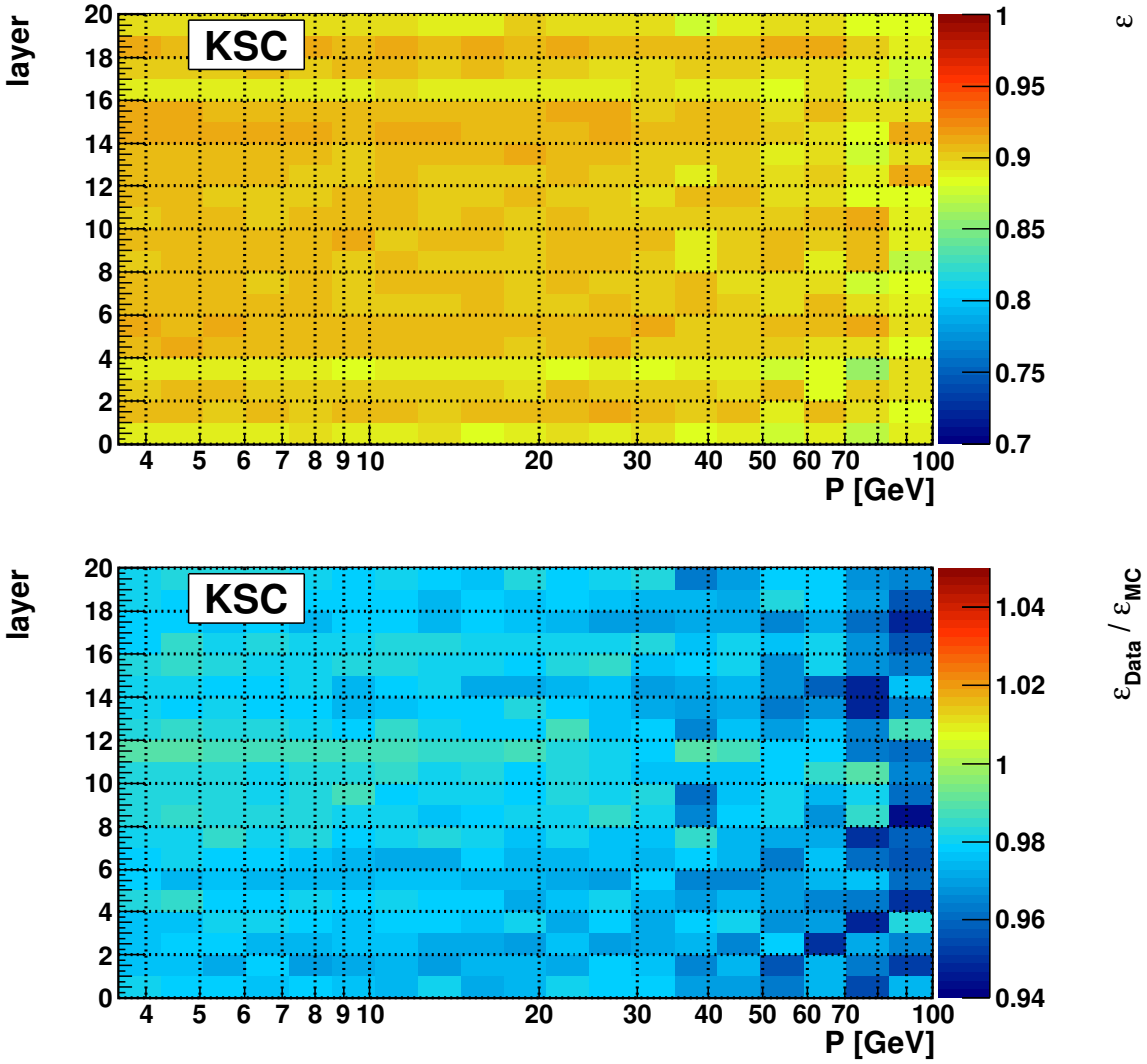

Figure 4.35: Efficiency ε to find a hit in a TRD layer on a reconstructed TRD track as function of momentum for atmospheric muon data (top) and in comparison $\frac{\varepsilon_{Data}}{\varepsilon_{MC}}$ to simulations (bottom).

and the average is lowered to 97.8 ± 0.1 %. As discussed above, a decreasing efficiency with increasing muon momentum is observed in data, which leads to a non-gaussian tail towards lower efficiency ratios of $94 - 96$ %.

4.3.4 Track Matching

The track matching of inner Tracker and TRD tracks is based on their extrapolations to the upper TOF plane, which is located between them. A matching between the reconstructed TRD track and the track from inner Tracker is performed by requiring that the intersections are close to each other, distance $dr < 1$ cm, and the opening angle between the tracks is small $d\alpha < 2^\circ$. The upper TOF plane, as the region of highest density on the particles trajectory into the inner Tracker, is chosen in order to allow for kinks introduced by multiple scattering.

The angular deviation of the TRD track from the inner Tracker track is shown for space data in figure 4.36. Relative to the inner Tracker extrapolation the TRD resolution in zenith angle is $\sim 0.39 \pm 0.01^\circ$ and in azimuth angle $\sim 1.34 \pm 0.01^\circ$. The momentum and zenith angle dependency of $d\Theta = \Theta_{TRD} - \Theta_{TK}$ and $d\varphi = \varphi_{TRD} - \varphi_{TK}$ is shown in figure 4.37 and 4.38 respectively. The obtained mean values of $d\Theta$ and $d\varphi$ results are $\lesssim 0.05^\circ$. The width of $d\Theta$ and $d\varphi$ distributions are dominated by the TRD resolution and almost independent of particle momentum. The momentum dependence of the width of $d\Theta$ clearly reveals the weak point of the TRD track reconstruction. As the TRD tubes are arranged below each other and the trajectory passing the tube can not be localized inside the tube volume, ambiguities are created. In the simplified 2D view of figure 4.39, angles of $\psi \equiv \frac{dy}{dz} \gtrsim \frac{d_{tube}}{dz}$ can be resolved. For tube diameter $d_{tube} = 6$ mm and span $dz \approx 60$ cm in yz projection between highest and lowest layer this corresponds to $\psi \gtrsim 0.01$. All events in the angular range of the ambiguity are seen by the reconstruction algorithm as straight downward going particles and will not necessarily match the expected 3D track extrapolation from the inner Tracker. Correspondingly, the azimuth angle cannot be reconstructed if the track is passing a column of tubes in both projections. Thus, for $\Theta \to 0$ the uncertainty on φ is increasing. A similar effect occurs for other lining-ups of the tubes, observable here at $\Theta \approx 13^\circ$. As $\Theta > 0$ here, this mainly affects the uncertainty on Θ and just a slight increase of uncertainties on φ is observable, which can be explained by the vertical incidence in one of the projections xz or yz at $\varphi = n \times \frac{\pi}{2}$.

The spatial deviation of the TRD track from the tracker extrapolation in the upper TOF plane is shown in figure 4.40. The distribution of residuals dx and dy is shifted from zero, indicating a relative dis-alignment of the TRD with respective to the inner Tracker. The width of the distributions, 31.62 ± 0.04 mm in x- and 20.81 ± 0.02 mm in y-projection, reflect the spatial resolution of the TRD extrapolated to the upper TOF plane. The momentum

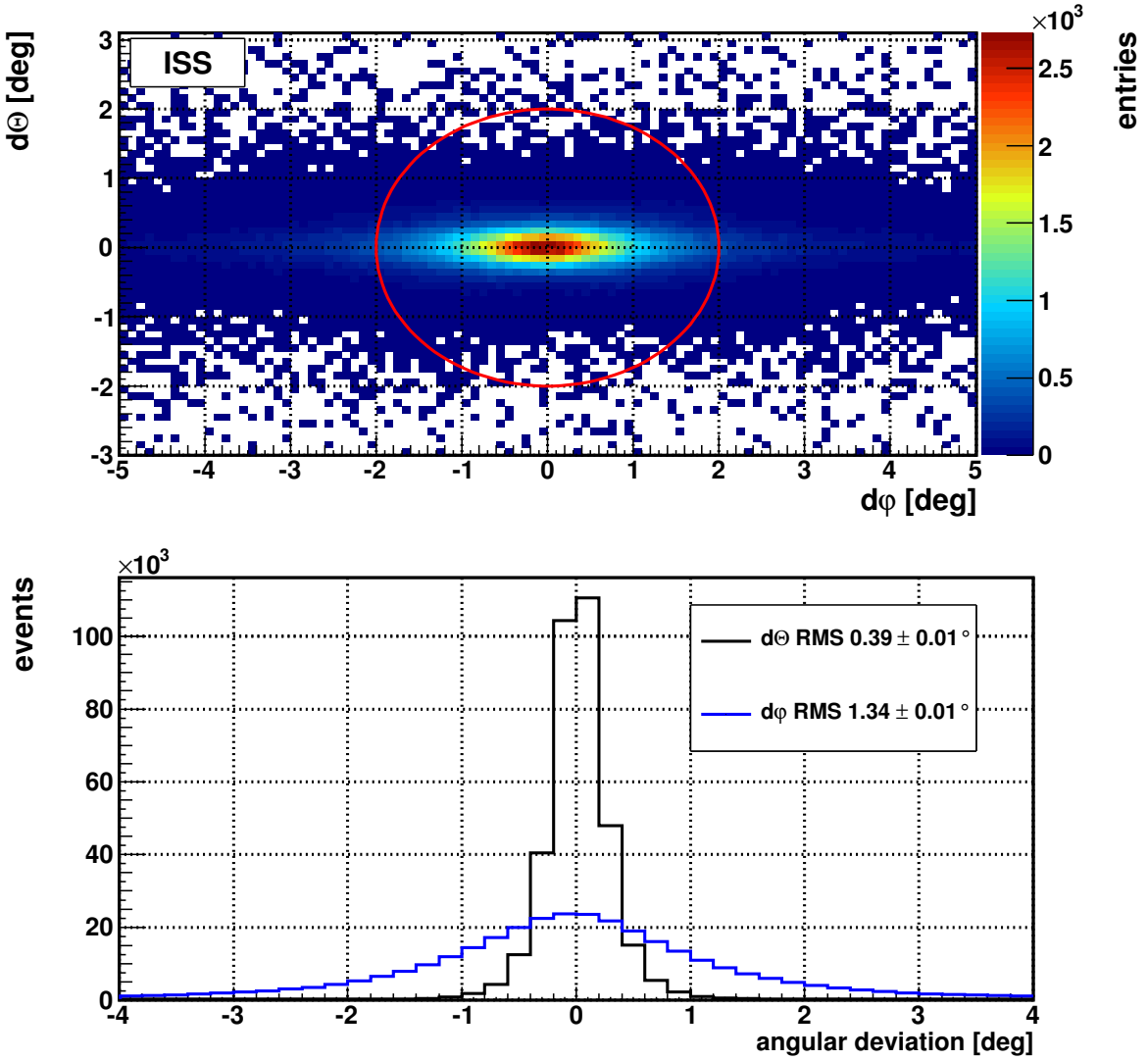

Figure 4.36: Opening angle between the reconstructed TRD track and the extrapolated track from inner Tracker in the upper TOF plane at $z \approx 63\,\text{cm}$. The cut on opening angle $\alpha < 2^\circ$ is indicated in the zenith and azimuth parameter plane (top). The width of the projected distributions (bottom) of $\Theta_{rms} = 0.39^\circ$ and $\varphi_{rms} = 1.34^\circ$ reflects the TRD angular resolution.

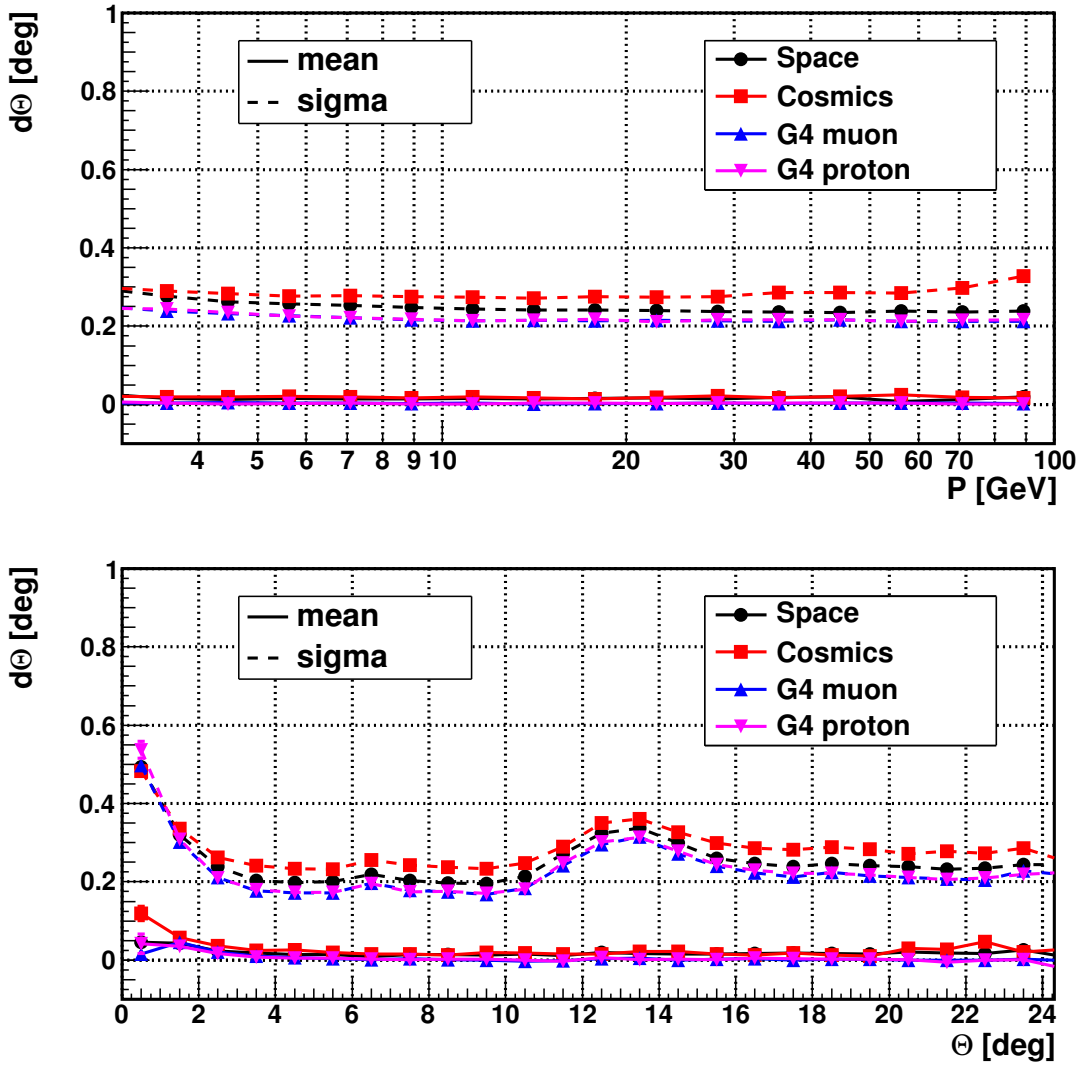

Figure 4.37: TRD resolution in zenith angle as function of particle momentum (top) and incident angle (bottom) in the upper TOF plane.

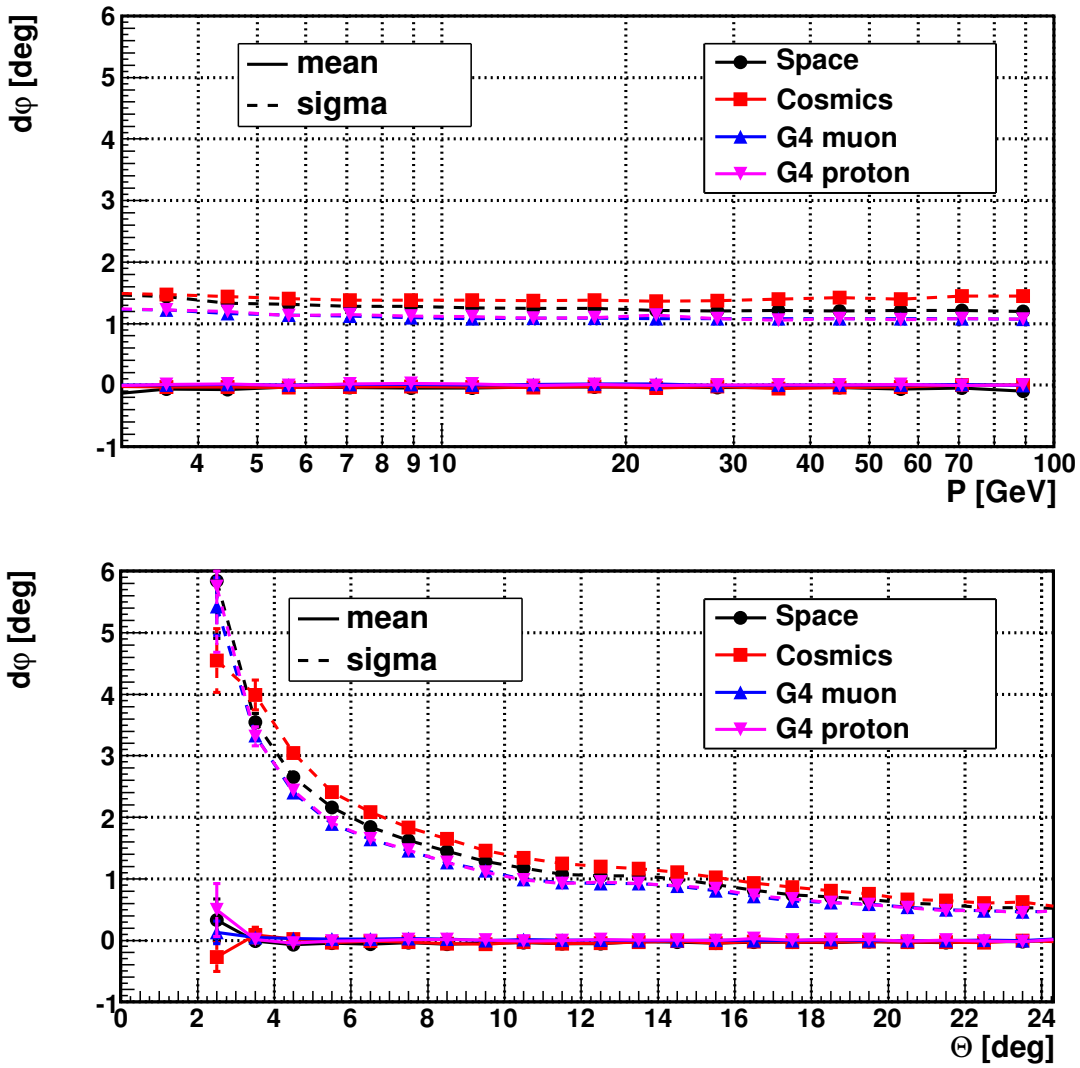

Figure 4.38: TRD resolution in azimuth angle as function of particle momentum (top) and incident angle (bottom) in the upper TOF plane.

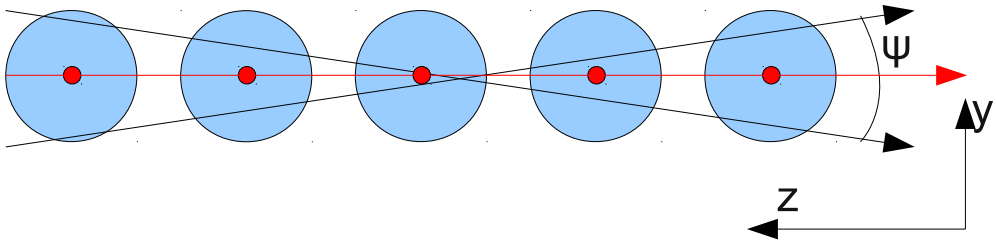

Figure 4.39: Schematic view of the TRD tracking ambiguity. Tracks, which are quasi-perpendicular in one of the 2D-projections (black arrows), are passing one column of straw tubes located each below the other. In an angular range indicated by ψ different tracks can not be disentangled by the single hit positions, which are assigned to the tube wire positions (red) in the center of the tubes, and are reconstructed as straight downward (red arrow).

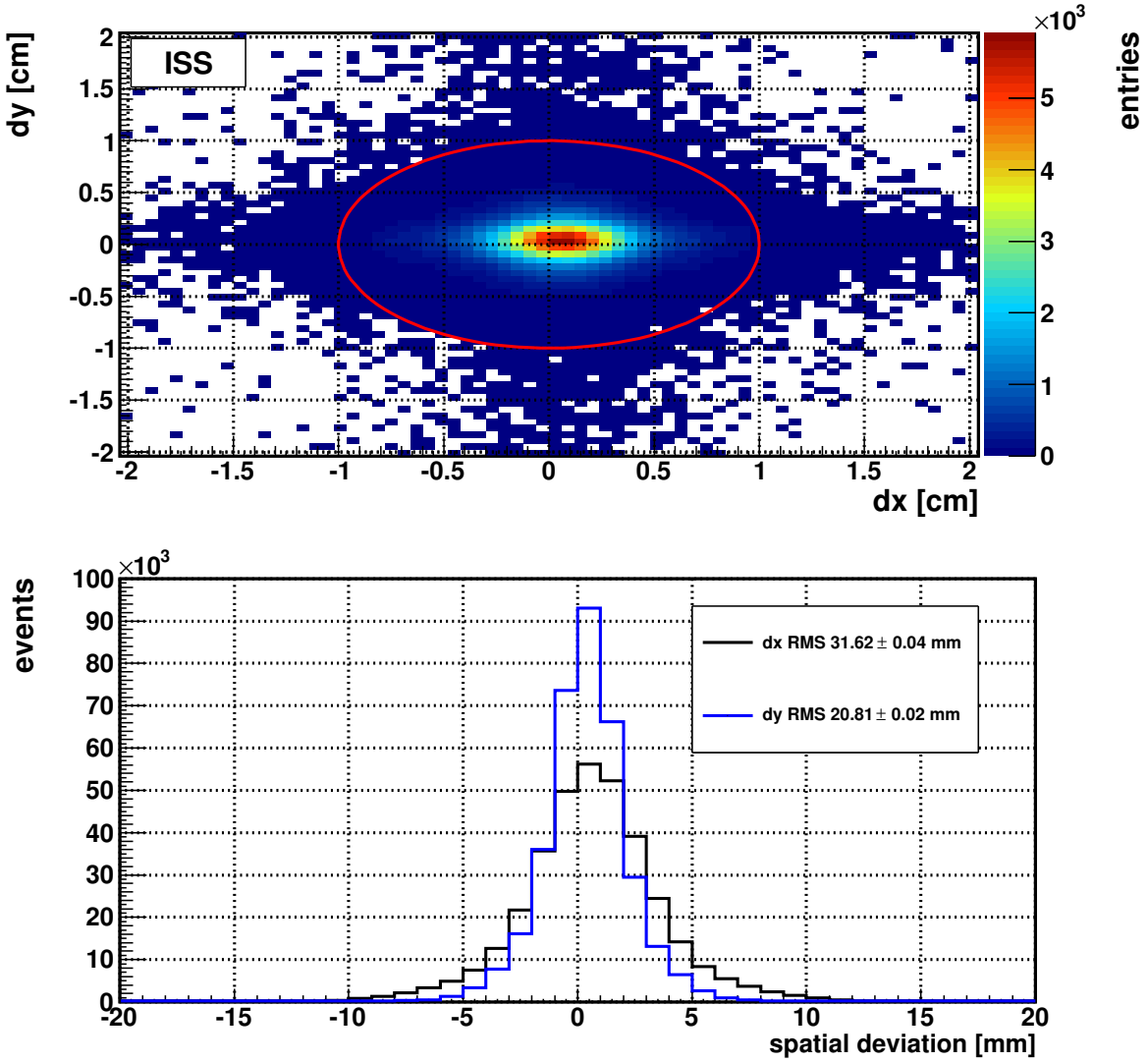

Figure 4.40: Distance of intersections of the reconstructed TRD track and the extrapolated track from inner Tracker in the upper TOF plane at $z \approx 63\,\text{cm}$. The cut on distance $dr < 1\,\text{cm}$ is indicated in the zenith and azimuth parameter plane (top). The width of the projected distributions (bottom) of $dx_{rms} = 31.6\,\text{mm}$ and $dy_{rms} = 20.8\,\text{mm}$ reflects the TRD spatial resolution.

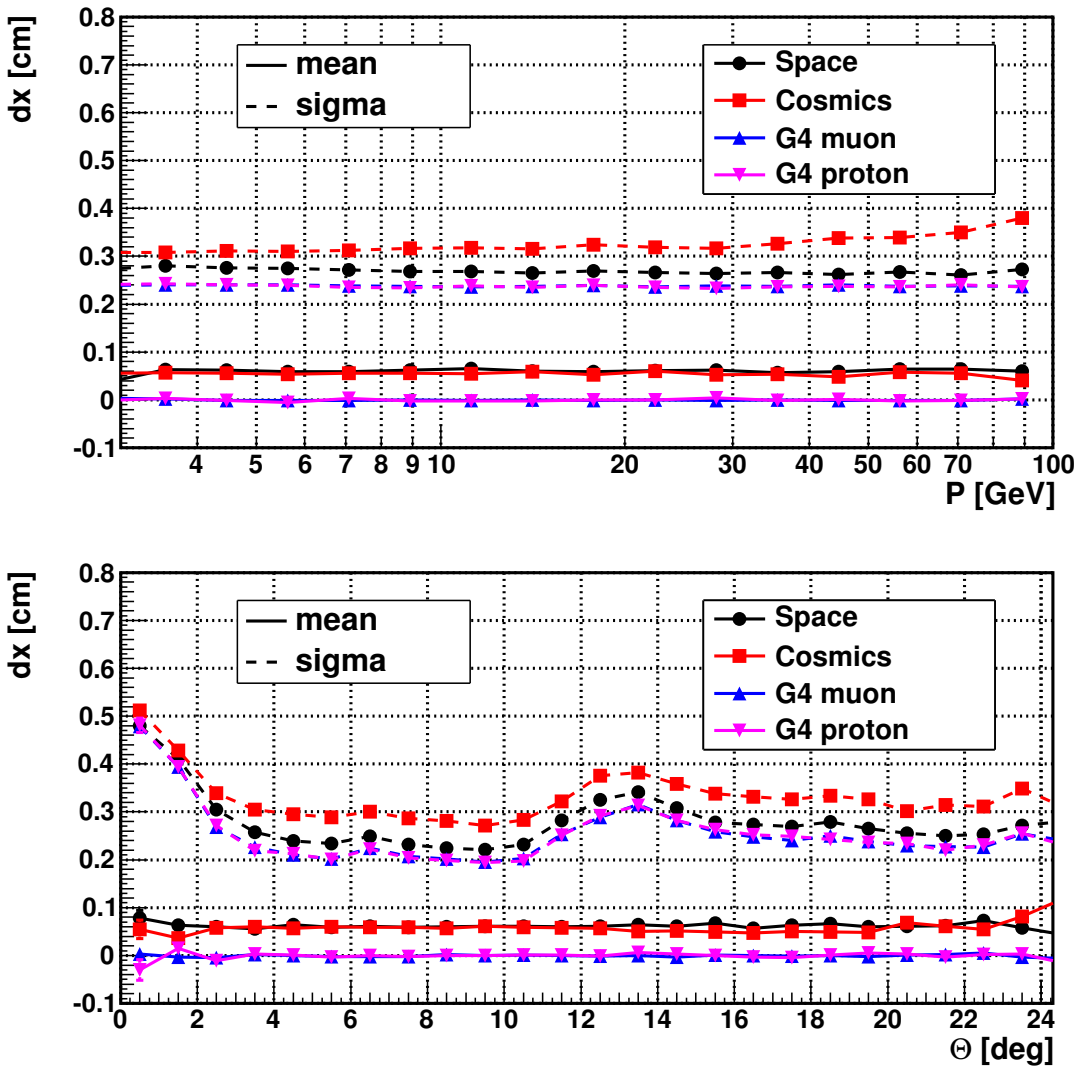

Figure 4.41: TRD resolution in x-coordinate (non-bending plane) as function of particle momentum (top) and incident angle (bottom) in the upper TOF plane.

and zenith angle dependency of dx and dy is shown in figure 4.41 and 4.42 respectively. As expected from the previous figures, the mean values of residual distributions is not peaked at zero like expected from nominal geometry as implemented in simulations. The mean values $\langle dx \rangle = 600 \pm 10\,\mu$m and $\langle dy \rangle = 382 \pm 3\,\mu$m are independent of the considered data period, particle momentum and incident angle. The mechanical precision of the TRD is $\lesssim 100\,\mu$m and an assembly precision on the order of 1 mm seems reasonable. Similar to the angular resolution, the widths of dx and dy are increased at zenith angles associated to the mentioned tracking ambiguities.

The spatial, angular and combined matching efficiency is shown in figure 4.43. For muon and proton simulations the total matching efficiency is $\sim$ 98 %, decreasing to $\sim$ 96 % at 3 GeV due to multiple scattering. The spatial matching provides a lower efficiency than the angular one for all data sets. For data samples the influence of the dis-alignment further

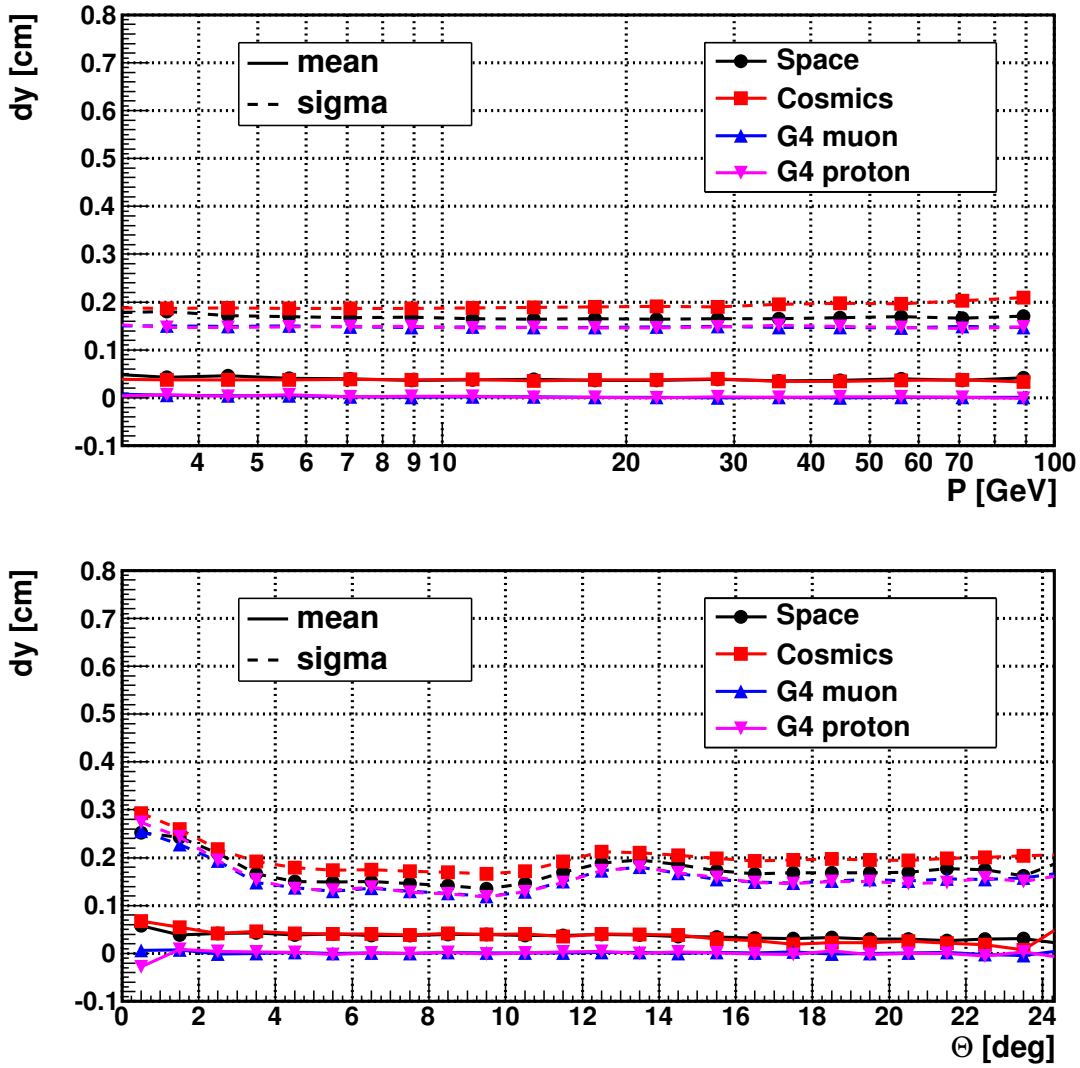

Figure 4.42: TRD resolution in y-coordinate (bending plane) as function of particle momentum (top) and incident angle (bottom) in the upper TOF plane.

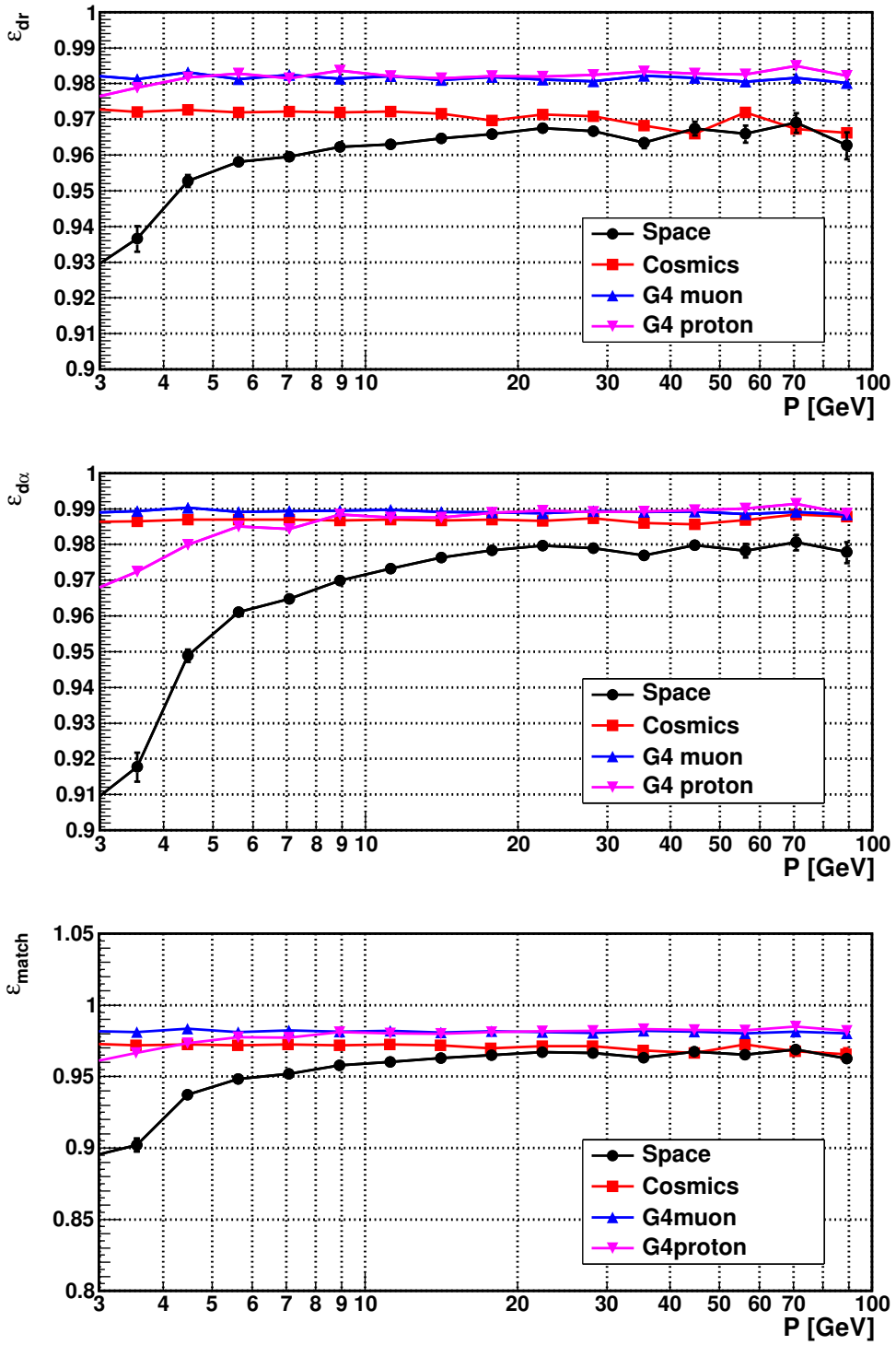

Figure 4.43: Efficiency of the matching of the TRD and Tracker track in the TOF plane based on distance of intersection points (top) and opening angle (center) and the combined efficiency denoted matching efficiency.

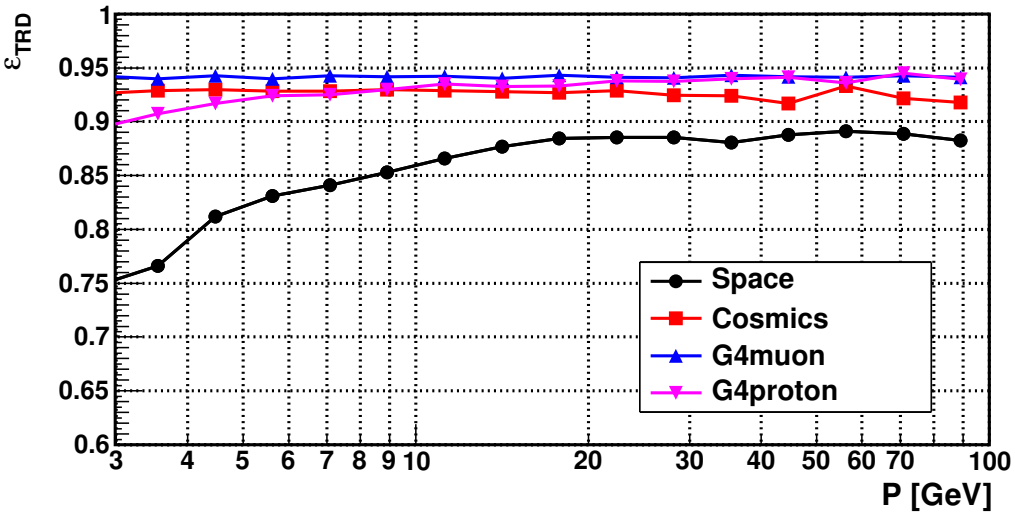

Figure 4.44: Total TRD efficiency, the convolution of reconstruction, selection and matching efficiency, as function of particle momentum.

reduces the efficiency of the spatial cut. The total matching efficiency for data is about 2 % lower than for simulation.

Additionally the influence of multiple scattering in proton data is presumably increased by the dis-alignment as the allowed parameter space is decreased. In case the shift of the distribution from origin in figure 4.40 would be enhanced, to e.g. 1 cm, it becomes obvious that the efficiency of the cut around the origin is reduced. The decrease of efficiency due to multiple scattering is enhanced because the radial-symmetric spread more likely departs further away from the allowed parameters space than towards it.

The total TRD efficiency as function of particle momentum is shown in figure 4.44. The total TRD efficiency is the convolution of reconstruction efficiency for quality selected tracks (figure 4.29), the single track efficiency (figure 4.30) and the matching efficiency (figure 4.43). For simulated proton and muon events the total efficiency is $\sim$ 94 %, decreasing for protons with decreasing momenta. The slightly lower total efficiency of $\sim$ 93 % for muon data is due to lower matching efficiencies introduced by dis-alignment. For space data the efficiency is further lowered by the reconstruction and single track efficiency to $\sim$ 88 %. This is expected to be introduced by the high particle flux in space which leads to more TRD multi-track events and lowers the corresponding efficiencies. The decrease of total efficiency towards low particle momenta is enhanced for space data. Low-energy particles are more likely to be produced in regions of low geomagnetic cutoff. Hence, the rate of particle is increased and the reconstruction and single track efficiency is further reduced. Also the efficiency loss due to multiple scattering is enhanced by dis-alignment, like discussed above.

The number of TRD layers with hits on the reconstructed TRD track $N_{layer}^{TRDtrack}$, as defined above, after the application of all selections is shown in figure 4.45. In comparison to figure

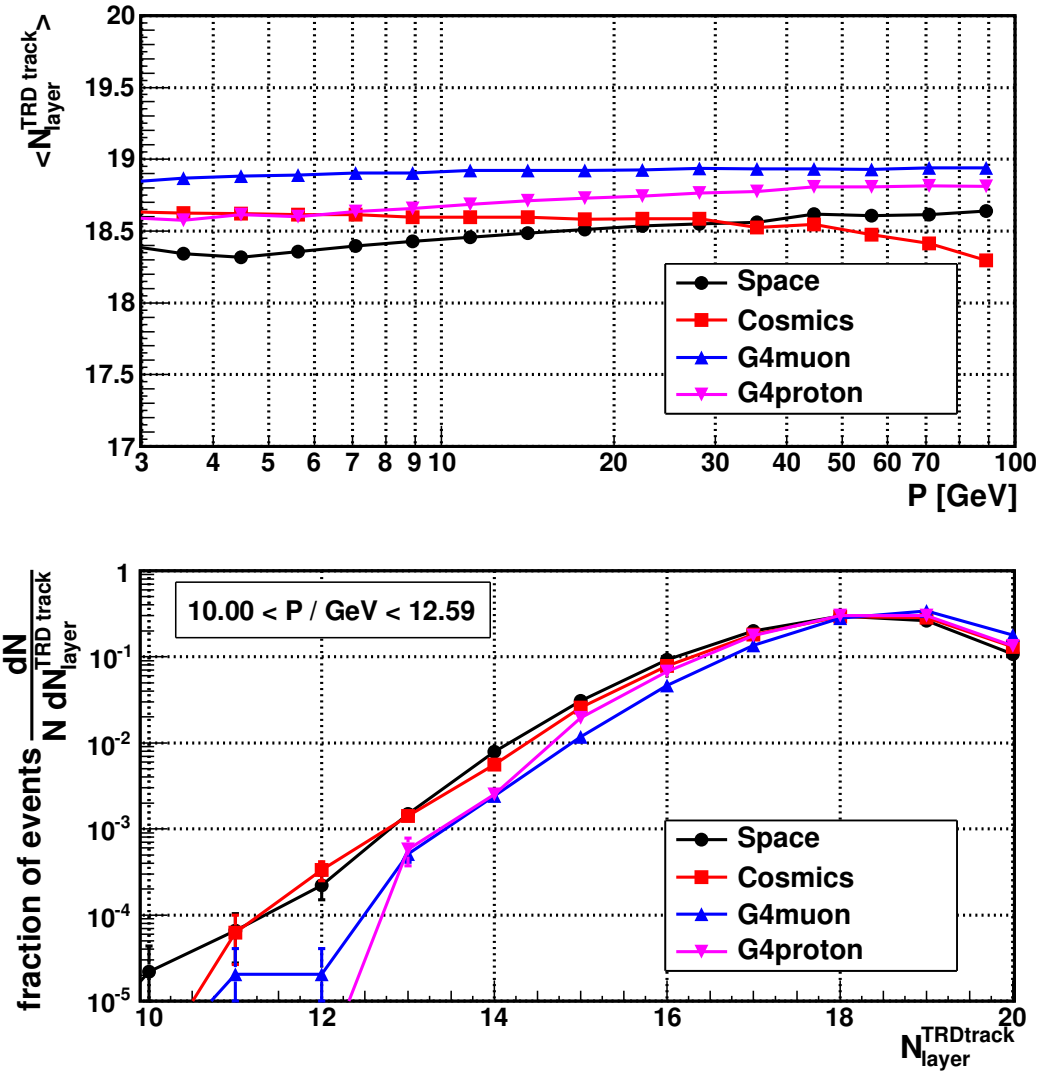

Figure 4.45: Number of TRD layers with hits on the reconstructed TRD track for different datasets after all selections as function of particle momentum (top) and the corresponding distribution in momentum interval $10.00 < P/\text{GeV} < 12.59$ (bottom).

4.33 the matching of tracks leads to an increase in $\langle N_{layer}^{TRDtrack} \rangle$ of $\lesssim 0.1$ and to a suppression of the tails of the distributions. This is expected to arise due to the increasing tracking precision with rising number of TRD hits, which represent the supporting points of the track reconstruction. The pulse heights associated to these hits on a TRD track are used in the following for the calibration of the TRD and the discrimination between different particle types.

4.4 TRD Calibration

The ionization signal in the TRD tubes on a reconstructed track (see section 3.2) depends on the one hand on the number of primary ionizations, proportional to the amount of traversed matter and the properties of the primary particle, and on the other hand on the modification of the primary ionization energy due to the applied high voltage and the amplification inside the tube. The latter two effects are combined in the concept of gas gain.

As the TRD is constantly loosing gas due to diffusion through the tube walls, the total density is a function of time. Since mainly CO_2 is lost, the gas composition is time-dependent and the reduced amount of quenching gas leads to an increase in signal amplification. This is compensated by regular HV adjustments in regular detector operations. Additionally, temperature gradients in the TRD, mainly caused by solar radiation, lead to density gradients. Changes in the local gas density and composition have an impact on the primary ionizations, the gas gain and the absorption of transition radiation photons. The convolution of these effects complicates the identification of particles in the TRD (see section 4.5).

The following algorithms have been developed to take into account the variation of energy depositions: gas gain correction (see section 4.4.1), rigidity correction (see section 4.4.2), path length correction (see section 4.4.3) and temperature fit (see section 4.4.4). The measured variation of gas pressure and temperature is shown in the following for beamtest, atmospheric muon and space period.

The temperature profile and gas pressure of the TRD in the beamtest period is shown in figure 4.46. The temperature at the center of the TRD is constant at $\sim 19^\circ$ C with a span between maximum and minimum of measured temperatures of $\sim 2^\circ$ C. The temperature corrected pressure is stable at ~ 1080 mbar and the estimated Xe : CO_2 ratio is 80% : 20% with $\sim 1\%$ uncertainty. The variation of energy depositions in the beamtest is dominated by the change in particle beam properties, e.g. composition, energy and incident angle. Due to this irregular particle flux the application and evaluation of calibration methods provide significantly larger systematic uncertainties. However, the particle identification performance in beamtest data, discussed in section 4.5, and the spectra shown in section 4.4.5 are based on calibrations performed with pions.

At KSC the variation of environmental parameters is controlled and in general kept low. The TRD temperature and pressure is shown as function of time in figure 4.47. The lowest measured temperature T_{min} was constant at $\sim 20^\circ C$, reflecting the stable environmental conditions in the High-Bay. The mean and maximum temperature are increased in the beginning by the warm-up of detector electronics. After the initial thermally induced drop by ~ 4 mbar the stabilized thermal environment provides a stable gas pressure, constant on the $\lesssim 1\,‰$ level.

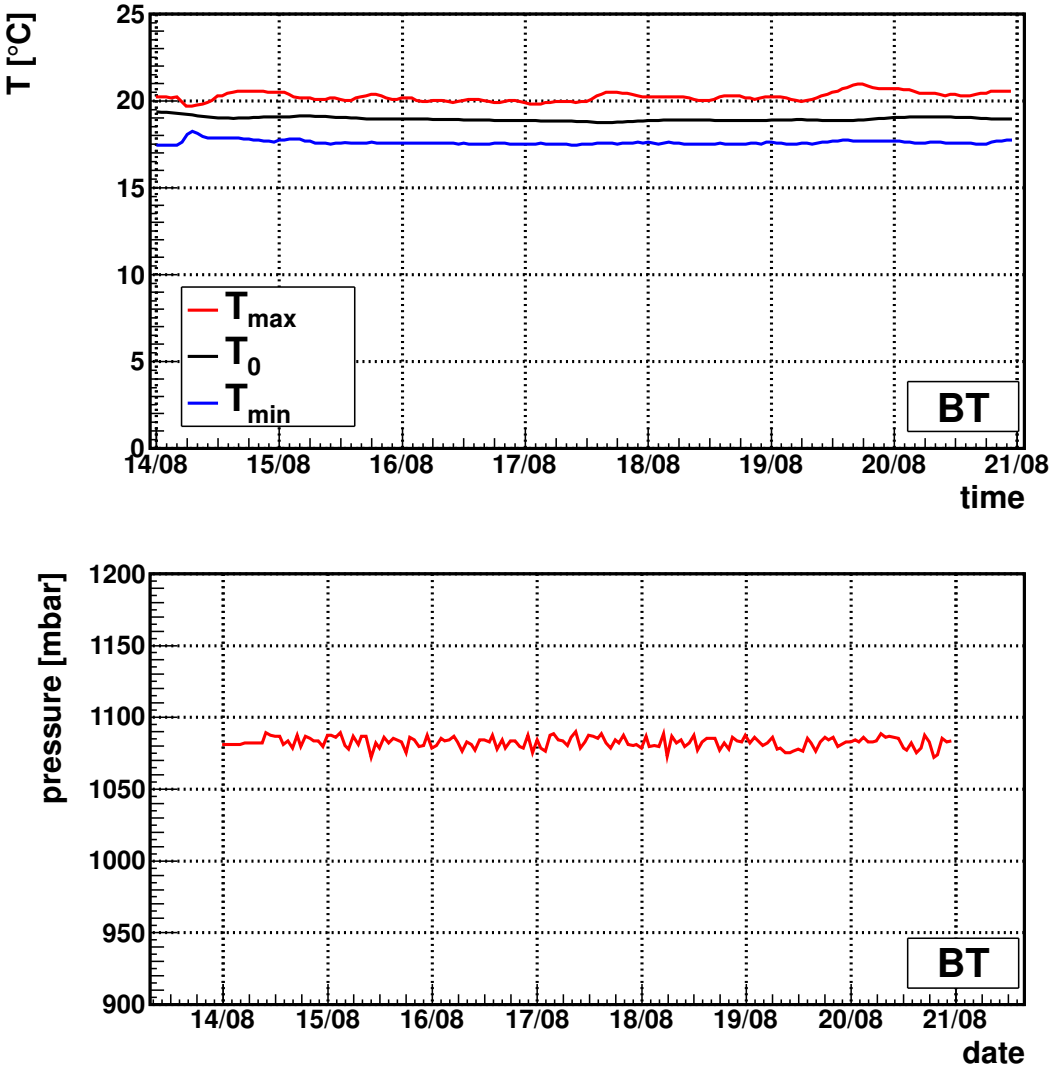

Figure 4.46: TRD temperature (top) and gas pressure (bottom) evolution in the beamtest period.

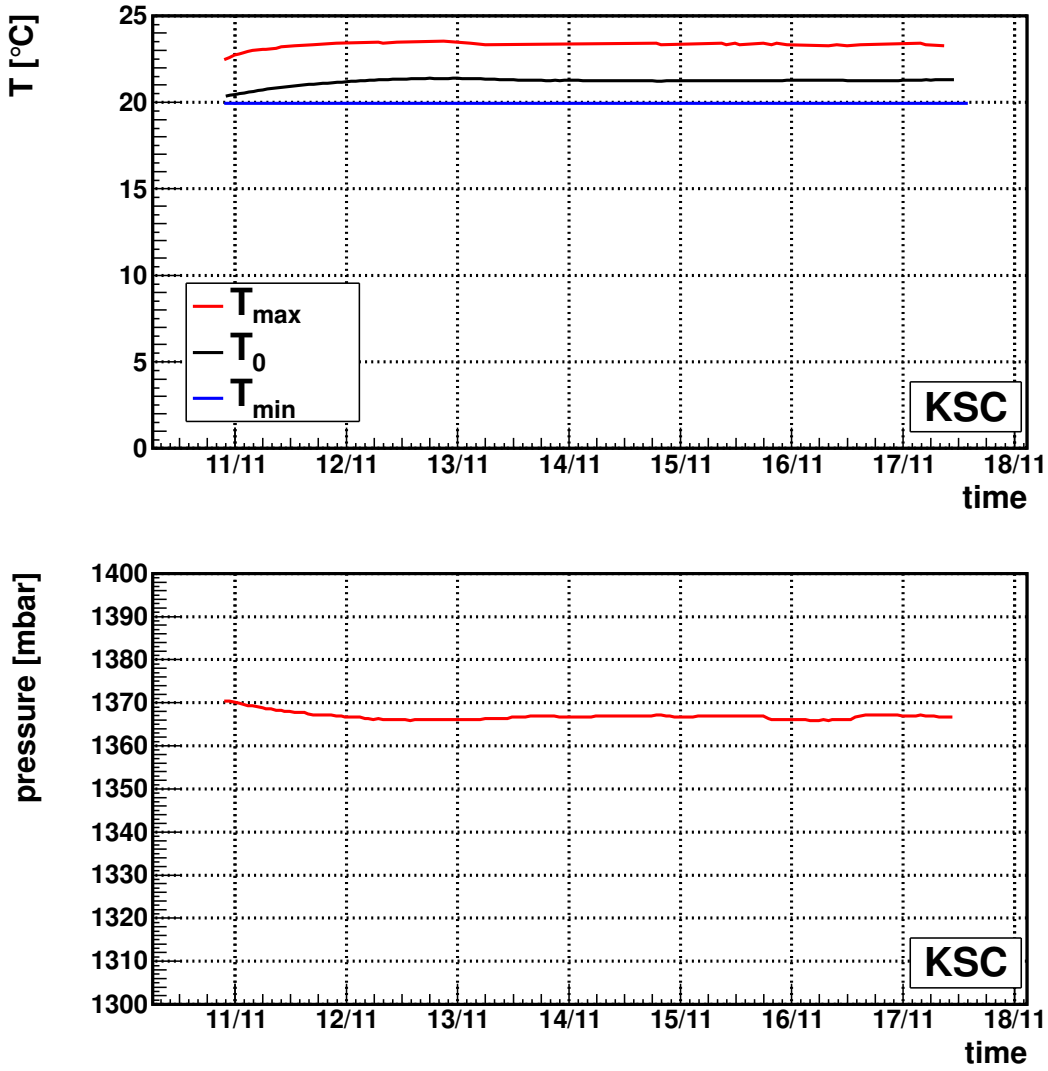

Figure 4.47: TRD temperature (top) and gas pressure (bottom) evolution in the time period at KSC.

In contrast to the controlled and stable clean-room environments in the previous data taking periods the environmental parameters are fluctuating in space. One of the main differences is the heat exchange, which is influenced by the sunlight as heat source and thermal radiation as cooling. Especially in periods of high beta angle[1] the detector is illuminated from a fixed direction and temperature gradients on the order of several degrees can be measured inside the TRD. In figure 4.48 the TRD temperature and gas pressure variation is shown as function of time. The temperature at the center of the TRD is $\sim 14^{\circ} C$ and mainly a function of slowly varying parameters like the ISS beta angle. The high fluctuations observed at the outer surface of the TRD, where typically the minimum and maximum of all measured temperatures are located are damped in the center of the TRD by low thermal conductivity. A typical temperature profile is discussed in section 4.4.4. The pressure drop due to gas losses is on the order of 4 mbar per day and is a combination of two effects: regular diffusion through the straw tube walls and gas leakage (see section 4.4.1). The former is mainly affecting CO_2 and the latter also Xe. While diffusion occurs everywhere through the straw tube surface, gas leakage can be located by investigating the evolution of signal heights of particles passing the detector. To account for such signal height variations the gain calibration method introduced in the following section has been developed.

4.4.1 Gas Gain

The concept of gas gain describes the amplification of the primary energy deposition inside the tube gas to an electrical signal on the anode wire. There are mainly two effects: the partial densities of the Xe/CO_2 gas and the applied high voltage (HV). Due to HV the electrons produced by ionization are accelerated towards the anode wires. During this process they gain energy and secondary ionizations may occur (Townsend avalanche [91]). On the other hand in the ionization process also positive ions are produced which are drifting slowly towards the cathode. As they reach the cathode they may gain an electron and become excited neutral atoms, which return to the ground state by emitting a photon, which in turn can initiate an avalanche. This process is leading to spurious pulse discharges. As a particle passage is reconstructed by discharge it has to be reset to be able to detect subsequent particles. Therefore this process needs to be suppressed by CO_2 as quencher gas. Excited Xenon atoms return to a lower state by transferring energy to CO_2 molecules in collisions. These ions on the other hand, after gaining an electron from the cathode, loose their energy in radiation-less degrees of freedom [92]. Hence the spurious discharges and the gas gain itself are suppressed.

For a given time the gas gain is considered as a fixed value scaling the primary ionization spectrum to the measured pulse height spectrum. Therefore, if one determines the position

[1] angle between the ISS orbital plane and the vector pointing from the Sun towards the Earth

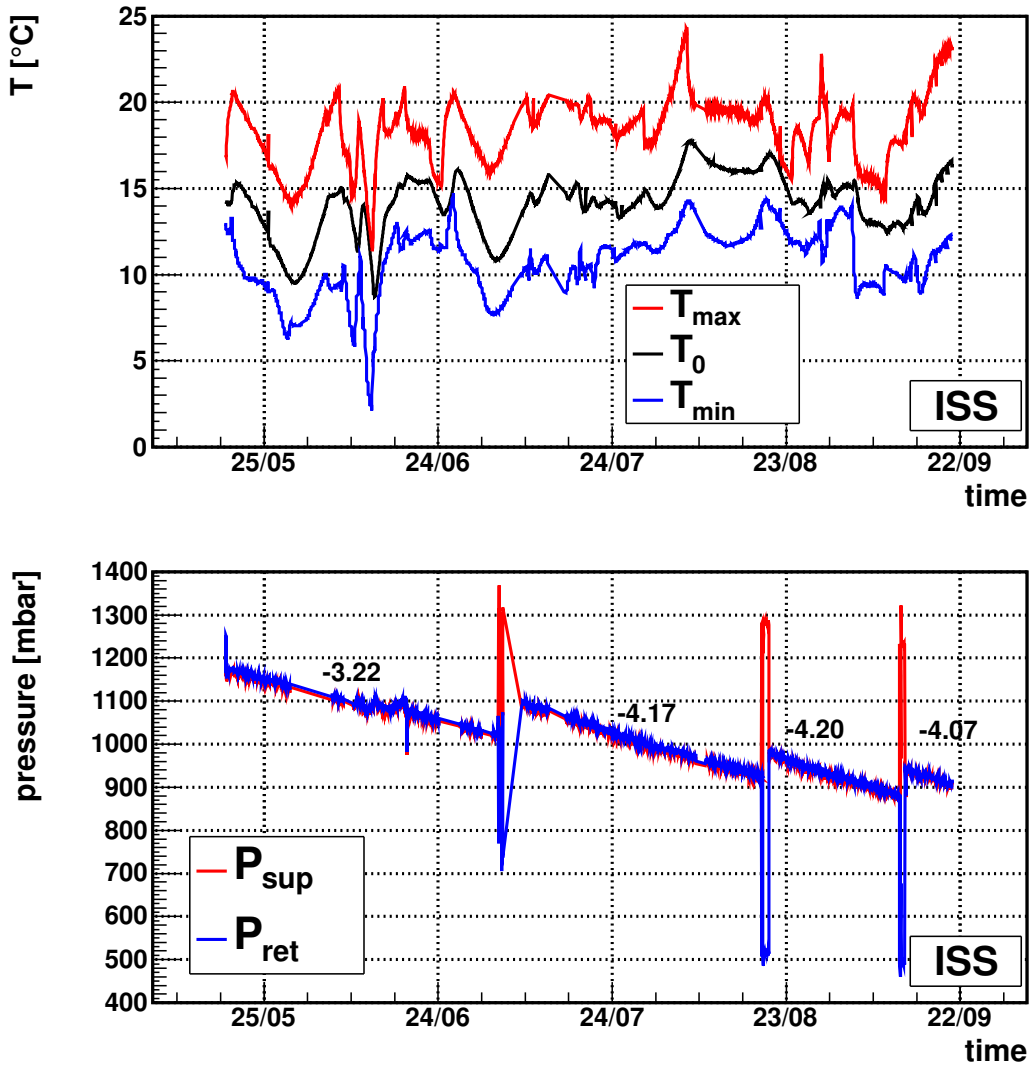

Figure 4.48: Evolution of TRD temperature (top) and temperature corrected gas pressure (bottom) for the period of space data. The pressure is decreasing slowly due to gas losses and increasing rapidly when gas is refilled, with pressure difference between supply pressure P_{sup} and return pressure P_{ret} when pumps are operated. The gas loss rate in units of mbar per day is denoted for different periods separated by gas refills.

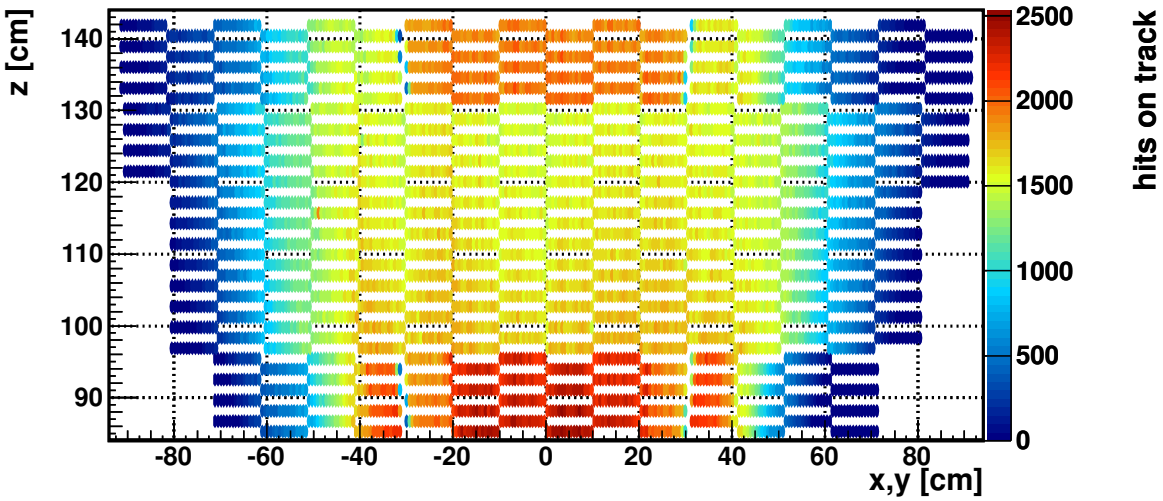

Figure 4.49: TRD straw tube occupancy for quality selected events in the runs recorded on 14th of June 2011 with total data taking time corresponding to $\sim$ 24.16 h.

of a unique value, like e.g. the most probable value (MPV) of the spectrum, as a function of time, the intrinsic scaling of the pulse height spectra can be corrected for. As mentioned above the gain variation is a convolution of many influences which all are valid for different subgroups of the detector. To account for all effects at the same time, the gas gain is determined for each individual channel as a function of time. The frequency of particles passing a given tube depends on its position inside the detector (see figure 4.49). The tubes in the center, lower part above the upper TOF show the highest occupancy and the tubes located on the outside of the detector the lowest ones. This geometrical effect is introduced by the trigger and dominated by the TOF plane below the central part of the TRD. In the vicinity of the bulkheads, observable as gaps at $\pm$32.9 cm in the top and bottom 4 layers, the relative occupancy of straw tubes is reduced by tracking efficiency. On the order of some thousand events are necessary to determine the most probable value of a pulse height spectrum with an accuracy on the percent level by fitting a Landau function. So to decouple all tubes and most probable values a dynamic method without the need of fitting is used: the 'running median'. It consists of one value, the 'median' m, and a simple modification algorithm:

$$m = \begin{cases} m + 0.001\,\text{ADC} & \text{for } A > m \\ m - 0.0025\,\text{ADC} & \text{for } A < m \end{cases}, \tag{4.4.1}$$

where A is an amplitude in ADC units associated to a track passing the corresponding tube. The step size is a trade-off between median stability against statistical fluctuations and response time to systematic variations. The asymmetry in step size reflects the relation between the mean and most probable value of $\sim \frac{2}{5}$ for 'typical' landau functions. In this algorithm each single tube has its own gain value which is updated according to its occupancy. Contrary to a fit method where the data is first gathered over a period and then

fitted once for this period the data is intrinsically weighted based on its actuality. This way an interpolation or time evolution is incorporated.

To improve the performance of the gain calibration for low occupancy channels tubes are grouped according to physical properties. Each tube has first its own characteristics which influence its gas gain, e.g. wire properties. The next higher logical group is a module of 16 tubes which share the same electronics. Four modules on top of each other share the same HV supply channel and represent a HV group. 2×4 modules in two adjacent HV groups form a gas group and $4 - 5$ gas groups are supplied by the same gas manifold channel. All these groups may show correlated gas gain variations, like e.g. the change of HV settings in a HV group or an isolated, leaking gas group. Thus, all channels of an individual group contribute to the group median and the corresponding A is corrected for higher level group medians, e.g.

$$A_{TUBE} = A/m_{DET}/m_{GG}/m_{HV}/m_{MOD} \ , \tag{4.4.2}$$

where DET denotes the top level median, corresponding all tubes, and $GG/HV/MOD$ the median of the gas group / HV group / module of tube, denoted $TUBE$. Thus, global fluctuations are absorbed by higher level groups and the reaction time to gas gain variations is decreased.

Apart from the signal enhancement due to gas gain, the partial densities directly influence the primary ionization and the photon absorption probability. Hence the shape of a spectrum is a function of partial densities. This leads to the main drawback of this method. As it relies on a constant relation between median and MPV of a distribution, a systematic deviation is introduced by changes in the spectrum. Accordingly, the TRD has to be operated in constant gas conditions and the loss of partial pressures has to be corrected by gas refills.

The performance of the gain calibration algorithm is shown in figure 4.50 for atmospheric muon data and in figure 4.51 for space data. The variation of most probable pulse height (mpv) as function of time is canceled out by the gain calibration algorithm. The relative width, quantified by the ratio of root mean square to mean of the mpv distribution, is reduced from 1.9 to 1.2 % for atmospheric muon data and from 35.9 to 1.9 % for space data. The main difference between the two data samples is the increased duration for space data and hence a larger variation in gas parameters, including HV readjustments observable as steps in the uncorrected mpv evolution. The response time of the calibration method at the largest observed step is illustrated in figure 4.52. The staggered running median is capable to follow the HV readjustment, leading to a drop of the median value from ~ 125 ADC to ~ 45 ADC, within ~ 5 minutes.

The gain calibration method is not only capable to correct for time-dependent variations but also for spatial variations in the different detector channels at given time. To evaluate this correction the mpv for each detector module in the considered period is determined

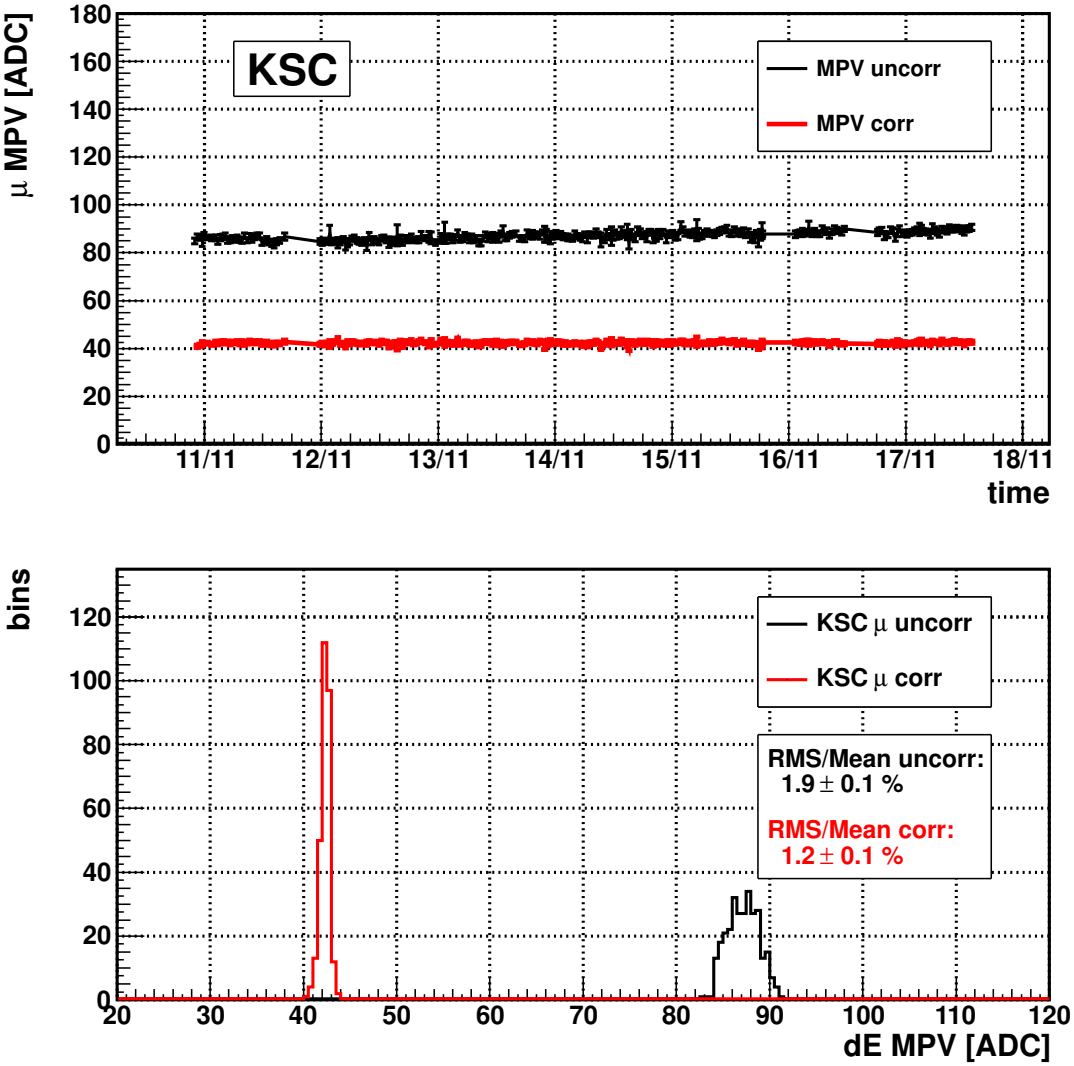

Figure 4.50: Gain correction performance for atmospheric muon data. The increase of uncorrected most probable pulse height (black) observed as function of time (top) is compensated by the correction algorithm (red). The relative width of the distribution of most probable values (bottom) is decreased.

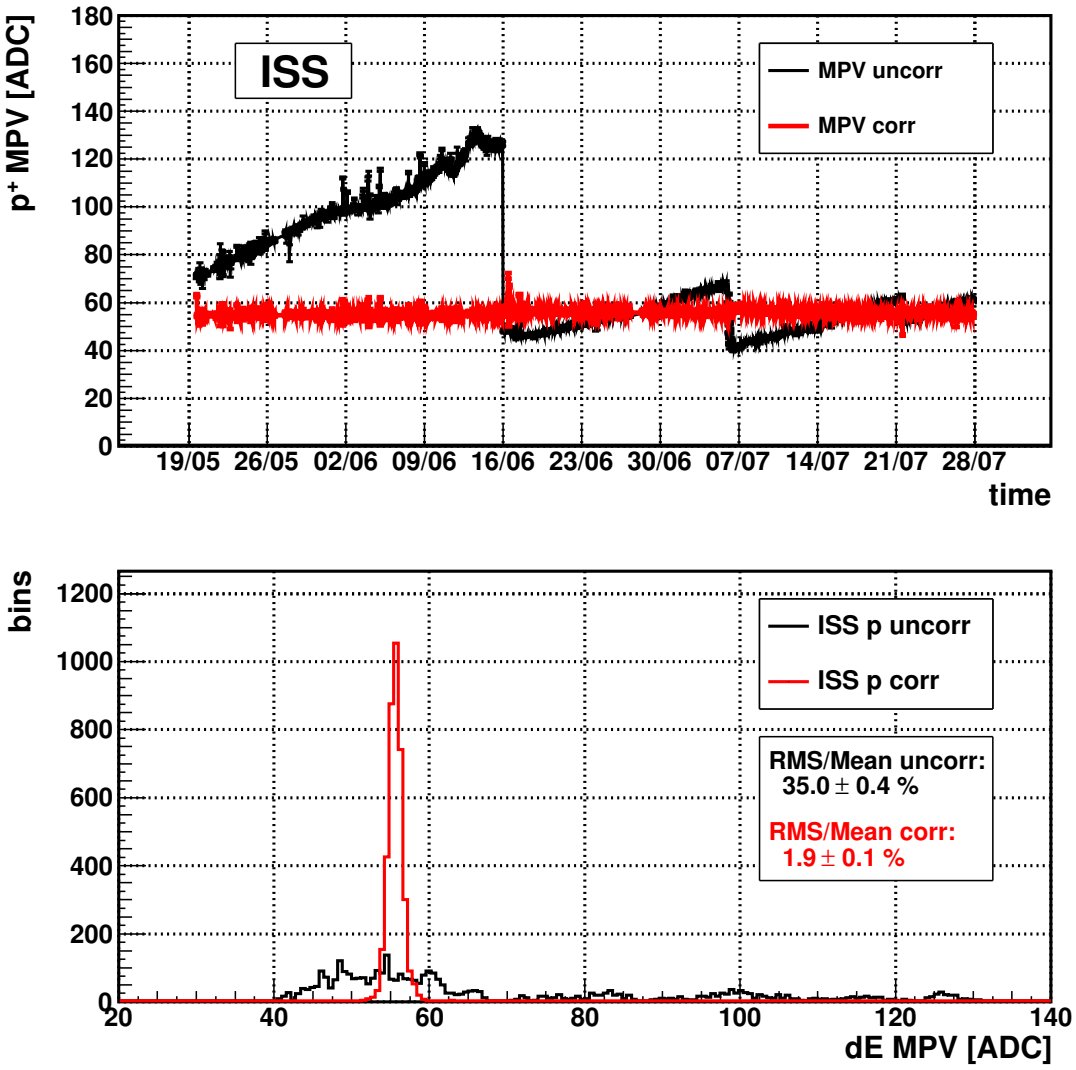

Figure 4.51: Gain correction performance for space data. The variation of uncorrected most probable pulse height (black) observed as function of time (top) is compensated by the correction algorithm (red). The relative width of the distribution of most probable values (bottom) is decreased.

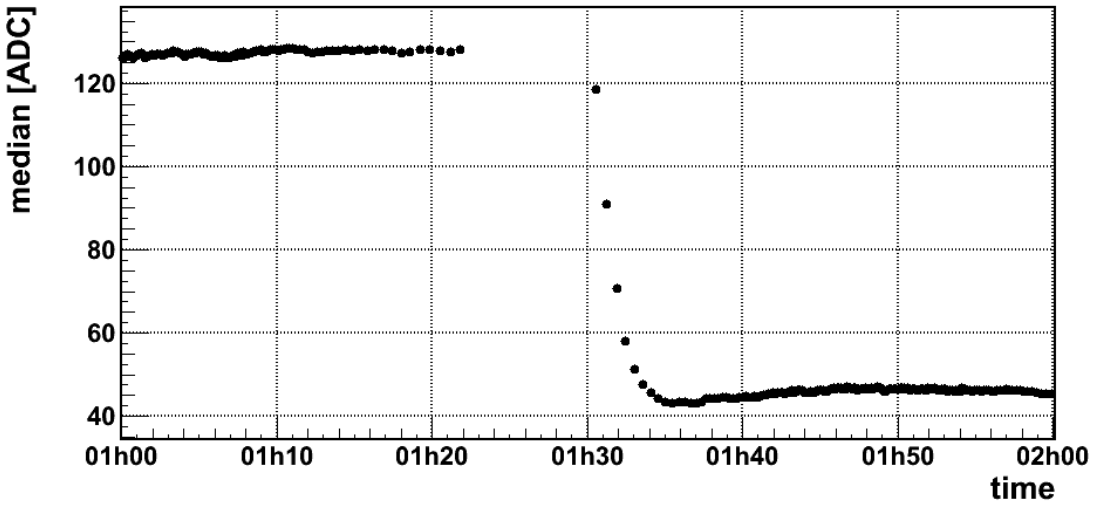

Figure 4.52: Response time of gain calibration method. The staggered median associated to one tube converges after HV readjustments to a new value within a few minutes.

separately and shown in figure 4.53 for atmospheric muon data and in figure 4.54 for space data. The gain calibration method improves the uniformity of the module mpvs. The relative width of the mpv distribution is reduced from 6.4 to 3 % for atmospheric muon data and from 6.6 to 1.6 % for space data, where the difference of about factor 2 is introduced by lower fluctuations at the edge of the detector in space data due to quadi-isotropic particle flux and thus increased statistics.

The performance of the gain calibration and a motivation for the staggering logical gain groups becomes evident when comparing the pulse height spectra of an isolated group of channels to the rest of the detector as function of time in figure 4.55. The loss of TRD gas, mainly in form of CO_2 diffusion, leads to a rise in gas gain and hence in most probable pulse height. High voltage adjustments, necessary to compensate the increase in gas gain, can be seen here as distinct drops to lower values. In the presented period the TRD was operated with closed flipper valves to separate different gas manifold channels, observable as a deviation of mpvs in specific sub-periods. It became evident that one of the gas groups, gas group GG-4, has a higher gas loss than the detector average. By applying the gain correction the time dependency and the individual behavior of GG-4 is mitigated. The remaining difference at about June 16th is expected to arise due to the change in the shape of the pulse height spectrum caused by the significantly lower gas density. Only in this period the difference in signal between the pulse GG-4 and the rest of the detector went up to a factor $\lesssim 2$. The impact of gain correction on single tube signal distributions of proton and lepton events is discussed in section 4.4.5.

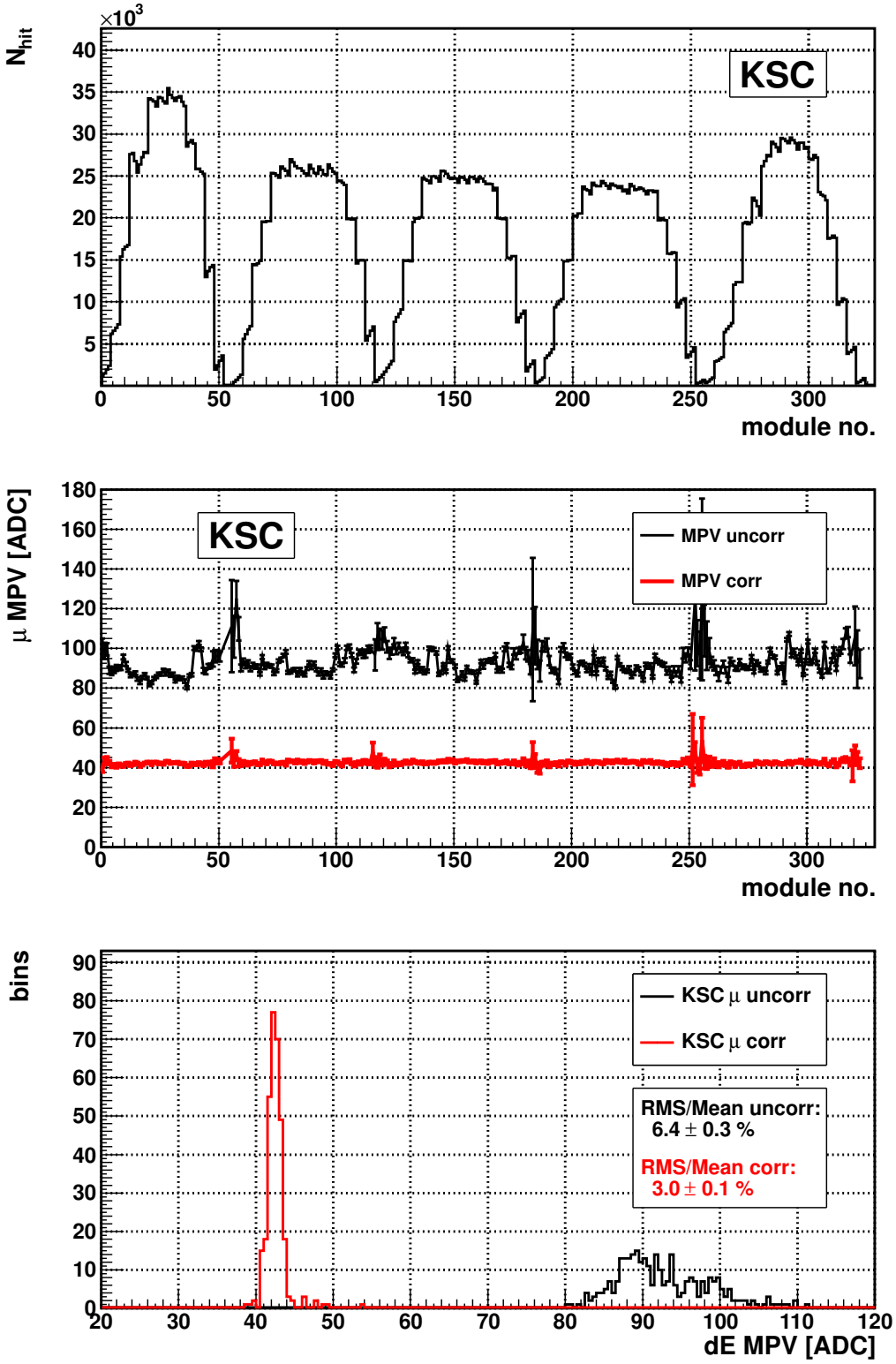

Figure 4.53: Spatial uniformity after gain correction for atmospheric muons. *Top:* total number of TRD hits on tracks in each of the 328 TRD modules. *Center:* uncorrected (black) and gain corrected (red) most probable pulse height observed in the TRD modules. *Bottom:* relative width of the corresponding most probable value distributions.

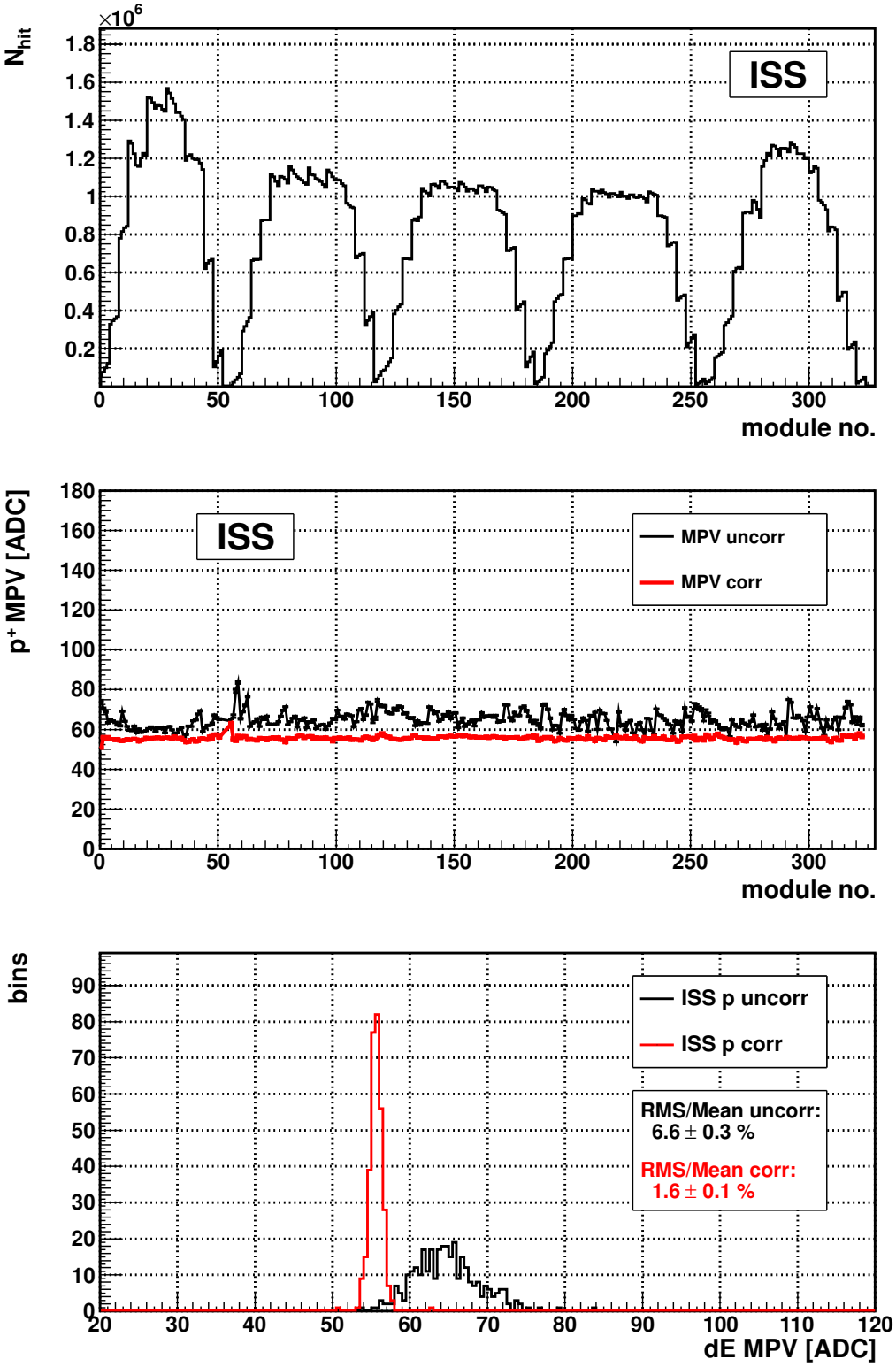

Figure 4.54: Spatial uniformity after gain correction for space data. *Top:* total number of TRD hits on tracks in each of the 328 TRD modules. *Center:* uncorrected (black) and gain corrected (red) most probable pulse height observed in the TRD modules. *Bottom:* relative width of the corresponding most probable value distributions.

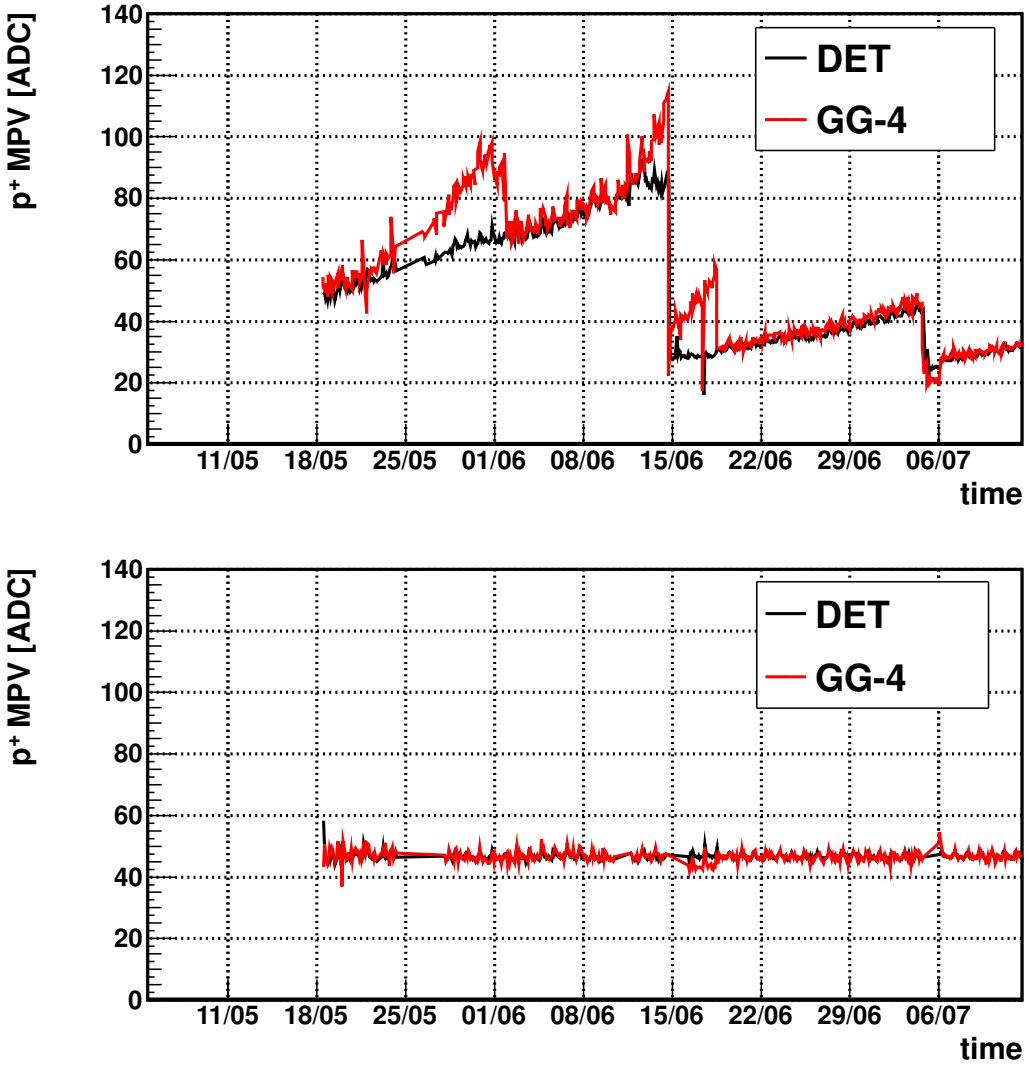

Figure 4.55: Time evolution of the most probable proton pulse height of gas group GG-4 (red marker) compared to the detector average (black marker) before (top) and after gain calibration (bottom).

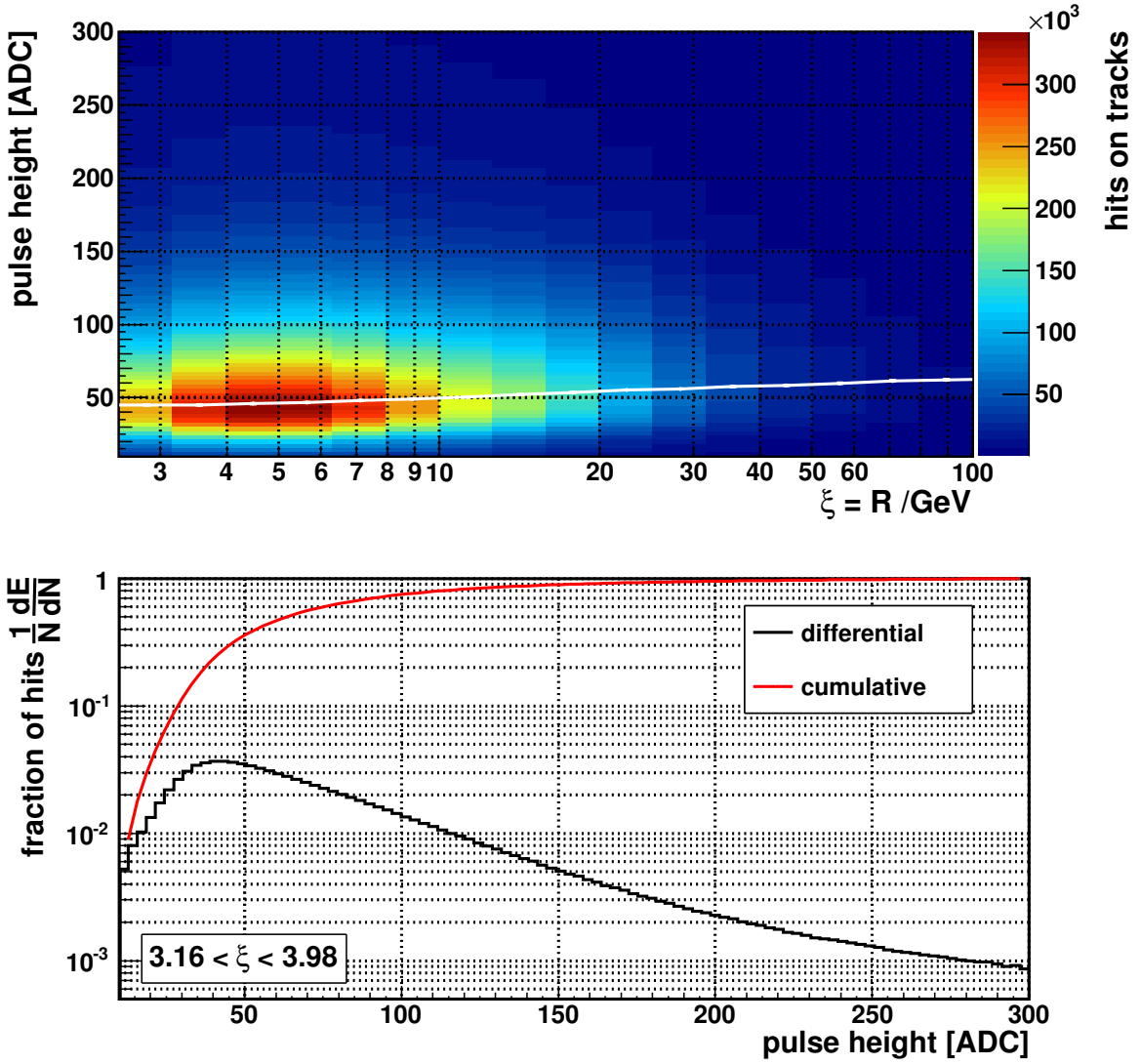

Figure 4.56: Cumulative pulse height spectrum as function of particle rigidity. For the developed correction the distribution of pulse heights (top) for a given value of variable ξ is turned into a cumulative one (bottom).

4.4.2 Particle Rigidity

Following the approach in [73], the dependency of the measured pulse height on particle rigidity, denoted $\xi = R/\text{GeV}$ here, is determined and corrected for. Hereby, the pulse height distribution is used and not only its most probable value. This becomes especially important when going to low number of collisions, e.g. short path length, where the shape of the distribution is changing more significantly (see section 3.2).

In the initial step the differential and the cumulative pulse height distributions are determined (see figure 4.56). Then, as illustrated in figure 4.57, the values dE_i of pulse heights for defined values of the inverted cumulative spectrum are stored as function of ξ. A target value ξ' for the correction is chosen and the values dE_i are plotted in dependency of dE',

being the values dE_i at ξ'. The resulting data points for a given ξ can now be approximated analytically. A linear scaling of the pulse height spectrum would result in a straight line with slope $\neq 1$. Here, the two parameter fit in [73], corresponding a linear function, was modified to a second order polynomial function to describe the observed dependencies. Now any pulse height dE for a given ξ can be corrected to a corresponding signal at ξ' by taking the value $f_{\tilde{\xi}}(dE)$ of the corresponding curve at dE by $dE_{corr} = f_{\tilde{\xi}}(dE)$. For computational processing the fit parameters are stored for fixed ξ and interpolated in between.

This polynomial correction of parameter dependencies is for rigidity or rather $\beta\gamma$ correction of space data. The performance of the correction is shown in figure 4.58 for atmospheric muon data and in figure 4.59 for space data. The relativistic rise in particle rigidity is corrected out by the presented algorithm. The relative width of most probable values is reduced from 8.4 to 4.4 % for atmospheric muon data and from 13.4 to 1.8 % for space data. The lower performance for muons above 300 GeV is presumably generated by the commence of transition radiation, which distorts the approximation of a landau function and pulls the mpv to higher values.

4.4.3 Path length

The energy deposited inside the gas-filled tubes depend on the amount of matter traversed by a particle, which is the product of density and path length l. The path length itself can be calculated if the particle track and the tube alignment is known. One solution would be to extrapolate the Tracker track into the TRD as its spatial and angular resolution is higher than for the TRD. This approach is hindered by the upper TOF which is in between the Tracker and the TRD and has a radiation length of about 0.1 X_0. In this dense material the probability for scattering is enhanced leading to a kink in the particle trajectory. Commonly, the deviation from the original particle direction is represented by the width Θ_0 of the projected angular distribution gained by the use of a Gaussian approximation for the central 98% region [39]. This can be calculated for given momentum p, velocity βc, charge z and material thickness in radiation lengths x/X_0 as:

$$\Theta_0 = \frac{13.6\,\mathrm{MeV}}{\beta c p} z \sqrt{x/X_0}[1 + 0.038 \ln(x/X_0)] \ . \tag{4.4.3}$$

Hence for a 2 GeV proton and $x/X_0 = 0.1$ the angle is $\Theta_0 \approx 2.34$ mrad $\approx 0.14°$ leading to an uncertainty in the extrapolation from the upper TOF to the center of TRD of about 1.2 mm. This is in the same order of magnitude as the single hit resolution in one TRD tube $6\,\mathrm{mm}/\sqrt{12} \approx 1.7\,\mathrm{mm}$. As the uncertainty of the TRD spatial resolution is reduced by TRD track reconstruction and Θ_0 is dependent on particle type and momentum it is consequential to use the TRD track to calculate the path length. Additionally, the relative alignment of TRD to inner Tracker limits the precision of a extrapolation from inner Tracker

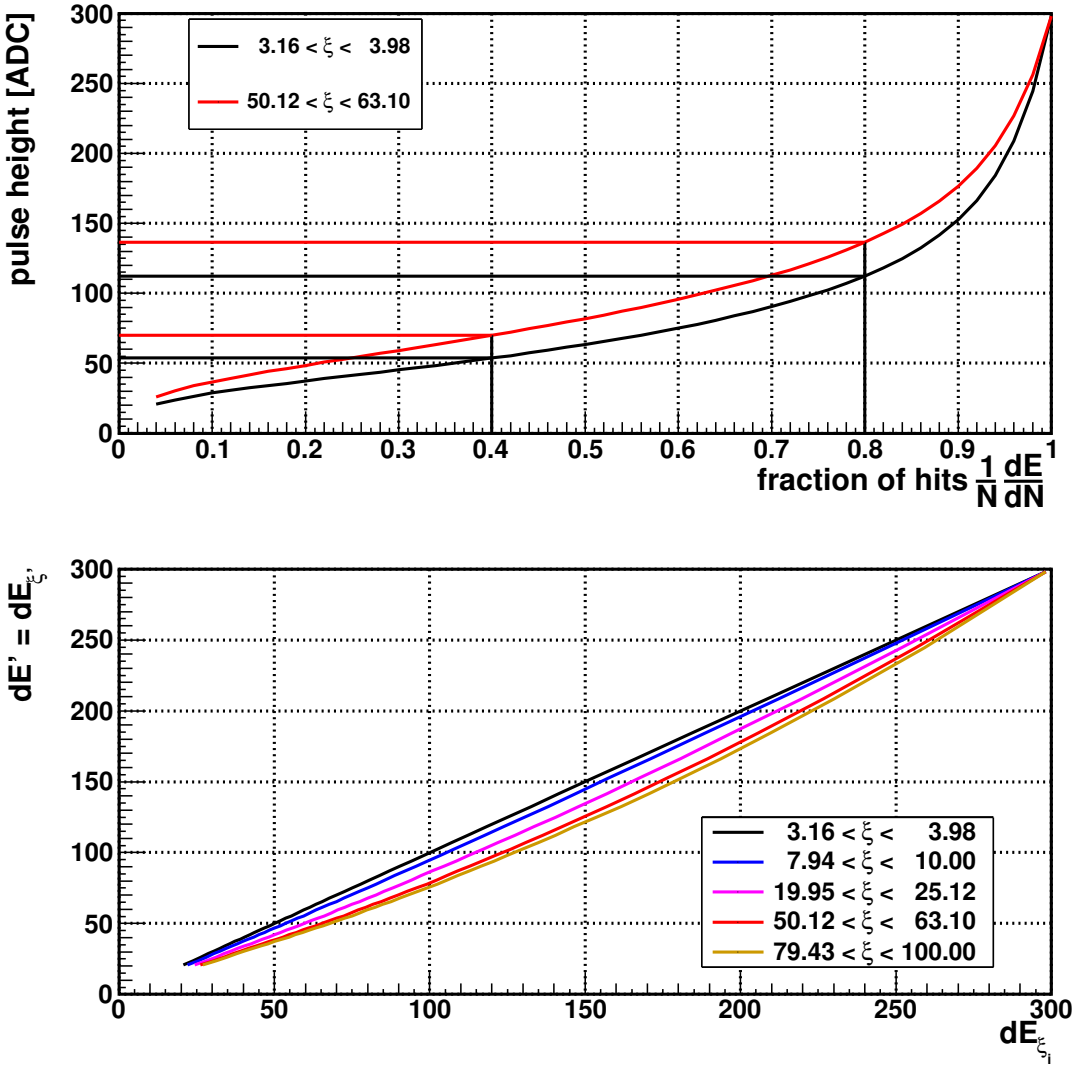

Figure 4.57: Polynomial correction of pulse height spectra. The pulse height values dE_i for fixed fractions of hits are retrieved from the cumulative pulse height spectra for all ξ intervals separately (top) and plotted against corresponding values for target value ξ' (bottom). Analytical fits to the data points return the corrected pulse height values $dE_{corr} = f_{\xi'}(dE)$.

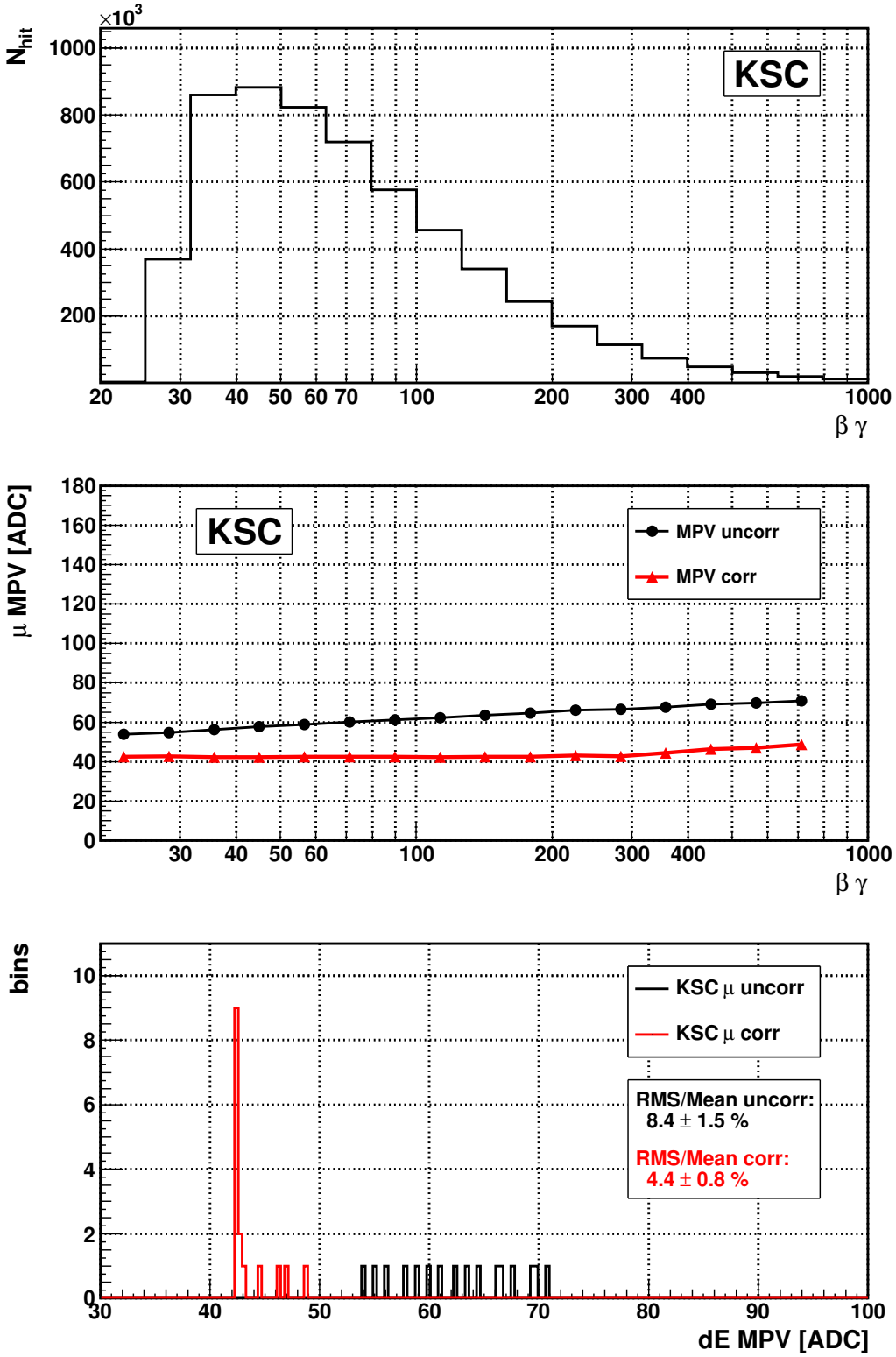

Figure 4.58: Particle $\beta\gamma$ correction performance for atmospheric muons. *Top:* distribution of $\beta\gamma$ for atmospheric muon events. *Center:* variation of uncorrected most probable pulse heights (black) observed as function of particle $\beta\gamma$ is compensated by the correction algorithm (red). *Bottom:* relative width of the corresponding distribution of most probable values is reduced.

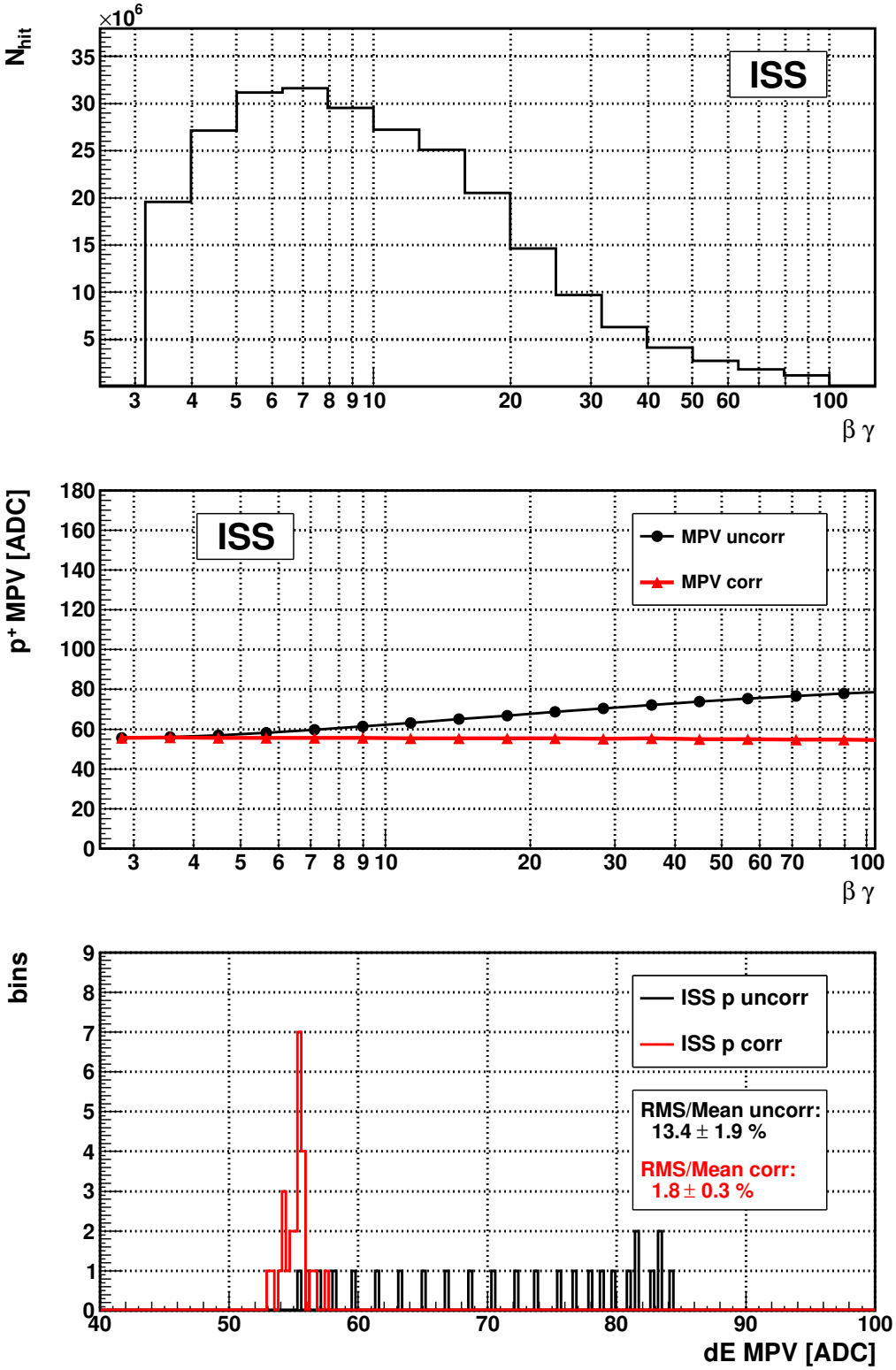

Figure 4.59: Particle $\beta\gamma$ correction performance for space data. *Top:* distribution of $\beta\gamma$ for proton events recorded in space. *Center:* variation of uncorrected most probable pulse height (black) observed as function of particle $\beta\gamma$ is compensated by the correction algorithm (red). *Bottom:* relative width of the corresponding distribution of most probable values is reduced.

to the TRD even for high momentum particle with $\Theta_0 \to 0$.

An algorithm has been developed to calculate the length of track segments inside a tube for a given track and to correct for the path length identical to the polynomial correction approach in section 4.4.2. The performance of the path length correction is shown in figure 4.60 for atmospheric muon and in figure 4.61 for space data. Two regions in the uncorrected correlation of most probable pulse height and path length can be identified: an upper region with an approximately linear correlation, at about $dx \gtrsim 3\,\text{mm}$ containing $\sim 90\%$ of hits, and a lower region with almost no dependency. This non-linearity arises partially from the fact that the path length could not be determined exactly due to the limited tracking resolution. Low path lengths can just be achieved when the track is crossing the tube close to the tube wall. In this sensitive region a small absolute change in the radial distance can change the path length dramatically. Additionally, the mean number of ionizing collisions scales with the traversed amount of matter and the fluctuation around the mean is increased for lower mean values (see section 3.2). Hence, the correlation of most probable pulse height and path length is expected to be non-linear, especially for low mean number of ionizing collisions corresponding to low path lengths here. The main reason for the observed non-linearity is expected to be the influence of electronics noise represented by the pedestal and its width (see section 3.3). For low path lengths the most probable pulse height is approaching the pedestal distributions at $\lesssim 15\,\text{ADC}$ and the maximum of the distribution cannot be determined anymore.

The chosen target value for the applied polynomial correction is 6 mm, where most of the hits are located. There is an upper limit on the path lengths due to geometrical acceptance. A simple estimation shows that for a track with an incident angle of 23° to a tube wire the expected path length is $l_{23^\circ} = \frac{d_{tube}}{cos(23^\circ)} \approx 6.5\,\text{mm}$. This angle is in good approximation the highest observed incident angle for the applied selection (see figure 4.19). The estimation relies on the assumption that tracks are going straight through the center of the wire along the wire dimension. Loosening this requirement leads to lower values of l.

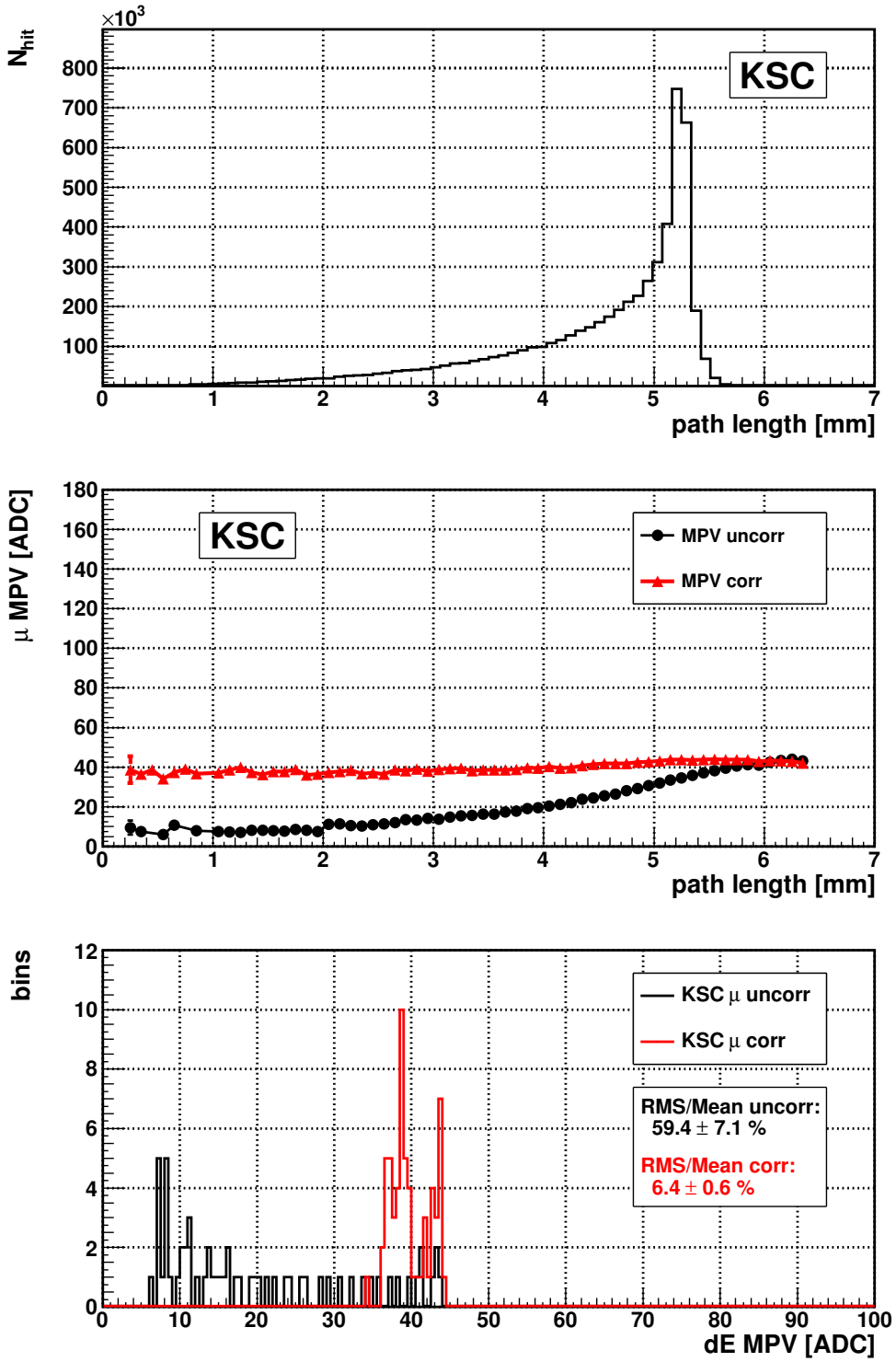

Figure 4.60: Path length correction performance for atmospheric muon data. *Top:* distribution of reconstructed path lengths for atmospheric muon events. *Center:* variation of uncorrected most probable pulse height (black) observed as function of path length is compensated by the correction algorithm (red). *Bottom:* relative width of the corresponding distribution of most probable values is reduced.

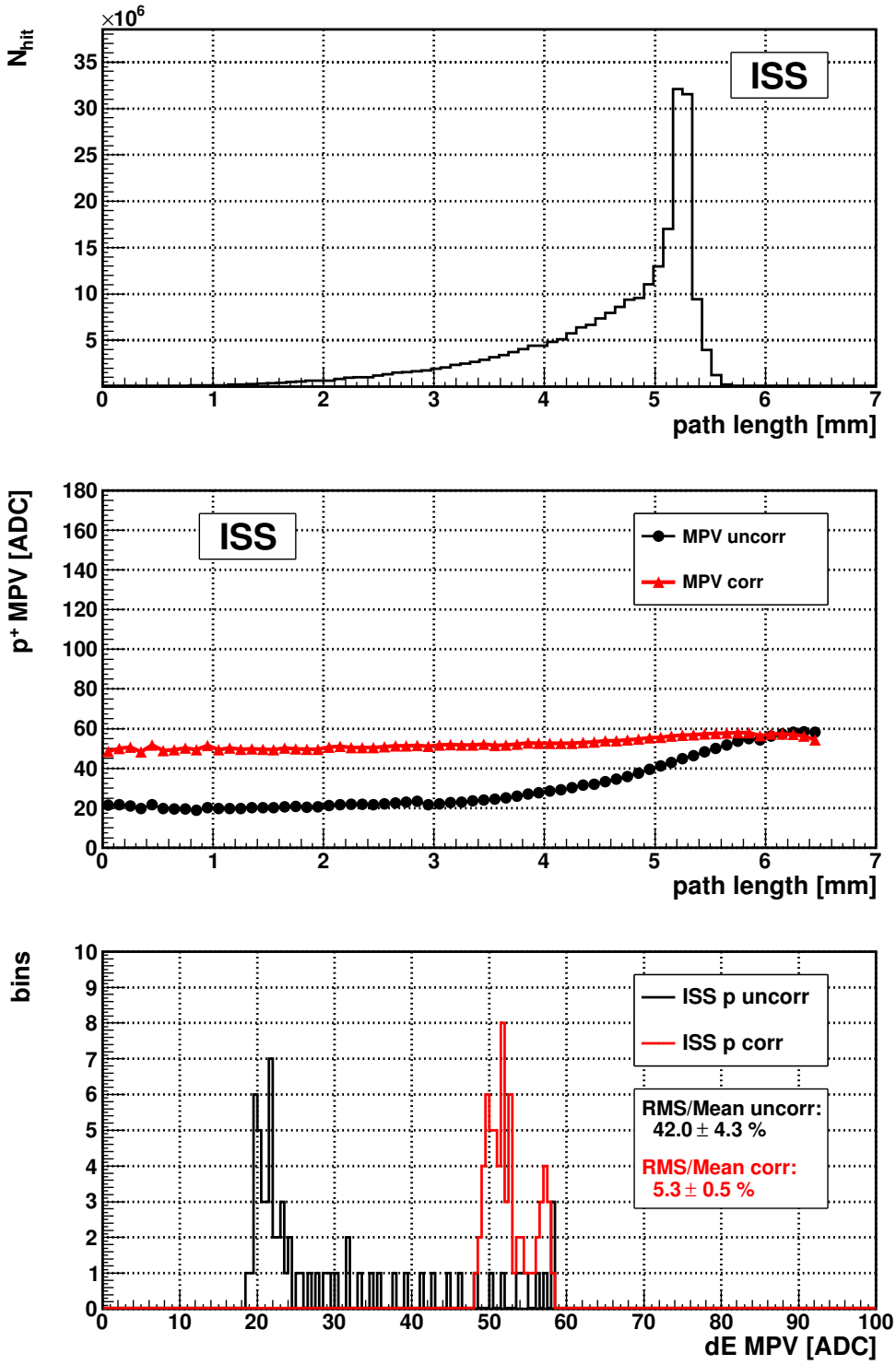

Figure 4.61: Path length correction performance for space data. *Top:* distribution of reconstructed path lengths for proton events in space. *Center:* variation of uncorrected most probable pulse height (black) observed as function of path length is compensated by the correction algorithm (red). *Bottom:* relative width of the corresponding distribution of most probable values is reduced.

4.4.4 Temperature Gradient

The TRD Gas System, presented in section 2.1, is a closed system. An overall increase of temperature does not change the mean density but the mean pressure in the TRD. The only way the temperature can influence the density, and hence the energy deposited in the tubes, is a gradient inside the detector. The TRD gas pressure and total volume is assumed to be constant. Therefore, the local density is inversely proportional to the local temperature:

$$pV = nRT = \frac{m}{M}RT \Rightarrow p\frac{M}{R} = const. = \rho T \Rightarrow \frac{\rho}{\rho_0} = \frac{T_0}{T} \ . \tag{4.4.4}$$

As the energy deposition is predominantly proportional to the density, the temperature dependency of a hit can be corrected according to $A' = A\frac{T_0}{T}$ if the mean temperature T_0 inside the TRD and the local temperature T at the hit position are known.

To measure the temperature profile, there are in total 404 temperature sensors installed on the mechanical support structure of the TRD (see figure 4.62). The implemented twofold redundancy limits the number of concurrent measurements to 202 positions. The sensors are located on strips of about 10 sensors each and can roughly be divided according to their position into bulkhead, wall and outer sensors (see figure 4.63). The first two sensor types are located on the corresponding mechanical structure and the third ones are located outside the TRD mechanical structure close to the connector patch panel. The TRD is packed into multilayer insulation (MLI) to suppress fast temperature variations, e.g. during an orbit cycle. The MLI increases the time constant of the thermal conductivity between its out- and inside. The first sensors observing an upcoming temperature variation are the outer sensors and the temperature variation in the center of the detector is decelerated.

To convert the temperature data at distinct positions to a temperature at a given position a 3D map of the temperature is fitted. The developed fit function consists of polynomials of second order in each projection (x,y,z) and temperature θ_0 at the origin of the TRD coordinate system:

$$\theta(x,y,z) = \theta_0 + p_x x + p_{x^2}x^2 + p_y y + p_{y^2}y^2 + p_z z + p_{z^2}z^2 \ . \tag{4.4.5}$$

This function is fitted to the 190 inner temperature sensors by a Simulated Annealing algorithm [94], which has been implemented into the AMS software framework in the scope of this thesis. The incorporated Metropolis algorithm, used to escape local minima in a general parameter space Θ, is closely related to the cool-down in solid-state physics, where crystals can recover from structural defects, leading to local potential minima. Slowly decreasing the temperature reduces the probability to have such defects after cool-down. In Simulated Annealing an equivalent temperature parameter T is introduced and decreased with each minimization step. The probability for a step to higher 'potential' $f(\Theta)$, corresponding to χ^2 in the case of minimization, is $e^{-\frac{\Delta f}{T}}$.

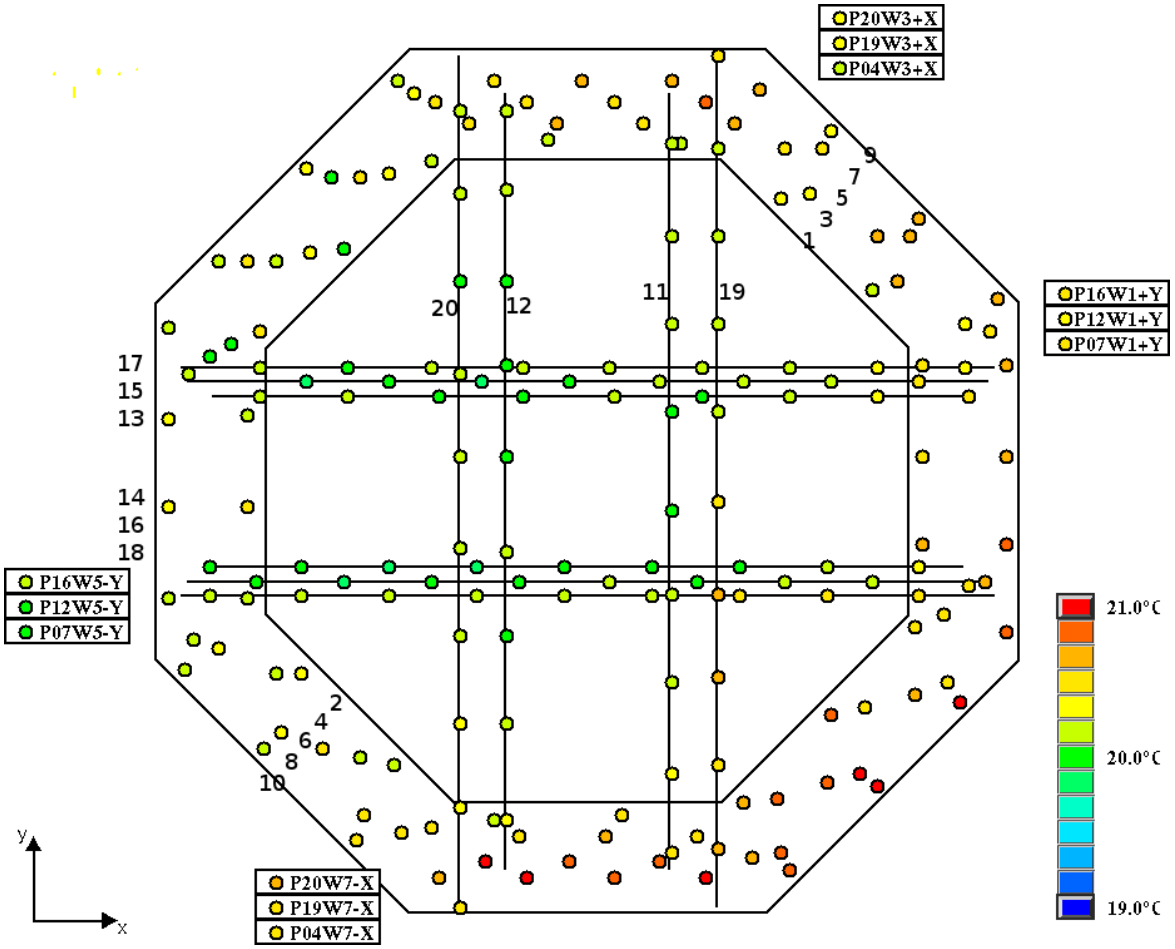

Figure 4.62: The TRD temperature profile is measured redundantly at 202 positions in the TRD with a total of 404 temperature sensors. This example from ground operations at KSC shows the approximate positions of the sensors and the measured temperature in an exploded view from the top of the TRD. The central lines denote sensor strips along the TRD bulkheads. Sensors located outside of the TRD volume, are listed in boxes close to their positions.

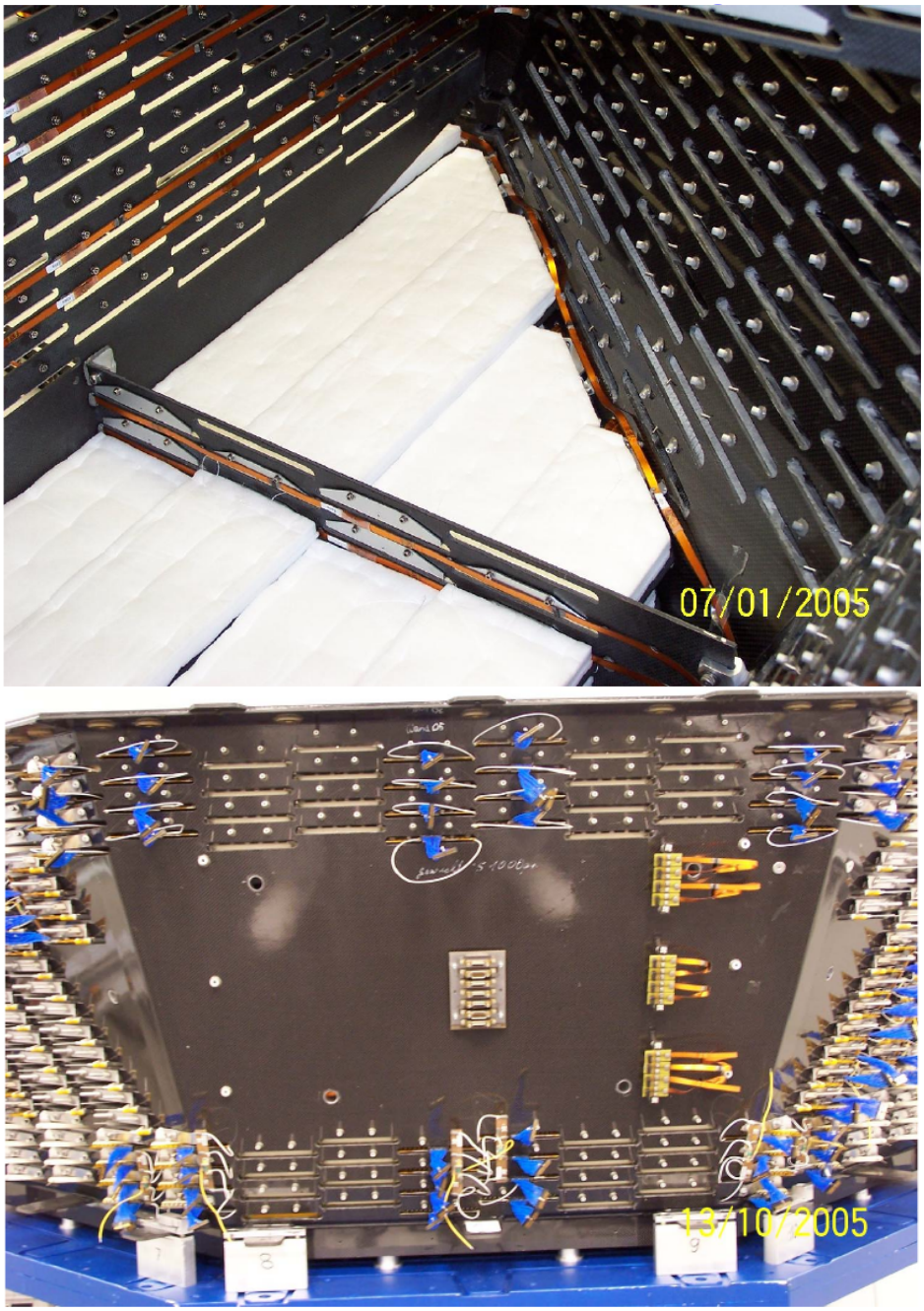

Figure 4.63: Integrated TRD temperature sensor strips. *Top:* In the lower and in the left part of the picture some strips (golden-brown bands) mounted on the bulkheads are shown. On the right a single sensor strip mounted on the inner side of the TRD outer walls can be seen. *Bottom:* A view on octagon wall number 5 of the assembled TRD detector. The temperature sensors located outside the TRD volume are shown here on the right part of this wall, where the sensor strips are connected to the patch panel [93].

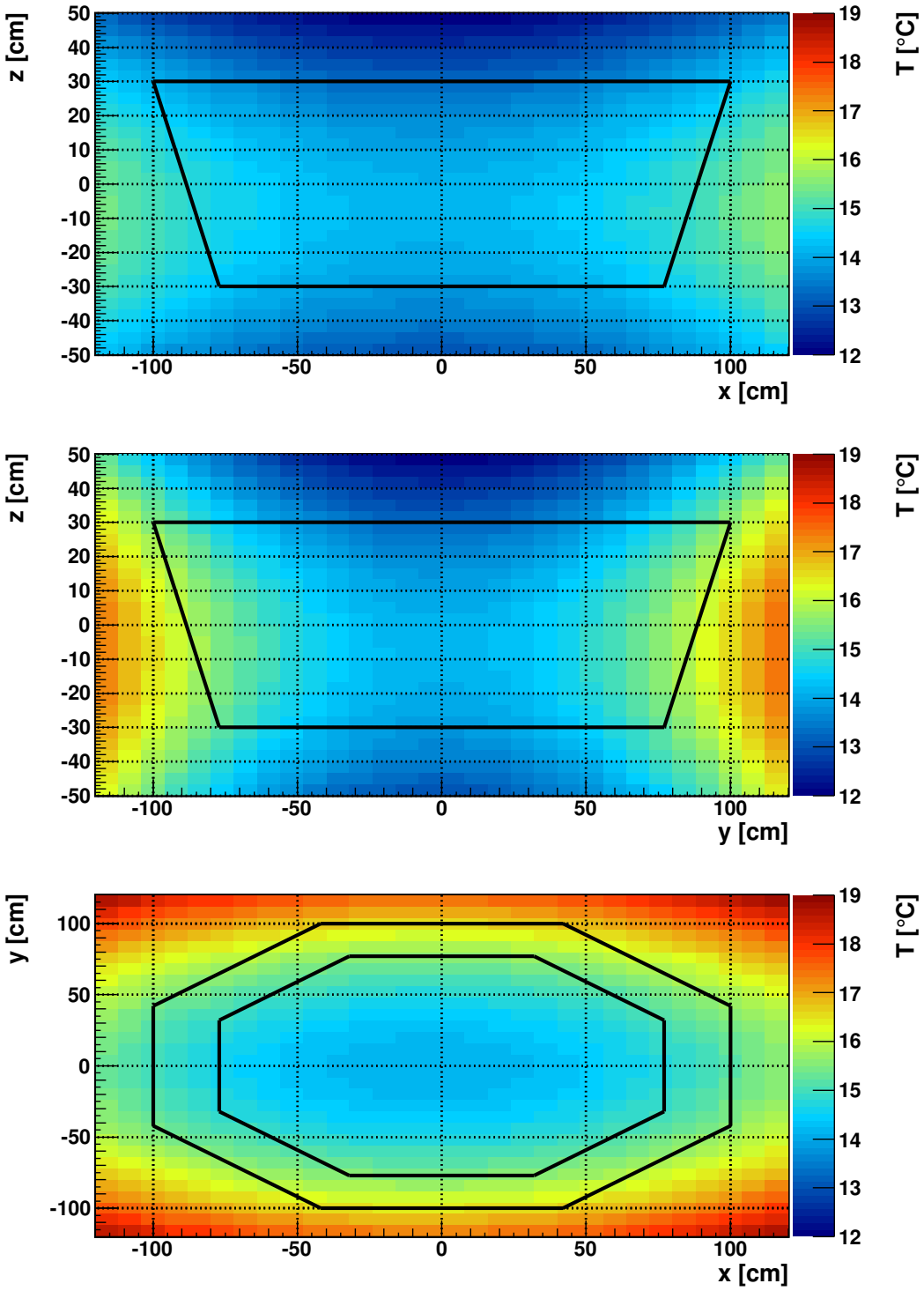

Figure 4.64: Temperature profile in the TRD in xz (top) ,yx (center), xy (bottom) in the TRD local coordinate system with the geometrical center of the TRD (0,0,113.5 cm) as origin. The profile is fitted to the inner TRD temperature sensor data. The extrapolation outside the TRD volume (black lines) does not reflect realistic temperatures.

An example fit to a temperature dataset taken in space is shown in figure 4.64. The warmest spots are located on the $\pm y$ side of the TRD. There are two main heat sources: solar radiation (SR) and detector electronics (DE). DE mainly occurs on the $\pm y$ size of the TRD, where the readout electronics are located. SR depends on the ISS orbit and may in principle irradiate from any direction. The TRD is shielded from SR by the ISS and AMS-02 detector components. The incidence of SR might shift the axis of symmetry from the origin in the xy projection. Additionally the top of the TRD is cooled indirectly by the cooling system of the topmost Tracker layer. The resulting profile looks like a perpendicular sand-glass slightly shifted from the origin here by about (-10,0,-5).

The average deviation of single temperatures from the fit is shown in figure 4.65. For the period considered here the average deviation is $\langle \Delta T \rangle \approx 0.68\,\mathrm{K}$. High values of $\langle \Delta T \rangle$ typically occur when the gradient, quantified by the span of highest and lowest measured temperature $T_{max} - T_{min}$, in the TRD is large. In conclusion large gradients lead to profiles which cannot be described well by the applied fit function. One should keep in mind that the dallas sensors have a limited resolution on the order of 0.5 K and are not calibrated. Therefore the mean deviation is consistent with the intrinsic single sensor uncertainty.

The correlation between the solar incident angle the reconstructed temperature profile as function of time is indicated in figure 4.66. Inclination and azimuth angle characterize the solar vector, pointing towards the sun, in the AMS reference frame. The position of an extremum in the temperature profile is difficult to interpret as it may suddenly 'jump' to another position. Imagine a 'U'-shaped temperature profile in the TRD. In case one side of the U is higher than the other the maximum might jump from one side to the other. However, some correlations are observable. In the period of high beta angle shown here, the inclination is low and the azimuth angle close to zero. This means solar radiation irradiates from $+x$ direction and hence the $+x$ side of the detector gets warmer and the $-x$ side cools down. In the low beta period shown here, the inclination is oscillating with larger amplitudes around 0 and hence the similar effect is not clearly observable. Additionally, the relative orientation of the ISS was changed around mid of July leading to solar vector variations which are clearly traceable in the fitted temperature profile. Additional parameters, like shadowing effects of ISS components and the operation of detector heaters, are neglected here to reduce the multi-parameter space.

The correlation of pulse height to local temperature determined by the 3D profile fit is presented in figure 4.67. For all runs in the period 07-18 July 2011 the temperature profile was fitted. The relative amplitude $\frac{dE-\langle dE \rangle}{\langle dE \rangle}$ and local temperature variations $\frac{T-\langle T \rangle}{<T>}$ of each hit on proton tracks are set in correlation. A linear fit to the most probable pulse height as function of temperature does not show the expected proportional dependency. The slope of 0.012 ± 0.007 is consistent with zero.

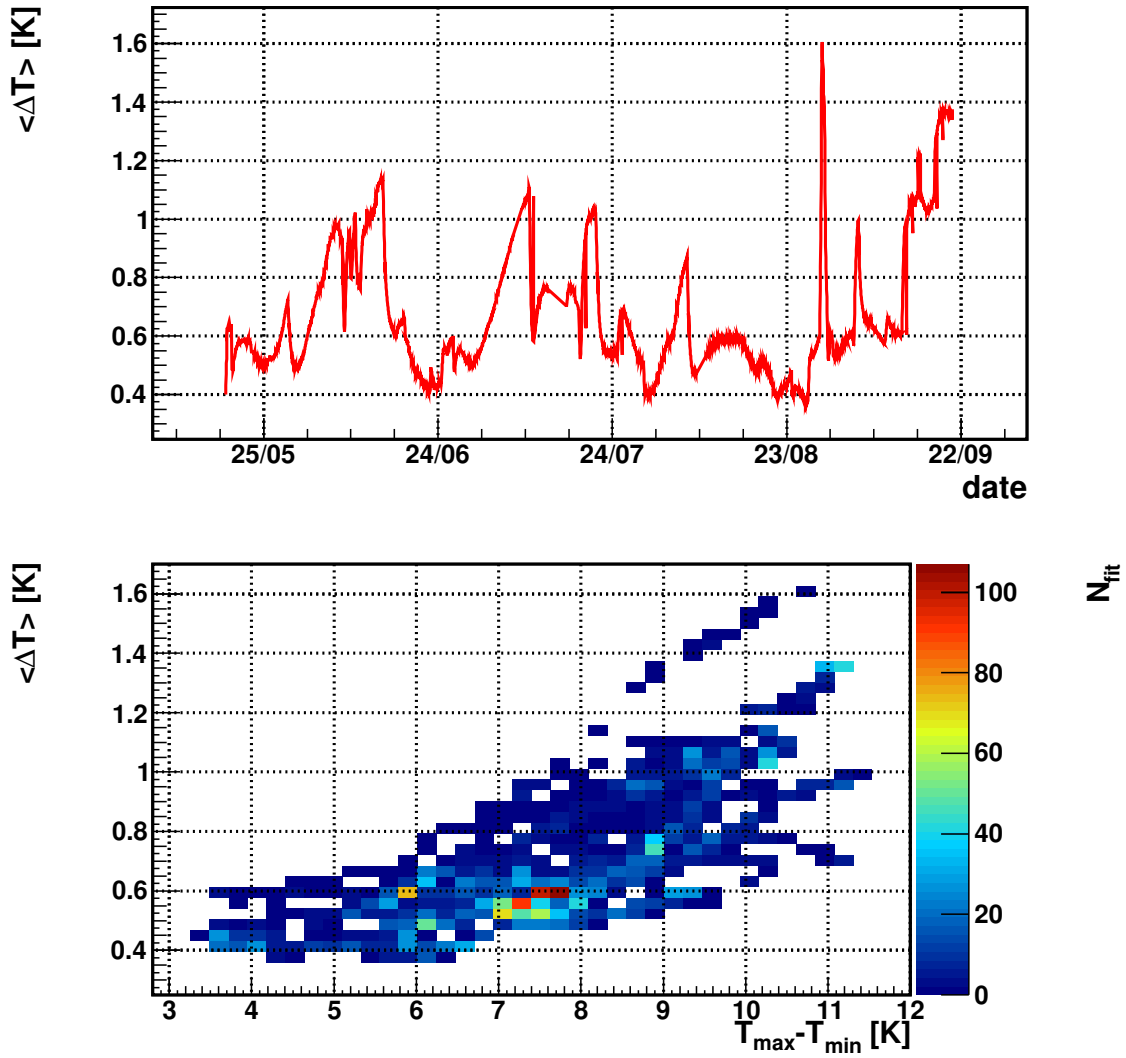

Figure 4.65: Mean deviation of measured temperatures from 3D-fit as function of time (top) and span of maximum to minimum (bottom). At low temperature gradients ($T_{max} - T_{min} \to 0$) the mean deviation of single sensor temperatures is on the order of the single measurement uncertainty of 0.5 K. Large gradients are not described well by the applied fit function.

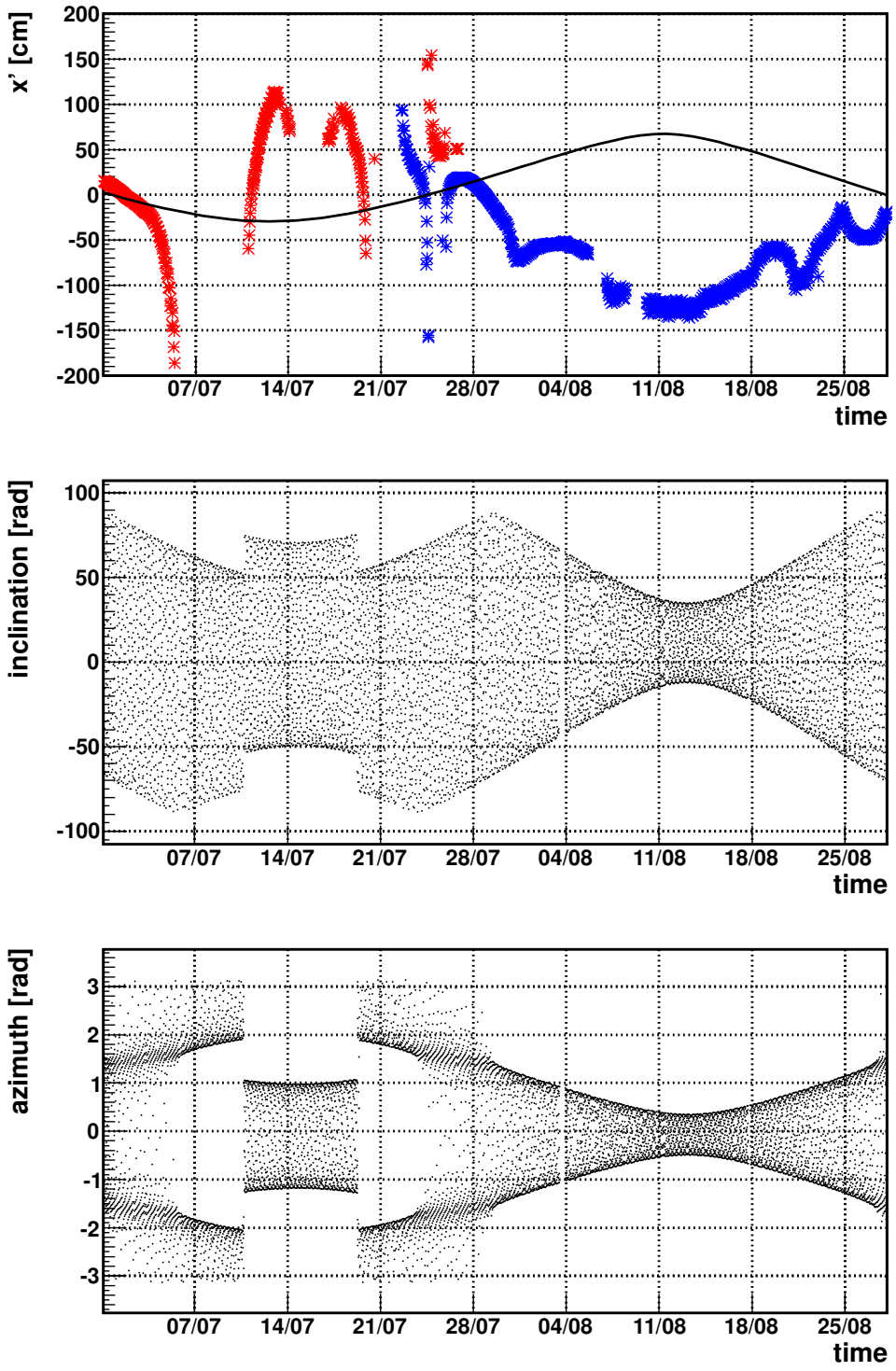

Figure 4.66: Time evolution of temperature extremum coordinate x'. *Top:* the location of the extremum of type maximum (red) or minimum (blue) as function of time. The beta angle is indicated by a black line. *Center:* inclination angle of the solar vector relative to the AMS xy coordinate plane. *Bottom:* azimuth angle of the solar vector in the AMS xy coordinate plane.

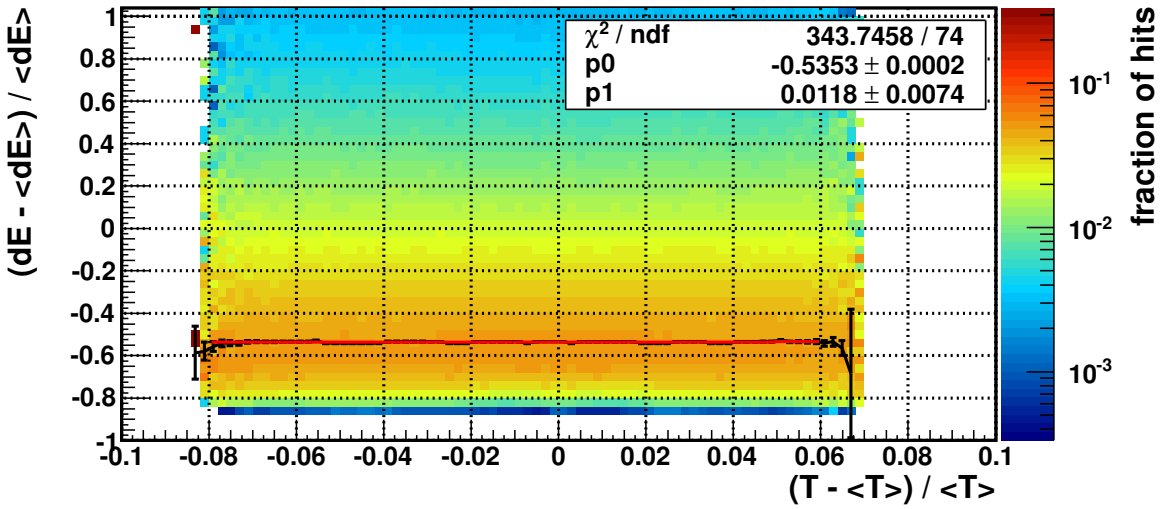

Figure 4.67: Correlation between hit pulse height and local temperature variation $\frac{T-<T>}{<T>}$, where local temperature T is determined by the 3D fit. Slices along y axis are normalized to area 1. The bin-wise most probable pulse heights (black data points) are fitted by a linear function (red line).

As no dependency of pulse heights on local temperatures could be observed this fit routine is only used to determine the temperature T_0 at the center of the TRD as function of time. The corresponding data are shown in the discussion of environmental parameters in the beginning of this section.

4.4.5 Impact on pulse height spectra

Typical pulse height spectra on selected TRD tracks are shown in figure 4.68. The pulse height spectrum of electrons can be divided into two components: ionization and transition radiation. Due to the low electron mass and its consequently relativistic velocities, ionization losses and transition radiation contributions are nearly independent of the electron rigidity above few GeV. As not necessarily all transition radiation photons are absorbed in the same layer as they are generated (see section 3.1) the fraction of energy deposited by corresponding photon absorption is increasing with the detector depth and saturated after the first layers. For beamtest pions both pulse height contributions depend on the beam energy. This leads to a rise of the most probable pulse height due to ionization (Bethe-Bloch) and to an increasing number of generated transition radiation photons, observable as fractional rise of the transition radiation contributions.

The impact of the combination of presented calibrations on the particle spectra are shown in figure 4.69. By reducing the variation of most probable values as function of time, detector channel, particle momentum and path length like presented in the previous sections also

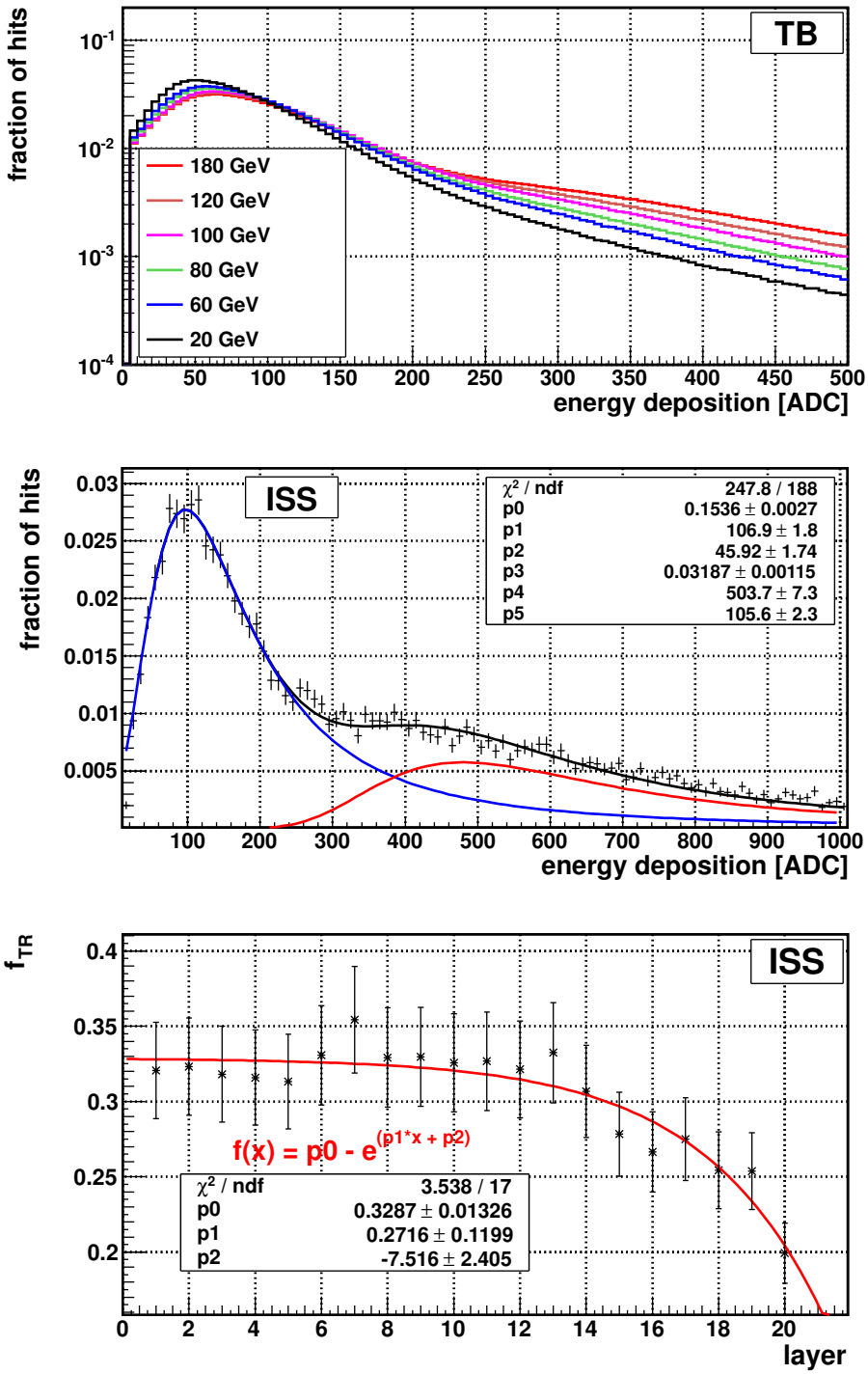

Figure 4.68: TRD pulse height spectra for pion and electron events *Top:* the ionization peak position is shifting for beamtest pion events to higher pulse heights with rising particle momentum (Bethe-Bloch) and the contribution of transition radiation is increasing. *Center:* the contribution of ionization (blue) and transition radiation (red) to the total electron spectrum observed in space is approximated by the sum of two landau functions. *Bottom:* the contribution of transition radiation to the total pulse height, quantified by the fraction $f_{TR} = \frac{I_{TR}}{(I_{TR}+I_{Ion})}$ of fit function integrals I, is shown for electron events observed in space as function of layer number.

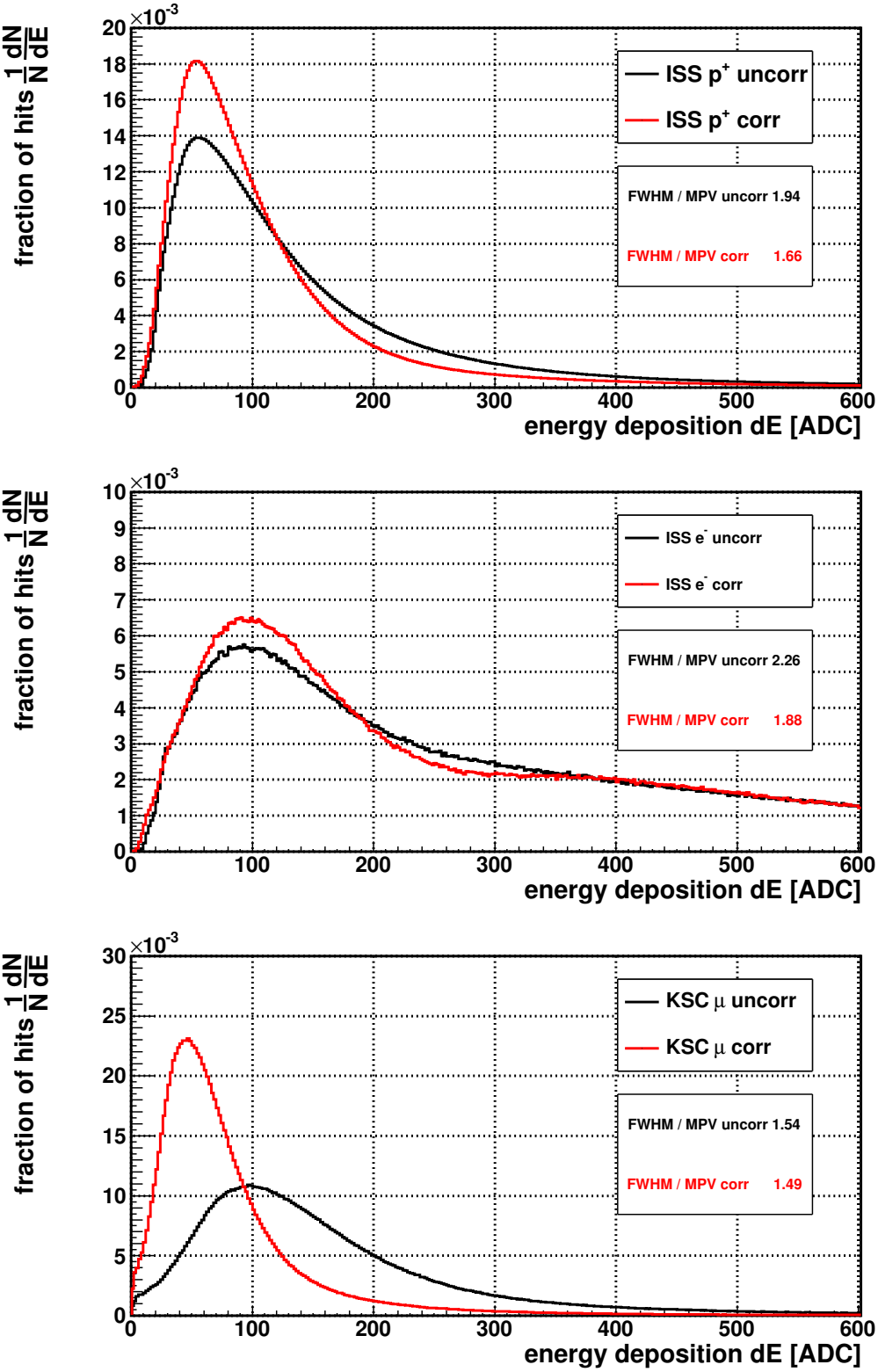

Figure 4.69: The impact of calibration on the pulse height spectra for proton (top), electron (center) and muon (bottom) events.

the width of the pulse height spectrum is reduced towards the intrinsic width generated by the energy deposition straggling (see section 3.2). The width of the landau spectrum is reduced for atmospheric muons, space protons and for space electrons. Additionally, the separation and resolution of the two peaks in the electron spectrum, associated with ionization solely and an additional transition radiation contribution, is enhanced.

4.4.6 MC Comparison

A Geant4 simulation of an isotropic muon flux is analyzed and compared to data in the following. The muon events are generated uniformly in $\log_{10}(P)$, $\cos^2\Theta$ and φ, with corresponding ranges $0.99 < P/\mathrm{GeV} < 2500$, $-1 < \cos\Theta < -0.7$ and $-\pi < \varphi < \pi$ on a cubic area of $a = 3.9\,\mathrm{m}$ width at $z = 195\,\mathrm{cm}$. In the comparison of simulated and reconstructed pulse height spectrum the effects of the time-dependent environment during data taking and the different particle spectra have to be taken into account. The former will be addressed by applying the presented gain correction algorithm. The latter can be addressed in two ways: either the simulation has to be weighted to the expected flux or the parameter space has to be divided into bins. It was decided to proceed with the second option because otherwise a prior knowledge of the muon flux is required and hence an additional source of uncertainty is introduced.

To determine the agreement of the spectra at given momentum P and zenith angle Θ a quality parameter χ^2 is introduced according to [95] The distribution of χ^2/n_A, where n_A is the number of bins, is shown in figure 4.70. In this comparison the most probable value (MPV) of data and simulation has been matched by a global correction factor of 0.6 to all data pulse heights. One can see that apart for two regions of increased χ^2/n_A the parameter space is characterized by $\chi^2/n_A \lesssim 3$. The low energy region of increased χ^2/n_A is expected to be caused by the high statistics on data events, which reveal systematic differences to the simulated expectation. Apparently the simulated spectrum provides the similar MPV but less fluctuations as indicated by the lower width of the distribution. This may indicate a higher gas density in simulation which is scaled to same MPV. At high particle momenta the amount of simulated transition radiation contribution is higher than observed. On the one hand this supports the idea of higher gas density in the simulation because the absorption of photons is proportional to the electron density. On the other hand it may also hint at unoptimized radiator material parameters for the simulation of transition radiation emission.

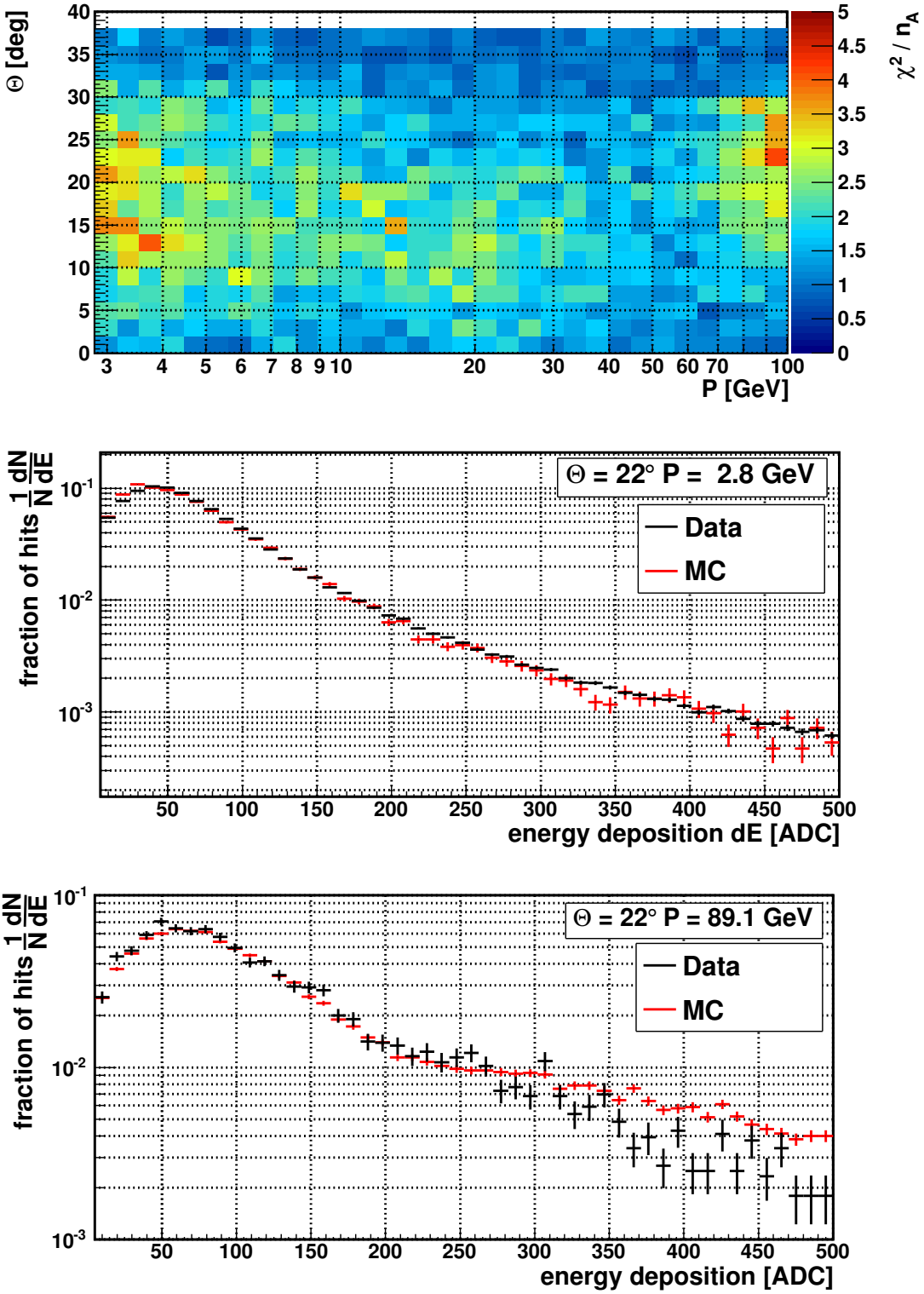

Figure 4.70: Comparison of pulse height spectra obtained from cosmic muon data and simulations. For each bin in the considered (P, Θ) parameter space a χ^2 value is calculated (top), quantifying the agreement between simulated and measured pulse height spectrum. Energy deposition spectra corresponding the low-(center) and high-momentum (bottom) regions of increased χ^2 are displayed.

4.5 TRD Particle Identification

The TRD is capable to differentiate between different particle types according to their energy depositions. The transition radiation effect allows to disentangle fast from slow particles at given rigidity, needed to separate leptons from hadrons. The basic concept of the identification algorithm is to compare the pulse heights on track with the expected pulse heights for different particle hypothesis in form of probability density functions (PDFs). In this so-called 'likelihood method' each particle hypothesis has an associated PDF and each event has its individual probabilities to match the hypotheses. The likelihood analysis is described in section 4.5.1. Its optimization and performance are discussed in section 4.5.2 and section 4.5.3 respectively.

4.5.1 Likelihood Analysis

The pulse height dE_l on track per layer l is calculated by summing up the corresponding single hit pulse heights. The single layer probability $P^p_{dE_l}$ for particle p hypothesis is determined by evaluating the associated PDF at the given pulse height value. The probability for an event signature to be generated by p is determined by multiplying all single layer probabilities $P^p_{event} = \prod_{l=1}^{N} P_{dE_l}$. As just layers with significant ($dE_l > 15$ ADC) pulse heights are taken into account the total probability is normalized by taking the N-th square root, where N is the number of utilized layers. Finally to compare different particle hypotheses the likelihood ratio is introduced as

$$L = -\ln\left(\frac{P^{p_j}_{event}}{\sum_{i}^{m} P^{p_i}_{event}}\right) \ , \tag{4.5.1}$$

where m is the number of hypotheses and p_j is the particle of interest (e.g. leptons). The negative logarithm is used to convert the typically small probabilities to order one values. The argument of the logarithm can be interpreted as the normalized fraction of the particle hypothesis probability. Accordingly, the likelihood value depends on the number of hypotheses. In general, two hypotheses are compared with the TRD likelihood method: hypothesis for proton and electron. As the TRD signal is independent of the particle charge sign, the two hypotheses also contain the corresponding antiparticles, antiprotons and positrons respectively. The decision which kind of particle type has passed the detector is based on the highest probability hypothesis and an upper limit on the likelihood value. A cut on the electron likelihood ratio $L = -\ln(P^e/(P^e + P^p))$ is used to identify leptons. The efficiency curve of the cut on the two particle samples, reflecting the identification performance of the TRD, is extracted by varying the cut value. The uncertainty on the identification efficiencies are in general close to either one for electrons or zero for protons. Therefore binomial uncertainties are calculated. As a trade-off has to be performed between efficiency and purity of

the identified electron sample the ratio of the two efficiencies, the so-called proton rejection, is introduced as $R = \varepsilon_e/\varepsilon_p$. The propagation of efficiency uncertainties to uncertainties on R has been developed by Dr. Obermeier following inter alia [96]. In a toy MC random events are generated according to the binomial approximation of particle efficiencies to determine the distribution of R_i. The most probable value of R_i defines R and the uncertainties are determined by the smallest confidence interval.

In figure 4.71 the electron likelihood ratio $L = -\ln(P^e/(P^e + P^p))$ and the corresponding distribution of pre-selected particles from space data, electron and proton events in momentum interval $3 \lesssim P/\text{GeV} < 100$, are shown. The corresponding distributions for beamtest data is shown in figure 4.72. Obviously, proton/pion and electron events can be separated by the likelihood method. The transition radiation effect manifests in a second peak for electrons in the logarithmic pulse height spectra at high pulse heights. This leads to a separation of electron and hadron distributions of L. A one-sided gaussian fit to the distribution of L for proton and pion events shows that the distribution of beamtest pions has a high purity while the distribution of protons in space is contaminated. The contamination in beamtest is suppressed by the controlled particle flux of charge one particles in combination with the external trigger system (see section 4.2.1). In space particles with higher charge or misidentified momentum passing the TRD mimic electrons, due to an increased ionization energy deposition, but might be classified by the TRD independent selection as protons. This effect is observable deep in the tails of the distribution on the 10^{-5} level and requires detailed studies. These few events limit the determination of the proton rejection. Accordingly, the proton rejection is decreasing towards low electron efficiencies in space data while the rejection of high purity beamtest pions is steadily increasing.

The PDFs implemented in the likelihood method are extracted for each data period by the TRD-independent selection of particle samples and the corresponding normalized pulse height spectra. The ionization energy deposition of hadrons depends in general on the particle momentum (see section 3.2). Therefore, generating PDFs for multiple momentum intervals presumably increases the separation of leptons and hadrons. A different approach is chosen in this analysis: to solve the problem of binning effects and low statistics at high momenta a correction of the pulse height for particle momentum is implemented optionally (see section 4.4.2). Apart from the temperature correction all pulse height corrections presented in section 4.4 are applied in the likelihood analysis to generate an pulse height spectrum of a given particle type with a single PDF independent of time, incident angle and particle rigidity. To provide an optional momentum correction PDFs generated per particle type: one independent of the particle momentum measured in the Tracker and the respective correcting into account. With their typically high gamma factors leptons are at the Fermi plateau of the Bethe-Bloch function. This manifests in a momentum-independent ionization spectrum. Also the emission of transition radiation photons is independent of

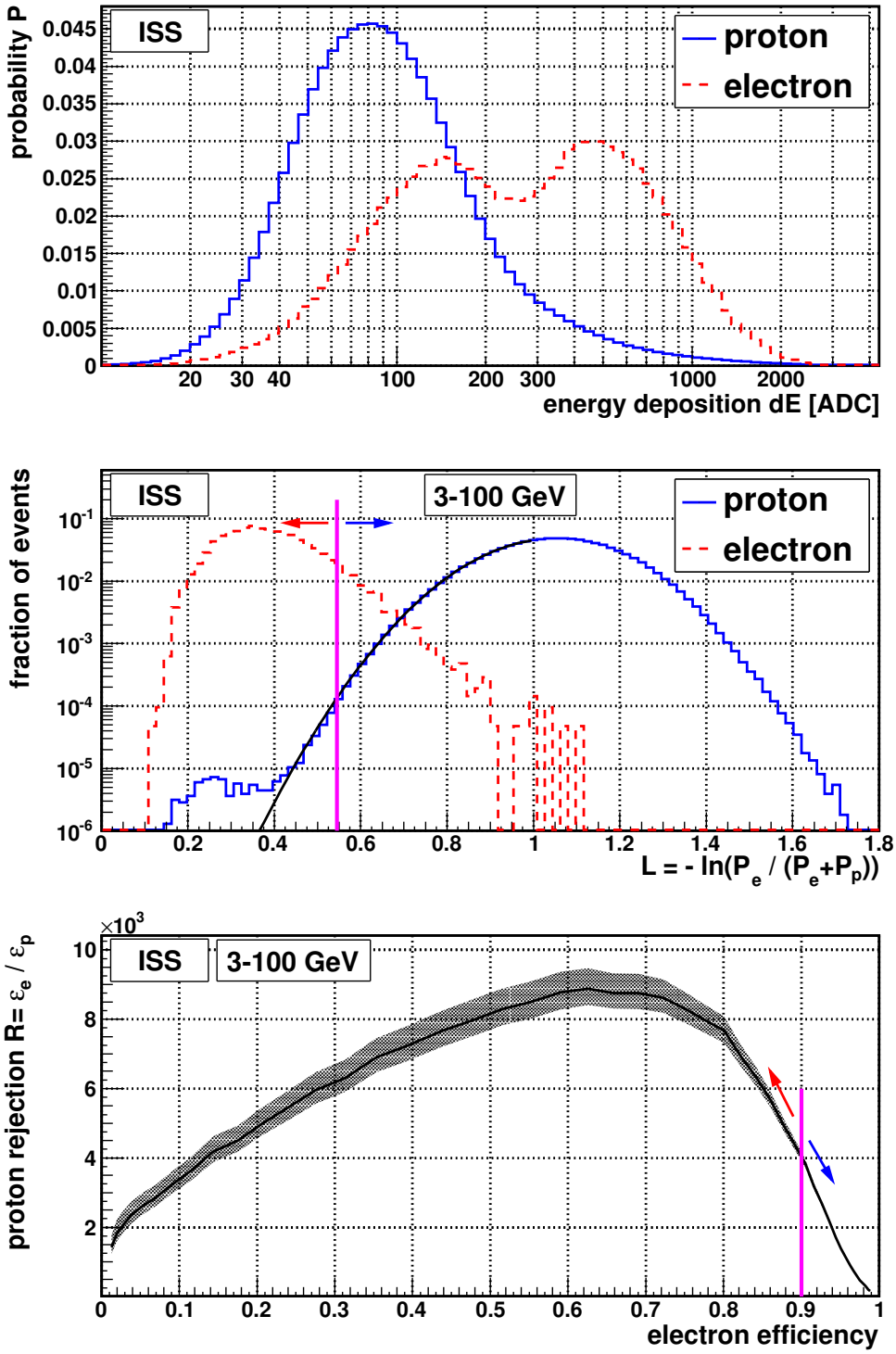

Figure 4.71: TRD particle identification by likelihood analysis in space. The probability density functions for proton and electron events (top) are extracted from space data. The electron likelihood ratio $L = -\ln(P^e/(P^e + P^p))$ (center) is calculated for a given event to disentangle electron (red) from proton (blue) events. An adjustable cut on L is used to control the particle identification efficiencies (bottom).

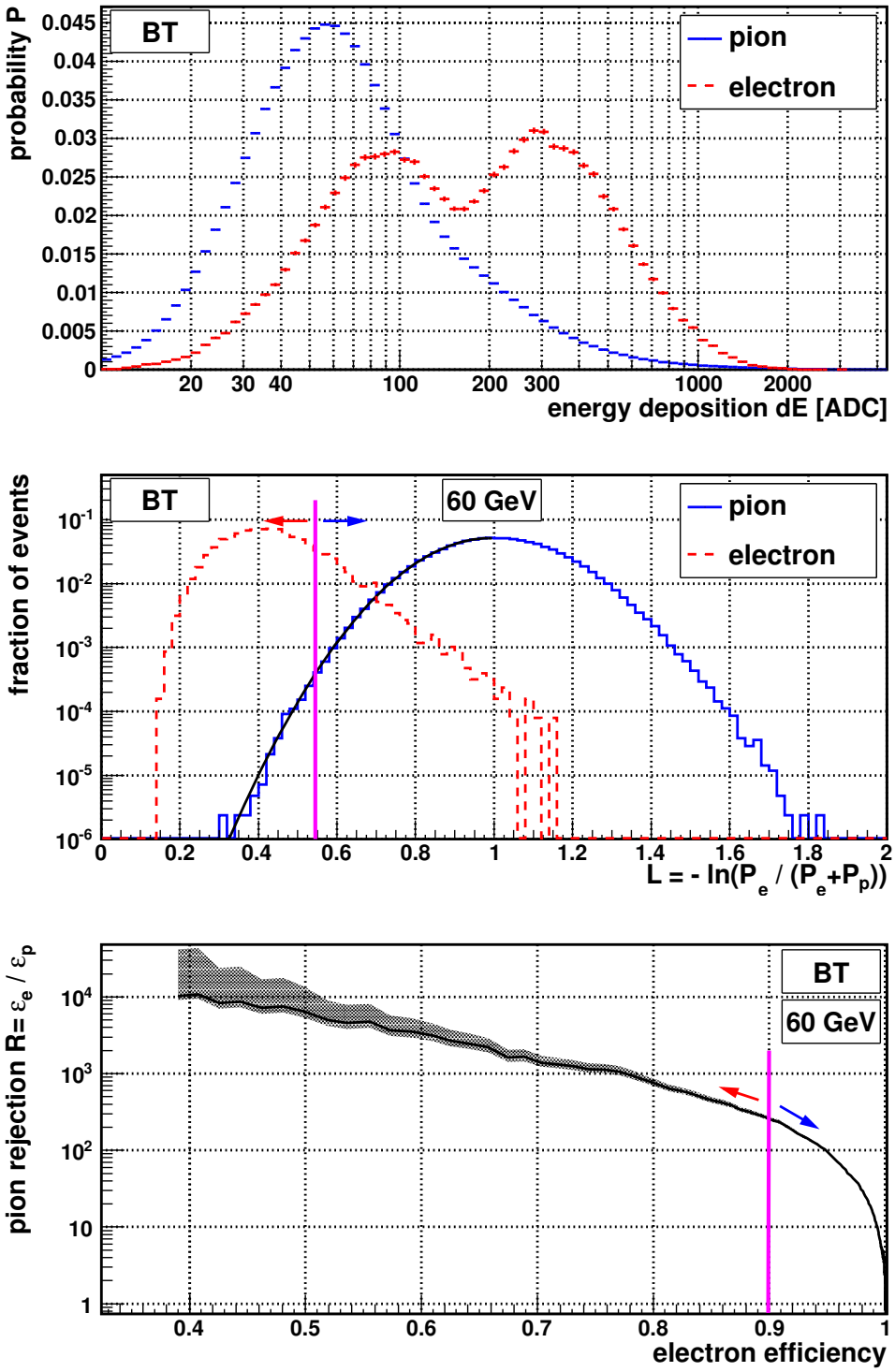

Figure 4.72: TRD particle identification by likelihood analysis in beamtest. The probability density functions for pion and electron events (top) are extracted from beamtest data. The electron likelihood ratio $L = -\ln(P^e/(P^e + P^p))$ (center) is calculated for a given event to disentangle electron (red) from pion (blue) events. An adjustable cut on L is used to control the particle identification efficiencies (bottom).

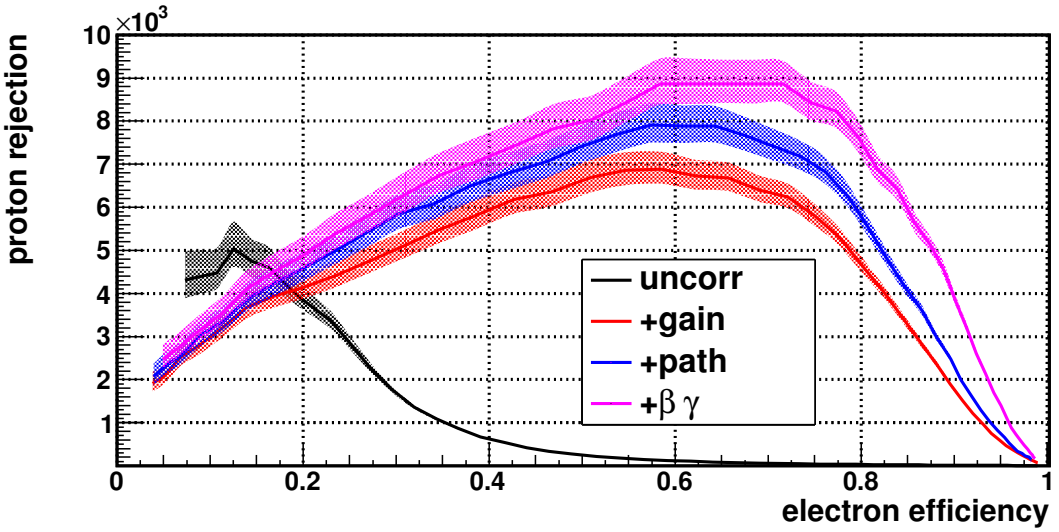

Figure 4.73: The impact of pulse height corrections on the TRD particle identification performance. The proton rejection is increased by the successive application of pulse height corrections gain (red), path length (blue) and $\beta\gamma$ (magenta).

particle momentum at high gamma factors (see section 3.1). Therefore no momentum correction is applied for the electron hypothesis.

4.5.2 Optimization

In figure 4.73 the impact of pulse height corrections on the separation of protons and electrons in the $3 - 100\,\mathrm{GeV}$ range is presented. All the presented correction algorithms, especially the gain calibration, have a positive impact on the proton rejection. The proton rejection at 90 % electron efficiency can be increased from ~ 15 to ~ 4000 by applying all pulse height corrections. At low electron efficiencies some combinations of pulse height corrections lead to lower rejection values. This is generated by broader likelihood distributions, which reflects the worse separation of the hypotheses. Systematically increased pulse heights, due to e.g. higher gas gain in special periods, increases the probability of the electron hypothesis for proton events and decreases the probability of the proton hypothesis for electron events. The resulting lower cut on electron efficiency decreases the number of proton events passing the cut and thus increases the proton rejection value. The $\beta\gamma$ correction introduces additional TRD-independent uncertainties by the usage of particle rigidity, measured by Tracker. This motivates two likelihood analysis approaches: a TRD standalone (SA) and a rigidity dependent (+TK) one, where the latter utilizes the $\beta\gamma$ correction in addition to the gain and path length correction.

The angular dependency of the proton rejection is shown in figure 4.74. Here, the total event sample in momentum range $3 - 100\,\mathrm{GeV}$ is split into angular bins and the proton rejection

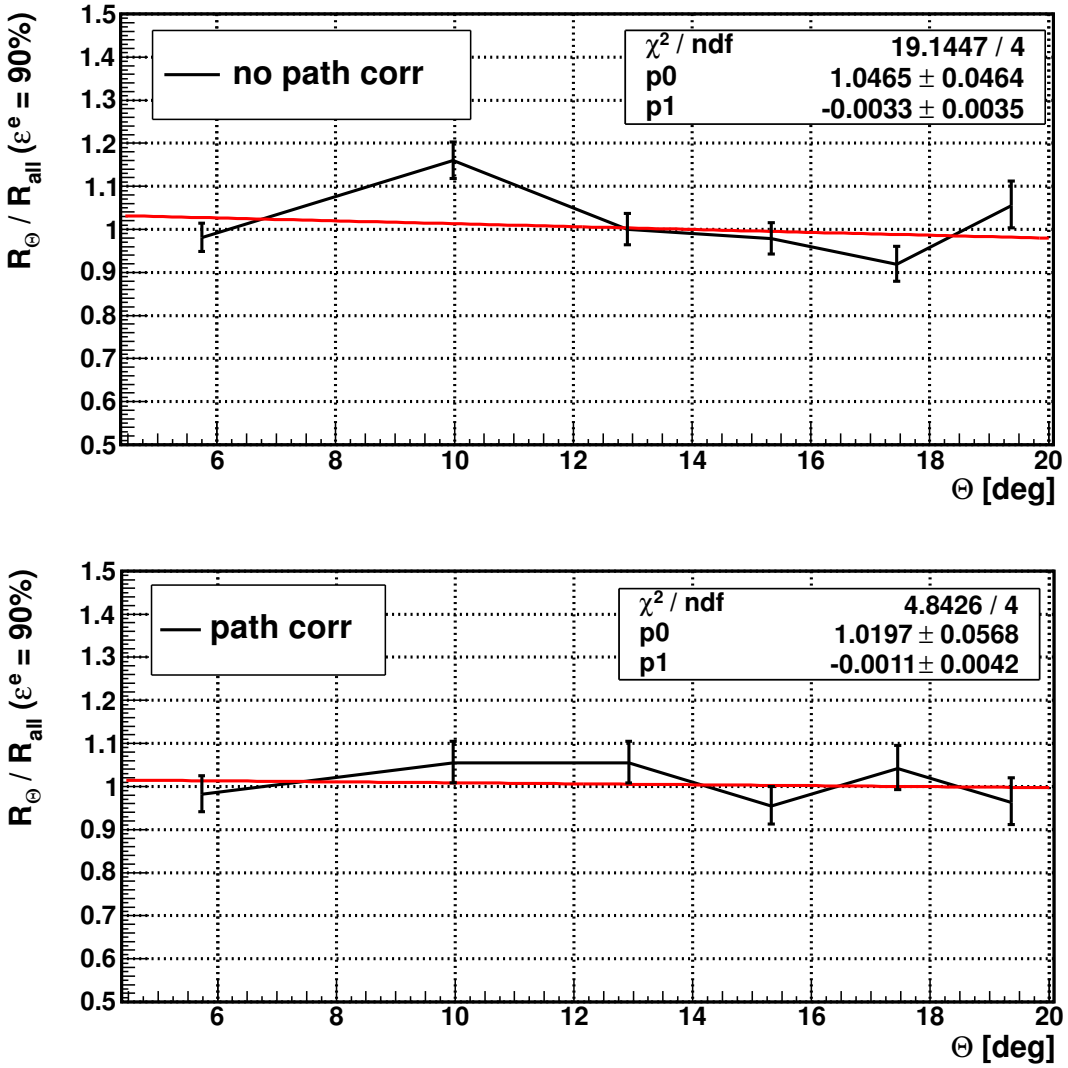

Figure 4.74: The impact of path length correction on the angular dependency of the TRD particle identification performance. Without path length correction (top) the observed angular dependency cannot be described by a flat linear fit. The path length corrected angular dependency is in good approximation linear and compatible with slope zero.

obtained in each bin is set into relation R_Θ / R_{all} to the overall value R_{all}. As expected, the angular dependency, observable as an angular decrease of the ratio and a low χ^2/ndf of the linear fit, is reduced by the path length correction. After correction the angular dependency is in good approximation compatible with zero.

After fixing the pulse height corrections the influence of PDF parameters is investigated. As discussed in section 3.1 the contribution of transition radiation to the pulse height spectrum is a function of particle gamma factor and detector depth. Therefore, the production of layer-wise lepton PDFs is expected to increase the separation of leptons and hadrons. Additionally, a logarithmic binning of PDFs is intended to accumulate less frequent high pulse heights in the pulse height spectra and thus to flatten out statistical fluctuations. The particle identification efficiencies for PDF parameter combinations is shown in figure 4.75. Apparently, the impact of PDF parameters on the particle identification is significantly lower than for pulse height corrections. The definition of single layer electron PDFs has a positive impact on the proton rejection. Although an additional logarithmic binning apparently slightly reduces the proton rejection, it is selected in both approaches to flatten statistical fluctuations. Hence, single layer electron PDFs and logarithmic binning is used in all presented likelihood analyses.

A further optimization might be a cut on the number of layers which contribute to the likelihood analysis. Here, the pulse heights on track per layer have to pass the pulse height threshold of 15 ADC. The path length correction disregards a fraction of hits with low path lengths (see section 4.4.3) and may therefore directly exclude layers from the likelihood analysis. All corrections may reduce the deposited energy below the threshold and therefore indirectly exclude layers. The impact of a cut on the number of layers utilized in the likelihood analyses is shown in figure 4.76. The number of layers available for the analyses is in average ~ 18.5 (see section 4.3.3). Introducing a cut on N_{layer} has a negative impact on the TRD particle identification. The electron efficiency is reduced significantly with increasing cut value[2]. Towards low electron efficiencies the different proton rejection curves recover to the same trend. Only for restrictive cuts, here at least 18 layers utilized in the likelihood analysis, the proton rejection is slightly increased at low electron efficiencies. However, the same rejection values can be obtained with higher electron efficiencies without a cut on N_{layer}. Lowering the electron efficiency without increasing the proton rejection is not useful in the scope of this analysis and hence it is refrained from introducing a cut on N_{layer} in the following.

[2] particle efficiencies are determined relative to all events available for likelihood analysis after TRD track selection and matching, excluding the cut on the number of layers

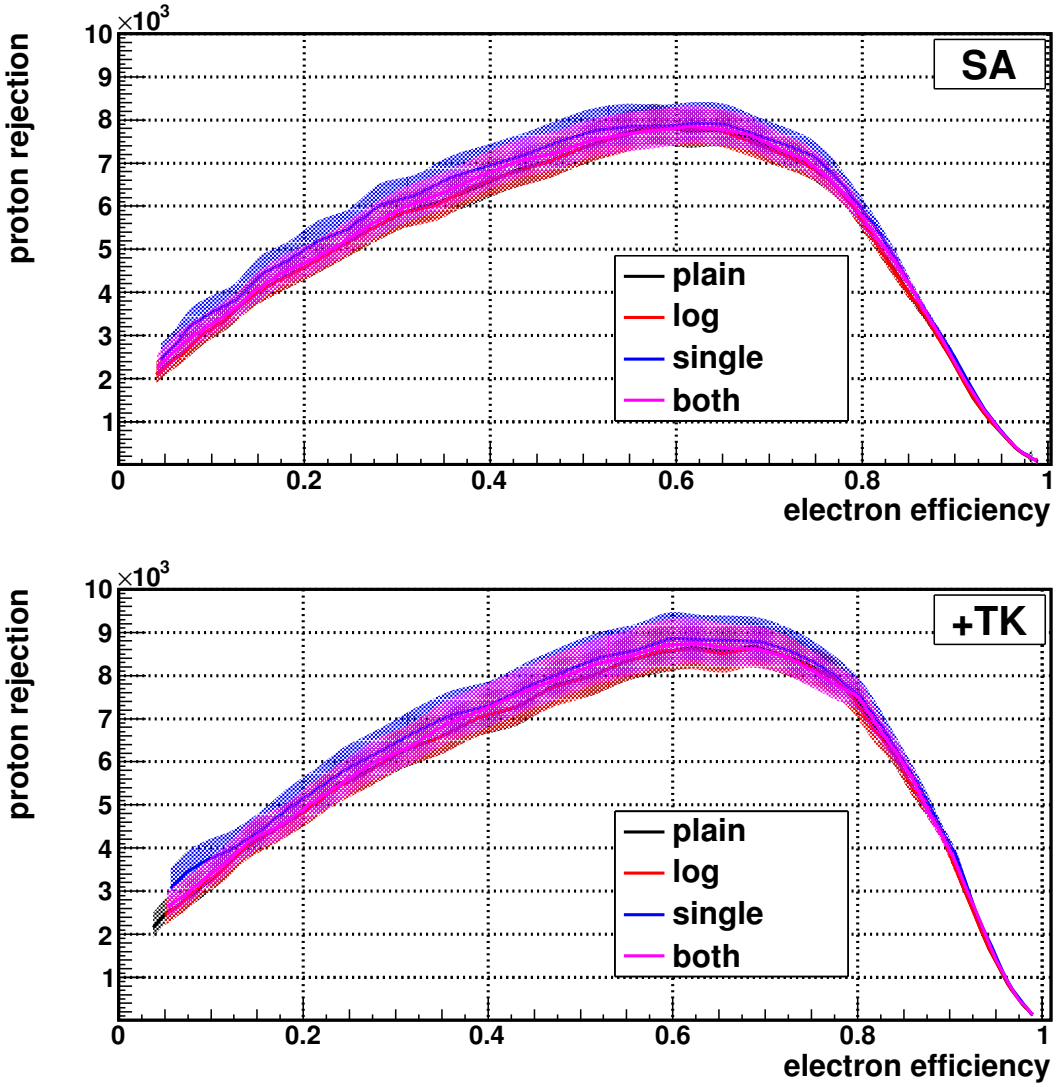

Figure 4.75: Proton rejection of TRD standalone 'SA' (top) and '+TK' (bottom) analysis as function of electron efficiency for different probability density function parameters. Logarithmic binning is denoted by 'log' and single-layer electrons PDFs are denoted by 'single'.

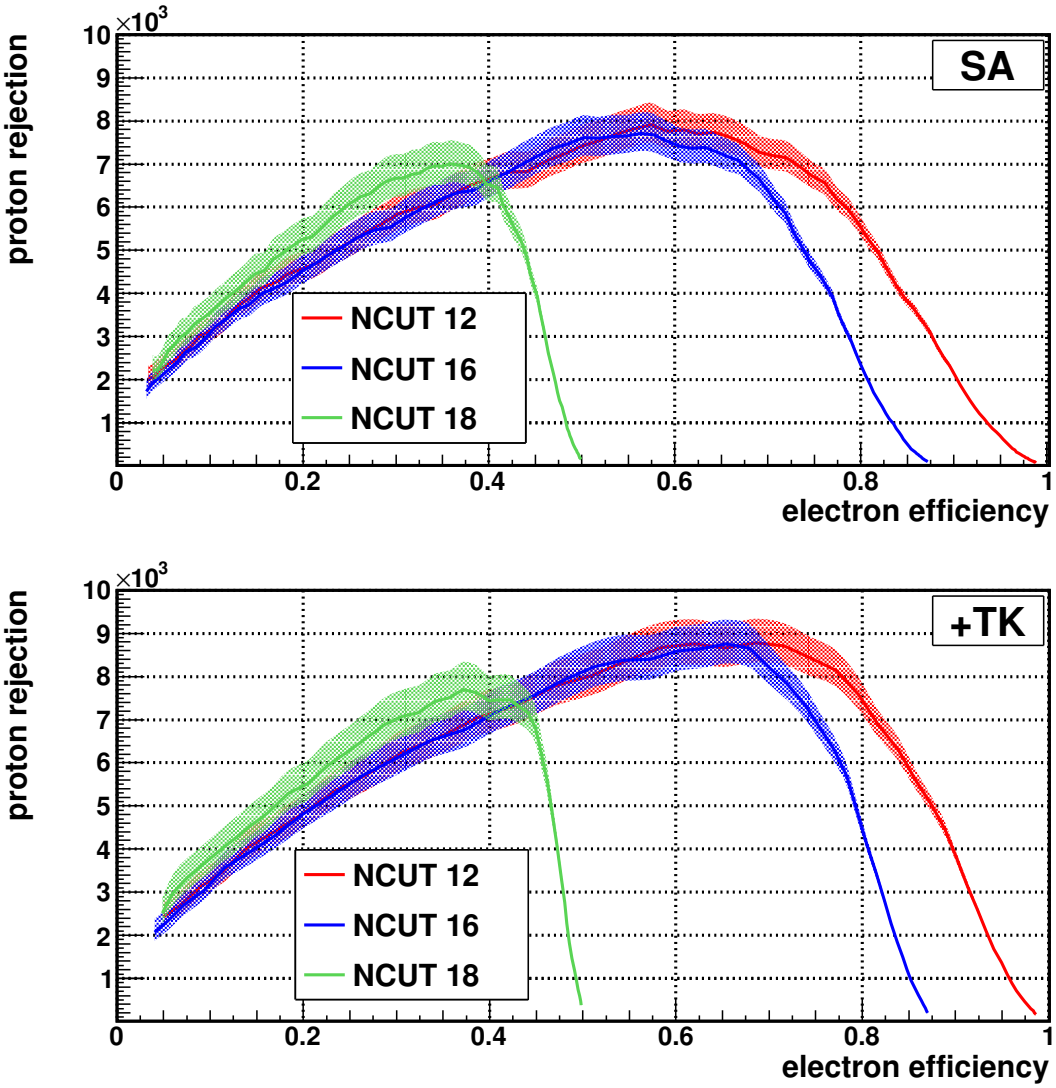

Figure 4.76: The impact of a cut $N_{layer} >= NCUT$ on the number of layers utilized in the likelihood analysis on the proton rejection for standalone 'SA' (top) and rigidity dependent '+TK' (bottom) likelihood analysis.

4.5.3 Performance

The momentum dependence of the '+TK' likelihood values L of electron and proton events is shown in figure 4.77 and 4.78 respectively. The correction of pulse heights for particle momentum results in momentum-independent likelihood values for electron and proton events. In the tails of the distributions mainly statistical fluctuations and possibly systematical deviations lead to a structure in the selection efficiencies for fixed cut $L < 0.525$. This cut provides in combination with the particle flux an integral electron efficiency of 90 % and an integral proton rejection of $\sim$ 4000. The electron efficiency might also be defined bin-wise for each momentum interval. In this case the event statistics, especially at high momenta, leads to increased statistical uncertainties.

The proton rejection obtained for 90 % bin-wise and overall electron efficiency for the two likelihood analyses is shown in figure 4.79. The difference in proton rejection between the two electron efficiency definitions is in general low, with a slightly increased performance for the bin-wise definition, especially for higher momenta. To reduce the statistical uncertainty for bin-wise electron efficiency the number of bins had to be reduced. The standalone proton rejection is steadily decreasing from $\sim$ 3500 at $\sim$ 3 GeV to $\sim$ 300 at $\sim$ 90 GeV. The proton rejection obtained by rigidity-dependent likelihood analysis is independent of particle momentum. The slope obtained by a linear fit is 2.0 ± 14.9 is compatible with zero. Due to the negligible difference between the two efficiency definitions and the uncertainties introduced by event statistics the proton rejections presented in this work are produced with 90 % overall electron efficiency in the $3 - 100$ GeV interval.

The resulting proton rejection obtained from space data is compared to equivalent beamtest results in figure 4.80. All obtained results indicate a TRD proton rejection well above the minimum design specifications of proton rejection factor 100 for particle momenta $|P| \leq$ 250 GeV. In the likelihood analysis of AMS-02 beamtest data, pions and not protons were separated from electrons. Due to their lower mass pions correspond to higher momentum protons. In this figure the beam energies and the corresponding pion momenta were scaled by the mass ratio $\frac{m_{p^+}}{m_{\pi^\pm}} \approx 6.7$ to equivalent proton momenta of $134 \leq P/\text{GeV} \leq 1206$. This equivalent momentum is used to correct the pion pulse heights according to the $\beta\gamma$ correction extracted from space protons (see section 4.4.2). The proton rejection obtained in the beamtest analysis is in good approximation the continuation of corresponding space results. However, there are significant differences in the TRD operational parameters between beamtest and space setup (see section 4.1). Additionally, the TRD-independent classification of protons presented in this work apparently produces a significant contamination, which constrains the determination of proton rejection to lower limits. Further optimization of the event classification to suppress the contamination of data samples has to result in an increased and more realistic estimation of the proton rejection.

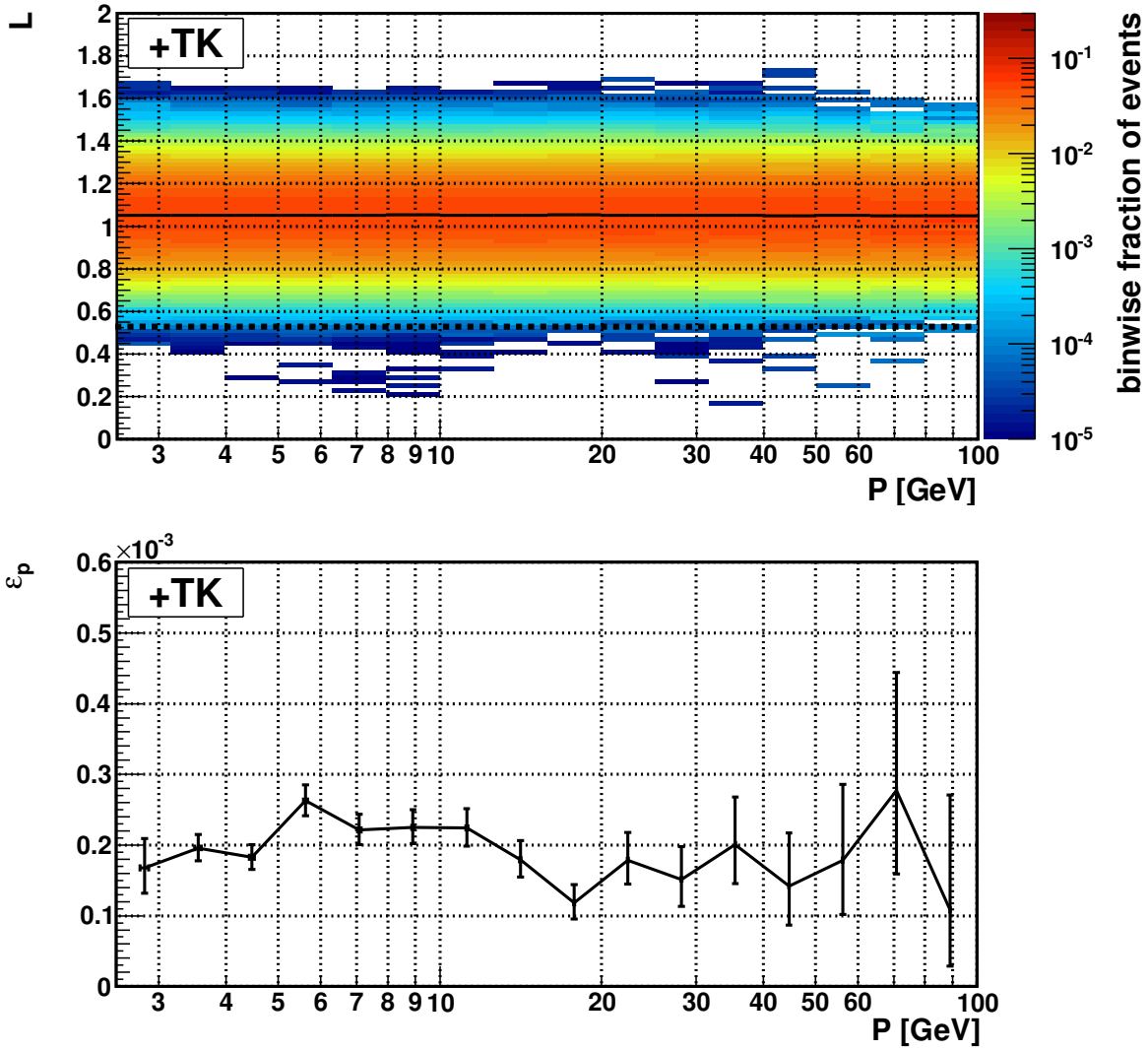

Figure 4.77: TRD likelihood values for proton events as function of momentum for rigidity-dependent likelihood analysis '+TK'. The distribution of L normalized to one in each momentum interval (top) with average value per bin (black markers) and the efficiency (bottom) of a fixed cut $L < 0.525$ (dotted line) in the corresponding momentum intervals.

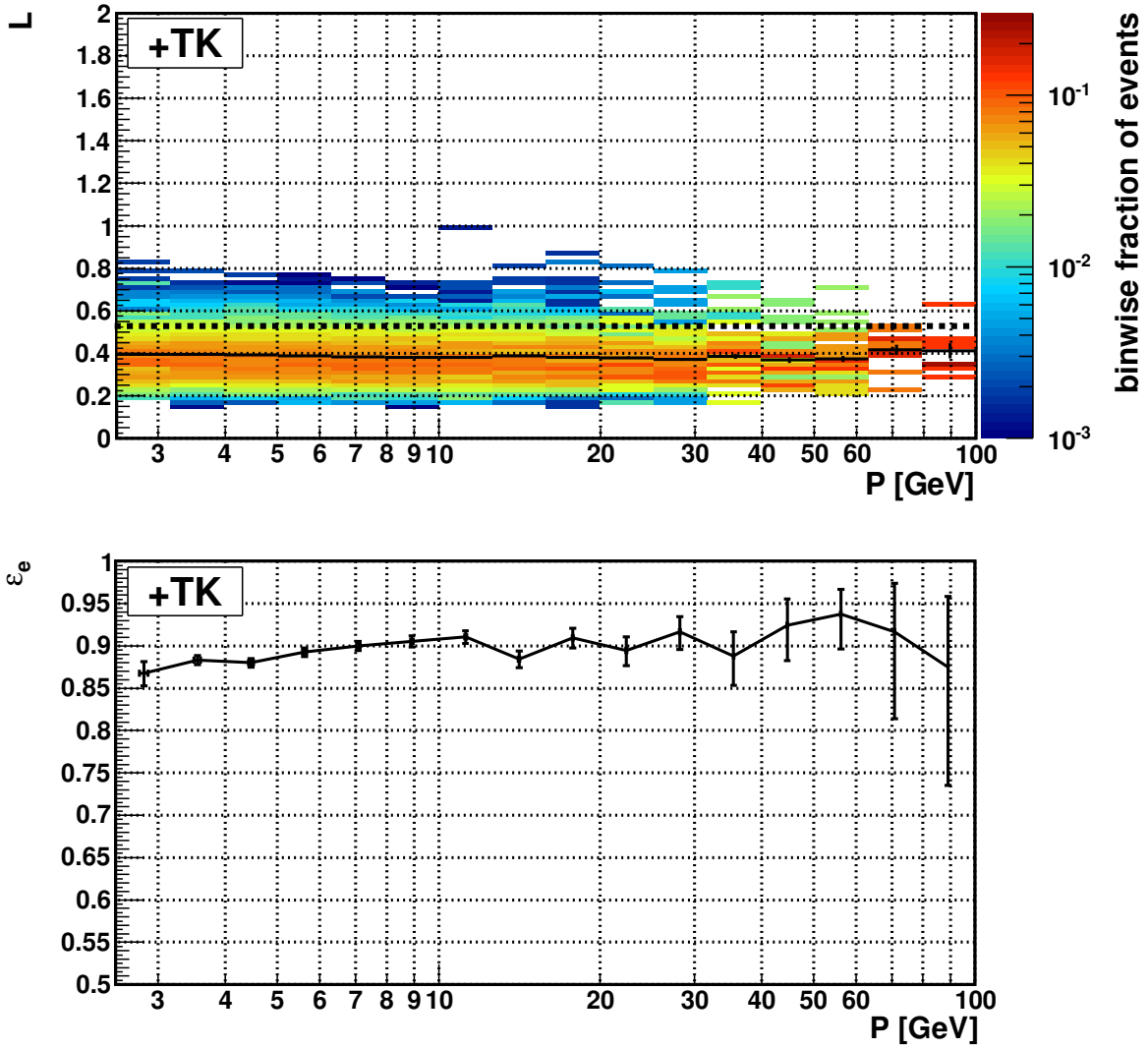

Figure 4.78: TRD likelihood values for electron events as function of momentum for rigidity-dependent analysis '+TK'. The distribution of L normalized to one in each momentum interval (top) with average value per bin (black markers) and the efficiency (bottom) of a fixed cut $L < 0.525$ (dotted line) in the corresponding momentum intervals.

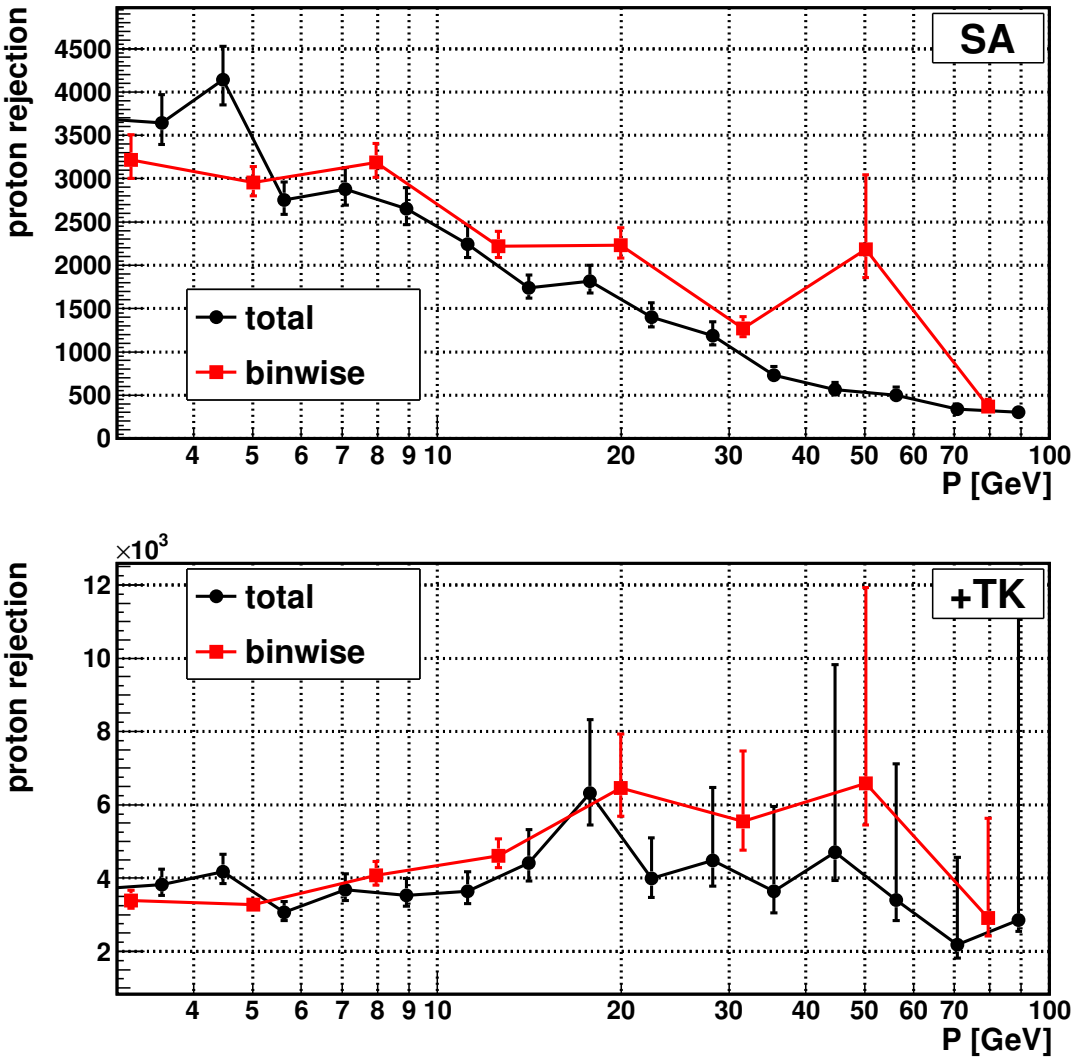

Figure 4.79: Proton rejection for standalone (top) and rigidity dependent (bottom) likelihood analysis at 90 % electron efficiency in the total momentum interval $3 - 100$ GeV (black) and in each individual momentum interval (red).

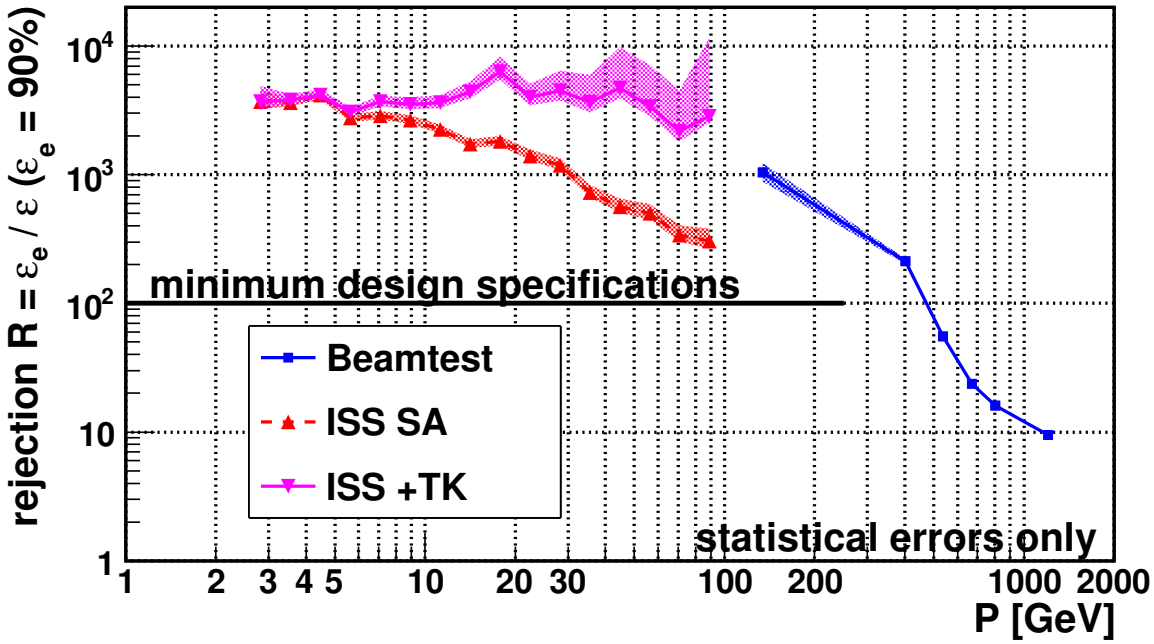

Figure 4.80: Comparison of the particle identification performance obtained for space and beamtest data. The $\beta\gamma$ correction of pulse heights, which discriminates '+TK' (magenta) from 'SA' (red) analysis, corrects the momentum dependency of proton rejection. Beamtest pions (black), which mimic high-momentum protons ($\frac{m_p}{m_\pi} \approx 6.7$), are evaluated by the '+TK' analysis and are in good approximation a continuation of the corresponding space data.

Summary

The measurement of the cosmic ray positron fraction up to several hundred GeV has finally come into reach. The most recent highest-energy results are provided by PAMELA and Fermi and support consistently an unexpected excess. The main difference between AMS-02 and these detectors is the combination of larger acceptance and lower uncertainty introduced by proton contamination of the positron sample. Due to the increased acceptance AMS-02 already outdistanced the statistics collected by many other astroparticle physics experiments. The combination of electromagnetic calorimeter and transition radiation detector is designed to suppress the proton background by more than factor 10^6 to allow for the identification of clean lepton samples.

In the scope of this thesis a subset of the AMS-02 atmospheric muon data of about one week has been analyzed. The acceptance of the corresponding event selection has been determined by Geant4 simulations. In combination with the determined particle rate the differential flux of sea-level muons is obtained (see figure 4.14). The obtained flux and charge ratio results are compatible with BESS-TeV and world average data in the $5 - 50\,\mathrm{GeV}$ region. At low momenta the experimental setup, especially the geomagnetic cutoff and additional traversed material like ceilings, might introduce systematic deviations. Above $50\,\mathrm{GeV}$ the limited inner Tracker momentum resolution, with determined maximum detectable rigidity $MDR \approx 230\,\mathrm{GeV}$, might generate an excess in the observed particle flux, due to misreconstructed high-momentum muons, and a lower charge ratio by charge sign confusion.

The geomagnetic cutoff as function of geodetic latitude and longitude is reconstructed (see figure 4.17). The shape of the resulting geomagnetic cutoff map matches the IGRF predictions. A systematic deviation on the $\lesssim 5\,\%$ level is observed. This is most likely due to the impact of isotropic data analysis in contrast to the vertical rigidity cutoff predicted by simulations. The magnetic deflection of inclined tracks is enhanced, especially for higher magnetic fields at the equator, and therefore the corresponding reonstructed cutoff value is increased.

The emphasis of this thesis is set on development and evaluation of an algorithm to disentangle leptons from hadrons with the transition radiation detector. The necessary steps, starting from particle tracking through event selection to detector calibration and particle

identification by likelihood analysis, are taken. The particle identification performance of the TRD is evaluated on space data (see figure 4.80). A positive impact of energy deposition corrections on the separation performance is found. A TRD standalone and a momentum-dependent likelihood analysis, taking the momentum reconstructed in the inner Tracker into account, are developed and compared. As just one probability density function is used for protons in this work, the momentum correction increases the performance of the likelihood analysis especially at high momenta, where the relativistic rise of ionization energy depositions is compensated. In the highest analyzed momentum bin, centered at 90 GeV, the proton rejection, defined as the ratio of electron and proton efficiency, is 305^{+76}_{-38} for standalone and 2847^{+8764}_{-306} for momentum-dependent likelihood analysis at 90 % electron efficiency.

In the momentum-dependent likelihood analysis of beamtest data pions were separated from electrons. By their higher Lorentz gamma factor pions mimic higher momentum protons. This is used to investigate the transition radiation threshold, limiting the identification performance by the commence of proton-induced transition radiation. The obtained pion efficiency for a given beam energy was therefore scaled by the mass ratio to the corresponding proton momentum. The pion rejection at 90 % electron efficiency is limited to ~ 10 at 1 TeV equivalent proton momentum. A higher rejection of $\gtrsim 100$ can be achieved by applying a harder cut on the electron sample, lowering the electron efficiency to ~ 60 %. The identification performance obtained for beamtest data is in good approximation a continuation of the space data results.

Above ~ 100 GeV systematic uncertainties introduced by the limited momentum resolution of the inner Tracker constrain the analyses presented in this work. With fully aligned detector and optimized particle identification efficiencies a measurement of the positron fraction up to 1 TeV might be feasible.

List of Figures

List of Tables

Bibliography

[1] Charles D. Dermer et al., *Adiabatic Losses and Stochastic Particle Acceleration in Gamma-Ray Burst Blast Waves*, Astrophys.J. 556:479-493, 2001

[2] G. Barbiellini et al., *Stochastic wake field particle acceleration in Gamma-Ray Bursts*, arXiv:astro-ph/0604235v1,2006

[3] M. Risse et al., *Upper limit on the photon fraction in highest-energy cosmic rays from AGASA data*, Phys.Rev.Lett. 95 (2005) 171202

[4] The pierre Auger Collaboration, *Update on the correlation of the highest energy cosmic rays with nearby extragalactic matter*, Astropaticle Physics 34:314-326, 2010

[5] K.Lake, *All static spherically symmetric perfect fluid solutions of Einstein's Equations*, Phys.Rev. D67, 104015, 2003

[6] M.D. Roberts, *A Fluid Generalization of Membranes*, arXiv:hep-th/0406164v2, 2011

[7] Astronomy Notes, *http://www.astronomynotes.com/ismnotes/rotcurv2-big.gif*

[8] WMAP homepage, *http://wmap.gsfc.nasa.gov*

[9] E. Komatsu et al., *Seven-Year Wilkinson Microwave Anisotropy Probe (WMAP) observations: Cosmological Interpretation*, Astrophys.J. 192:18 (47pp), 2011

[10] V. Sahni, *Dark Matter and Dark Energy*, Lect.NotesPhys. 653,141-180,2004

[11] Chandra X-ray Observatory, http://chandra.harvard.edu/photo/2006/1e0657

[12] T.M. Nieuwenhuizen et al., *Do micro brown dwarf detections explain the galactic dark matter?*, arXiv:1011.2530, 2010

[13] E.W Otten, C. Weinheimer, *Neutrino mass limit from tritium beta decay*, Reports on Progress in Physics 71, 86201, 2008

[14] F. Cerutti, *Determination of the upper limit on m_{ν_τ} from LEP*, arXiv:hep-ex/9903062v2, 1999

[15] S.A. Thomas et al., *Upper Bound of 0.28 eV on Neutrino Masses from the Largest Photometric Redshift Survey*, Phys. Rev. Lett. 105, 031301, 2010

[16] J. Feng, *Dark Matter Candidates from Particle Physics and Methods of Detection*,

Ann.Rev.Astron.Astrophys. 48, 495, 2010

[17] Y. Shadmi et al.,*Dynamical supersymmetry breaking*, Rev. Mod. Phys 72 (25-64), 2000, arXiv:hep-th/9907225

[18] The CDMS II Collaboration, *Dark Matter Search Results from the CDMS II Experiment*, Science Vol. 327 no, 5973 pp. 1619-1621, 2010

[19] K.S. Babu, *Recent Progress in SUSY GUTs*, arXiv:1103.3491v1, 2011

[20] S.S. McGaugh et al., *The baryonic Tully-Fisher Relation*, Astrophys.J. 533:L990-L192, 2000

[21] S. McGaugh, *A Novel Test of the Modified Newtonian Dynamics with Gas Rich Galaxies*, Phys. Rev. Lett. 106, 121303, 2011

[22] M.A. Malkov et al., *Mechanism for spectral break in cosmic ray proton spectrum from Suernove remnant W44*, Nature Communications 2 #194, 2011

[23] T. Shibata et al., *A possible approach to three-dimensional cosmic-ray propagation in the Galaxy IV. Electrons and electron-induced gamma-rays* , Astrophys.J. 727:38, 2011

[24] Kamae et al., *Diffractive Interaction and Scaling Violation in* $pp \to \pi^0$*Interaction and GeV Excess in Galactic Diffuse Gamma-Ray Spectrum of EGRET*, Astrophys.J. 620, 244-256, 2005

[25] R. Bayes et al., *Experimental Constraints on Left-Right Symmetric Models from Muon Decay* , Phys. Rev. Lett. 106, 041804, 2011

[26] J.A. Abreu et al., *Past and Future Solar Activity from Cosmogenic Radionuclides*, ASP Conference Series, Vol 428:287, 2010

[27] I.G. Usoskin et al., *Solar modulation parameter for cosmic rays since 1936 reconstructed from ground-based neutron monitors and ionization chambers*, Journal of Geophysical Research, Vol. 116, A02104, 2011

[28] S. Parhi et al., *Toward an Ab Initio Theory of the Solar Modulation of Cosmic Rays*, Astrophys.J. 582:502, 2003

[29] J.S. Perko, *Solar modulation of galactic antiprotons*, Astron.& Astrophys. 184,119-121,1987

[30] C. Rastoin et al., *Time and space variations of the Galactic cosmic ray electron spectrum in the 3-D heliosphere explored by Ulysses*, Astron. Astrophys. 307, 981-995, 1996

[31] C.M. Tiwaru et al., *Study of anisotropic variation of cosmic rays intensity with solar activity*, Natural Science Vol.3, No.2, 101-103, 2011

[32] IGRF homepage, *http://www.ngdc.noaa.gov/IAGA/vmod/igrf.html*

[33] N.A. Tsyganenko, *On the reconstruction of magnetospheric plasma pressure distributions from empirical geomagnetic field models*, Journal of Geophysical Research Vol.115, A07211, 2010

[34] WJ Hughes, *The magnetopause, magnetotail and magnetic reconnection*, Introduction to

space physics, edited by MG Kivelson and CT Russel, Cambridge University Press, 1995

[35] R. Vainio in J.Lilensten et al., *Developing the Scientific Basis for Monitoring, Modelling and Predicting Space Weather*, Acta Geophysica 57, Number 1, 1-14, 2009

[36] PLANETOCOSMICS homepage, *http://cosray.unibe.ch/ laurent/planetocosmics*

[37] F. Fürst, *Temporal variations of strength and location of the South Atlantic Anomaly as measured by RXTE* , EPSL Vol. 281, Issues 3-4, 2009

[38] J. van Buuren, *Untersuchung der myonischen Komponente ausgedehnter Luftschauer mit dem KASCADE-Grande Experiment*, PhD Thesis, Karlsruhe, 2005

[39] K. Nakamura et al., *Particle Data Group*, J. Phys. G 37, 075021 (2010)

[40] T. Shibata et al., *A Possible Approach to Three-dimensional Cosmic-Ray Propagation in the Galaxy. II. Stable Nuclei with Energy Change*, Astrophys. J. 642, 882-901, 2006

[41] I. Moskalenko et al., *Secondary Antiprotons and Propagation of Cosmic Rays in the Galaxy and Heliosphere*, Astrophys.J. 565, 280-296, 2002

[42] K. Blum, *Cosmic ray propagation time scales: lessons from radioactive nuclei and positron data*, arXiv:1010.2836, 2010

[43] T. Hams et al., *Measurement of the Abundance of Radioactive 10Be and Other Light Isotopes in Cosmic Radiation up to 2 GeV Nucleon-1 with the Balloon-borne Instrument ISOMAX*, Astrophys.J., 611:892:905, 2004

[44] D. Grasso et al., *On possible interpretations of the high energy electron-positron spectrum measured by the Fermi Large Area Telescope*, Astropart.Phys 32, 140-151,2009

[45] T. Kamae et al., *Cosmic Ray* $e^+/(e^- + e^+)$, $\bar{p}/p$ *Ratios Explained by an Injection Model Based on Gamma-ray Observations*, arXiv:10103477, 2011

[46] M. Perelsten, B. Shakya, *Antiprotons from Dark Matter: Effects of a Position-Dependent Diffusion Coefficient*, arXiv:1012.3772, 2010

[47] X. Bi et al., *Parameters in a class of leptophilic dark matter models from PAMELA, ATIC and FERMI*, Phys.Lett.B 678, Issue 2, 2009

[48] O. Adriani et al., *PAMELA Results on the Cosmic-Ray Antiproton Flux from 60 MeV to 180 GeV in Kinetic Energy*, Phys.Rev.Lett. 105, 121101, 2010

[49] R.A. Lineros, *Positrons from cosmic rays interactions and dark matter annihilations*, Nuovo Cim.125B, 1053-1070, 2010

[50] Alpha Magnetic Spectrometer homepage, *http://www.ams02.org*

[51] STS-134 Mission homepage, *http://www.nasa.gov/mission_pages/shuttle/shuttlemissions/sts134/main/index.html*

[52] S. Fopp, *Entwicklung und Bau eines auf Proportionalkammern basierenden Uebergangsstrahlungsdetektors für das AMS-02-Weltraumexperiment*, PhD Thesis, Aachen, 2004

[53] T. Kirn, homepage, *http://accms04.physik.rwth-aachen.de/ kirn*

[54] T. Siedenburg, *Technical drawing for internal purposes*, 27. October, 2008

[55] AMS-02 TRD group, *TRD / ACC / TAS Slow Control and Data Monitoring*, internal paper, 2011

[56] V. Bindi et al., *The scintillator detector for the fast trigger and time-of-flight (TOF) measurement of the space experiment AMS-02*, NIM A 623, 968-981, 2010

[57] P. von Doetinchem, *Search for Cosmic-Ray Antiparticles with Balloon-borne and Space-borne Experiments*, PhD Thesis, Aachen, 2009

[58] A. Goerres, *Kalibration und Integration des AMS-02 Anti-Koinzidenz-Detektors*, Diploma thesis, 2010

[59] K. Lübelsmeyer et al., *Upgrade of the Alpha Magnetic Spectrometer (AMS-02) for long term operation on the International Space Station (ISS)*, NIM A 654, 639-648, 2011

[60] B. Alpat et al., *The internal alignment and position resolution of the AMS-02 silicon tracker determined with cosmic-ray muons* , NIM A 613, 207-217, 2010

[61] R. Pereira et al., *The AMS-02 RICH detector: Performance during ground-based data taking at CERN* , NIM A 639, 37-31, 2011

[62] M. Pohl, *GeV to Multi-TeV Cosmic Rays: AMS-02 Status and Future Prospects*, PoS 443, ICHEP, 2010

[63] A. Kounine, *AMS Level 3 Algorithms*, AMS internal note, 2011

[64] A.L. Avakian et al., *X-ray transition-radiation yield dependence on the parameters of a stack of plates*, NIM 129, Issue 1, 303-306, 1975

[65] X. Artru et al., *Practical theory of the multilayered transition radiation detector*, Phys.Rev. D 12, 1289-1306, 1975

[66] V.M. Grichine, *Generation of X-ray Transition Radiation Inside Complex Radiators*, Phys.Lett.B 525, 225-239, 2002

[67] Ph.v. Doetinchem et al., *Performance of the AMS-02 Transition Radiation Detector*, NIM A 558, 526-535, 2006

[68] Andronic et al., *Transition Radiation Spectra of Electrons from 1 to 10 GeV/c in Regular and Irregular Radiators*, NIM A 558, 516-525, 2006

[69] M.J. Berger et al., *XCOM: Photon Cross Sections Database*, http://www.nist.gov/pml/data/xcom/index.cfm

[70] J.F. Ziegler, *The Stopping on Energetic Light Ions in Elemental Matter*, J. Appl. Phys / Rev.

Appl. Phys. 85, 1249-1272, 1999

[71] C. Grupen, *Physics of Particle Detection*, arXiv:physics/9906063v1, 1999

[72] L.D. Landau, *On the energy loss of fast particles by ionization*, J. Phys. U.S.S.R. 8, 201, 1944 Reprinted in *Collected papers of L.D. Landau*, Pergamon Press, Oxford, p. 417-424, 1965

[73] H.Bichsel, *A method to improve tracking and particle identification in TPCs and silicon detectors*, NIM A 562, 154-197, 2006

[74] H. Bichsel, *The Interaction of Radiation with Matter*, edited in Landolt-Börnstein - Group I Elementary Particles, Nuclei and Atoms, Springer-Verlag Berlin Heidelberg, 2011

[75] GEANT4 homepage, *http://geant4.cern.ch*

[76] C. Chung, *Space Qualification of the Transition Radiation Detector of the AMS-02 Experiment and Indirect Search for Dark Matter*, PhD thesis, Aachen, 2007

[77] A.Sabellek, *The Space Qualified Data Acquisition for the Transition Radiation Detector of the AMS-02 Experiment on the International Space Station*, PhD Thesis, Karlsruhe, 2009

[78] V. Choutko, A. Klimentov *Status of the AMS Experiment*, Talk at TeV Particle Astrophysics, 2010

[79] A. Kounine, *Computing strategy of Alpha-Magnetic Spectrometer experiment*, NIM A 502, 461–466, 2003

[80] V. Choutko, *Aug 2010 AMS Test Beam Plan*, internal talk, 2010

[81] S.D. Falco, *Results of 2007 test beam of AMS-02 Electromagnetic Calorimeter*, Adv.Space Res. 45, 112–122, 2010

[82] S. Haino et al., *The AMS-02 Silicon Tracker*, ICATPP Conference, 2010

[83] A. Basili, *Technical drawing for internal purposes*, 2010

[84] C. Goy et al., *AMS external trigger for August test beam* , internal talk, 2011

[85] S.Haino et al., *Measurements of Primary and Atmospheric Cosmic-Ray Spectra with the BESS-TeV Spectrometer*, Phys Lett.B 594, 35-46, 2004

[86] T.Hebbeker, Charles Timmermans, *A compilation of high energy atmospheric muon data at sea level*, Astropart.Phys. 18, 107-127, 2002

[87] I. Usoskin et al., *Solar modulation of cosmic rays since 1936: Neutron monitors and balloon-borne data*, J. Geophys. Res. 116, A02104, 2011

[88] V. Naumov, *Atmospheric muons and neutrinos*, Proceedings of 2nd Workshop on Methodical Aspects of Underwater/Underice Neutrino Telescopes, Hamburg, 2001

[89] J. Alcaraz et al., *Protons in near earth orbit*, Phys. Lett. B 472, 215-226, 2000

[90] O. Adriana et al., *PAMELA Measurements of Cosmic-ray Proton and Helium Spectra*, Sci-

ence 332, 69-72, 2011

[91] J.S.E. Townsend, *The theory of ionization of gases by collision*, London, Constable & Company, ltd., 1910

[92] H. Morii et al., *Quenching effects in nitrogen gas scintillation*, NIM A 526, 399-408, 2004

[93] T. Kirn et al., *TRD Integration Status Report*, internal report, AMS TRD Meeting, Rome, 2005

[94] S. Kirkpartick et al., *Optimization by Simulated Annealing*, Science Vol. 220, 671-680, 1983

[95] N.D. Gagunashvili, *Comparison of weighted and unweighted histograms*, PoS(ACAT) 054, 2007

[96] P.A.R. Koopman, *Confidence Intervals for the Ratio of Two Binomial Proportions*, Biometrics Vol. 40 No. 2, 513-517, 1984